Extension of the Aerothermodynamics Modelling in Direct Simulation Monte Carlo

Clément Henri Bernard Civrais

Submitted in fulfilment of the requirements for the
Degree of Doctor of Philosophy

School of Engineering
College of Science and Engineering
University of Glasgow

May 2024

Abstract

The modelling of aerothermodynamic flows is extremely challenging as it combines both aerodynamics and thermodynamics disciplines. Aerothermodynamic applications typically involve high-speed and high-temperature gas flows, giving rise to many processes to the extent of large variation in the transport properties of the gas. This thesis concentrates on expanding the current state of the art of aerothermodynamic modelling for a moderate to high degree of rarefaction. Over the years, the direct simulation monte carlo method (DSMC) has emerged as the standard method for simulating rarefied gas flows due to its ability to model complex non-equilibrium effects in the flows such as non-equilibrium in the internal degrees of freedom of molecules or non-equilibrium chemical processes in great detail. However, the traditional approaches for modelling the vibrational excitation of molecules, the chemical reactions and the interaction between internal modes in the DSMC method present some limitations.

The first research axis focuses on the vibrational modelling of molecular species with an anharmonic oscillator model. This has been motivated by the fact that high-fidelity calculations or state-of-the-art radiation solvers compute the vibrational excitation with an anharmonic oscillator model, whereas the standard approach in the DSMC method relies on a harmonic oscillator model. Therefore, the first objective of this thesis is to quantify the difference between the standard approach in the DSMC method and an anharmonic oscillator mode for the reproduction of the thermodynamic properties. The quantification analysis is then extended to the context of an Earth's planetary reentry of a cylindrical body at an altitude of about 75 km.

The second research axis focuses on the extension of the quantum kinetics (QK) chemistry models, in which vibrational excitation is modelled with an anharmonic oscillator model. This custom version of the QK models has been constructed by a generalisation of the reaction rates to incorporate the modelling of the vibrational excitation with an anharmonic oscillator model. These formulations are extensively investigated for the most representative dissociation reactions occurring in an Earth's atmospheric reentry under thermal equilibrium and non-equilibrium conditions. The new formulations are compared against an extensive compilation of well-established theoretical chemistry models, experimental measurements, and high-fidelity calculations. Through this comprehensive study, the limitations of the new formulations are identified, demonstrating an excessive utilisation of the relative translational energy and under-utilisation of the vibrational energy to promote dissociation reactions. Based on these observa-

tions, an extension of these formulations of QK models is herein proposed incorporating tunable parameters to accurately reproduce the most representative experimental measurements and high-fidelity calculations in both thermal equilibrium and non-equilibrium conditions. These formulations are then applied for the reproduction of in-flight measurements of the surface heat flux experienced by the Space Shuttle Columbia during its second mission at an altitude of about 92.35 km.

The third research axis focuses on the development of a novel model for electronic excited states of molecular species in DSMC. The standard approach in the DSMC method is to treat separately each mode of a chemical species which prohibits any interaction between internal modes. However, aerothermodynamic processes involve the coupling between all internal modes which becomes particularly significant in the analysis of molecular radiation, where achieving the correct distribution of vibrational and electronic excitation energy is crucial. As a result, a novel model that assumes a coupling between the vibrational and electronic modes allowing each electronic excited state to excite its vibrational quantum levels is proposed. Considering the challenge of measuring experimentally chemical processes involving electronic excited states, the novel model is verified against an extensive compilation of theoretical studies. Additionally, the model is applied for a canonical hypersonic flow in Earth's atmosphere past an infinite cylindrical body at an altitude of 85 km.

List of Publications

In Journals

C. H. B. Civrais, M. Pfeiffer, C. White and R. Steijl. Modelling of the electronic excited states in direct simulation Monte Carlo , *Physics of Fluids*, 36(8):086112, 2024.

C. H. B. Civrais, C. White and R. Steijl. Quantum kinetics chemistry models with an anharmonic oscillator model. Model extension and validation, *Physics of Fluids*, submitted.

C. H. B. Civrais, C. White and R. Steijl. Quantum kinetics chemistry models with an anharmonic oscillator model. Model derivation and limitations, *Physics of Fluids*, 36(8):086120, 2024.

C. H. B. Civrais, C. White and R. Steijl. Extension of the normal shock wave relations for calorically imperfect gas. *Shock Waves*, 33:533–551, 2023.

C. H. B. Civrais, C. White and R. Steijl. Vibrational modelling with an anharmonic oscillator model in direct simulation Monte Carlo, *Journal of Thermophysics and Heat Transfer*, 37(3):534–548, 2022.

In Conference Proceedings

C. H. B. Civrais, M. Pfeiffer, C. White and R. Steijl. Development of a coupled vibrational-electronic model in DSMC, *AIP Conference Proceedings*, submitted.

C. H. B. Civrais, C. White and R. Steijl. Influence of anharmonic oscillator model for flows over a cylindrical body, *AIP Conference Proceedings*, 2996(1):080008, 2024.

C. H. B. Civrais, C. White and R. Steijl. Evaluation of a kinetic-theory approach for chemical-reaction rates in upper-atmosphere hypersonic flows, *AIAA AVIATION Forum*, San Diego, CA & Virtual, AIAA Paper 2023-3809, 2023.

Presentation Without Proceedings

C. H. B. Civrais, M. Pfeiffer, C. White and R. Steijl. Modelling of the electronic excited states in DSMC, *Deutsches Zentrum für Luft- und Raumfahrt (DLR)*, Göttingen, Germany, 2023.

C. H. B. Civrais, C. White and R. Steijl. Modelling of the internal modes of chemical species

in hypersonic flows, *Rarefied Gas Dynamics NextGen Meeting*, online, 2023.

C. H. B. Civrais, C. White and R. Steijl. Influence of anharmonic oscillator model for flows over a cylindrical body, *35th Scottish Fluid Mechanics Meeting*, Oban, UK, 2022.

C. H. B. Civrais, C. White and R. Steijl. Vibrational modelling with an anharmonic model in DSMC, *Pre-Rarefied Gas Dynamics 32 Online Workshop on Recent Hot Topics in Rarefied Gas Dynamics*, online, 2021.

Contents

List of Tables

List of Figures

Nomenclature

Latin Symbols

B_e, K_e	Rotational-vibrational coupling parameters
c	Celerity of light in vacuum
c_P, c_V	Isobaric and isochoric specific heat capacity
c_r	Relative speed
d	Diameter
E	Total energy
e	Specific energy or Elementary charge
E_a	Activation energy
F	Helmholtz free energy
f	Distribution function
f'	Normalised distribution function
f_{max}	Normalisation factor
G	Cumulative distribution function
g	Degeneracy
g_e	Electronic degeneracy
g_r	Rotational degeneracy
g_v	Vibrational degeneracy
H	Hamiltonian
h	Planck constant
h_f	Heat of formation
I	Moment of inertia
i	Vibrational quantum level
K	Kinetic energy
k	Boltzmann constant
k_b	Backward reaction rate
k_d	Dissociation reaction rate
k_f	Forward reaction rate
k_s	Bound stiffness
K_{eq}	Equilibrium constant
Kn	Knudsen number
l	Orbital quantum number
L_e	Orbital angular momentum
m	Mass
m_l	Magnetic orbital quantum number
m_s	Magnetic spin quantum number
m_λ	Total magnetic orbital quantum number
m_σ	Total magnetic spin quantum number
Ma	Mach number
N	Number of particle
n	Number density or Electronic quantum level
N_A	Avogadro constant
n_x, n_y, n_z	Translational quantum numbers
N_e	Number of electronic rearrangement
p	Momentum
P_d	Dissociation probability
P_{ex}	Exchange probability
P_e	Electronic relaxation probability
P_v	Vibrational relaxation probability
Q	Partition function

q	Position
R	Specific gas constant
r	Radius
R_{AB-M}	Collision rate
r_{eq}	Inter nuclei equilibrium distance
S	Entropy
s	Spin quantum number
S_e	Spin angular momentum
T	Temperature
T_e	Electronic temperature
T_r	Rotational temperature
T_t	Translational temperature
T_v	Vibrational temperature
T_c	Collision temperature
T_{eq}	Equilibrium temperature
T_{ref}	Reference temperature
U	Potential energy
V	Volume
W_{BE}	Bose-Einstein statistics
W_{FD}	Fermi-Dirac statistics
x, y, z	Cartesian coordinates
Z	Atomic charge
Z_e	Electronic collision number
Z_r	Rotational collision number
Z_v	Vibrational collision number
Z_{neq}	Nonequilibrium factor

Greek Symbols

α	Potential width parameter
β	Thermodynamic beta
Δp	Momentum uncertainty
Δq	Position uncertainty
Δt	Time step
Δx	Spacial discretisation
η	Temperature exponent of the modified Arrhenius equation
γ	Specific heat capacity ratio
γ_{AB-M}	Collision fraction
ι	Total angular momentum quantum number of atomic systems
Λ	Total angular momentum quantum number of molecular systems
λ	Total angular momentum quantum number of atomic systems or Mean free path
μ	Reduced mass
ν	Fundamental frequency
Ω	Observable
ω	Viscosity exponent
ω_e	Harmonic spectroscopic constant
$\omega_e\chi_e$	Anharmonic spectroscopic constant
Ψ	Time-dependant wave function
ψ	Time-independent wave function
Σ	Total spin angular momentum quantum number of molecular systems
σ	Total spin angular momentum quantum number of atomic systems
θ	Asymptotic half-body angle
θ_d	Dissociation temperature
θ_r	Characteristic rotational temperature
θ_v	Characteristic vibrational temperature
υ_1, υ_2	QK models' tunable parameter
ε	Internal energy
ε_0	Vacuum permittivity
ε_c	Collision energy
ε_d	Dissociation energy
ε_e	Electronic internal energy

ε_r	Rotational internal energy
ε_t	Translational internal energy
ε_v	Vibrational internal energy
ς	Symmetry factor
Ξ	Mean internal degree of freedom
ξ_r	Rotational degree of freedom
ξ_t	Translational degree of freedom
ξ_v	Vibrational degree of freedom

Subscripts

$(.)_\infty$	Freestream
$(.)_{e^-}$	Electron
$(.)_f$	Final
$(.)_g$	Gerade
$(.)_i$	Initial
$(.)_n$	Nuclei
$(.)_u$	Ungerade

Superscripts

$(.)^\star$	Post-collision property
$(.)^{DSMC}$	DSMC
$(.)^{theo}$	Theory

Acronyms

aHO	Anharmonic Oscillator
CEA	Chemical Equilibrium with Applications
CFD	Computational Fluid Dynamics
CPU	Central Power Unit
DMS	Direct Molecular Simulation
DSMC	Direct Simulation Monte Carlo
EAST	Electric Arc Shock Tube
HO	Harmonic Oscillator
LB	Larsen-Borgnakke
LCAO	Linear Combination of Atomic Orbitals
MF	Macheret-Fridman
NIST	National Institute of Standards and Technology
NSF	Navier-Stokes-Fourier
OpenFOAM	Open Field Operation And Manipulation
PES	Potential Energy Surface
QCT	Quasi-Classical Trajectory
QK	Quantum-Kinetic
QSS	Quasi-Steady State
STS	Space Transport System
TM	Treanor-Marrone
VHS	Variable Hard Sphere

Acknowledgements

First and foremost, I would like to express my gratitude to my supervisors, Dr Craig White and Dr Rene Steijl, for their guidance, support and technical expertise. Their door was always open for all questions and ideas I brought to them.

The financial support for this project was provided by the College of Science and Engineering through the School of Engineering Scholarship 2020 and is gratefully acknowledged. Additionally, I would like to thank the University of Glasgow and the Jim Gatheral Travel Scholarship 2023 for facilitating a secondment at the University of Stuttgart, during which, a portion of technical work has been completed.

Throughout my education, I have encountered numerous individuals who have served as a source of inspiration, and I would like to take this opportunity to express my gratitude to three of them. First of all, I would like to thank Prof. Sylvain Dubois for introducing me to the world of research. It was through this experience that I discovered the professional career I wished to embrace. Then, I would like to acknowledge Dr Pierre Duquesne for empowering me, which you enjoy passing on to your students. Finally, I would also like to thank Dr Marcel Pfeiffer for welcoming me to his research group and for his guidance. Meeting you at the Rarefied Gas Dynamics Symposium 32^{nd} in Seoul was both unexpected and the beginning of a fruitful collaboration. Your technical skills on the football pitch during the Wednesday Football games were astonishing, and so was your knowledge about physical gas dynamics. I hope one day, we can play against each other. On a more serious note, working alongside you has been enriching, and I hope we can explore further collaborative opportunities on many exciting research projects.

I would like to thank all my friends and colleagues at the James Watt School of Engineering for creating a friendly work environment. A special thanks to Andrea (SPM), Murray (Boilerman), Geng (The Legend) and Rinaldo (Gymboy) for the countless moments shared over the years. If I may offer one piece of advice, it would be this: go easy on the hot sauce next time! Furthermore, I would like to thank Hassam and Thomas for the many fun conversations we have had over the first two years. However, I must reiterate once more: bread does not contain eggs. If it does, it is nothing but a pastry or a brioche. Still, on the culinary theme, I would like to thank Gaargi

for the many discussions about food from the world and for introducing me to the delicacy of India. It was interesting to learn about the Indian's history throughout its food diversity. On a different note, I would also like to thank my colleagues at the University of Stuttgart for the fun time during my secondment. I sincerely hope to meet you all at the next Rarefied Gas Dynamics Symposium in Göttingen.

Finally, a massive thank you to my family for their continuous support and motivation throughout my whole life and education. None of this would have been possible without you. I like to think that this thesis is largely yours. Last but not least, I would like to express my gratitude to my partner for her unconditional love over the past years.

Date: 9 May 2024 Signature: Clément Henri Bernard Civrais

Declaration

I certify that the thesis presented here for examination for a PhD degree of the University of Glasgow is solely my own work other than where I have clearly indicated that it is the work of others (in which case the extent of any work carried out jointly by me and any other person is clearly identified in it) and that the thesis has not been edited by a third party beyond what is permitted by the University's PGR Code of Practice.

I declare that the thesis does not include work forming part of a thesis presented successfully for another degree.

I declare that this thesis has been produced in accordance with the University of Glasgow's Code of Good Practice in Research.

I acknowledge that if any issues are raised regarding good research practice based on review of the thesis, the examination may be postponed pending the outcome of any investigation of the issues.

Date: 9 May 2024 Signature: Clément Henri Bernard Civrais

Chapter 1

Introduction

1.1 Context

The present thesis falls within the research area referred to as aerothermodynamics which couples the discipline of aerodynamics and thermodynamics [1]. Specifically, aerothermodynamics is encountered in hyper-velocity propulsion systems [2], high enthalpy wind tunnels [3] or in planetary reentry [4]. A common aspect of all these applications involves high-speed and high-temperature flows, giving rise to many processes such as the excitation of the internal modes of chemical species, e.g. rotational, vibrational and electronic and chemical reactions, e.g. dissociation and exchange reactions [5]. When these processes occur, the gas exhibits strong deviation from the definition of thermal and caloric perfect gases, with the results of large variation of the specific heat capacity ratio [6].

A schematic representation of the most dominant processes occurring alongside the stagnation streamline of a vehicle entering from near-orbital or sub-orbital velocities into Earth's atmosphere is illustrated in Fig. 1.1. Physically, a high-velocity air mixture gas flow experiences a compression through the shock wave that envelops the vehicle. Throughout the shock, most of the kinetic energy of the gas is converted into translational energy by collision with the dense gas lying in the shock layer. Through inelastic collisions, the internal modes of the chemical species become largely activated. The different relaxation times of the internal modes lead to a strong thermal and chemical non-equilibrium region in which numerous chemical processes occur. Specifically, the molecules quickly build up large amounts of vibrational energy to the point where molecules possess sufficient energy to overcome the intra-molecular bond and experience a dissociation reaction. Concurrently, these atomic species react with molecular species resulting in the production of nitric oxide through the Zeldovich exchange reactions [7, 8]. Simultaneously, the highly energetic inelastic collisions result in the excitation of electronic excited states.

The modelling of aerothermodynamics flow must account for non-equilibrium effects which are the consequence of the finite rate processes illustrated in Fig. 1.1. These processes are in-

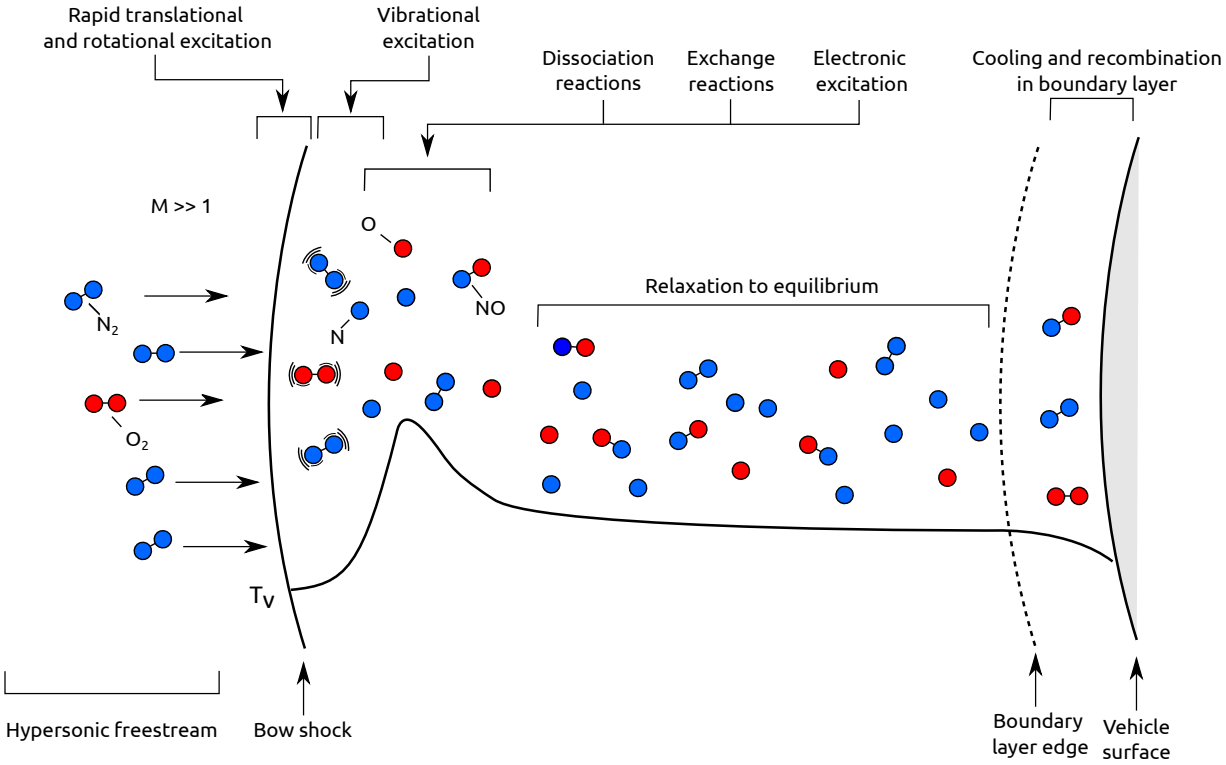

Figure 1.1: Illustration of the aerothermodynamic processes along the stagnation streamline for Earth's atmospheric reentry at near-orbital velocity (Adapted from Potter [9]).

herently dependent on molecular collisions and the density of the gas [10]. Specifically, these non-equilibrium effects arise in moderate to high rarefied flow regimes but also persist to a lower degree of rarefaction. These rarefied regimes are classified by the Knudsen number, a dimensionless parameter defined as the ratio between the molecular mean free path and a characteristic flow dimension. Depending on its values, distinct flow regimes and appropriate mathematical models are distinguished. Figure 1.2 presents a classification of four flow regimes and the limits of applicability of continuum and particle methods in terms of the Knudsen number. In the context of a planetary reentry, all these flow regimes must be considered to accurately describe the aerothermodynamic coefficients of the vehicle and correctly plan the reentry path. These flow regimes not only differ by their respective Knudsen number but also from the relevant aerothermodynamics processes characteristic to each of these regimes.

In the continuum flow regime, the velocity distribution deviates only slightly from the Maxwellian distribution function, allowing the transport properties derived from Chapman-Enskog theory to remain valid throughout [12]. The resulting mathematical formulations yield the Navier-Stokes-Fourier (NSF) equations. In the limiting case of the Knudsen number equals zero, the flow is in local thermodynamic equilibrium imposing the velocity distribution function to equal in any point in space the Maxwellian distribution function. Consequently, the NSF equations simplify to the inviscid Euler equations.

As the Knudsen number increases, molecular-surface interactions become less frequent, leading

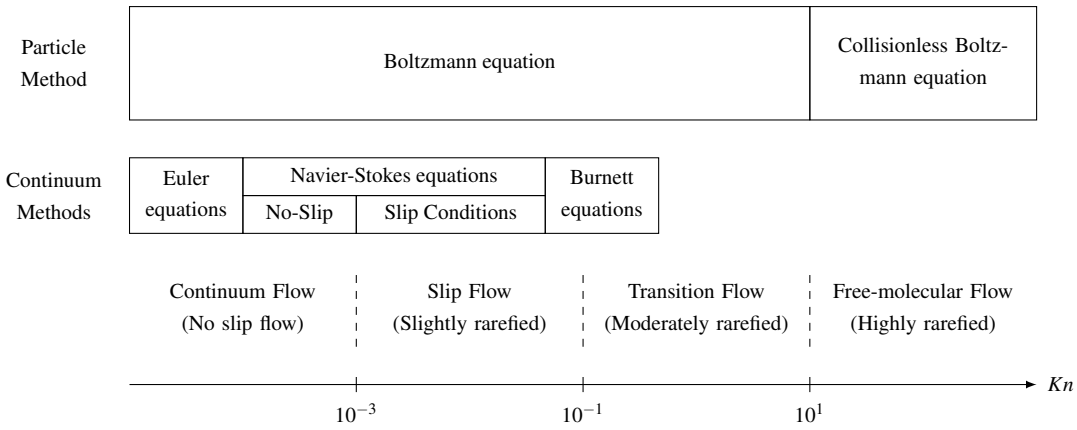

Figure 1.2: Knudsen number limits and flow regime classifications (Adapted from Bird [11]).

to the emergence of non-equilibrium regions near the surface, i.e. velocity slip and temperature jump. This regime is commonly referred to as slip flow. Despite these non-equilibrium effects, the Navier-Stokes-Fourier equations remains valid by applying velocity slip and temperature jump boundary conditions. For moderate Knudsen numbers, the velocity distribution largely deviates from the Maxwellian velocity distribution and the Navier-Stokes equations cease to be valid. One extension of the traditional continuum method consists of applying a second-order Chapman-Enskog to obtain the Burnett equations [13] which enhances the capabilities of conventional continuum methods to a certain extent.

In both transition and free-molecular regimes, non-equilibrium effects dominate the physics of the flow and the only closed equation applicable to such a degree of rarefaction is the Boltzmann equation [14]. The Boltzmann equation can govern all ranges of Knudsen number, i.e. from continuum ($\mathrm{Kn} \to 0$) to free-molecular ($\mathrm{Kn} \to \infty$), so long as the assumption of a dilute gas is valid. In the limit of the Knudsen number tending to infinity and for relatively simple geometries, analytical solutions to the Boltzmann equation can be obtained by disregarding the collision integral. For finite Knudsen numbers, inter-molecular collisions remain significant, complicating the derivation of analytical solutions. Several analytical methods for solving the Boltzmann equation have been proposed. These methods rely on arbitrary assumptions about the form of the velocity distribution function [15] or involve simplifications of the collision term [16].

However, rarefied high-temperature gas dynamics involve intricate aerothermodynamic and chemical processes, e.g. internal mode excitation, chemical reactions or thermal radiation, which are not captured by the Boltzmann equation. Consequently, this combined with the mathematical challenge associated with the Boltzmann equation has stimulated the development of numerical methods to find solutions to the Boltzmann equation. The particulate nature of the gas has enabled the development of direct simulation methods to find a solution to the Boltzmann equation. By far the most common numerical method to simulate rarefied gas flows in the transition regime is the direct simulation Monte Carlo (DSMC) [17]. The DSMC method is a stochastic particle-based method based on the kinetic theory of dilute gases.

This thesis primarily focuses on moderate to high degree of rarefaction, for which the method of choice is the DSMC method. Throughout this thesis, the DSMC method is utilised to develop improved models for the modelling of the aerothermodynamic processes occurring during a planetary reentry, as illustrated in Fig. 1.1.

1.2 Literature Review

The present section provides an overview of the state-of-the-art for the vibrational modelling, chemistry modelling and electronic excited state modelling. Additionally, the discussion concludes on the necessity of a fully coupled approach to describe the aerothermodynamics process and the feasibility of such an approach to be implemented in a DSMC solver.

Vibrational Modelling

For many applications, there are large variations of thermodynamic and transport properties leading to regions of the flow that are in the continuum regime and regions of the flow that are in the rarefied regime. Consider a planetary reentry, the flow downstream of the bow shock typically lies in the continuum regime, while some regions in the wake may exist in the rarefied regime. Although simulating such flows with either continuum or particle methods is attractive, exclusively relying on one method may lead to challenges. Specifically, for regions of the flow that lie in the continuum regime, the particle method is prohibitively expensive. On the other hand, for rarefied regions of the flow, physical assumptions behind the continuum method break down. Therefore, the development of multidisciplinary hybrid numerical solvers taking advantage of both continuum or particle methods remains an active field of research [18–20]. One requirement for both methods to be combined is that thermodynamic and transport properties are consistent on both sides of the interface to ensure the accuracy and global stability of the flow field. Consequently, this necessitates both methods to achieve similar mathematical modelling of the excitation of the internal modes.

In high-speed and high-temperature Navier-Stokes based methods, the thermodynamic properties are sometimes modelled with a polynomial curve fitted on high-fidelity calculation databases such as Cantera [21] or the Chemical Equilibrium with Applications (CEA) software [22–24] that incorporates real gas effects. These real gas effects involve the interactions between internal modes. Specifically, the rotational excitation is modelled with a non-rigid rotor, accounting for rotational-vibrational coupling effects and the vibrational mode is modelled with an anharmonic oscillator (aHO) model. Additionally, these databases incorporate electronic excitation enabling each electronic excited state to excite a unique set of rotational and vibrational quantum levels that hold different spectroscopic constants to its ground electronic configuration [25, 26]. While at room temperatures these effects are particularly insignificant, for temperatures relevant to planetary reentry, these effects are of major importance [27].

In the DSMC method, the internal excitation of chemical species is, in contrast, divided into four distinctive modes: translational, rotational, vibrational and electronic. The DSMC method assumes individual treatment of all internal modes prohibiting any interaction between modes. Specifically, the translational and rotational modes are frequently treated continuously whereas the vibrational and electronic modes are treated with a discrete approach in which the vibrational excitation is modelled with a harmonic oscillator (HO) model. For temperatures relevant to planetary reentry, where high-lying vibrational quantum levels become significantly excited, the assumption of a harmonic oscillator model for describing the vibrational excitation of chemical species is inadequate. Specifically, such an assumption is undesirable leading to an inaccurate description of the thermal conductivity; hence, influencing the Prandtl number of the flow and the specific heats of the chemical species [28–30].

Therefore, the first aim of this thesis consists of implementing a similar model to describe the vibrational excitation to the current high-fidelity databases [21–24]. It involves the modelling of the vibrational quantum levels with an anharmonic oscillator model [31–33]. Several anharmonic oscillator models have been utilised in continuum and particle methods. The two main vibrational models are the Morse anharmonic oscillator model [34] derived from the Morse potential energy function which provides an analytical solution to the Schrödinger equation, and the Dunham anharmonic oscillator model [35] which relies on a power series expansion of a potential energy about an equilibrium position.

The Morse anharmonic oscillator model has largely been employed in the DSMC community for the development of improved models. Specifically, The forced harmonic oscillator (FHO) model was initially developed [36–38] for co-linear collisions of simple harmonic oscillators. It has been found that anharmonicity effects are shown to largely impact the vibrational relaxation time of $CO + N_2$ within a factor of 2 for temperatures below 4500 K. For higher temperatures at which vibrational quantum levels become excited and chemical reactions start playing a noticeable role, these anharmonic effects are expected to be of primary importance. This observation has motivated the extension of the FHO model by integrating three-dimensional collisions of anharmonic oscillators following the Morse potential energy function [39]. In the DSMC method, the FHO model supersedes the traditional Larsen-Borgnakke (LB) technique and is often associated with the terminology high-fidelity DSMC method [40]. Indeed, the FHO model describes the probability transitions between pre-collision and post-collision vibrational quantum levels based on the sequential mechanism of single-quantum steps in a single collision which has shown to demonstrate excellent agreement with semi-classical calculations [41]. However, this approach is severely limited in its application to nonequilibrium flow modelling due to their prohibitive computational requirements [42]. Additionally, Luo *et al*. [43] developed a version of the Macheret-Fridman (MF) chemistry model [44] for the DSMC method by describing the inter-atomic interactions with the Morse potential energy function [34]. The study demonstrates that the Morse anharmonic oscillator model plays an important role for molecules with high vi-

brational energy and also in high-temperature conditions and recommends the modelling of the vibrational energy with the anharmonic oscillator model over the traditional harmonic oscillator model. While it is shown that the anharmonic oscillator model plays a significant role in the investigation of the dissociation reaction rates, the temperature and species profiles in shock-wave flows are not strongly influenced by this addition. Nonetheless, it must be emphasised that an accurate description of the vibrational quantum levels remains important when microscopic properties such as the internal energy distribution are of interest.

The Morse anharmonic oscillator model is constituted of a second-order formulation to describe the vibrational energy of a molecule. The first term is identical to the traditional harmonic oscillator model, whereas the negative second-order term accounts for anharmonicity effects. Each of these two terms is multiplied by a spectroscopic constant which is commonly extracted from the NIST database [25]. While the Morse model is a basis for model developments in the DSMC community, the model only models the vibrational excitation of molecules and any interaction between modes is disregarded.

Another anharmonic oscillator model is the Dunham anharmonic oscillator model which is largely preferred over the Morse anharmonic oscillator model for the modelling of vibrational excitation in continuum methods [28–30, 45], high-fidelity chemistry calculations [46, 47] and radiation solvers [48, 49]. The benefits of the Dunham model lie in the modelling of the rotational and vibrational coupling effects, i.e. change in moment of inertia and centrifugal force, in the calculation of the internal energies of molecules. These internal energies are described with an infinite number of terms which are limited to a certain order due to the availability of the spectroscopic constants. The most popular source for obtaining these spectroscopic constants is the NIST database. However, these spectroscopic constants are relatively old data which convey uncertainties [50, 51]. Furthermore, the spectroscopic data used to interpolate the Dunham coefficients are limited to relatively low quantum numbers leading to large uncertainties of their range of applicability.

Both the Morse and Dunham models accurately describe vibrational quantum levels below the dissociation energy but cannot be used beyond it, as they predict negative spacing between levels. A more realistic description of these quasi-bounded levels would require a fit to some polynomial which would produce rapidly decreasing but still positive level spacing as suggested by Carlson and Bird [52]. Another approach consists of a truncation of the series of internal energy to the dissociation energy and restricting the vibrational energies to positive gradients. This technique has been utilised for the calculation of the thermodynamic properties of several chemical species showing excellent reproduction of the baseline databases [45].

While the Dunham model presents the advantage of describing the interaction between the internal mode, this model is unsuitable for the current state of the DSMC method which is limited by its primary assumption that each internal mode is treated individually and any interaction between mode is disregarded. For the Dunham model to be incorporated into DSMC, signif-

icant modifications would be necessary. Nonetheless, the Dunham model remains attractive, especially for coupling DSMC solvers with radiation transport solvers [49, 53].
Given the uncertainties of the spectroscopic constants reported in the NIST database [25], the availability of high-order anharmonic spectroscopic constants and the current limitations of the DSMC method, the Morse anharmonic oscillator model is preferred in this thesis. The implementation of the Morse anharmonic oscillator model will be the subject of Chapter 4.

Chemistry Modelling

Furthermore, the interaction between internal modes not only plays a major role in the calculation of the thermodynamic and transport properties [29, 30] but also changes the chemical reactivity of the chemical species [27]. It has long been known that the excitation of the internal states strongly influences chemical processes [5, 54, 55].
The first approach for gaining insight into the chemical activity of non-equilibrium flow is through experimental measurements. A compilation of the most representative experimental measurements for the 19 most dominant chemical reactions occurring during an Earth's reentry is presented in Tabs. 1.1 and 1.2 for thermal equilibrium and non-equilibrium conditions, respectively. Many more experimental measurements are available for temperatures relevant to combustion applications, especially for exchange reactions. However, the recommendation of Baulch [56] highlights the failure of extrapolating combustion-relevant temperatures below 3000 K to high-speed and high-temperature flows. Consequently, these studies have been discarded from the compilation in Tabs. 1.1 and 1.2. Ongoing experimental measurements in several shock-tube facilities expand on the research conducted in the previous century [57–72]. While the earlier experimental measurements carry significant information and are important for model validation, recent studies benefit from more accurate techniques and instruments and in many cases provide better descriptions of the chemical processes with a higher standard of accuracy. Specifically, the recent experimental measurements [73–81] offer chemical reaction rates with high-fidelity measurements for temperatures relevant to hypersonic conditions. These recent experimental measurements combined with the past studies provide comprehensive ground for model development and adjustment of tunable parameters.
A complementary approach for understanding key aspects of non-equilibrium flows involves computational chemistry. Over the past two decades, the quasi classical trajectory (QCT) method [120] has gained interest from the aerospace community to study the main chemical reactions in typical Earth re-entry, see Tabs. 1.1 and 1.2. The QCT calculations yield reaction rates with a high degree of fidelity, typically associated with an excellent reproduction of the most accurate experimental measurements. This technique has been integrated into direct simulation Monte Carlo (DSMC) simulations and the method is referred to as the direct molecular simulation (DMS) method [121] or classical trajectory direct simulation Monte Carlo (CT-DSMC) method [122, 123]. The DMS method can be regarded as an *ab initio* version of the DSMC

Table 1.1: Overview of the thermal equilibrium reaction rates for the 19 most dominant chemical reactions in an Earth's reentry.

Reaction	Experimental Measurements	Review/Models	QCT Calculations	DMS Simulation
		Dissociation reactions		
$O_2 + O_2 \longrightarrow O + O + O_2$	[68–70, 73, 75–77]	[54, 56, 82–84]	[85–87]	[88–90]
$O_2 + O \longrightarrow O + O + O$	[70, 77]	[54, 56, 82–84]	[85, 86, 91–94]	[90]
$O_2 + N_2 \longrightarrow O + O + N_2$	[57, 69, 81]	[54, 56, 82–84]	[85, 86, 90, 95]	[89, 90]
$O_2 + N \longrightarrow O + O + N$		[54, 56, 82–84]	[90, 96, 97]	[90]
$O_2 + NO \longrightarrow O + O + NO$		[54, 56, 82–84]		
$N_2 + O_2 \longrightarrow N + N + O_2$		[54, 56, 82–84]	[86, 90, 95]	[90]
$N_2 + O \longrightarrow N + N + O$		[54, 56, 82–84]	[98–101]	
$N_2 + N_2 \longrightarrow N + N + N_2$	[58, 59, 66, 67]	[54, 56, 82–84]	[86, 102–104]	[90, 105]
$N_2 + N \longrightarrow N + N + N$	[58, 59, 66, 67]	[54, 56, 82–84]	[86, 106–109]	[90, 110]
$N_2 + NO \longrightarrow N + N + NO$		[54, 56, 82–84]		
$NO + O_2 \longrightarrow N + O + O_2$		[54, 56, 82–84]		
$NO + O \longrightarrow N + O + O$		[54, 56, 82–84]	[90]	[90]
$NO + N_2 \longrightarrow N + O + N_2$	[74, 79]	[54, 56, 82–84]	[111]	
$NO + N \longrightarrow N + O + N$		[54, 56, 82–84]	[90, 99]	[90]
$NO + NO \longrightarrow N + O + NO$	[62, 63, 65, 78]	[54, 56, 82–84]		
		Exchange reactions		
$N_2 + O \longrightarrow NO + N$	[64, 65, 80]	[54, 56, 82–84]	[98–101, 112, 113]	[90]
$NO + N \longrightarrow N_2 + O$	[60, 65, 80]	[54, 56, 82–84]	[99, 100]	[90]
$O_2 + N \longrightarrow NO + O$	[80]	[54, 56, 82–84]	[96, 97, 114–116]	[90]
$NO + O \longrightarrow O_2 + N$	[61, 80]	[54, 56, 82–84]	[90, 116]	[90]

Table 1.2: Overview of the thermal non-equilibrium reaction rates for the 19 most dominant chemical reactions in an Earth's reentry.

Reaction	Experimental Measurements	Review/Models	QCT Calculations	DMS Simulation
		Dissociation reactions		
$O_2 + O_2 \longrightarrow O + O + O_2$	[71, 73]	[5, 44, 117–119]	[85]	[88]
$O_2 + O \longrightarrow O + O + O$		[5, 44, 117–119]	[91]	
$O_2 + N_2 \longrightarrow O + O + N_2$		[5, 44, 117–119]	[85, 95]	
$O_2 + N \longrightarrow O + O + N$		[5, 44, 117–119]		
$O_2 + NO \longrightarrow O + O + NO$		[5, 44, 117–119]		
$N_2 + O_2 \longrightarrow N + N + O_2$		[5, 44, 117–119]	[95]	
$N_2 + O \longrightarrow N + N + O$		[5, 44, 117–119]		
$N_2 + N_2 \longrightarrow N + N + N_2$	[72]	[5, 44, 117–119]	[102]	
$N_2 + N \longrightarrow N + N + N$		[5, 44, 117–119]	[107]	
$N_2 + NO \longrightarrow N + N + NO$		[5, 44, 117–119]		
$NO + O_2 \longrightarrow N + O + O_2$		[5, 44, 117–119]		
$NO + O \longrightarrow N + O + O$		[5, 44, 117–119]		
$NO + N_2 \longrightarrow N + O + N_2$		[5, 44, 117–119]		
$NO + N \longrightarrow N + O + N$		[5, 44, 117–119]		
$NO + NO \longrightarrow N + O + NO$		[5, 44, 117–119]		
		Exchange reactions		
$N_2 + O \longrightarrow NO + N$		[5, 44, 117–119]	[98, 113]	
$NO + N \longrightarrow N_2 + O$		[5, 44, 117–119]		
$O_2 + N \longrightarrow NO + O$		[5, 44, 117–119]		
$NO + O \longrightarrow O_2 + N$		[5, 44, 117–119]		

method as it supersedes the phenomenological models by computing on the flight actual molecular dynamics trajectories integrated on an *ab initio* PES. The DMS method was initially applied to canonical flows around cylinders [124, 125]. Recently, the DMS method has been successfully applied to the reproduction of the experimental measurements [126] of spontaneous thermal fluctuations around a given equilibrium state of pure oxygen [127], to simulate a reactive, near-continuum, Mach 21 nitrogen flow over a blunt wedge [128] and to a large-scale, fully resolved computation of a non-equilibrium, reactive flow of pure oxygen over a double cone [129]. However, due to the cost of trajectory integration, the DMS method is significantly more computationally expensive than the standard DSMC method. Nevertheless, owing to their high fidelity, QCT calculations and DMS simulations provide an extensive basis for the validation and analysis of DSMC models.

While a large number of the chemical reactions have been experimentally studied, Tab. 1.1 shows that for 7 chemical reactions, no experimental measurements have been reported in the literature. Table 1.1 also demonstrates that most of these chemical reactions are covered by high-fidelity calculations which, in combination with experimental measurements provide an extensive for model development, validation, and analysis. However, for thermal non-equilibrium conditions, Tab. 1.2 shows that only two chemical reactions have been experimentally studied, i.e. O_2 + O_2 and N_2 + N_2, and 7 chemical reactions have been studied with high-fidelity calculations. Due to the challenges of measuring high-energy collisions experimentally and the significant gap in thermal equilibrium conditions, there is a need for the development of chemistry models that can closely reproduce the compilation of studies presented in Tabs. 1.1 and 1.1 but also provide an estimation of the reaction rates when no experimental measurements or high-fidelity calculations are reported. This is primarily achieved using phenomenological models which are commonly utilised in the DSMC community.

One example is the quantum-kinetic (QK) chemistry model which was developed by Bird [130]. The QK models are a series of molecular-level chemistry models that rely solely on the fundamental properties of the colliding particles, including their total collision energy, quantised vibrational levels and molecular dissociation energies. These models can be easily integrated into a DSMC solver and use the quantum Larsen-Borgnakke (LB) technique [131] to derive simple models for dissociation, recombination and exchange reactions. The advantage of the QK chemistry model is that it has limited dependence on macroscopic data; instead, it depends on vibrational energy at the microscopic level and does not require the gas to be in thermal equilibrium. Preliminary evaluations [130, 132, 133] indicated that the resultant reaction rates are in excellent agreement with measured Arrhenius rates for near-equilibrium conditions and with both measured rates and other theoretical models for far-from-equilibrium conditions. Nowadays, the QK models are still actively employed for the modelling of Earth re-entries [19, 133–137], for Mars reentry [138–140] involving the modelling of polyatomic molecular systems, Lunar reentry [141] and for combustion applications [142].

Other phenomenological chemistry models are typically the total collision energy (TCE) model [17], the vibrational favoured dissociation (VFD) model [143] or the bias model [144]. Most of these chemistry models have been inferred on experimental measurements or theoretical calculations to improve their predictive capabilities, e.g. MF-DSMC model [145, 146], bias model [147] and GCE model [148]. Despite being actively utilised for numerous applications [19, 133–142], the QK models have received limited attention.

The QK models were developed around the assumption of the harmonic oscillator model for the treatment of vibrational excitation. As highlighted in the preceding section, real gas effects involve the interactions between all the internal modes where the current state-of-the-art for modelling the vibrational excitation is an anharmonic oscillator model. Therefore, this thesis aims to propose an extension to the QK models to accurately reproduce the most representative experimental measurements and high-fidelity calculations, in which the vibrational excitation is modelled with the current state-of-the-art for the vibrational modelling [135–137]. The detailed description and comparison with an extensive compilation of past studies is the basis of Chapters 5 and 6.

Electronic Excited States Modelling

Another important aerothermodynamic process is the excitation of the electronic excited states of the chemical species. In the DSMC community, four methods have been developed to address this aerothermodynamic process.

The first method has been introduced by Liechty and Lewis [141, 149] and similarly treats the electronic excitation to the vibrational energies. In this method, each chemical species is initialised with an electronic quantum number sampled from the Boltzmann distribution. During collisions, energy exchange with the translational degrees of freedom occurs through the LB model [150]. The primary advantage of this technique lies in the storage of only one additional energy value per particle, while many aspects of vibrational modelling can be incorporated. However, a drawback of this method is that it exhibits significant noise, especially at low temperatures, requiring a large number of particles to compensate for the noise.

The second method, initially introduced by Bird [151], improved by Carlson *et al*. [152, 153], and later expanded by Burt and Josyula [154, 155], partially addresses this problem by equipping each particle with a complete distribution function of electronic excitation instead of an electronic quantum number. However, this leads to a significant increase in storage requirements.

The third method developed by Li *et al*. [156] treats each transition between two electronic states as a chemical process during collisions, where each electronic excited state is regarded as a distinct species. However, to maintain a reasonable level of complexity, assumptions are made on the total number of electronic excited states involved. The merits of this method are that the transition rates can be tuned to reproduce any experimental measurements or high-fidelity

calculations; albeit, noise remains a problem.

The fourth method has been designed by Gallis and Harvey [157, 158]. While the preceding methods rely on the assumption of an equilibrium distribution of the electronic state after a collision, this method computes the probability of an electronic excitation resulting from a collision with the aid of electronic excitation cross-sections. To achieve a realistic description of the electronic excitation, accurate cross-sections are required. However, the experimental measurement of accurate cross-sections is extremely challenging and covers only a fraction of the electronic transitions of interests. Consequently, electronic excitation cross-sections are typically either calculated from theoretical considerations or approximated from other known cross-sections for similar interactions.

A common aspect of all methods is that each internal mode, i.e. rotational, vibrational, and electronic, is regarded separately. However, real-gas effects involve coupling between all internal modes, such as rotational-vibrational coupling and rovibronic coupling [4]. This becomes particularly significant in the analysis of molecular radiation, where achieving the correct distribution of vibrational and electronic excitation energy is crucial.

In recent years, coupling of DSMC methods with radiation transport solvers, e.g. PARADE [159], NEQAIR [160] or Specair [161], has emerged for such investigations [49, 53, 162–165]. In contrast to the DSMC solvers, these radiation solvers adopt a fully coupled approach in which all types of interactions between the internal modes are incorporated. To perform such coupling, previous coupled radiation-DSMC simulations introduced additional assumptions, i.e. Boltzmann distribution [49, 53] or quasi-steady-state (QSS) [5, 156, 165–167], to transfer uncoupled information from DSMC into the coupled models of radiation solvers. With an ever-increasing number of missions involving spectral studies of flows during in-flight or experimental measurements, a detailed description of the physics of the flow is fundamental to allow for spectral comparison. However, a limitation arises due to the assumption of decoupling each internal mode of the chemical species in DSMC simulations, preventing the achievement of this level of detail.

In this thesis, a new model is developed that is more sophisticated than any of the four models previously introduced. Specifically, the model involves the coupling of the vibrational and electronic modes of molecular species, enabling each electronic excited state to excite its unique vibrational quantum levels [168, 169]. The derivation and description of this model is the basis of Chapter 7.

1.3 Aims & Objectives

The review of the existing work has evidenced the need for adopting a coupled approach to model the internal modes of the chemical species. Therefore, the main aim of this thesis is to incorporate similar considerations in the DSMC method. It involves the development and im-

plementation of new models to improve modelling of the physico-chemical processes occurring in any aerothermodynamics applications. The objectives of this thesis are as follows:

Vibrational Modelling

- To implement a similar model to that utilised by high-fidelity databases for modelling the vibrational excitation of molecular species.
- To verify the implementation of the new vibrational model and assess its predictive capabilities in the context of a canonical reentry into Earth's atmosphere.
- To quantify the difference between the traditional models utilised in DSMC solvers against a more sophisticated model.

Chemistry Modelling

- To modify the original quantum kinetics chemistry models by modelling the vibrational excitation with an anharmonic oscillator model and verify the derivation and implementation of these formulations for the most representative chemical reactions occurring during a planetary reentry.
- To evaluate the predictions of the new formulations against an experimental compilation of experimental measurements, high-fidelity calculations and well-established chemistry models and assess their limitations to reproduce the baseline database.
- To derive an extension to the new formulations to accurately reproduce the most representative database, to validate these formulations for all the chemical reactions occurring during an Earth's reentry and to apply these new formulations for the reproduction of in-flight measurements.

Electronic Excited States Modelling

- To develop a new mathematical model for coupling the vibrational and electronic modes based on the same considerations utilised for a fully coupled approach.
- To verify the derivation and implementation of the new formulations in a DSMC solver.
- To quantify the difference between the traditional approach utilised for modelling the electronic excited states and the newly derived model.

1.4 Thesis Outline

Chapter 2 provides an overview of the theoretical background to appreciate the novelty of this thesis by supporting the derivation, implementation and validation of the new aerothermodynamics models. It provides a comprehensive overview of the fundamental principles of quantum mechanics, statistical mechanics and atomic and molecular orbital theories is presented.
Chapter 3 reviews the key concept of the DSMC method. The basic DSMC algorithm and the main routines involving the internal modes are extensively described. The DSMC solver used to perform all of the simulations in this thesis along with the contribution of this thesis to the solver are presented.
Chapter 4 presents the implementation of an anharmonic oscillator model in a DSMC solver. The anharmonic oscillator model is verified against theoretical predictions for a series of adiabatic reactor simulations involving both thermal equilibrium and non-equilibrium conditions. The anharmonic oscillator model is then applied to a canonical hypersonic flow past an infinite cylindrical body re-entering Earth's atmosphere at an altitude of about 75 km.
Chapter 5 presents a custom version of the original QK chemistry models, in which vibrational excitation is modelled with an anharmonic oscillator model. The new formulations are compared against an extensive compilation of well-established theoretical chemistry models, experimental measurements and high-fidelity calculations. Then, the limitations of these formulations are assessed for thermal non-equilibrium conditions relevant to planetary reentry applications.
Chapter 6 presents an extension to the modified QK models presented in Chapter 5 to accurately reproduce recent experimental measurements and high-fidelity calculations. These new formulations are extensively investigated for 19 chemical reactions, dissociation and exchange reactions, for Earth's upper-atmospheric reentry under thermal equilibrium and non-equilibrium conditions. The extended QK models are then utilised to reproduce in-flight measurements of the space transport system's second mission (STS-II) at an altitude of 92.35 km.
Chapter 7 presents a new model for coupling the vibrational and electronic modes of molecular species in DSMC. The new model is verified against an extensive compilation of theoretical studies. The model is applied for a canonical Earth's atmospheric reentry at an altitude of 85 km.
Chapter 8 summarises the key findings of the research presented in this thesis and discusses future perspectives.

Chapter 2

Theoretical Background

The present chapter presents an overview of the theoretical background to appreciate the novelty of this thesis by supporting the implementation, verification and validation of the new aerothermodynamics models. Specifically, it provides a comprehensive introduction to the fundamental principles of quantum mechanics, statistical mechanics and atomic and molecular orbital theories. The main aim of this chapter is threefold. First, it intends to review the derivation and limitations of the most common models, e.g. rigid rotor and harmonic oscillator models, utilised in the DSMC method, Chapter 3, for modelling the internal modes of chemical species. These models will be used as a baseline model for the development of more sophisticated approaches in Chapter 4. Then, it aims at understanding the assumption around the derivation of the thermodynamic properties of a chemical species and the internal temperatures that are widely used to provide physical insight about the excitation of the internal modes, see Chapters 5 and 6. Finally, it aims at understanding the different electronic configurations of a given chemical species allowing for the development of partially coupled and fully coupled approaches which will be the focus of Chapter 7 and Appendix A, respectively.

2.1 Quantum Mechanics

Quantum mechanics aims at describing the behaviour of elementary particles. In quantum mechanics, particles have wave-like properties and are governed by a particular wave equation, commonly known as the Schrödinger equation, from which the internal energy of a particle can be calculated. Therefore, the main purpose of this section is to understand the fundamental of quantum mechanics to later be used in subsequent sections to derive the thermodynamic properties of a system and understand the many electronic configuration a particle may excite.

2.1.1 Heisenberg's Uncertainty Principle

Before proceeding deeper into quantum mechanics, it is helpful to begin with the Heisenberg's uncertainty principle. The existence of the quantum energy states is merely the results of the Heisenberg's uncertainty principle that is,

$$\Delta q \Delta p \geq \frac{\hbar}{2}, \tag{2.1}$$

where Δq and Δp are the uncertainties in the position coordinates and momentum, respectively and $\hbar$ is the reduced Planck constant.

A common physical interpretation of Eq. (2.1) is that the measurement of a particle's position with accuracy $|\Delta q|$ must tolerate inaccuracy of $\Delta p \approx \frac{\hbar}{\Delta q}$ in a simultaneous measurement of the corresponding momentum. Theoretically, Eq. (2.1) demonstrates that for a particle to have a definite absolute position, i.e. $\Delta q = 0$, the momentum is indeterminate. Instead, Eq. (2.1) guides us to adopt a probabilistic interpretation of a particle's position. The notion of an absolute position for a particle is impracticable; instead, it is preferable to refer to its probability to lie in the vicinity of that position. It is important to emphasise that the Heisenberg's uncertainty principle is not a measurement-specific result rather a mathematical consequence of the wave nature of matter [170].

2.1.2 Postulates

Quantum mechanics can be expressed in terms of a small set of postulates. The plausibility of these postulates can be mathematically demonstrated, however, these derivations are beyond the scope of this thesis. The existence of these postulates is herein not questioned and a comprehensive discussion on this topic can be consulted in Lowe and Peterson [171].

Postulate 1: States and Wave functions

The state of a system is fully described by a function, $\Psi(\overrightarrow{x},t)$.

In this Postulate, $\overrightarrow{x}$ represents the spatial coordinates of the system and t is the time. This function is the so-called wave function and it is one of the most important concepts of quantum mechanics theory. If the system is time-dependent, the wave function is formulated as $\Psi(\overrightarrow{x},t)$ whereas if the system is time-independent, the wave function is written $\psi(\overrightarrow{x})$.

Postulate 2: Probabilistic Interpretation of the Wave Functions

The probability that a particle will be found in a volume element dV at point $\overrightarrow{x}$ and time t is $P(\overrightarrow{x},t)dV = |\psi(\overrightarrow{x},t)^2|dV$.

Postulate II, commonly referred as Born's interpretation [170], arises as a consequence of Heisenberg's uncertainty principle and observations made on the Mach-Zehnder interferometer. The first accepted interpretation has been proposed by Born introducing a probabilistic interpretation of the wave function. The wave function represents a probability amplitude and has no physical significance. However, it is mathematically defined such that the product of its modulus by a volume element, i.e. $\Psi(\overrightarrow{x},t)\overline{\Psi}(\overrightarrow{x},t)dV$, represents the probability density that a particle lies in the volume dV, at position $\overrightarrow{x}$ and time t.
The probability density must satisfy the condition that the particle is located somewhere in space. This is also known as the normalisation condition which reads

$$\int_{-\infty}^{+\infty} \Psi(\overrightarrow{x},t)\overline{\Psi}(\overrightarrow{x},t)dV = 1. \tag{2.2}$$

Furthermore, for the wave function to be fully mathematically defined, it must be well-behaved, i.e. single-valued in all coordinates, finite and continuous. The requirement for the wave function to be well-behaved allows solutions of the Schrödinger equation to specific quantized values of the energy.

Postulate 3: Outcome Measurements

When a system is described by a wave function, the expectation (mean) value of the observable Ω in a series of measurements is equal to the expectation value of the corresponding operator.

Postulate III implies that, for a state $\psi(\overrightarrow{x})$, the expectation value of an operator Ω denoted $<\Omega>$, is defined as,

$$<\Omega>=\frac{\int_{-\infty}^{+\infty}\psi(\overrightarrow{x})\Omega\overline{\psi}(\overrightarrow{x})dV}{\int_{-\infty}^{+\infty}\psi(\overrightarrow{x})\overline{\psi}(\overrightarrow{x})dV.}. \tag{2.3}$$

If the system is chosen to be normalised, the expectation value simplifies as,

$$<\Omega>=\int_{-\infty}^{+\infty}\psi(\overrightarrow{x})\Omega\overline{\psi}(\overrightarrow{x})dV. \tag{2.4}$$

Consider the example of the particle's position. Heisenberg's Uncertainty Principle has demonstrated that a particle's position cannot be exactly determined. However, let $\Psi(x_1,t)$ be a given state and $P(x_1,t)$ be the probability for a particle to lie in between x_1 and x_1+dx_1 and the system is normalised, then, the mean particle position is

$$<x_1>=\int_{-\infty}^{+\infty}\Psi(x_1,t)x_1\overline{\psi}(x_1,t)dx_1. \tag{2.5}$$

Postulate 4: Observables and Operators

Observables are represented by Hermitian operators chosen to satisfy the commutation relations,

$$[q, p_{q'}] = i\hbar\delta_{qq'} \quad [q, q'] = 0 \quad [p_q, p_{q'}] = 0, \tag{2.6}$$

where i is the unit imaginary number, $\hbar = \frac{h}{2\pi}$ is the reduced Planck' constant, q and q' each denote one of the coordinate x, y, z and p_q and $p_{q'}$ the corresponding linear momenta.

In classical mechanics, an observable which represents any dynamic quantity is defined by mathematical functions. In contrast, quantum mechanics characterises an observable by a mathematical operator which act on the wave functions. This difference constitutes one of the biggest mathematical changes between these two theories.

Postulate IV indicates that there exists a linear Hermitian operator for every observables in classical mechanics. The Hermitian characteristic of the operator is herein not demonstrated. An extensive discussion on the mathematical definition of the operators and their characteristic can be consulted in Lowe and Peterson [171].

In classical mechanics, the total energy, H, of a particle of mass m is conventionally expressed as the summation of two contributions; the particle's momentum and potential energy function. This function is most commonly known as the Hamiltonian function, named after William Rowan Hamilton for his significant contribution to the field of classical mechanics and formulated,

$$H(\vec{x}, t) = \frac{1}{2m} p^2(\vec{x}, t) + U(\vec{x}, t), \tag{2.7}$$

where U denotes the potential energy of the particle.

The corresponding operator is named the Hamiltonian operator and it is expressed

$$H = K(\vec{x}, t) + U(\vec{x}, t), \tag{2.8}$$

where K is the kinetic energy of the particle.

Postulate 5: Wave Function Equations

The wave function $\psi(\vec{x}, t)$ evolves in time according to

$$i\hbar \frac{\partial \psi(\vec{x}, t)}{\partial t} = H\psi. \tag{2.9}$$

This partial differential equation was first introduced in 1926 by Erwin Schrödinger and it is commonly known as Schrödinger equation [172]. In this thesis, Eq. (2.9) is regarded as an established and accepted equation, its plausibility will not be a subject of further investigation. An extensive discussion on the validity of the Schrödinger equation can be consulted in Lowe

and Peterson [171].

Injecting the Hamiltonian operator, Eq. (2.8), in Eq. (2.9), it yields the time-dependent Schrödinger equation,

$$ih\frac{\partial\Psi(\vec{x},t)}{\partial t} = -\frac{\hbar^2}{2m}\nabla^2\Psi(\vec{x},t) + U(\vec{x})\Psi(\vec{x},t). \tag{2.10}$$

When the system is time-independent, the temporal dependence of the wave functions can be dropped leading to a spatial wave function equation,

$$-\frac{\hbar^2}{2m}\nabla^2\psi(\vec{x}) + U(\vec{x})\psi(\vec{x}) = \varepsilon\psi(\vec{x}), \tag{2.11}$$

where ε is the internal energy of the system.

Eq. (2.11) can be reduced to a compact expression commonly known as the time-independent Schrödinger equation,

$$H\psi(\vec{x}) = \varepsilon\psi(\vec{x}), \tag{2.12}$$

In light of the Schrödinger equations, it is evident that the primary challenge in quantum mechanics lies in the selection of the appropriate potential energy function and form of a Hamiltonian operator that accurately reproduces the behaviour of Nature. Once the potential energy function is carefully chosen, a secondary challenge arises with the resolution of the corresponding Schrödinger equation.

In certain specific cases, such as a particle in motion in the absence of any field forces, a two-particle system modelled with a rigid rotor or a harmonic oscillator, the Schrödinger equation yields analytical solutions. However, in scenarios involving more complex representations of intra-molecular interactions within chemical species, the Schrödinger equation may not result in analytical solutions. Complementary derivations can be consulted in Atkins and Friedman [170], while comprehensive discussions on numerical resolution techniques are presented in Jensen [173].

2.2 Statistical Mechanics

Statistical mechanics is a branch of physics that uses statistical principles to predict the behavior of a large number of particles in a system. It provides a bridge between the microscopic behavior of individual particles, such as atoms and molecules and the macroscopic properties of the system. In this context, the primary objective of this section is to derive the thermodynamic properties of a system in thermal equilibrium exclusively from statistical considerations.

2.2.1 Description of Gases

The primary goal of this section is to derive the Boltzmann distribution and understanding its inherent limitations. Similar to the other parts of this chapter, the emphasis is on gain-

ing understanding rather than looking at the complete derivation of the solution which can be found in high-temperatures textbooks dealing with aerothermodynamics such as Vincenti and Kruger [174], Boyd and Schwartzentruber [10] or Anderson [6]. This section also introduces the concept of the partition function, a property that plays a central role in bridging the microscopic and macroscopic properties of a system.

Microstates and Macrostates

In statistical mechanics, a system is described by its microstates and macrostates which are characterised by three properties,

- ε_j: Characteristic energy of quantum level j,
- g_j: Degeneracy of quantum level j,
- N_j: Number of particle in quantum level j.

While ε_j and g_j are inherent to each system, hence, fixed properties, the number of particle in each quantum level may vary in time.
Before deriving the traditional expression of statistical mechanics, it is helpful to first clarify the terms microstates and macrostates. Consider a fictitious system at some given instant constituted with $N = 9$ particles and five energy states. This situation corresponds to Macrostate I described in Fig. 2.1 in which each energy state is denoted by a straight line and particles are represented by a cross. At some later instant and with the aid of particle collisions, the population of some quantum levels may change; hence, resulting in a different macrostate (Macrostate II). A macrostate can therefore be defined as the certain distribution of the particles over the quantum levels at one instant in time.

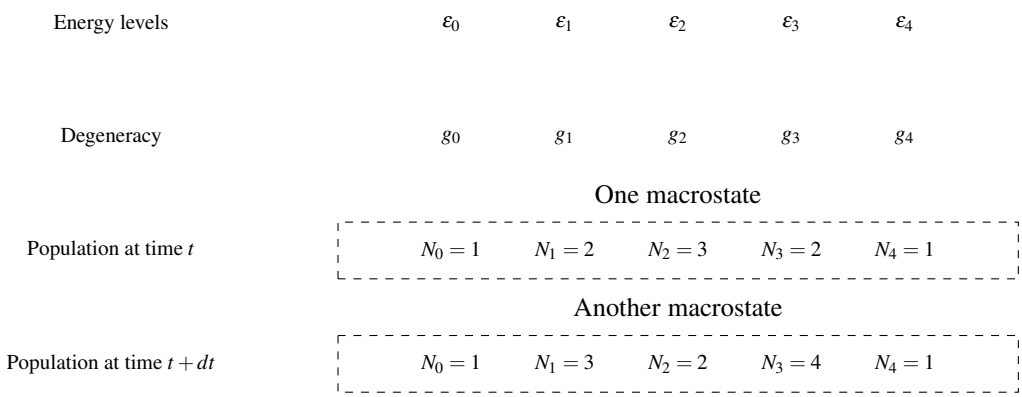

Figure 2.1: Illustration of macrostates (Adapted from Anderson [6]).

Figure 2.2 illustrates a simplified representation of a given macrostate for a system constituted of $N = 9$ particles, total energy E and five internal energies. The degeneracy of each energy is depicted by a horizontal line and its value as well as the population of the quantum level

are indicated at the right of each level. Each particle is represented with a cross. The energy value of each energy state is disregarded. Consider each of the microstates presented in Fig. 2.2 conserve the total energy of the system. At any instant in time, these particles are uniformly distributed across the five quantum levels. At some later instant, the population of the highest degeneracy of quantum levels 2 and 3 sees a depletion of a particle. However, the number of particles populating these levels remains identical to Microstate I. Hence, this microstate belongs to the same macrostate as Microstate I. At another instant, the population of the second and third quantum levels have changed again, however, the population remains constant throughout the temporal evolution of the system, hence, it is another microstate of the macrostate considered. As a result, a macrostate may therefore have multiple microstates. A microstate can therefore be defined as a permissible rearrangement of the N_j over the quantum levels j without changing the total number of particles and energy of the system.

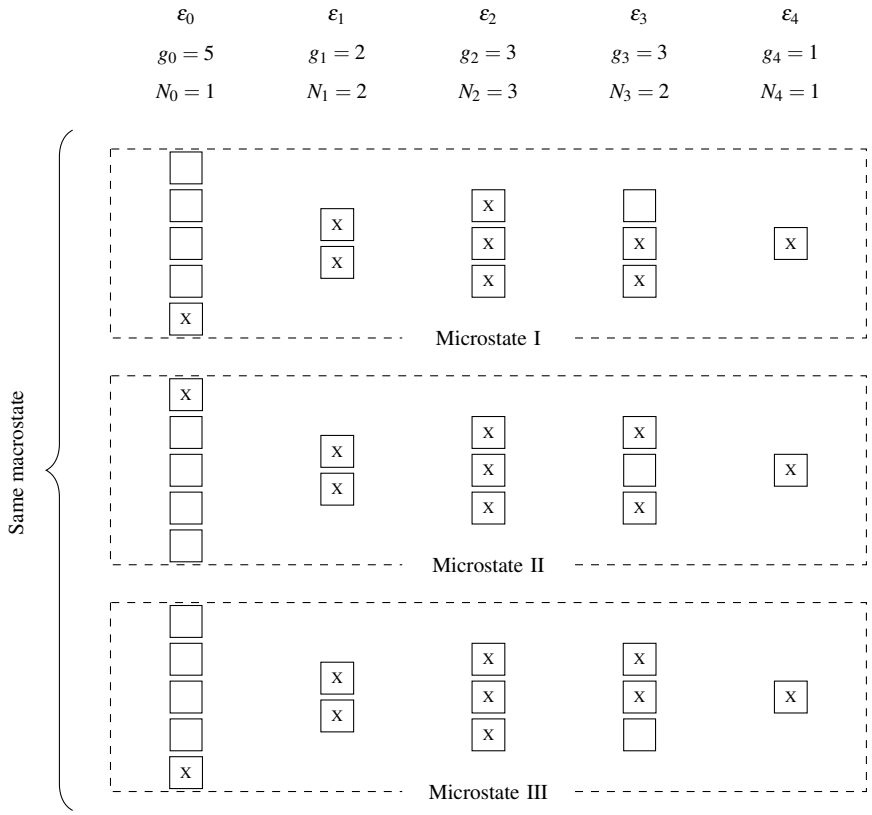

Figure 2.2: Illustration of three microstates of a macrostate (Adapted from Anderson [6]).

Let generalise the concept highlighted in Figs. 2.1 and 2.2 for an arbitrary system. Consider a system with total energy E constituted of N microscopic identical particles, each of which occupies at any instant one of the permissible energy of the system, $\varepsilon_0, \varepsilon_1, \varepsilon_2 \cdots$. Let N_j be the number of particles in an arbitrary energy state, i.e. ε_j. The value of N_j defines the population of each energy state.

Therefore, the total number of particles in the system satisfies,

$$N = \sum_j N_j, \tag{2.13}$$

and that the total energy of the system is

$$E = \sum_j N_j \varepsilon_j. \tag{2.14}$$

Over time, one macrostate emerges with more occurrence than any other. This macrostate is known as the most probable macrostate and is characterised as the thermodynamic equilibrium of the system. It is also characterised as the macrostate which has the maximum number of microstates. Therefore, counting the number of microstates is of primary importance to determine the most probable macrostate that will later conduct us to the thermodynamic properties of the system.

General Case

In quantum mechanics, chemical species are classified into two distinct categories depending on their constitutive number of elementary particles.

1. Chemical species constituted from an even number of elementary particles obey the Bose-Einstein statistical distribution. Such chemical species are called *bosons*. Examples of bosons include C, O or N_2.

2. Chemical species constituted from an odd number of elementary particles obey the Fermi-Dirac statistical distribution. Such chemical species are called *fermions*. Examples of bosons include p^+, e^- or N.

The Bose-Einstein statistics allow any number of N_j particles in any one quantum level. On the contrary, the Fermi-Dirac statistical distribution requires that no more than one particle populate each quantum level. This difference results in two different numbers of microstate for a given macrostate which, for the Bose-Einstein statistics reads,

$$W_{BE} = \prod_j \frac{(N_j + g_j - 1)!}{(g_j - 1)! N_j!}, \tag{2.15}$$

an for the Fermi-Dirac statistics,

$$W_{FD} = \prod_j \frac{g_j!}{(g_j - 1)! N_j!}. \tag{2.16}$$

The reason for the two systems to allow different numbers of microstates lies in the symmetry properties of the wave functions. The explanation is beyond the scope of this thesis and comprehensive explanations can be consulted in Atkins and Friedman [170].
Searching the most probable macrostate consists of searching the specific sets of N_j which allows the maximum of Eqs. (2.15) and (2.16). The derivation is of minor importance and it is therefore disregarded for clarity. The full derivation can be consulted in Anderson [6] or Vincenti and Kruger [174]. These derivation results show that for the Bose-Einstein statistics, the maximum value of W is obtained for

$$N_{BE,j} = \frac{g_j}{e^{\alpha} e^{\beta \varepsilon_j} - 1}, \tag{2.17}$$

and for the Fermi-Dirac statistics, it yields,

$$N_{FD,j} = \frac{g_j}{e^{\alpha} e^{\beta \varepsilon_j} + 1}. \tag{2.18}$$

Eqs. (2.17) and (2.18) correspond to the most probable distribution of particles over the energy levels ε_j. The value of the two parameters α and β remain undetermined. However, Eqs. (2.17) and (2.18) only differ by the sign in the denominator which will prove beneficial to determine these parameters. Furthermore, the total number of particles in the system and its corresponding total energy can, at this stage, be computed by inserting Eqs. (2.17) and (2.18) into Eqs. (2.13) and (2.14) which reads,

$$N = \sum_j \frac{g_j}{e^{\alpha + \beta \varepsilon_j} \pm 1}, \tag{2.19}$$

$$E = \sum_j \frac{g_j \varepsilon_j}{e^{\alpha + \beta \varepsilon_j} \pm 1}. \tag{2.20}$$

For brevity, a $\pm$ symbol has been added to distinguish the two statistical distributions.

Limiting Case

The determination of α and β is essential to later determine the thermodynamics properties of the system. This is only possible in a limiting situation which fortunately covers most practical interest applications. In the limit of the temperature being high enough to promote a spare distribution of the particle over the permissible energy levels of the system, i.e. $g_j >> N_j$, the denominator in Eqs. (2.17) and (2.18) must be large enough for the denominator to be approximated by $e^{\alpha} e^{\beta \varepsilon_j} \pm 1 \approx e^{\alpha} e^{\beta \varepsilon_j}$. Note that this limiting situation is also known as the Boltzmann limit. In this situation, the two statistical distributions yield a common limiting result,

$$N_j = g_j e^{-\alpha} e^{-\beta \varepsilon_j}. \tag{2.21}$$

Once again, the mathematical derivation is disregarded and the final results for α and β read,

$$\beta = \frac{1}{kT}, \tag{2.22}$$

where k is Boltzmann's constant and T is the temperature and,

$$e^{-\alpha} = \frac{N}{\sum_j g_j e^{-\varepsilon_j \beta}}. \tag{2.23}$$

Although succinct, Eq. (2.22) is an important result as it bridges statistical mechanics and classical mechanics. A detailed explanation of this aspect can be consulted in Vincenti and Kruger [174, p. 104-118].
Substituting Eqs. (2.22) and (2.23) into Eq. (2.21), it comes,

$$N_j = N \frac{g_j e^{-\frac{\varepsilon_j}{kT}}}{\sum_j g_j e^{-\frac{\varepsilon_j}{kT}}}. \tag{2.24}$$

This result is also known as the Boltzmann distribution. It corresponds to the most probable distribution of particles over all the energy levels of a system in thermal equilibrium. The denominator of Eq. (2.24) is called the partition function and it is denoted by,

$$Q = \sum_j g_j e^{-\frac{\varepsilon_j}{kT}}. \tag{2.25}$$

Physically, the partition function represents a statistical ensemble of a thermodynamic system in thermal equilibrium conditions. Although this property is dimensionless, the partition function has a pivotal role in connecting microscopic and macroscopic properties which will be addressed in subsequent sections.

2.2.2 Quantum Energy States

After a detailed discussion on how particles occupy their allowed quantized energy states, this section creates a bridge between the aforementioned discussion on quantum mechanics and statistical mechanics theories. The primary objective of this section is not to present a comprehensive mathematical derivation of quantum energy levels but, rather, to provide physical insights into these quantum energy levels. Full derivations can be found in quantum chemistry textbooks [170, 171].

Particles Representation

In the development of statistical mechanics, diatomic chemical species are conventionally represented with a dumbbell model sketched in Fig. 2.3. In this representation, the constitutive atoms are represented as solid spheres, while the chemical bonds connecting these atoms are represented as solid lines. This simple representation facilitates a clear examination of the internal modes that a chemical species can exhibit, namely, translational, rotational, vibrational and electronic modes.

Chemical species are free to move in space. Thus, chemical species have a translational mode with a corresponding translational kinetic energy, i.e. ε_t'.

For temperatures beyond absolute zero, chemical species rotate in space due to its angular momentum and angular velocity. This mode is known as the rotational mode with corresponding rotational energy, i.e. ε_r'.

The vibrational mode with vibrational energy, i.e. ε_v', of a chemical species is characterised by two sources: the kinetic energy associated to the vibration of the constitutive atoms and the description of the intra-molecular forces through a potential energy function.

The electronic mode refers to the location and the motion of the electron orbiting around its nuclei. Depending on thermal conditions, a chemical species may experience rearrangement in its electronic configuration. The activation of the electronic mode of a chemical species relies on its ability to transition from one electronic configuration to another. The corresponding electronic energy, i.e. ε_e', refers to the difference of energy between two adjacent electronic configurations. These distinct electronic configurations are referred to as electronic excited states and will be thoroughly discussed in subsequent sections.

Translational Energy

Consider a free particle of mass m in motion inside a three-dimensional box with side lengths $L_x = L_y = L_z$ in the absence of any field force inside the box and an infinite repulsive force outside the box. For such conditions, the time-independent Schrödinger, Eq. (2.11), reads,

$$-\frac{\hbar^2}{2m}\left(\frac{\partial^2}{\partial x^2}+\frac{\partial^2}{\partial y^2}+\frac{\partial^2}{\partial z^2}\right)\psi(\overrightarrow{x}) = \varepsilon\psi(\overrightarrow{x}). \tag{2.26}$$

The mathematical resolution of Eq. (2.26) to determine the translational energy has been consciously omitted for the sake of clarity. Its full derivation can however be consulted in Lowe and Peterson [171]. The final results of the derivation demonstrates that the translational energy are the eigen-values of Eq. (2.26) formulated,

$$\varepsilon_t = \frac{h^2}{8m}\left(\frac{n_x^2}{L_x^2}+\frac{n_y^2}{L_y^2}+\frac{n_z^2}{L_z^2}\right) \quad \forall n_x, n_y, n_z \in \mathbb{Z}^3_{>0}, \tag{2.27}$$

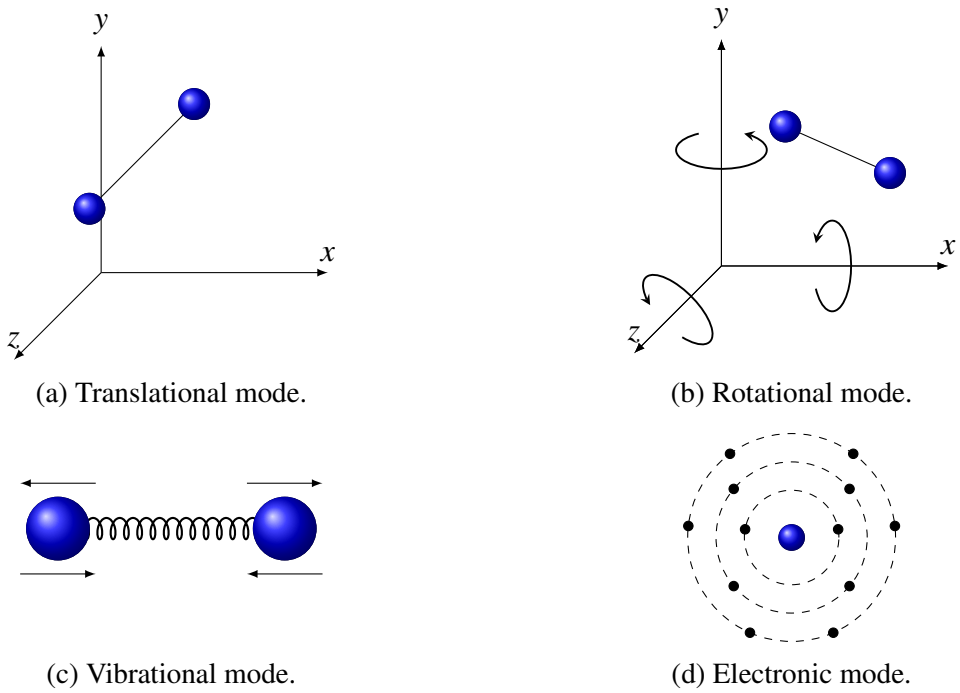

(a) Translational mode.

(b) Rotational mode.

(c) Vibrational mode.

(d) Electronic mode.

Figure 2.3: Modelling of the internal modes of chemical species (Reproduced from Anderson [6]).

where n_x, n_y and n_z are the translational quantum numbers.

While the derivation of Eq. (2.27) has not been shown, some lessons can be deduced from its formulation. It indicates that the translational energy of a particle is quantized and it can only take specific values. It also reveals that these translational energy levels are inversely proportional to the square of the length. This means that the spacing between energy levels depends on the spatial confinement. Furthermore, it demonstrates that Eq. (2.27) admits a finite zero-energy point equal to $\varepsilon_t = \frac{h^2}{8m}$ even at a temperature of absolute zero. Finally, it shows that the energy is proportional to the inverse of the mass, which leads to an interesting consequence: the spacing between allowed translational levels decreases as the mass increases. Ultimately, for heavy particles, the translational levels become practically indistinguishable from the continuum of levels expected in classic mechanics.

Rotational Energy

The derivation of the rotational, vibrational and electronic quantum levels requires to consider a two-particle system. Let two particles of masses m_1 and m_2 located at position (x_1,y_1,z_1) and (x_2,y_2,z_2) separated by a constant distance r with associated momentum p_1 and p_2. The corresponding time-independent Schrödinger equation of the system, also known as a rigid-rotor, reads

$$\frac{\hbar^2}{2m_1}\nabla_1^2\psi(\overrightarrow{x}) + \frac{\hbar^2}{2m_2}\nabla_2^2\psi(\overrightarrow{x}) + (\varepsilon - U)\psi(\overrightarrow{x}) = 0 \tag{2.28}$$

Table 2.1: Characteristic rotational and vibrational temperatures of diatomic molecules.

Molecule	Molecular weight (g.mol^{-1})	θ_r (K)	θ_v (K)
H_2	2.02	87.37	6319.4
N_2	28.01	2.869	3386.5
CO	28.01	2.773	3115.5
NO	30.00	2.470	2734.1
O_2	32.00	2.064	2268.9
F_2	38.00	1.278	1316.1
Cl_2	70.91	0.350	803.70

Similar to the derivation of the translational quantum levels, the full mathematical derivation is disregarded. The rotational energy of such a system is the eigen-energy of Eq. (2.28) which reads,

$$\varepsilon_r = \frac{\hbar^2}{2\mu r_{eq}^2} J(J+1) \; \forall J \in \mathbb{Z}_{\geq 0}, \tag{2.29}$$

where μ is the reduced mass, r_{eq} is the distance between the two particles at rest and J is the rotational quantum number.

The derivation of Eq. (2.29) demonstrates that for each J, the system admits $2J+1$ eigenfunctions, i.e. $g_r = 2J+1$. The minimum rotational energy is zero which contrast with the translational mode that has a finite value. Eq. (2.29) also shows that the spacing between two adjacent rotational quantum levels increases as J increases.

The rotational energy is commonly reformulated to express the energy in term of the characteristic rotational temperature, i.e. θ_r,

$$\varepsilon_r = k\theta_r J(J+1). \tag{2.30}$$

A compilation of characteristic rotational temperatures of diatomic molecules is presented in Tab 2.1. It reveals that as a molecule's mass increases, its characteristic rotational temperature decreases. Specifically, in the case of heavy molecules, the spacing between rotational energy is small enough for the quantum effects to be neglected in most applications. In contrast, lighter molecules, such as molecular hydrogen, exhibit larger characteristic rotational temperature resulting in larger spacing between rotational quantum levels. A quantised approach of the rotational mode is therefore preferable which can be put to good use for nanoscale technology applications.

Vibrational Energy

Consider a diatomic molecule in which the constitutive atoms vibrate back and forth along the inter-nuclear axis and the intra-molecular interactions are dictated by a potential, U,

$$U = \frac{1}{2}k_s\left(r - r_{eq}\right)^2, \tag{2.31}$$

where k_s is the bound stiffness.
The corresponding one dimensional time-independent Schrödinger equation for such a system reads,

$$-\frac{\hbar^2}{2\mu}\frac{d^2\psi(x)}{dx^2} + \frac{1}{2}k_s x^2\psi(x) = \varepsilon\psi(x). \tag{2.32}$$

For the reasons previously mentioned, the full mathematical derivation of the internal energy is herein disregarded. This extensive mathematical derivation ultimately reveals the vibrational energy under the assumption of the harmonic oscillator,

$$\varepsilon_v = h\nu\left(i + \frac{1}{2}\right) \ \forall i \in \mathbb{Z}_{\geq 0}, \tag{2.33}$$

where ν is the fundamental frequency of the bound and i is the vibrational quantum number.
The derivation of the vibrational energy shows that the eigenfunctions are either symmetric or anti-symmetric leading to each vibrational quantum level being non-degenerate, i.e. $g_v = 1$. Furthermore, Eq. (2.33) shows that the vibrational energy allows a finite zero-point energy of exactly $\frac{h\nu}{2}$. Additionally, the vibrational energy presents a constant spacing between adjacent vibrational quantum levels.
Similar to the rotational energy, it is common to define the internal energy in term of their corresponding characteristic temperature,

$$\varepsilon_v = ik\theta_v. \tag{2.34}$$

Table 2.1 provides insight into the characteristic vibrational temperatures for various diatomic species. These temperatures serve as an indicator for investigating the spacing between adjacent quantum levels. Notably, the characteristic vibrational temperature follows a similar trend to that of the characteristic rotational temperature: lighter particles exhibit higher characteristic temperatures, while heavier ones have lower characteristic temperatures. However, a notable distinction emerges when comparing the rotational and vibrational modes. In contrast to rotational energy, Tab 2.1 shows that the characteristic vibrational temperature is approximately two to three orders of magnitude higher than the characteristic rotational temperature. This significant disparity implies that while rotational quantum effects can be disregarded in certain applications, this assumption does not stand for the vibrational mode, where quantum effects play a crucial role.

Electronic Energy

A chemical species, i.e. atom or molecule, can have multiple electronic excited states corresponding to different arrangement of the electrons surrounding its nucleus. Generally, the most stable electronic configuration is represented by the ground state.
Consider the two-particle system utilised for the derivation of the rotational energy. Let the system be constituted of an electron with corresponding charge $-e$ orbiting in a Coulomb field about a nucleus composed of Z atomic number and Ze charge. The corresponding electrostatic potential energy function representing the intra-molecular interactions is

$$U = -\frac{Ze^2}{4\pi\varepsilon_0\left[(x_n - x_{e^-})^2 + (y_n - y_{e^-})^2 + (z_n - z_{e^-})^2\right]^2}, \tag{2.35}$$

where ε_0 is the vacuum permittivity; hence, the time-independent Schrödinger equation for this system becomes,

$$\frac{\hbar^2}{2m_1}\nabla_1^2\psi(\overrightarrow{x_n},\overrightarrow{x_{e^-}}) + \frac{\hbar^2}{2m_2}\nabla_2^2\psi(\overrightarrow{x_n},\overrightarrow{x_{e^-}}) + U\psi(\overrightarrow{x_n},\overrightarrow{x_{e^-}}) = \varepsilon\psi(\overrightarrow{x_n},\overrightarrow{x_{e^-}}). \tag{2.36}$$

where the subscript $()_n$ and $()_{e^-}$ are the position of the nucleus and the electron respectively.
This system is known as the special theoretical case of the hydrogenic particles and its derivation ultimately leads to the formulation of the electronic energy,

$$\varepsilon_e = -\frac{\mu e^4}{8\varepsilon_0^2 h^2}\left(\frac{Z}{n}\right)^2 \quad \forall n \in \mathbb{Z}_{>0}, \tag{2.37}$$

where n is the electronic quantum number.
The ground electronic excited state is characterised by zero electronic energy and it acts as a reference energy state. Eq. (2.37) describes the amount of energy required for a particle to transition from one electronic excited state to another. The derivation of Eq. (2.37) shows that all of the electronic excited states are degenerate. The particularity of the electronic excited states, i.e. electronic configuration, nomenclature and degeneracy, will later be assessed in subsequent discussions concerning atomic and molecular structures.

2.2.3 Relation to Thermodynamics

The present section consists in bridging statistical thermodynamics and classical thermodynamics. For such a purpose, it is convenient to introduce the Helmholtz free energy,

$$F = E - TS = -NkT\left[ln\left(\frac{Q}{N}\right) + 1\right], \tag{2.38}$$

where S and Q are the entropy and the partition function of the system, respectively.

The benefits of these variables is that, all other variables of interests can be found by differentiating Eq. (2.38), such as the entropy

$$S = -\left(\frac{\partial F}{\partial T}\right)_{V,N} = Nk\left[\ln\frac{Q}{N} + 1 + T\frac{\partial(\ln Q)}{\partial T}\right], \tag{2.39}$$

of the pressure of the system,

$$P = -\left(\frac{\partial F}{\partial V}\right)_{T,N} = NkT\frac{\partial\,(lnQ)}{\partial T}. \tag{2.40}$$

Rearranging Eq. (2.38) and substituting the solution for the entropy, Eq. (2.39), the internal mean energy of a system reads,

$$E = F + TS = NkT^2\frac{\partial(\ln Q)}{\partial T}. \tag{2.41}$$

The partition function plays a pivotal role in establishing the connection between statistical thermodynamics and classical thermodynamics, as it serves as a function upon which all the macroscopic thermodynamic variables are constructed. A crucial attribute of the partition function is its factorization property, which enables the overall partition function for a system to be expressed as the product of individual partition functions,

$$Q = Q_t\prod_{int} Q_{int} = Q_tQ_rQ_vQ_e, \tag{2.42}$$

where $(.)_t$, $(.)_\mathrm{r}$, $(.)_v$ and $(.)_e$ subscripts refer to the translational, rotational, vibrational and electronic contributions, respectively.

It is important to realise that Eq. (2.42) implies that each mode is individually regarded and any interaction that may occur has been disregarded. Specifically, the non-adiabatic electronic transitions and the rotational-vibrational coupling, in which the rotation of the molecule gives rise to a centrifugal force that affects vibration of the molecule while the vibrational excitation is accompanied by changes in the moment of inertia, are disregarded. A number of examples where these interactions are important will be presented throughout this thesis. Specifically, Chapter 7 will focus on the modelling of the former interaction and the later interaction will be thoroughly examined in Appendix A.

For molecular species, the thermodynamic variables specific to each internal contribution can therefore be obtained by substituting Eq. (2.42) into Eqs. (2.40)–(2.41). For the energy, written now in term of the specific energy, i.e. $e = \frac{E}{mN}$, it becomes,

$$e = e_t + \sum_{int} e_{int} = e_t + e_r + e_v + e_e. \tag{2.43}$$

The isochoric specific heat capacity can be directly obtained by differentiating Eq. (2.41) for each internal modes as,

$$c_V = \left(\frac{\partial e_t}{\partial T}\right)_V + \sum_{int}\left(\frac{\partial e_{int}}{\partial T}\right)_V = c_{V,t} + c_{V,r} + c_{V,v} + c_{V,e}. \tag{2.44}$$

The equipartition theorem links the macroscopic temperature to the average of the microscopic energies. Specifically, for a system in thermal equilibrium, an internal mode, namely m, with degree of freedom ξ_m contributes $\frac{kT}{2}$ to the total energy,

$$e = \frac{\xi kT}{2}. \tag{2.45}$$

For atomic species, Eqs. (2.43) and (2.44) are drastically simplified as atoms can only excite translational and electronic modes. The evaluation of the thermodynamic properties has now become a matter of investigating each contribution.

Translational Mode

Consider the translation partition function, i.e. Q_t. Inserting the internal translational energy, Eq. (2.27), into the global definition of the partition function, Eq. (2.25), it reads,

$$Q_t = \sum_{n_1=1}^{\infty} e^{-\frac{h^2}{8mkT}\frac{n_1^2}{a_1^2}} \sum_{n_2=1}^{\infty} e^{-\frac{h^2}{8mkT}\frac{n_2^2}{a_2^2}} \sum_{n_3=1}^{\infty} e^{-\frac{h^2}{8mkT}\frac{n_3^2}{a_3^2}} \tag{2.46}$$

Considering the close spacing between adjacent translational quantum levels, the translational mode can be regarded as continuous which means that the summation can be substituted by an integral. The resulting translational partition function yields,

$$Q_t = V\left(\frac{2\pi mkT}{h^2}\right)^{\frac{3}{2}}, \tag{2.47}$$

where the volume is defined by $V = a_1 a_2 a_3$.
The corresponding translational specific mean energy is,

$$e_t = \frac{3}{2}RT, \tag{2.48}$$

where $R = \frac{k}{m}$ is the specific gas constant and the translational isochoric specific heat capacity reads

$$c_{V,t} = \frac{3}{2}R. \tag{2.49}$$

Rotational Mode

Consider the rotational mode of the particle. As discussed previously, the rotational quantum levels are described according to Eq. (2.30) with a degeneracy of $g_r = 2J+1$. Substituting these elements into Eq. (2.25), the rotational partition function reads,

$$Q_r = \sum_J (2J+1) e^{-\frac{J(J+1)h^2}{8\pi^2 IkT}}, \tag{2.50}$$

where I is the moment of inertia.
For $T < \theta_r$, Eq. (2.50) indicates that the partition function equals unity, which implies zero specific mean energy and specific heat capacity. For most applications, this limit is rarely encountered, see Tab. 2.1. For $T > \theta_r$, Tab. 2.1 suggests that for the most dominant chemical species in an air mixture, the spacing between adjacent quantum levels is small, hence, the rotational mode can be regarded as continuous. By analogy with the translational partition function, the summation of Eq. (2.50) can be substituted by integral which leads to

$$Q_r = \frac{1}{\varsigma}\frac{T}{\theta_r}, \tag{2.51}$$

where ς is a symmetry factor that has a value of 2 for homonuclear molecules, e.g. O_2 or N_2, and 1 for hetero-nuclear molecules, e.g. NO or CO.
On the basis of Eq. (2.41), the rotational specific mean energy is,

$$e_r = RT, \tag{2.52}$$

hence,

$$c_{V,r} = R. \tag{2.53}$$

With the knowledge of the contribution of the translational and rotational modes to the specific heat capacities, the ratio of specific heat capacity becomes, i.e. γ,

$$\gamma = \frac{(c_{V,t} + c_{V,r}) + R}{c_{V,t} + c_{V,r}} = \frac{7}{5} = 1.4, \tag{2.54}$$

which is typically expected for an air mixture at room temperature.

Vibrational Mode

Consider the quantum harmonic oscillator with vibrational energy described by Eq. (2.34) and all vibrational quantum levels being non-degenerate. The corresponding vibrational partition function is

$$Q_v = \sum_{i=0}^{\infty} e^{-\frac{i\theta_v}{T}}. \tag{2.55}$$

Due to the absence of a degeneracy factor, an analytical expression can be derived by recognising the geometric series which yields,

$$Q_v = \frac{1}{1 - e^{-\frac{\theta_v}{T}}}. \tag{2.56}$$

Substituting Eq. (2.56) into Eq. (2.25),

$$e_v = \frac{R\theta_v}{e^{\frac{\theta_v}{T}} - 1} \tag{2.57}$$

thus,

$$c_{V,v} = R\left[\frac{\frac{\theta_v}{2T}}{sinh(\frac{\theta_v}{2T})}\right]^2. \tag{2.58}$$

In the limit of $T < \theta_v$, the vibrational partition function equals unity, hence, the vibrational mode does not contribute to the specific heat capacity of the particle. For $T > \theta_v$ and under the assumption of a harmonic oscillator, the vibrational specific mean energy tends to RT, hence, the vibrational mode ultimately contributes to the specific heat capacity by R. Therefore, for a fully vibrationally excited gas, the ratio of specific heat capacity reads,

$$\gamma = \frac{(c_{V,t} + c_{V,r} + c_{V,v}) + R}{c_{V,t} + c_{V,r} + c_{V,r}} = \frac{9}{7}. \tag{2.59}$$

Electronic Mode

Finally, consider the electronic excitation of a chemical species. Its electronic energy is governed by Eq. (2.37) with all electronic excited being degenerate. The corresponding electronic partition function is

$$Q_e = \sum_i g_i e^{-\frac{\varepsilon_{e,i}}{kT}}. \tag{2.60}$$

Differentiating Eq. (2.60) in accordance with Eq. (2.41), the internal energy yields,

$$e_e = \frac{\sum_i g_i \varepsilon_{e,i} e^{-\frac{\varepsilon_{e,i}}{kT}}}{\sum_i g_i e^{-\frac{\varepsilon_{e,i}}{kT}}}. \tag{2.61}$$

The corresponding isochoric specific heat capacity is derived from differentiating Eq. (2.61) with respect to T which reads,

$$c_{V,e} = \frac{\sum_i g_i \frac{\varepsilon_{e,i}^2}{kT^2} e^{-\frac{\varepsilon_{e,i}}{kT}} \sum_i g_i e^{-\frac{\varepsilon_{e,i}}{kT}} - \sum_i g_i \varepsilon_{e,i} e^{-\frac{\varepsilon_{e,i}}{kT}} \sum_i g_i \frac{\varepsilon_{e,i}}{kT^2} e^{-\frac{\varepsilon_{e,i}}{kT}}}{\left(\sum_i g_i e^{-\frac{\varepsilon_{e,i}}{kT}}\right)^2}. \tag{2.62}$$

2.3 Atomic & Molecular Orbital Theory

Atomic and molecular orbital theory aims to understand the possible arrangements of electrons around nuclei and their distribution in electron shells and sub-shells. These distinct arrangements lead to different electronic states, typically accompanied by a change in spectroscopic properties. Therefore, understanding the electronic structure of a chemical species is crucial for understanding its chemical reactivity and spectroscopy properties. The objective of this section is threefold: to understand the nomenclature of the electronic states, to recognise the electronic ground and excited states and to identify the important spectroscopic characteristics.

2.3.1 Atomic Orbital Theory

The primary goal of this section is to provide a comprehensive overview of the quantum numbers and rules that define the electronic states of atomic species. The ground electronic configuration of atomic oxygen is used as an example.

Electronic Classification

An electronic state of an atom corresponds to a specific arrangement of the electrons orbiting around its nuclei. These electrons orbit in shells that are defined by a principal quantum number, i.e. n and a corresponding electronic energy, Eq. (2.37). The orbit gives rise to an orbital angular momentum vector, i.e. $\overrightarrow{\lambda}$ and a spin angular momentum vector, i.e. $\overrightarrow{\sigma}$. The magnitude of $\overrightarrow{\lambda}$ and $\overrightarrow{\sigma}$ is governed by the orbital quantum number l and spin quantum number s, respectively, such that $|\overrightarrow{\lambda}| = \sqrt{\frac{l(l+1)}{\hbar}}$ and $|\overrightarrow{\sigma}| = \sqrt{\frac{s(s+1)}{\hbar}}$. Additionally, the direction of both $\overrightarrow{\lambda}$ and $\overrightarrow{\sigma}$ is governed by magnetic quantum numbers m_l and m_s, respectively. The orbital and spin angular momentum vectors are illustrated in Fig. 2.4. Therefore, an electronic state of an atomic species is fully defined by a set of five quantum numbers summarised in Tab. 2.2

Table 2.2: Set of quantum levels defining an atomic term symbol.

Quantum Level	Notation	Values
Principal	n	$0,1,2,3\cdots$
Orbital	l	$0,1,2\cdots n-1$
Magnetic orbital	m_l	$0,\pm1,\pm2\cdots\pm l$
Spin	s	$\frac{1}{2}$
Magnetic spin	m_s	$\pm\frac{1}{2}$

The electronic configuration of the first three shells and their corresponding sub-shell is represented in Tab. 2.3. Each electron with the same principal quantum number occupies the same orbital shell denominated by K, L and M. Similarly, each electron with the same value of n and l occupy the same sub-shell denoted by s, p and d depending on their orbital quantum number.

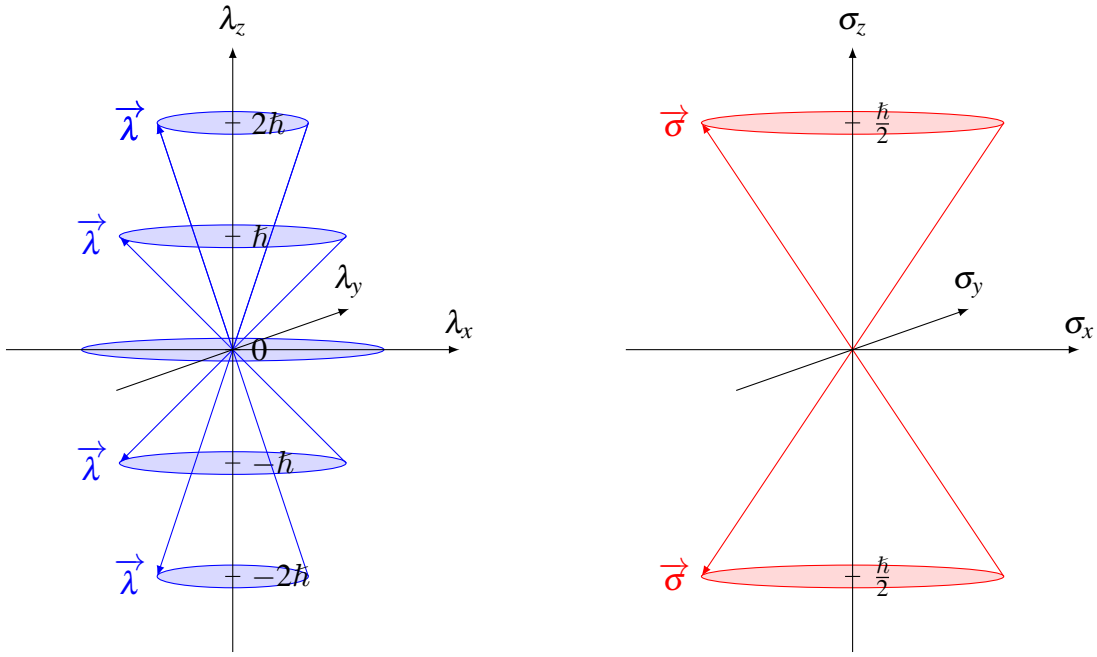

(a) Orbital angular momentum vector for $l = 2$ and $m_l = -2, -1, 0, 1, 2$.

(b) Spin angular momentum vector for $m_s = -\frac{1}{2}, \frac{1}{2}$.

Figure 2.4: Illustration of the orbital and spin angular momentum vectors.

The electronic shells and sub-shells are filled following the *aufbau* principle *. A graphical illustration of the atomic orbitals of the first three sub-shells is depicted in Fig. 2.5. For atomic oxygen with atomic number $Z = 8$, the corresponding ground electronic configuration reads $(1s)^2(2s)^2(2p)^4$. Table 2.3 indicates that the $1s$ and $2s$ sub-shells are fully filled with a total of two electrons for each sub-shell and the $2p$ sub-shell is partially filled with four electrons. The four electrons lying in the $2p$ sub-shell give rise to different electronic rearrangement; hence, different electronic states.

Table 2.3: Electronic configuration of the first three shells (Reproduction from Boyd and Schwartzentruber [10]).

Shell	K	L				M								
n	1	2				3								
Sub-shell	s	s	p			s	p			d				
l	0	0	1			0	1			2				
m_l	0	0	-1	0	1	0	-1	0	1	-2	-1	0	1	2
m_s	$\pm\frac{1}{2}$	$\pm\frac{1}{2}$	$\pm\frac{1}{2}$	$\pm\frac{1}{2}$	$\pm\frac{1}{2}$	$\pm\frac{1}{2}$	$\pm\frac{1}{2}$	$\pm\frac{1}{2}$	$\pm\frac{1}{2}$	$\pm\frac{1}{2}$	$\pm\frac{1}{2}$	$\pm\frac{1}{2}$	$\pm\frac{1}{2}$	$\pm\frac{1}{2}$
g_e	2	8				18								

The derivation of Eq. (2.37) has demonstrated the degeneracy of electronic energy levels. In Eq. (2.37), electronic energy levels are solely determined by their respective principal quantum

*From the German *Aufbauprinzip* which means the build-up principle. Note that this rule is also known as Klechkowsky rule.

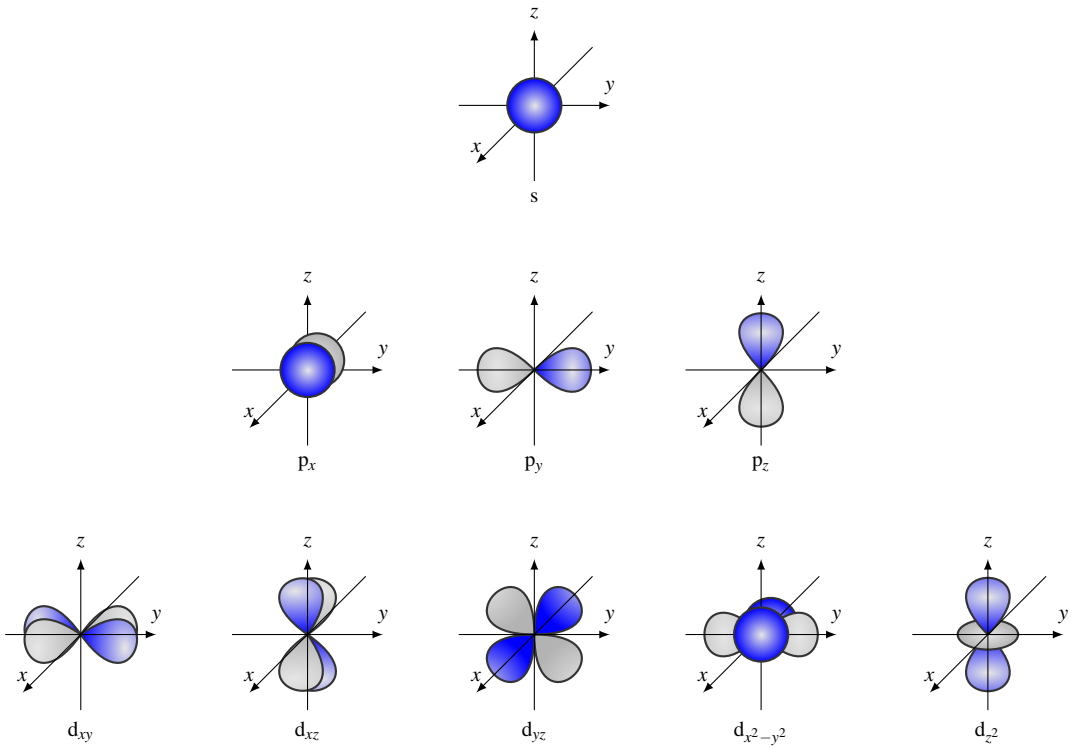

Figure 2.5: Illustration of the atomic orbitals of the first three sub-shells.

numbers. Therefore, various combinations of the remaining three quantum numbers result in degenerate states. Specifically, for each orbital quantum number, there exists $2l+1$ magnetic quantum numbers and two possible spin quantum numbers. The total degeneracy or number of states per shell reads,

$$g_e = \sum_{l=0}^{n-1} 2(2l+1) = 2n^2. \tag{2.63}$$

Number of Electronic Rearrangement

For each electronic configuration, such as O $(1s)^2(2s)^2(2p)^4$, there exists a maximum number of possible electron rearrangements. This number corresponds to the total number of different ways, denoted as N_e, in which N_{e^-} free electrons can be assigned to N_l orbital quantum numbers. Mathematically, this number is given by

$$N_e = \frac{N_l!}{N_{e^-}!(N_l - N_{e^-})!}. \tag{2.64}$$

In the case of atomic oxygen, as shown in Tab. 2.3, there are only four free electrons in the $2p$ sub-shell. Notably, this sub-shell can accommodate a maximum of six electrons. Therefore, atomic oxygen in its ground electronic configuration, i.e. O$(1s)^2(2s)^2(2p)^4$, holds 15 distinct rearrangement possibilities, which are summarized in Tab. 2.4.

Atomic Term Symbols

The magnetic fields associated with the orbital and spin angular momentum vectors give rise to diverse forms of angular momentum coupling: orbital-orbital, $\vec{\lambda}\vec{\lambda}$, spin-spin, $\vec{\sigma}\vec{\sigma}$ and orbital-spin, $\vec{\lambda}\vec{\sigma}$. For light atoms in which the $\vec{\lambda}\vec{\sigma}$ coupling is weak in comparison with Coulombic interactions between electrons, the atomic term symbols can be described by the Russell–Saunders coupling. In contrast, for heavy atoms in which the $\vec{\lambda}\vec{\sigma}$ coupling is strong, the $\vec{\iota}\vec{\iota}$ formalism must be applied. In the present thesis, only light atoms are considered; hence, only the Russell–Saunders coupling is considered. A vector illustration of the Russell–Saunders coupling in represented in Fig. 2.6. The classification of the electronic state of atoms is given by the Russell-Saunders term symbol,

$$^{2\sigma+1}\lambda_{\iota}, \tag{2.65}$$

where each term symbol is characterised by the total orbital angular momentum quantum number, λ, the total spin angular momentum quantum number, σ, and the total angular momentum quantum number, ι.

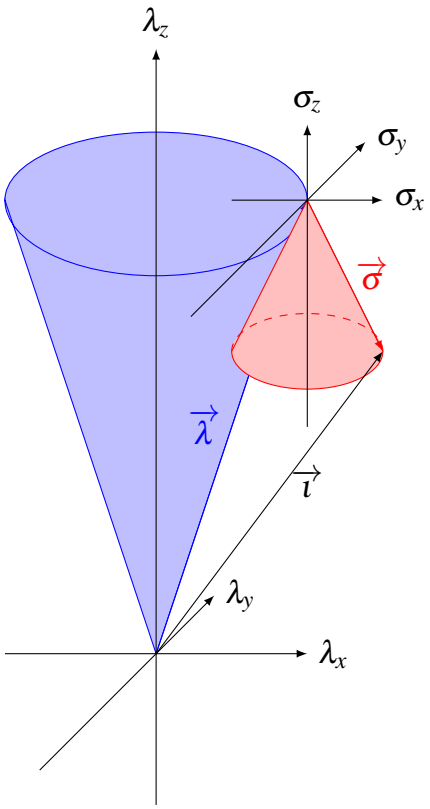

Figure 2.6: Illustration of the Russell–Saunders ($\vec{\lambda}\vec{\sigma}$) coupling (Adapted from Atkins and Friedman [170]).

Additionally, each term symbol is defined by two subsequent quantum numbers describe the direction of the orbital and spin angular momentum vectors, i.e. $\vec{\lambda}$ and $\vec{\sigma}$, respectively. For a

system with two free electrons are defined, the total magnetic and spin orbital quantum numbers take the form of $m_\lambda = |m_{l,1} + m_{l,2}|, \cdots, |m_{l,1} - m_{l,2}|$ and $m_\sigma = |m_{s,1} + m_{s,2}|, \cdots, |m_{s,1} - m_{s,2}|$, respectively. For a system constituted of more than two free electrons, an additional term in between the absolute value of each term is added for each supplementary electron. For a system with three free electrons, the total magnetic orbital quantum number becomes $m_\lambda = |m_{l,1} + m_{l,2} + m_{l,3}|, \cdots, |m_{l,1} - m_{l,2} - m_{l,3}|$.

The values of these quantum numbers for the 15 electronic arrangements of atomic oxygen in its ground electronic configuration, i.e. $O(1s)^2(2s)^2(2p)^4$, are presented in Tab. 2.4. Note that only the unfilled orbitals are useful for determining the different electronic states of atoms. Therefore, for O $(1s)^2(2s)^2(2p)^4$, only four electrons are represented in Tab. 2.4. The electrons are represented by half-arrows with the direction of the arrows indicating the spin of the electron: upward arrows refer to a positive spin and downward arrows refer to a negative spin. The first three columns in the table corresponds to the magnetic quantum number values (m_l). The fourth and fifth columns refer to the total orbital and spin quantum numbers (m_λ and m_σ). The sixth and seventh columns characterise the orbital and spin angular momentum quantum numbers for each specific rearrangement of free electrons in the sub-shell (λ and σ). The last column provides a summary of the corresponding term symbol for each unique electronic distribution ($^{2\sigma+1}\lambda$). It is important to mention that the table does not include the total angular momentum quantum number ($(.)_\iota$), which will be addressed in at a later stage. To ease the understanding of these quantum numbers, each one of these will be individually addressed.

Table 2.4: Electronic rearrangement and electronic states for a $(1s)^2(2s)^2(2p)^4$ electronic configuration (Adapted from Catling and Kasting [175, Appendix C]).

$m_l = +1$	$m_l = 0$	$m_l = -1$	m_λ	m_σ	λ	σ	State
	↑↓	↑↓	-2	0	2	0	^1D
↑↓		↑↓	0	0	0	0	^1S
↑↓	↑↓		2	0	2	0	^1D
↓	↓	↑↓	-1	-1	1	1	^3P
↓	↑↓	↓	0	-1	1	1	^3P
↓	↑	↑↓	-1	0	2	0	^1D
↓	↑↓	↑	0	0	1	1	^3P
↑	↓	↑↓	-1	0	1	1	^3P
↑	↑↓	↓	0	0	2	0	^1D
↑	↑	↑↓	-1	1	1	1	^3P
↑	↑↓	↑	0	1	1	1	^3P
↑↓	↓	↓	1	-1	1	1	^3P
↑↓	↓	↑	1	0	2	0	^1D
↑↓	↑	↓	1	0	1	1	^3P
↑↓	↑	↑	1	1	1	1	^3P

Total Magnetic Orbital and Spin Quantum Numbers, m_λ and m_σ Consider the total magnetic orbital and spin quantum numbers, m_λ and m_σ. The total magnetic orbital and spin quantum numbers are obtained by summing the m_l and m_s values weighted by their corresponding population. In the case of $O(1s)^2(2s)^2(2p)^4$, there are four free electrons in the $(2p)$ sub-shell, i.e. $l = 1$; hence, the corresponding values for the magnetic orbital quantum number are $m_l = 1, 0, -1$. Consider the first row of the table, two electrons occupy the magnetic orbital quantum number $m_l = 0$ and two occupy $m_l = -1$. Therefore, $m_\lambda = 0 \times (+1) + 2 \times (0) + 2 \times (-1) = -2$ and $m_\sigma = 0 + (+\frac{1}{2} - \frac{1}{2}) + (+\frac{1}{2} - \frac{1}{2}) = 0$.

Total Orbital Angular Momentum Quantum Number, λ The total orbital angular momentum quantum number, λ, defines the state of the electronic configuration of the atom. This quantum number can only take positive integers for which each values corresponds to a unique term symbol summarised in Tab. 2.5. For a system with two free electrons, this quantum number can be determined by

$$\lambda = |l_1 + l_2|, \cdots, |l_1 - l_2|. \tag{2.66}$$

Table 2.5: Total orbital angular momentum quantum number and their associated symbols for atomic species.

λ	0	1	2	3	4
Symbol	S	P	D	F	G

For a $(2p)$ sub-shell populated with two electrons, e.g. C, or two gaps, e.g. O, which corresponds to $l_1 = 1$ and $l_2 = 1$; hence, the allowed values for λ are 2, 1 and 0. Consider the first row of Tab. 2.4, $\lambda = |0 \times (+1)| + |2 \times (0)| + |2 \times (-1)| = 2$. In light of Tab. 2.5, the electronic arrangement in the first row corresponds to $O(^{2\sigma+1}D_\iota)$.

Total Spin Angular Momentum Quantum Number, σ The total spin angular momentum quantum number, denoted as σ, plays a pivotal role in defining the multiplicity of an electronic configuration. This quantum number is limited to positive values, with each value corresponding to a unique multiplicity as tabulated in Tab. 2.6. In a two-electron system, the calculation of this quantum number follows,

$$\sigma = |s_1 + s_2|, \cdots, |s_1 - s_2|. \tag{2.67}$$

Table 2.6: Spin momentum quantum number and their associated multiplicity.

σ	0	$\frac{1}{2}$	1	$\frac{3}{2}$	2
Multiplicity	Singlet	Doublet	Triplet	Quartet	Quintet

Consider the first row of Tab. 2.4. In this row, there is one unfilled sub-shell and two filled sub-shells, each occupied by two electrons with a positive spin. This configuration results in a total spin of $\sigma = 0 + \left|\frac{1}{2} - \frac{1}{2}\right| + \left|\frac{1}{2} - \frac{1}{2}\right| = 0$. Referring to Tab. 2.6, this row corresponds to a singlet state, denoted as $2\sigma + 1 = 1$ and the term symbol reads $O(^1D_\iota)$.

Total Angular Momentum Quantum Number, ι The total angular momentum quantum number is the results of the orbit-spin coupling, i.e. $\overrightarrow{\lambda}\overrightarrow{\sigma}$. The total angular momentum vector is merely a linear combination of the orbit and spin angular momentum vector, respectively, $\overrightarrow{\lambda}$ and $\overrightarrow{\sigma}$ as described in Fig. 2.6.
While λ informs on the term symbol and σ informs on the multiplicity, ι provides the degeneracy of the term symbol which is calculated as:

$$g = 2\iota + 1, \tag{2.68}$$

where the associated quantum number is computed as,

$$\iota = |\lambda + \sigma|, \cdots, |\lambda - \sigma|. \tag{2.69}$$

Let's now return to the task of assigning the degeneracy of the term symbols presented in Tab. 2.4. So far, three states have yet been identified which are namely, ^{1}S, ^{1}D and ^{3}P.
With $\lambda = 0$ and $\sigma = 0$, Eq. (2.69) shows that there is only one possible quantum level: $\iota = 0$. Thus, the complete term symbol for this electronic state becomes $^1S_0$. The degeneracy of this state equals unity, i.e. $g(^1S_0) = 2\iota + 1 = 1$ which concurs with the number of occurrences of this state in Tab. 2.4.
For the ^{1}D term symbol obtained with $\lambda = 2$ and $\sigma = 0$, Eq. (2.69) demonstrates that this state has only one possible total angular momentum quantum number: $\iota = 2$. The complete term symbol is then $^1D_2$. This state appears five times in Tab. 2.4 and its degeneracy is accordingly $g(^1D_2) = 2\iota + 1 = 5$.
The triplet P state ^{3}P is obtained with $\lambda = 1$ and $\sigma = 1$. In contrast to the other two states, triplet P has three possible total angular momentum quantum numbers: $\iota = 0, 1, 2$. Consequently, there are three term symbols $^3P_2$, $^3P_1$ and $^3P_0$. The total degeneracy of triplet P is $g(^3P) = \sum_i (2\iota_i + 1) = 9$. This number aligns with the number of triplet P states in the last column of Tab. 2.4. The individual degeneracy of $^3P_2$, $^3P_1$ and $^3P_0$ are 5, 3 and 1, respectively.

Electronic Ground and Excited States

After identifying the term symbols corresponding to a specific electronic configuration, the final task consists of identifying the ground and excited electronic states and classifying them based on their respective electronic energy. To do this, Friedrich Hund has designed a set of three rules

also known as Hund's rules for identifying the lowest energy term symbol of a configuration. These rules classify the electronic configurations from ground to excited states as follows.

1. The term with the maximum multiplicity, i.e. σ, lies lowest in energy.

2. For a given multiplicity, i.e. σ, the term symbol with the highest value of λ lies lowest in energy.

3. For atoms with less than half-filled shells, the level with the lowest value of ι lies lowest in energy. Reciprocally, for atoms with more than half-filled shells, the level with the highest value of ι lies lowest in energy.

The first step consists of determining the ground electronic state of atomic oxygen. According to Hund's first rule, the most stable electronic state corresponds to the lowest total spin. Thus, the ground electronic state of atomic oxygen is a triplet P state. Recalling that the electronic configuration of atomic oxygen is $(1s)^2(2s)^2(2p)^4$ and given that the $2p$ sub-shell can accommodate up to 6 electrons, the sub-shell is more than half-filled. As a result, among the three triplet P states, the most stable state is $^3P_2$. Consequently, the first and second electronically excited states are $^3P_1$ and $^3P_0$. The Singlet S and D states hold the same multiplicity. To differentiate between them, Hund's second rule is applied, which states that the term symbol with the lowest λ value is the most stable state. Therefore, the third and fourth electronically excited states are $^1D_2$ and $^1S_0$, respectively. The first five electronic states of atomic oxygen are summarized in Tab. 2.4.

Table 2.7: First five electronic states of atomic oxygen (Adapted from Boyd and Schwartzentruber [10]).

Configuration	Term	Degeneracy	Energy (eV)
$(1s)^2(2s)^2(2p)^4$	$^3P_2$	5	0.00
$(1s)^2(2s)^2(2p)^4$	$^3P_1$	3	0.02
$(1s)^2(2s)^2(2p)^4$	$^3P_0$	1	0.03
$(1s)^2(2s)^2(2p)^4$	$^1D_2$	5	1.97
$(1s)^2(2s)^2(2p)^4$	$^1S_0$	1	4.20

2.3.2 Molecular Orbital Theory

This section provides an overview of the nomenclature principles used to determine the electronic states of molecular species. These principles are exemplified with the ground electronic configuration of molecular oxygen.

Born-Oppenheimer Approximation

The Born-Oppenheimer approximation assumes that the motion of the electronic and atomic nuclei can be regarded as two independent contributions. The origin of this approximation lies in the respective mass of a proton and an electron. Specifically, a proton is 1836 times heavier than an electron which means that an electron has a much faster response to forces than a proton. Moreover, these two particles possess opposite charges, resulting in an attractive force. The magnitude of the force is inversely proportional to the mass of the particle, therefore, an electron has a much larger acceleration in comparison to its counterpart. Consequently, the motion of the nuclei can be regarded as stationary in contrast to the motion of the orbiting electron.
From a statistical mechanics perspective, the Born-Oppenheimer approximation imposes each internal mode to be treated independently, neglecting any interactions between modes. This approximation imposes the specific energy of the system to be expressed as the summation of its contributions. Atomic species can only excite their translational and electronic modes, therefore, the total internal energy of an atomic system yields,

$$\varepsilon = \varepsilon_t + \varepsilon_e, \tag{2.70}$$

and for molecular systems,

$$\varepsilon = \varepsilon_t + \varepsilon_r + \varepsilon_v + \varepsilon_e. \tag{2.71}$$

The Born-Oppenheimer approximation holds for conditions where interactions between the internal modes are negligible, however, in the context of high-speed atmospheric reentries, the flow conditions may be sufficient enough to promote such interactions. This approximation is considered in the majority of the thesis with the exception of Chapter 7 in which the vibrational and electronic modes are coupled.

Linear Combinations of Atomic Orbitals

Consider the hydrogen molecule-ion $H_2{}^+$ consisting of two protons, denoted by H_A and H_B, separated by a variable distance $r_{H_A-H_B}$ and one electron with charge e separated from proton A by a distance $r_{H_A-e^-}$ and from proton B by a distance $r_{H_A-e^-}$. The corresponding Hamiltonian of this molecule reads,

$$H = -\frac{\hbar^2}{2m_{e^-}}\nabla^2 - \frac{e^2}{4\pi\varepsilon_0 r_{H_A-e^-}} - \frac{e^2}{4\pi\varepsilon_0 r_{H_B-e^-}} - \frac{e^2}{4\pi\varepsilon_0 r_{H_A-H_B}} \tag{2.72}$$

In the limit of the electron lying in the vicinity of nuclei A, $r_{H_A-e^-} << r_{H_B-e^-}$, the Hamiltonian simplifies to,

$$H = -\frac{\hbar^2}{2m_{e^-}}\nabla^2 - \frac{e^2}{4\pi\varepsilon_0 r_{H_A-e^-}} - \frac{e^2}{4\pi\varepsilon_0 r_{H_A-H_B}}. \tag{2.73}$$

Likewise, for the electron lying in the vicinity of nuclei B, the Hamiltonian becomes,

$$H = -\frac{\hbar^2}{2m_{e^-}}\nabla^2 - \frac{e^2}{4\pi\varepsilon_0 r_{\mathrm{H}_B-\mathrm{e}^-}} - \frac{e^2}{4\pi\varepsilon_0 r_{\mathrm{H}_A-\mathrm{H}_B}}. \tag{2.74}$$

With the only difference to the third term, Eqs. (2.73) and (2.74) describe a similar Hamiltonian to that of atomic hydrogen. Therefore, close to nuclei A or nuclei B, the wave-function of $H_2{}^+$ will be similar to a hydrogen atomic orbital. Under this hypothesis, a molecular orbital can be obtained by a linear combination of its constitutive atomic orbitals. This development will be considered as a sufficient justification to construct the molecular orbital theory. An extended discussion supported with mathematical derivations can be consulted in Atkins and Friedman [170].

Molecular Term Symbols

A molecular electronic configuration corresponds to a specific arrangement of its constitutive electrons on its molecular orbitals. This definition is analogue to that of the electronic configuration of atoms. Indeed, a molecular orbital is regarded as a linear combination of its constitutive atomic orbitals (LCAO). In a similar fashion to the atomic term symbols, the molecular term symbols aim at describing the orbital and spin angular momentum of the electrons orbiting around the nucleus. Moreover, the molecular term symbols follow the Russell–Saunders $\overrightarrow{\lambda}\,\overrightarrow{\sigma}$ coupling, see Fig. 2.6, and their corresponding formulation for homo-nuclear diatomic molecules read,

$${}^{2\Sigma+1}\Lambda^{+/-}_{u/g} \tag{2.75}$$

where Λ refers to the total angular momentum quantum number, Σ refers to the total spin angular momentum quantum number, the superscript $+/-$ refers to the molecular parity properties and the subscript u/g refers to the molecular reflection properties.

Each of the quantum numbers and symmetry properties within the molecular term symbol will be discussed individually and illustrated with the example of diatomic oxygen in its ground electronic configuration. This configuration is achieved by combining two atomic orbitals in a triplet P configuration, i.e. O(^{3}P). The molecular orbital energy diagram of molecular oxygen is depicted in Fig. 2.7. The electrons are denoted by half-arrows with directions indicating their respective spin following the convention used in Fig. 2.4. For completeness, the $1s$ and $2s$ sub-shells have been added to the diagram but do not contribute to the term symbol. It is important to emphasise that only the unfilled orbitals are important for determining the electronic state. Therefore, the attribution of the molecular electronic state of this configuration is merely the result of the combination of the two $2p$ sub-shells.

The combination of two $2p$ sub-shells yields four molecular orbitals: σ, σ^*, π and π^*, with the superscript $(.)^*$ distinguishing the anti bonding molecular orbitals. The distinction between σ

and π molecular orbitals lies in the orientation of the two combined atomic orbitals. σ molecular orbitals are generated by a head-to-head overlap along the inter-nuclear axis, while π molecular orbitals are formed through lateral overlapping. These justifications are regarded as sufficient for the scope of this thesis. For extensive discussion on molecular orbital theory, the reader is referred to Atkins and Friedman [170].

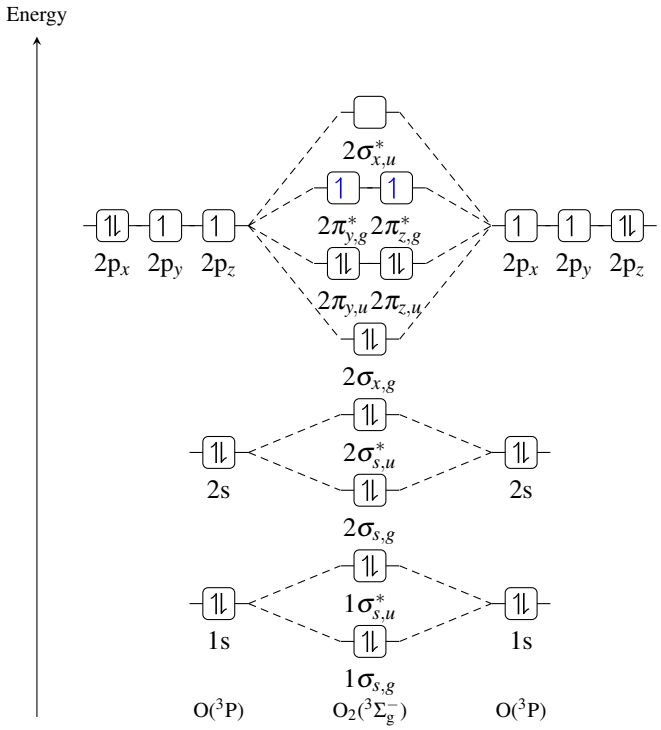

Figure 2.7: Molecular orbital energy level diagram of $O_2(X^3\Sigma^-_g)$ in the LCAO approximation.

Total Angular Momentum Quantum Number, Λ While the total angular momentum quantum number, Λ, yields similar definition to that for atomic orbital theory, its calculation remains different. The attribution of the corresponding symbol of a molecular electronic configuration consists of evaluating the distribution of the electrons on the unfilled molecular orbitals. It consists of summing each electron's contribution such that,

$$\Lambda = |\sum_i \lambda_i|, \tag{2.76}$$

where λ_i equals 0 for each electron occupying a σ molecular orbital and ± 1 for each electron occupying a π or π^* molecular orbital. Each value of Λ has a distinctive symbol which is summarized in Tab. 2.8.

In the case of oxygen molecule, two unpaired electrons occupy the π^*_y and π^*_z molecular orbitals which have been materialised by the blue arrows in Fig. 2.7. As a result, the total angular momentum quantum number is calculated as $\Lambda = |(-1)\times 1 + (+1)\times 1| = 0$. This leads to the

Table 2.8: Total orbital angular momentum quantum number and their associated symbols for molecular species.

Λ	0	1	2	3	4
Symbol	Σ	Π	Δ	Φ	Γ

corresponding term symbol for the oxygen molecule in its ground electronic configuration being ${}^{2\Sigma+1}\Sigma_{u/g}^{+/-}$.

Total Spin Angular Momentum Quantum Number, Σ The multiplicity of a molecular term symbol is determined in a similar manner to the approach used for atomic term symbols. It takes into account only the unpaired electrons in the molecule. Each electron with an upward spin is assigned a half-positive spin, while each electron with a downward spin is assigned a negative-half spin. The total spin angular momentum quantum number is then calculated by summing the contributions from all electrons. Similarly, the degeneracy of a molecular term symbol depends on the total orbital and spin angular momentum quantum numbers and is determined as follows,

$$g = \begin{cases} 2\Sigma + 1 & \text{if } \Lambda = 0 \\ 2(2\Sigma + 1) & \text{if } \Lambda > 0 \end{cases} \tag{2.77}$$

Consider the example of molecular oxygen, where two unpaired electrons occupy the $2\pi_y^*$ and $2\pi_z^*$ molecular orbitals and both electrons have upward spins. The total spin angular momentum is calculated as $\Sigma = (+\frac{1}{2}) + (+\frac{1}{2}) = 1$. This results in a multiplicity of 3 and the term symbol becomes ${}^3\Sigma_{u/g}^{+/-}$. This term symbol is characterised by $\Lambda = 0$, therefore, according to Eq. (2.77), it possesses a degeneracy of $g = 3$.

Molecular Parity The molecular parity informs whether the molecular orbital is symmetric or anti-symmetric when an inversion operator is applied. To ease the understanding, the molecular parity is herein approached through a graphical explanation. The example of two π molecular orbitals is depicted in Fig. 2.8. The constitutive atoms are represented in black spheres and the molecular orbitals are denoted in blue and red spheres. The inversion operator consists of two rotations denoted by the two numbers representing the application order. The molecular orbital illustrated in Fig. 2.8a remains indistinguishable from itself after inversion through its centre. Consequently, the molecular orbital is symmetric and designated by the subscript g [†]. On the contrary, the phase of the molecular orbital depicted in Fig. 2.8b changes. This molecular orbital is therefore anti-symmetric and it is designated by subscript u [‡]. Note that these subscripts are only permissible for molecules allowing a center of inversion. Therefore,

[†]The subscript g stands for *gerade* which means even in German.
[‡]The subscript u stands for *ungerade* which means uneven in German.

the molecular term symbol of hetero-nuclear molecules, e.g. NO or CO, do not possess such subscripts. Extensive discussion supported with mathematical derivations can be consulted in Atkins and Friedman [170].

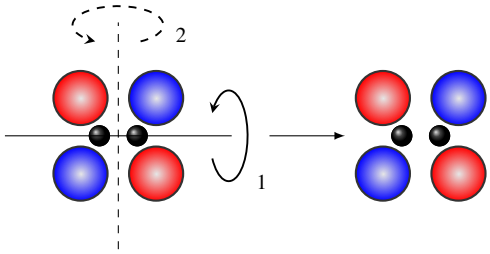

(a) π^* molecular orbital.

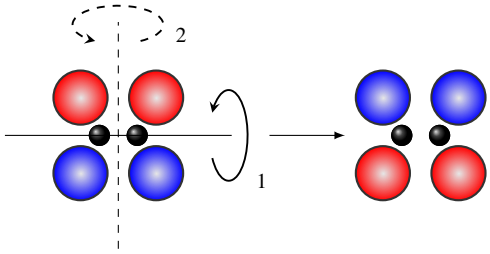

(b) π molecular orbital.

Figure 2.8: Parity classification for two π molecular orbitals.

The parity of a term symbol is determined by assessing the parity of each open-shell electron either from its molecular electronic configuration or from its molecular orbital energy diagram, see Fig. 2.7. In a simplified approach, each electron occupying a gerade open-shell can imaginarily be assigned a $+1$ contribution and for a ungerade open-shell a -1 contribution. The parity of the term symbol is then calculated as the product of each electron's contribution. For a system with two open-shell electrons, the parity follows these rules: $g \times g = g$, $g \times u = u$ and $u \times u = g$. For a system consisting of three open-shell electrons, it follows: $g \times g \times g = g$, $g \times u \times u = g$, $g \times g \times u = u$ and $u \times u \times u = u$.
To ease the understanding, the symmetry properties of the molecular orbitals have been added in subscripts to Fig. 2.7. In the case of the oxygen molecule, there are two open-shell electrons occupying the π_g^* molecular orbitals. Following the rules previously introduced, the ground electronic state of molecular oxygen exhibits gerade symmetry and its term symbol becomes ${}^3\Sigma_g^{+/-}$.

Molecular Reflection The molecular reflection informs on the symmetry of a given molecular orbital upon reflection about a reflection plane containing the inter-nulcear axis. A symmetric molecular orbital corresponds to a positive superscript sign and an anti-symmetric molecular orbital to a negative superscript sign. The overall reflection of a molecular orbital follows the rules aforementioned, i.e. $(-) \times (-) = (+)$, $(-) \times (+) = (-)$ and $(+) \times (+) = (+)$.

Consider a reflection through the plane aligned with the inter-nuclear axis of the π_y^* molecular orbital. Figure 2.9a presents the distribution of the wave functions on both side of the plane. The two atoms are denoted in black balls and the inter-nuclear axis corresponds to the segment between the two atoms. This reflection results in a different molecular orbital; this reflection is said to be anti-symmetric. Consider the reflection through the plane of the π_z^* molecular orbital as described in Fig. 2.9b. The resulting molecular orbital is identical to the initial molecular orbital. This reflection is therefore symmetric.

A symmetric reflection is labelled with a positive sign $(+)$ and an anti-symmetric reflection with a negative sign $(-)$. It is important to mention that the electronic configurations for which $\Lambda > 0$ have both symmetric and anti-symmetric states with respect to reflection; hence, the superscript $\pm$ is only attributed to molecular term symbol where $\Lambda = 0$.

In this operation, each σ molecular orbitals has the value $(+1)$; whereas π molecular orbitals have values $(+1)$ and (-1). Consider the case of molecular oxygen illustrated in Fig. 2.7 in which the two open-shell electrons occupy two π molecular orbitals. One of them is assigned a positive value and the other is assigned a negative value and the overall value of this configuration is $(+1) \times (-1) = (-1)$. Finally, the complete molecular term symbol of molecular oxygen corresponding to Fig. 2.7 is ${}^3\Sigma_g^-$.

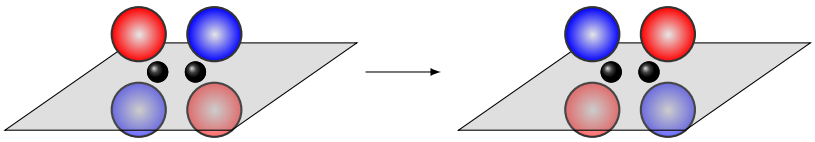

(a) Anti-symmetric reflection.

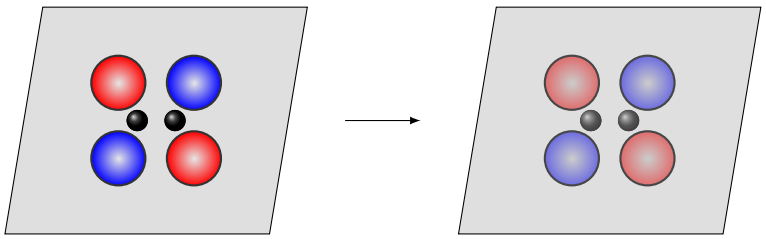

(b) Symmetric reflection.

Figure 2.9: Reflection symmetry classification of the π_y^* and π_z^* molecular orbitals.

Electronic Ground and Excited States

To differentiate the electronic ground state from its electronic excited states, a letter is assigned to the term symbol. The electronic ground state is typically denoted as X. Electronic excited states are represented by letters in alphabetical order. When an electronic excited state shares the same multiplicity as the ground state, its term symbol is expressed in uppercase letters. In contrast, if an electronic excited state has a different multiplicity, its term symbol is presented in lowercase letters.

The first seven term symbols for molecular oxygen are summarized in Table 2.9. The first three term symbols correspond to molecular oxygen in its ground electronic configuration, whereas the last four originate from an electronic excited configuration in which one electron has transitioned from a 2π to a $2\pi^*$ molecular orbital.

Table 2.9: Electronic excited states of molecular oxygen.

Electronic Configuration	State	ε_e (eV)	g	θ_v (K)	θ_r (K)
$(1\sigma)^2(1\sigma^*)^2(2\sigma)^2(2\sigma^*)^2(2\sigma)^2(2\pi)^4(2\pi^*)^2$	$X^3\Sigma_g^-$	0.00	3	2400.33	2.06
$(1\sigma)^2(1\sigma^*)^2(2\sigma)^2(2\sigma^*)^2(2\sigma)^2(2\pi)^4(2\pi^*)^2$	$a^1\Delta_g$	0.98	2	2130.05	2.05
$(1\sigma)^2(1\sigma^*)^2(2\sigma)^2(2\sigma^*)^2(2\sigma)^2(2\pi)^4(2\pi^*)^2$	$b^1\Sigma_g^+$	1.63	1	2057.25	2.01
$(1\sigma)^2(1\sigma^*)^2(2\sigma)^2(2\sigma^*)^2(2\sigma)^2(2\pi)^3(2\pi^*)^3$	$c^1\Sigma_u^-$	4.09	1	1140.33	1.31
$(1\sigma)^2(1\sigma^*)^2(2\sigma)^2(2\sigma^*)^2(2\sigma)^2(2\pi)^3(2\pi^*)^3$	$A'^3\Delta_u$	4.29	6	1220.45	1.38
$(1\sigma)^2(1\sigma^*)^2(2\sigma)^2(2\sigma^*)^2(2\sigma)^2(2\pi)^3(2\pi^*)^3$	$A^3\Sigma_u^+$	4.38	3	1147.32	1.31
$(1\sigma)^2(1\sigma^*)^2(2\sigma)^2(2\sigma^*)^2(2\sigma)^2(2\pi)^3(2\pi^*)^3$	$B^3\Sigma_u^-$	6.16	3	1018.43	1.18

Chapter 3

Direct Simulation Monte Carlo

The previous chapter has reviewed the most common models employed in the direct simulation Monte Carlo method for the modelling of the internal modes. The present chapter intends to describe the direct simulation Monte Carlo method and its general procedures. The chapter primarily focuses on routines involving internal modes such as the initialisation, post-collision and internal mean temperature measurements. Finally, the DSMC solver utilised to perform all the simulations presented in this thesis is introduced.

3.1 The Direct Simulation Monte Carlo Method

The direct simulation Monte Carlo method, pioneered by Bird, has become the predominant numerical approach for simulating rarefied gas flows in the transitional regime over the last six decades [176]. The DSMC method is a stochastic particle-based technique which emulates the physics of the Boltzmann equation. The DSMC method consists in tracking the motion of representative model particles in time and space while modifying their positions and velocities in such a way that mimic the statistical representation of a real gas flow. A DSMC simulator particle can represent any number of real gas particles and possesses molecular information such as position, velocity and internal energy.

The DSMC method relies on considerations from kinetic theory, imposing that the gas is dilute, i.e. the mean molecular diameter must be significantly smaller than the mean free path and that Boltzmann's molecular chaos assumption holds. The assumption of a dilute gas combined with the stochastic approach, enables both the particle motion and intermolecular collisions to be decoupled for time steps smaller than the mean collision time. Particle motion is addressed deterministically, with each DSMC simulator particle traveling a distance proportional to its individual velocity as long as no external forces act upon the gas. In contrast, intermolecular collisions are treated stochastically after updating the positions of all particles.

The DSMC method requires the creation of a numerical mesh composed of sampling cells and collisional subcells. The sampling cell grid provides volumes for evaluating macroscopic flow

properties based on sampling the microscopic properties of particles. The collisional subcell grid is utilised by the collision scheme, restricting interactions to particles within the subcell. To ensure correct reproduction of the transport of momentum and energy upon collisions, the usual recommendation is to ensure that the subcell size, Δx, is a fraction of the molecular mean free path, λ. One of the rules of thumb employed in DSMC simulations suggests that the collision cell size should be smaller than one-third of the local mean free path, i.e. $\Delta x < \frac{\lambda}{3}$. Another requirement of the DSMC method relates to the selection of an appropriate time step. To maintain the assumption of uncoupled particle collisions and movements, it is imperative that the time step is considerably smaller than both the mean collision time and the cell residence time.

In the early days of the DSMC method, questions were raised about the relationship between the Boltzmann equation and the DSMC method. Despite scepticism, the DSMC method grew in popularity accompanied by an increase in users which led to the development of numerous improvements, e.g. Larsen-Borgnakke redistribution scheme [131], the variable hard sphere model [177] or the no time counter collision scheme [178]. In 1992, Wagner [179] demonstrated that for a monoatomic gas in the limiting case of an infinitely small cell size and time-step, the DSMC method mathematically satisfies an equation close to the Boltzmann equation which removed ambiguity on the capabilities of the DSMC method to approach the Boltzmann equation. While the DSMC method can provide an asymptotic solution to the Boltzmann equation, the DSMC method can go beyond the Boltzmann equation including internal mode excitation, chemical reactions and thermal radiation [17].

The flowchart of typical DSMC simulations has not changed greatly since the method was first introduced. The general procedure is depicted in Fig. 3.1 and the typical steps in each DSMC time step are: (1) Move the particle over the time step Δt; (2) Index the particle into the cells and subcells; (3) Collide particles in each cell or subcell; (4) Sample the macroscopic flow properties.

The initial step consists of populating the numerical mesh with DSMC simulator particles. The DSMC simulator particles are assigned a thermal velocity sampled from the Maxwell distribution – centred around the local mean velocity – at the prescribed translational temperature and an internal energy or quantum level for each mode considered which is sampled from the Boltzmann distribution, Eq. (2.24), at the corresponding prescribed internal temperature.

Next, all particles are moved according to their velocity vector and the time step. Consequently, interactions with boundaries are addressed, including gas-surface interaction, e.g. specular or diffuse reflection or removal of particles at deletion boundaries. Computation of macroscopic properties at solid boundaries occurs during this step.

Following this, particles are then indexed by cell location to initiate the collision and sampling routines which depend on the cell occupancy. Intermolecular collisions are handled in a probabilistic manner which contrasts with the the deterministic treatment that characterised

the ballistic motion. Several colliding partner selection schemes have been formulated in the DSMC method, e.g. nearest neighbor [180], majorant collision frequency scheme [181], null-collision [182] or Bernoulli trials [183]. These selection schemes ensure that the correct collision rates between colliding partner is achieved. A comprehensive review of these collision schemes can be consulted in Roohi and Stefanov [184]. If a colliding pair is selected for collision, each partner is tested for internal energy relaxation, i.e. inelastic collision. If accepted, internal energy is exchanged; otherwise, the colliding partner conserves its internal energy and a new velocity vector is assigned. In DSMC, the LB model [131] is commonly employed for the redistribution of internal energy.

Lastly, macroscopic flow properties are sampled after all collisions have been processed. This procedure is repeated until the end time is reached. After a sufficiently large time has elapsed, a steady flow is established and macroscopic flow properties are measured over a large enough sample size to reduce the statistical error to an acceptable level. The following sections focus on reviewing the standard approaches of the DSMC method, which involves the internal modes of chemical species

3.2 Equilibrium Sampling

The equilibrium sampling procedures consist in initialising the internal energy or internal quantum levels of each DSMC simulator particle. These procedures occur at inlet boundaries and after a collision with a diffuse surface. The present section aims to present an overview of the equilibrium sampling technique employed in the DSMC method.

Consider a particle with internal mode, m, described continuously, internal energy, ε_m, and with internal degree of freedom, ξ_m, at an equilibrium temperature, T. Its equilibrium distribution follows the Hinshelwood distribution [186] which reads,

$$f(\varepsilon_m) = \left(\frac{\varepsilon_m}{kT}\right)^{\frac{\xi_m}{2}-1} e^{-\frac{\varepsilon_m}{kT}}. \tag{3.1}$$

The distribution function can be normalized such that the probability of ε_m lying between ε_m and $\varepsilon_m + d\varepsilon_m$ is given by $f(\varepsilon_m)d\varepsilon_m$. If ε_m ranges between a and b, the integration of $f(\varepsilon_m)$ from a to b equals unity, i.e., $\int_a^b f(\varepsilon_m)d\varepsilon_m = 1$. It is convenient at this point to define the cumulative distribution as follows,

$$G(\varepsilon_m) = \int_a^{\varepsilon_m} f(\varepsilon_m)d\varepsilon_m. \tag{3.2}$$

This function can be equated to a random number, $\mathcal{R}$, to determine the cumulative distribution value corresponding to a representative internal energy, ε_m. If Eq. (3.2) can be inverted, it provides an expression for a representative value of ε_m as a function of a random number; otherwise, ε_m is extracted using an acceptance-rejection method.

It is important to emphasise that this procedure is exclusively applicable to continuous internal

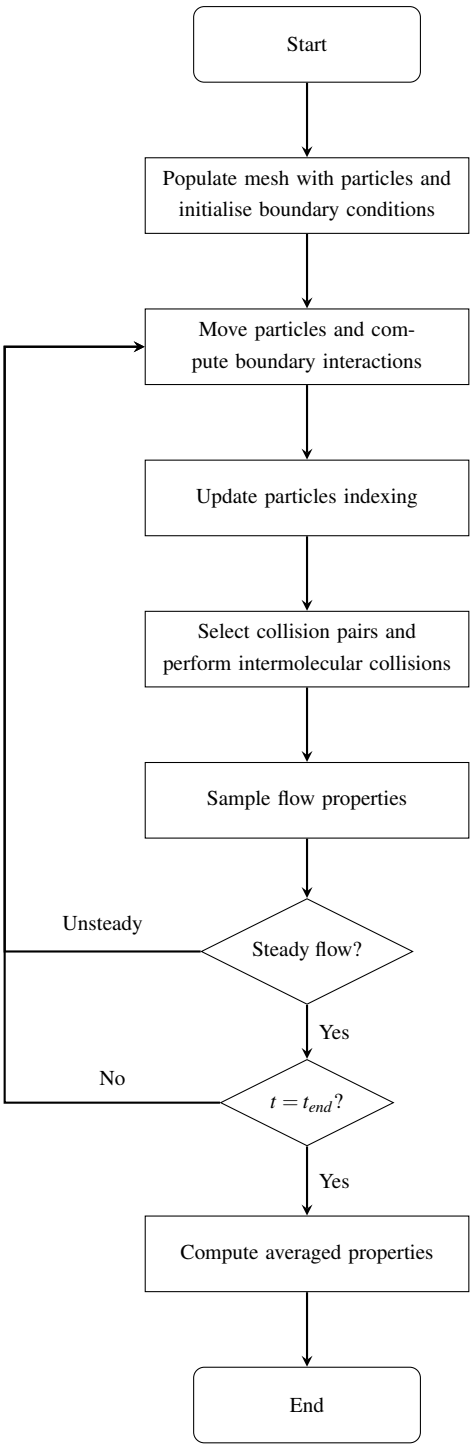

Figure 3.1: Flowchart of the standard DSMC algorithm (Adapted from White [185]).

modes which are typically the translational and rotational modes. For quantised internal modes, a different approach based on the acceptance-rejection method is employed.

3.2.1 Rotational Mode

Consider a continuous treatment of the rotational mode, see Chapter 2, the rotational energy of the particle can be sampled from Eq. (3.1) at an initialization temperature, T. As discussed in the preceding section, it is good practice to calculate the cumulative distribution associated with the distribution function which yields,

$$G(\varepsilon_r) = \int_0^{\frac{\varepsilon_r}{kT}} \left(\frac{\varepsilon_r}{kT}\right)^{\frac{\xi_r}{2}-1} e^{-\frac{\varepsilon_r}{kT}} d\left(\frac{\varepsilon_r}{kT}\right). \tag{3.3}$$

From Eq. (3.3), two scenarios arise depending on the value of ξ_r:

1. If $\xi_r = 2$, e.g diatomic molecules, the mean rotational degree of freedom equals 2 and the cumulative distribution greatly simplifies to,

$$G(\varepsilon_r) = 1 - e^{-\frac{\varepsilon_r}{kT}}. \tag{3.4}$$

   It is evident that Eq. (3.4) is reversible. Therefore, the rotational energy of the particle can be evaluated by mean of a random number, $\mathcal{R}$, uniformly distributed between 0 and 1 such that,

$$\varepsilon_r = -kT\,ln(\mathcal{R}). \tag{3.5}$$

2. If $\xi_r > 2$, e.g. polyatomic molecules, the cumulative distribution becomes irreversible, therefore, an acceptance-rejection method is employed using the distribution,

$$f' = \frac{f(\varepsilon_r)}{f_{max}} = \left(\frac{\left(\frac{\varepsilon_r}{kT}\right)}{\left(\frac{\xi_r}{2}-1\right)}\right)^{\frac{\xi_r}{2}-1} e^{\frac{\xi_r}{2}-1-\frac{\varepsilon_r}{kT}}. \tag{3.6}$$

   Specifically, an energy ratio, namely $\mathcal{R}_1 = \frac{\varepsilon_r}{kT}$, is chosen at random from the range 0 to 1. The distribution is evaluated from the above equation against a random fraction, i.e. $\mathcal{R}_2$, uniformly distributed between 0 and 1. The energy ratio is accepted if the distribution satisfies

$$f' > \mathcal{R}_2, \tag{3.7}$$

   otherwise, the energy ratio $\mathcal{R}_1$ is rejected. The procedure is repeated until an energy ratio, $\mathcal{R}_1$, is accepted and the rotational energy of the particle is calculated,

$$\varepsilon_r = -\mathcal{R}_1 kT. \tag{3.8}$$

3.2.2 Vibrational Mode

Under the hypothesis that the vibrational excitation of a particle is modelled with the harmonic oscillator model, described in Chapter 2, the distribution function of the vibrational energy is provided by the proportionality relation,

$$f(\varepsilon_v) \propto e^{-\frac{\varepsilon_v}{kT}} \delta\left(\varepsilon_v - \left(i + \frac{1}{2}\right)\theta_v\right), \tag{3.9}$$

and the cumulative distribution reads,

$$G(\varepsilon_v) = 1 - e^{-\frac{\varepsilon_v}{kT}}, \tag{3.10}$$

where $\delta(x)$ is the Dirac delta.
The cumulative distribution is reversible and the vibrational quantum level of a particle can be sampled from,

$$i = \left\lfloor -ln(\mathcal{R})\frac{T}{\theta_v} \right\rfloor. \tag{3.11}$$

where $\lfloor \cdots \rfloor$ denotes truncation to the lower integer value. The corresponding vibrational energy of the particle is then calculated with Eq. (2.34).

3.2.3 Electronic Mode

In thermal equilibrium, the Boltzmann distribution for the electronic excited states j at a given temperature follows,

$$f(\varepsilon_{e,j}) = \frac{g_j e^{-\frac{\varepsilon_{e,j}}{kT}}}{\sum_j g_j e^{-\frac{\varepsilon_{e,j}}{kT}}}. \tag{3.12}$$

In contrast with the previous two modes, this distribution does not simplify and an electronic quantum number cannot be directly sampled from Eq. (3.12). To overcome this problem, an acceptance-rejection method is applied by selecting an electronic quantum level from the following distribution,

$$f' = \frac{f_(\varepsilon_{e,j})}{f_{max}} = \frac{g_j e^{-\frac{\varepsilon_{e,j}}{kT_e}}}{g_{j'} e^{-\frac{\varepsilon_{e,j'}}{kT_e}}}. \tag{3.13}$$

The sampling of an electronic quantum level proceeds as follows. First, the electronic quantum level, i.e. j', corresponding to the maximum of Eq. (3.12) is determined. Next, a random electronic quantum number, i.e. $j^\star$, is sampled from a uniform distribution which takes the values between 0 and j'. A value of $j^\star$ is selected and Eq. (3.13) is evaluated for $j^\star$. Finally, the electronic quantum number $j^\star$ is accepted if Eq. (3.13) is greater than a random number; otherwise, the procedure is repeated until an accepted value for $j^\star$ is obtained.

3.3 Post Collision Sampling

In the event of a binary collision, the post-collision routines involve the molecular species, the three components of velocity and either the internal energy or quantum level of each mode. Two types of collisions can be distinguished: elastic collisions, which occur between particles that are not exchanging internal energy and inelastic collisions, in which the collision energy is redistributed through the internal mode of the particles. During such collisions, particles may be assigned post-collision velocities, post-collision internal energy or quantum levels and undergo chemical reactions, for reactive gases.
The present section focuses on the redistribution of internal energy during an inelastic collision. Elastic collisions are herein disregarded. A comprehensive discussion on elastic collisions can be consulted in Bird's monograph [17]. Chemical reactions are not investigated in the present chapter but will be later addressed in Chapters 5 and 6.

3.3.1 Larsen-Borgnakke Redistribution Scheme

The LB redistribution scheme is a phenomenological model first introduced by Larsen and Borgnakke [131] for a mixture of polyatomic gases in which the internal energy was regarded as continuous. Bird [17] later generalised this scheme to incorporate molecular model effects, introducing the Variable Hard Sphere (VHS) model for elastic collisions. Unlike the rotational mode, the vibrational mode is generally only partially excited and the classical extension of the LB model to the vibrational mode was inappropriate. The situation was significantly enhanced by the introduction of a quantum approach for the vibrational mode by Bergemann and Boyd [150], greatly simplifying DSMC procedures. Since then, the redistribution scheme has remained unchanged and is now widely adopted in the DSMC community.
Figure 3.2 illustrates the general procedure of the quantum LB method during a collision between colliding partners A and B, involving the redistribution of rotational, vibrational and electronic internal energies. The quantum LB technique consists of a six-step procedure for redistributing the internal energy. The purpose of step 1 (top left) and 4 (top right) is to allocate a portion of the collision energy to the rotational mode of particles A and B, respectively. Similarly, step 2 (left) and 5 (right) aim to redistribute the collision energy to the vibrational mode of the collision partners. Finally, step 3 (bottom left) and 6 (bottom right) intend to redistribute the collision energy to the electronic mode of the collision partners. Additionally, for each sequence presented in Fig. 3.2, the colliding partner is tested for energy redistribution and only a fraction, i.e. $\frac{1}{Z}$, is allowed for energy exchange. If an inelastic collision is accepted, the collision energy is redistributed as detailed in the subsequent sections; if not, the colliding partner conserves its pre-collision internal energy and the colliding partner is then considered for the following internal mode.
The general redistribution between the translational energy and an internal mode of the collid-

ing partners A and B, namely ε_A and ε_B, respectively, with respective mean internal degree of freedom $\Xi_A = \frac{1}{2}\xi_A$ and $\Xi_B = \frac{1}{2}\xi_B$ is formulated,

$$f\left(\frac{\varepsilon_A}{\varepsilon_c}\right) = f\left(\frac{\varepsilon_B}{\varepsilon_c}\right) = \frac{\Gamma(\Xi_A+\Xi_B)}{\Gamma(\Xi_A)\Gamma(\Xi_B)}\left(\frac{\varepsilon_A}{\varepsilon_c}\right)^{\Xi_A-1}\left(\frac{\varepsilon_B}{\varepsilon_c}\right)^{\Xi_B-1}. \tag{3.14}$$

The redistribution of the rotational, vibrational and electronic energy following a collision event is addressed separately in the subsequent sections following the example illustrated in Fig. 3.2.

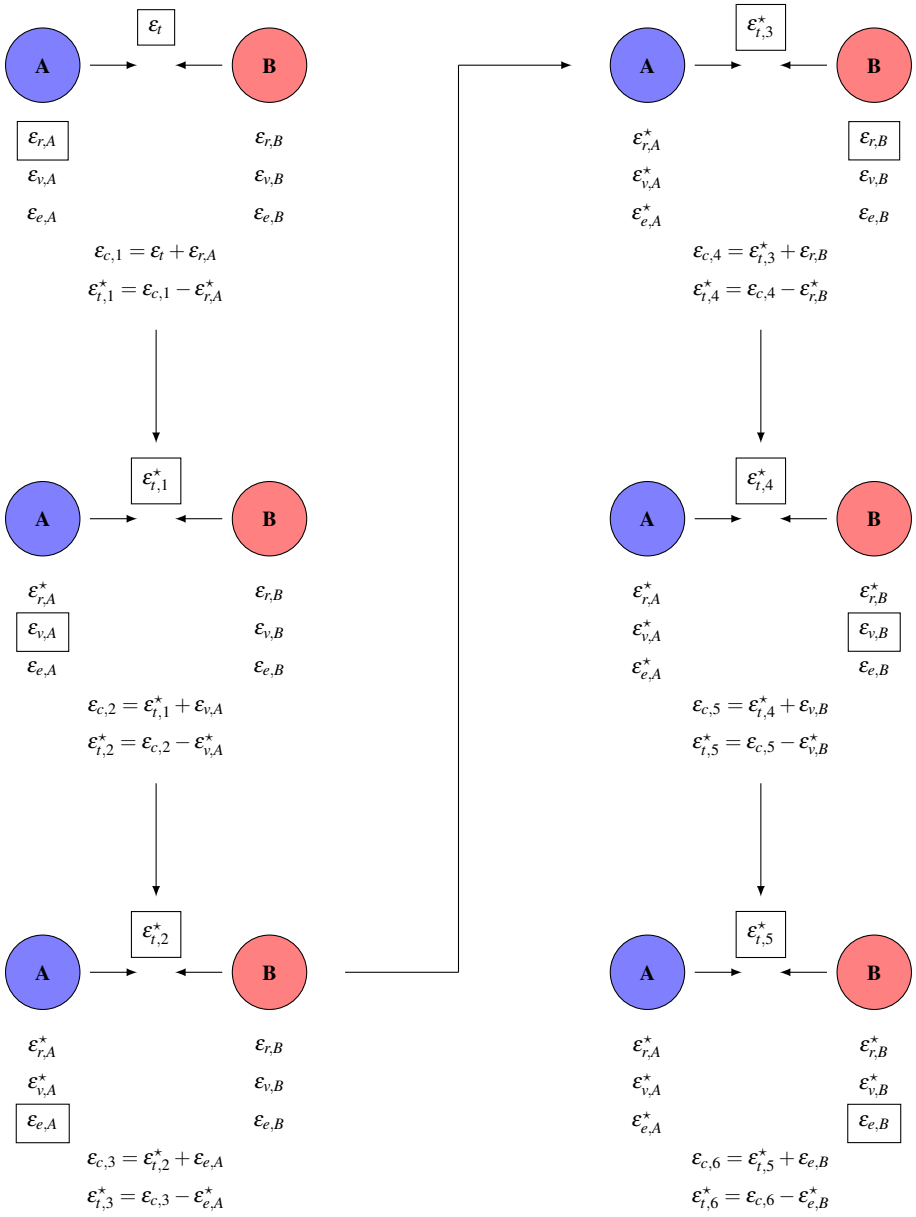

Figure 3.2: Flowchart of the serial application of the quantum Larsen-Borgnakke techniques.

3.3.2 Rotational Mode

Consider the first redistribution of internal energy which involves the translational and rotational modes, illustrated in bottom left Fig. 3.2. In the DSMC community, the rotational collision number is commonly defined as a constant number, typically suggested as $Z_r = 5$ and a collision is allowed to result in a rotational energy exchange if,

$$\frac{1}{Z_{r,A}} > \mathcal{R}. \tag{3.15}$$

If an inelastic collision is accepted, the pre-collision energy of the collision partners A and B, $\varepsilon_{c,1}$, is calculated as the sum of the relative translational energy of the pair A and B, ε_t and the pre-collision rotational energy of particle A, $\varepsilon_{r,A}$,

$$\varepsilon_{c,1} = \varepsilon_t + \varepsilon_{r,A}. \tag{3.16}$$

The LB method samples a post-collision energy from a combined distribution of the translational and an internal mode of the colliding particle. The translational distribution function inherently depends on the inter-molecular model employed as it defines the collision probability. For the VHS model, the probability distribution of translational energy during a collision is,

$$f(\varepsilon_t) = \frac{1}{\Gamma(\xi_t)} \left(\frac{\varepsilon_t}{kT}\right)^{\frac{3}{2}-\omega_{A,B}} e^{-\frac{\varepsilon_t}{kT}}, \tag{3.17}$$

where $\Gamma(s)$ is the ordinary gamma function and ξ_t is the mean translational degree of freedom, which, for the VHS gas, is given by averaging the relative translational collision between particles which yields,

$$\xi_t = \frac{5}{2} - \omega_{A,B}. \tag{3.18}$$

where $\omega_{A,B}$ is the mean viscosity exponent between colliding partners A and B.
The distribution function for the rotational mode of a particle with ξ_r rotational degree of freedom follows the Hinshelwood distribution function [186] that is,

$$f(\varepsilon_{r,A}) \propto \varepsilon_r^{\frac{\xi_r}{2}-1} e^{-\frac{\varepsilon_{r,A}}{kT}}. \tag{3.19}$$

For linear molecules, e.g. O_2 or N_2, there are two rotational degrees of freedom, i.e. $\xi_r = 2$, whereas for non-linear molecules, e.g. H_2O or CH_4, there are three rotational degrees of freedom, i.e. $\xi_r = 3$. Inserting the corresponding degree of freedom into Eq. (3.14), two scenarios arise depending on reversibility of the cumulative distribution.

If $\xi_r = 2$, Eq. (3.14) reduces,

$$f(\varepsilon_{r,A}) = \left(\frac{5}{2} - \omega_{A,B}\right)\left(1 - \frac{\varepsilon_{r,A}}{\varepsilon_{c,1}}\right)^{\frac{3}{2}-\omega_{A,B}}. \tag{3.20}$$

It is evident that Eq. (3.4) is reversible. Therefore, the rotational energy of the particle can be evaluated by mean of a random number uniformly distributed between 0 and 1 such that,

$$\varepsilon_{r,A} = -kTln(\mathcal{R}). \tag{3.21}$$

In this specific case, the cumulative distribution is reversible and the cumulative function can be equated to a random number uniformly distributed between 0 and 1 such that the post-collision rotational energy of colliding partner A is obtained by,

$$\varepsilon^{\star}_{r,A} = 1 - \mathcal{R}^{\frac{1}{\frac{5}{2}-\omega_{A,B}}}, \tag{3.22}$$

where the superscript $(.)^{\star}$ refers to post-collision properties.
If $\xi_r > 2$, Eq. (3.14) cannot be simplified to a reduced form. An acceptance-rejection method is required with the following distribution,

$$f' = \frac{f(\varepsilon_c, \varepsilon_{r,A})}{f_{max}} = \left(\frac{\frac{\xi_r}{2} + \frac{1}{2} - \omega_{A,B}}{\left(\frac{\xi_r}{2} - 1\right)}\mathcal{R}_1\right)^{\frac{\xi_r}{2}-1}\left(\frac{\frac{\xi_r}{2} + \frac{1}{2} - \omega_{A,B}}{\left(\frac{3}{2} - \omega\right)}(1 - \mathcal{R}_1)\right)^{\frac{3}{2}-\omega_{A,B}}. \tag{3.23}$$

A post-collision energy ratio, i.e. $\mathcal{R}_1 = \frac{\varepsilon_{r,A}}{\varepsilon_c}$, is chosen at random from the range 0 to 1. The distribution is evaluated from the above equation and is compared with a random fraction, $\mathcal{R}_2$, that is uniformly distributed between 0 and 1. The post-collision rotational energy is accepted if the distribution satisfies,

$$f' > \mathcal{R}_2. \tag{3.24}$$

The post-collision rotational energy of the colliding partner A is obtained by,

$$\varepsilon^{\star}_{r,A} = \mathcal{R}_1\varepsilon_{c,1}. \tag{3.25}$$

After this process, the collision energy is redistributed between a new translational energy, $\varepsilon^{\star}_{t,1}$ and the newly selected rotational energy $\varepsilon^{\star}_{r,A}$, such that

$$\varepsilon_{t,1} = \varepsilon_{c,1} - \varepsilon^{\star}_{r,A}. \tag{3.26}$$

This procedure is repeated for colliding partner B after all the internal mode of particle A has been addressed.

3.3.3 Vibrational Mode

Consider the second redistribution of internal energy that takes place between the translational and vibrational modes, shown in left of Fig. 3.2. In DSMC, a common approach is to assume a constant vibrational relaxation number, typically prescribed to $Z_{v,A} = 50$. This assumption implies that only a fixed fraction of collisions results in vibrational energy exchange. A more detailed approach, proposed by Bird [187], relies on microscopic information related to the colliding partners. The initial step is to define a quantized collision temperature, denoted as T_{col}, when a pair is selected for collision,

$$T_{col} = \frac{i^{\star}\theta_{v,A}}{(\frac{7}{2} - \omega_{A,B})} \tag{3.27}$$

where,

$$i^{\star} = \left\lfloor \frac{\varepsilon_{c,2}}{k\theta_{v,A}} \right\rfloor. \tag{3.28}$$

With this approach, the vibrational collision number is calculated

$$Z_{v,A} = \frac{\left(\frac{\theta_{d,A}}{T_{col}}\right)^{\omega_A} \left(\left(\frac{\theta_{d,A}}{T_{col}}\right)^{\frac{1}{3}} - 1\right)}{Z_{max}\left(\frac{\theta_{d,A}}{T_{ref}}\right)^{\omega_A} \left(\left(\frac{\theta_{d,A}}{T_{ref}}\right)^{\frac{1}{3}} - 1\right)}, \tag{3.29}$$

where θ_d is the dissociation temperature, T_{ref} is a reference temperature and Z_{max} is the reference collision number and it is formulated as,

$$Z_{max} = \left(\frac{C_1}{T_{max}^{\omega_A}}\right) e^{C_2 T_{max}^{-\frac{1}{3}}}, \tag{3.30}$$

where T_{ref} is usually taken to be the characteristic vibrational temperature of colliding partner A, C_1 and C_2 are constants from the Millikan and White data that can be consulted in Bird [17][Appendix A].

The colliding partner is tested for vibrational energy exchange and it is accepted if,

$$\frac{1}{Z_{v,A}} > \mathcal{R}. \tag{3.31}$$

If an inelastic collision is accepted, the pre-collision energy of the collision partners A and B, $\varepsilon_{c,2}$, is calculated as the sum of the remaining energy from the redistribution of the rotational energy of colliding partner A, $\varepsilon^{\star}_{t,1}$ and the pre-collision vibrational energy of particle A, $\varepsilon_{v,A}$,

$$\varepsilon_{c,2} = \varepsilon^{\star}_{t,1} + \varepsilon_{v,A}. \tag{3.32}$$

Following the approach adopted by Bergemann and Boyd [150], a Dirac delta function is ap-

plied to the Boltzmann distribution, Eq. (2.24), of the vibrational energy to define the following continuous distribution function,

$$f(\varepsilon_{v,i}) = \frac{e^{-\frac{\varepsilon_{v,i}}{kT}}}{\sum_j e^{-\frac{\varepsilon_{v,j}}{kT}}} \delta\left(\varepsilon_v - \left(i + \frac{1}{2}\right) k\theta_v\right). \tag{3.33}$$

Combining the translational and vibrational distribution function, Eqs. (3.17) and (3.33), the maximum probability of the resulting distribution is obtained for the ground vibrational quantum level, i.e. $i = 0$; hence, the normalisation factor, f_{max}, of the resulting distribution reads,

$$f_{max} = \varepsilon_c^{\frac{3}{2}-\omega_{A,B}} e^{-\frac{\varepsilon_c}{kT}}. \tag{3.34}$$

A post-collision vibrational quantum level $i^\star$ is uniformly chosen between 0 and i_{max} and an acceptance-rejection method is used to select a value of $i^\star$ from the distribution,

$$f' = \frac{f(\varepsilon_c, \varepsilon_{v,i^\star})}{f_{max}} = \left(1 - \frac{i^\star k\theta_v}{\varepsilon_c}\right)^{\frac{3}{2}-\omega_{A,B}}. \tag{3.35}$$

Finally, the post-collision vibrational quantum level $i^\star$ is accepted if the distribution satisfies,

$$f' > \mathcal{R}. \tag{3.36}$$

Then, the colliding partner is assigned a new vibrational energy which corresponds to,

$$\varepsilon^\star_{v,A} = i^\star k\theta_{v,A}. \tag{3.37}$$

The difference between the available collision energy $\varepsilon_{c,2}$ and the newly selected vibrational energy $\varepsilon^\star_{v,A}$ is allocated to a new translational energy, $\varepsilon^\star_{t,2}$ such that,

$$\varepsilon^\star_{t,2} = \varepsilon_{c,2} - \varepsilon^\star_{v,A}. \tag{3.38}$$

This procedure is repeated for colliding partner B after all the internal mode of particle A has been addressed.

3.3.4 Electronic Mode

Consider the third redistribution of internal energy which occurs between the translational and electronic modes, presented in top left of Fig. 3.2. In a similar fashion to the previous modes, the electronic collision number is traditionally regarded as constant, typically prescribed to $Z_e =$

500 [151]. An electronic energy exchange is then allowed if,

$$\frac{1}{Z_{e,A}} > \mathcal{R}. \tag{3.39}$$

If the collision process is inelastic, the pre-collision energy of the collision partners A and B, $\varepsilon_{c,3}$, is calculated as the sum of the remaining energy from the redistribution of the vibrational energy of colliding partner A, $\varepsilon^{\star}_{t,2}$ and the pre-collision electronic energy of particle A, $\varepsilon_{e,A}$,

$$\varepsilon_{c,3} = \varepsilon^{\star}_{t,2} + \varepsilon_{e,A}. \tag{3.40}$$

In a similar fashion to the construction of the distribution for the vibrational mode, a Dirac delta function is applied to the Boltzmann distribution of the electronic energy to form the continuous distribution function,

$$f(\varepsilon_{e,j}) = \frac{g_j e^{-\frac{\varepsilon_{e,j}}{kT}}}{\sum\limits_n g_n e^{-\frac{\varepsilon_{e,n}}{kT}}} \delta(\varepsilon_e - \varepsilon_{e,j}). \tag{3.41}$$

Combining Eq. (3.17) and Eq. (3.41), the resulting distribution reads,

$$f(\varepsilon_c, \varepsilon_{e,j}) = \frac{g_j e^{-\frac{\varepsilon_c}{kT}}}{\Gamma(\frac{5}{2} - \omega_{A,B}) \sum\limits_n g_n e^{-\frac{\varepsilon_{e,n}}{kT}}} \left(\frac{\varepsilon_c - \varepsilon_{e,j}}{kT} \right)^{\frac{3}{2} - \omega_{A,B}}. \tag{3.42}$$

The LB method assumes local thermal equilibrium prevails, which imposes the temperature to be constant in the process. Similarly, the total collision energy is constant through the redistribution. The distribution function can therefore be reduced to the simple form,

$$f(\varepsilon_c, \varepsilon_{e,j}) \propto g_j (\varepsilon_c - \varepsilon_{e,j})^{\frac{3}{2} - \omega_{A,B}}. \tag{3.43}$$

A post-collision electronic energy cannot be directly sampled from the above expression, therefore, an acceptance-rejection method is employed. The first step consists of normalising the distribution by its maximum and searching the corresponding electronic quantum level j'. The normalised distribution yields,

$$f' = \frac{f(\varepsilon_c, \varepsilon_{e,j})}{f_{max}} = \frac{g_j (\varepsilon_c - \varepsilon_{e,j})^{\frac{3}{2} - \omega_{A,B}}}{g_{j'} (\varepsilon_c - \varepsilon_{e,j'})^{\frac{3}{2} - \omega_{A,B}}}. \tag{3.44}$$

A post-collision electronic quantum number, $j^{\star}$, is sampled from a uniform distribution which admits the values between 0 and j'. Finally, $j^{\star}$ is accepted if the normalised distribution satisfies,

$$f' > \mathcal{R}. \tag{3.45}$$

The colliding partner is assigned a new electronic energy $\varepsilon^{\star}_{e,A}$ and the available collision energy

$\varepsilon_{c,2}$ is reduced accordingly to a new translational energy, $\varepsilon^{\star}_{t,3}$ such that,

$$\varepsilon^{\star}_{t,3} = \varepsilon_{c,2} - \varepsilon^{\star}_{e,A}. \tag{3.46}$$

At this stage of the procedure, the collision energy has been redistributed through all internal of the colliding partner A. The difference of energy between the collision energy $\varepsilon_{c,3}$ and the newly selected electronic energy $\varepsilon^{\star}_{e,A}$ is passed on to colliding partner B to sequentially redistribute the total collision through all its internal mode in a similar fashion as herein described for colliding partner A.

3.4 Internal Temperatures

The internal temperatures represent important properties for characterising the mechanisms governing the physics of the flow. These properties are also of major importance for distinguishing different models at a comparable level. Therefore, understanding the derivation of these internal temperatures is fundamental for gaining insights into the physics of the flow. This section presents an overview of the derivation of these properties, along with a discussion of their limitations.

3.4.1 Rotational Temperature

For most of the applications presented in this thesis, the temperature is sufficiently high for the rotational mode to be treated as continuous. In other words, the quantized effects of this mode are neglected, significantly simplifying the mathematical derivation of the rotational temperature. This temperature is derived from the equipartition theorem, which was previously introduced for the calculation of the internal degree of freedom, as seen in Eq. (2.45). The equipartition theorem establishes a connection between the mean internal energy, the degree of freedom and the internal temperature, expressed as,

$$T_r = \frac{2e_r}{\xi_r k}. \tag{3.47}$$

3.4.2 Vibrational Temperature

The vibrational temperature is computed as the ratio between the Boltzmann distribution of two adjacent vibrational quantum levels, specifically, the ground and first vibrational quantum levels. Their respective distribution are given by,

$$\frac{n_0}{n} = \frac{e^{-\frac{\varepsilon_0}{kT_v}}}{\sum_i e^{-\frac{\varepsilon_i}{kT_v}}}, \tag{3.48}$$

and,

$$\frac{n_1}{n} = \frac{e^{-\frac{\varepsilon_1}{kT_v}}}{\sum_i e^{-\frac{\varepsilon_i}{kT_v}}}, \tag{3.49}$$

where n_0 and n_1 are the number density of the ground and first vibrational quantum level, respectively and n is the total number density of the cell.
The division of Eq. (3.48) by Eq. (3.49) eliminates the partition function, resulting in a simple formulation from which the vibrational temperature can be extracted using the natural logarithm function. Assuming a harmonic oscillator model, where vibrational quantum levels are equally spaced with a constant increment energy $\Delta\varepsilon_v = k\theta_v$, the ratio of two adjacent quantum levels can be further simplified by demonstrating that the average vibrational quantum level is,

$$\langle i \rangle = \frac{e_v}{k\theta_v}. \tag{3.50}$$

Applying these transformations to the ratio of Eqs. (3.48) and (3.49), the formulation for the vibrational temperature reduces to,

$$T_v = \frac{\theta_v}{ln\left(1 + \frac{1}{\langle i \rangle}\right)}. \tag{3.51}$$

It is important to emphasise that the derivation of Eq. (3.51) relies on the assumption that the vibrational quantum levels follow the Boltzmann distribution. As highlighted in Chapter 2, the Boltzmann distribution applies only to a system in thermal equilibrium. Additionally, it is important to mention that for non-Boltzmann distribution of the vibrational energy, the ratio between two adjacent vibrational quantum levels may result in a different vibrational temperature to that defined in Eq. (3.51). Consequently, it is important to recognise that Eq. (3.51) is inherently limited to thermal equilibrium conditions.

3.4.3 Electronic Temperature

The electronic temperature implemented in *dsmcFoam+* follows the suggestion of Liechty [188]. This temperature is constructed on the same premises as the vibrational temperature. It consists in calculating the ratio between the Boltzmann distribution of the ground and first electronic excited states that are respectively,

$$\frac{n_{e,0}}{n} = \frac{g_0 e^{-\frac{\varepsilon_{e,0}}{kT_e}}}{\sum_i g_i e^{-\frac{\varepsilon_i}{kT_e}}}, \tag{3.52}$$

and,

$$\frac{n_{e,1}}{n} = \frac{g_{e,1} e^{-\frac{\varepsilon_{e,1}}{kT_e}}}{\sum_i g_{e,i} e^{-\frac{\varepsilon_{e,i}}{kT_e}}}, \tag{3.53}$$

where $n_{e,0}$ and $n_{e,1}$ are the number density of the ground and first electronic excited states, respectively.

From the above two equations, Eqs. (3.52) and (3.53), the derivation of the electronic temperature is straightforward and yields,

$$T_e = \frac{\varepsilon_1 - \varepsilon_0}{kln\left(\frac{n_0}{n_1}\frac{g_1}{g_0}\right)}. \tag{3.54}$$

The electronic temperature is fundamentally derived from similar considerations to the vibrational temperature, therefore, it shares the same limitations as its counterparts.

3.4.4 Overall Temperature

In thermal non-equilibrium conditions, it is sometime convenient to refer to the overall temperature which is a weighted mean of the translational and internal temperatures,

$$T_{ov} = \frac{\xi_t T_t + \xi_r T_r + \xi_v T_v + \xi_e T_e}{\xi_t + \xi_r + \xi_v + \xi_e}, \tag{3.55}$$

where ξ_v and ξ_e are the vibrational and electronic degrees of freedom, respectively, calculated from the equipartition theorem, Eq. (2.45).

The overall temperature represents the theoretical equilibrium temperature toward which a gas initialised in an adiabatic box in thermal non-equilibrium conditions will theoretically converge. This temperature can serve the purpose of a verification exercise to ensure the correct implementation of a new model in any DSMC solver.

3.5 *dsmcFoam+* Solver

The original version of *dsmcFoam* was developed by OpenCFD Ltd in collaboration with Scanlon *et al*. [189] at the University of Strathclyde, building upon the molecular dynamics (MD) solver *mdFoam* developed by Macpherson [190] and Borg [191]. *dsmcFoam* was built within the framework of the open-source C++ computational fluid dynamics toolbox open-source field operation and manipulation (OpenFOAM) [192]. The core DSMC capabilities of OpenFOAM was first released with OpenFOAM 1.7.0. Since then, the original version of *dsmcFoam* remains largely unchanged and can be found in the any of the release of OpenFOAM.

The original version of *dsmcFoam* encompassed essential features of any modern DSMC solver, but was lacking a number of crucial features for *dsmcFoam* to be practicable to engineering applications. Specifically, *dsmcFoam* was adequate for the simulation of rarefied gas flow with

noble gas, e.g. Ar, Ne or Xe, or strongly bounded diatomic molecules, e.g. N_2. However, it was inadequate for typical atmospheric reentry conditions in which real gas effects can no longer be neglected. In the view of these limitations, a significant extension of *dsmcFoam* was undertaken by White [185] and named *dsmcFoam+* [193]. This solver builds upon the capabilities of the original *dsmcFoam* and provides an enhanced set of DSMC capabilities, including parallel performance with dynamic load balancing, vibrational and electronic modes or chemical reactions.

In a similar philosophy to the work of White [185], this thesis contributes to elevating *dsmcFoam+* to state-of-the-art accuracy standards. This thesis extends the DSMC capabilities of *dsmcFoam+* with a sophisticated approach for modelling molecular vibrational excitation, an improved chemistry model fitted to reproduce experimental measurements and high-fidelity chemistry calculations and the consideration of real-gas effects through the coupling of electronic and vibrational modes. These individual contributions are comprehensively discussed in subsequent chapters.

Table 3.1: Comparison of *dsmcFoam* and *dsmcFoam+* capabilities (Adapted from White *et al*. [193]).

Feature	*dsmcFoam*	*dsmcFoam+*	This thesis
Arbitrary 2D geometries	✓	✓	✓
Arbitrary 3D geometries	✓	✓	✓
Arbitrary axisymmetric geometries	x	✓	✓
Chemical reactions (QK-HO)	x	✓	✓
Chemical reactions (QK-aHO)	x	x	✓
Coupling electronic-vibrational modes	x	x	✓
Dynamic load balancing	x	✓	✓
Electronic energy	x	✓	✓
Gravitational force controller	x	✓	✓
Landau-Teller relaxation correction	x	x	✓
Mass flow rate measurement	x	✓	✓
Normal shock wave stabilisation	x	x	✓
Parallel processing	✓	✓	✓
Rotational energy	✓	✓	✓
Simulation quality reports	x	✓	✓
Vibrational energy (HO)	x	✓	✓
Vibrational energy (aHO)	x	x	✓

Chapter 4

Vibrational Modelling with an Anharmonic Oscillator Model in DSMC *

This chapter presents the implementation of an anharmonic oscillator model in the *dsmcFoam+* solver. Firstly, the derivation of an anharmonic oscillator model is presented, including a detailed discussion of the difference between the harmonic and anharmonic oscillator models. The two vibrational models are then compared against a compilation of PES calculations for the calculation of the vibrational energies. A series of adiabatic scenarios relevant to high-speed flows is performed to verify the implementation of the anharmonic oscillator model. Finally, the two vibrational models are applied to a canonical high-speed flow of a cylindrical body entering Earth's atmosphere at about 75 km.

4.1 Theoretical Background

This section presents the derivation of vibrational energy under the assumption that the interatomic forces acting within the molecule are governed by the Morse potential [34]. Firstly, the differences in describing the potential energy function are discussed. Then, the vibrational energies of the two vibrational models are compared against a compilation of PES calculations [194] and a new set of spectroscopic constants are suggested. Finally, the vibrational quantum level reached at the dissociation energy of both vibrational models is discussed.

Consider a diatomic molecule consisting of two nuclear masses m_1 and m_2 with pure vibrational motion concentrated along the inter-nuclear axis which, in contrast to the harmonic oscillator model, is governed by the Morse potential energy function [34],

$$U = \varepsilon_d \left(1 - e^{-2\alpha \frac{r - r_{eq}}{r_{eq}}}\right)^2, \tag{4.1}$$

*A large portion of the work presented in this Chapter is published in **C. H. B. Civrais**, C. White and R. Steijl (2022). "Vibrational modelling with an anharmonic oscillator model in direct simulation Monte Carlo", *Journal of Thermophysics and Heat Transfer*, 37(3):534–548, 2022. doi: 10.2514/1.T6547.

where ε_d is the dissociation energy and α is a spectroscopic constant that controls the width of the potential energy function.

The time independent Schrödinger equation of this system becomes,

$$-\frac{\hbar^2}{2\mu}\frac{d^2\psi(x)}{dx^2}+\left(\varepsilon-\varepsilon_d\left(1-e^{-2\alpha\frac{r-r_{eq}}{r_{eq}}}\right)^2\right)\psi(x)=0. \tag{4.2}$$

Figure 4.1 presents a comparison between the Morse potential energy function and Eq. (2.31) for a selection of three diatomic molecules: N_2, O_2 and NO. The potential energy is normalised by the dissociation energy of the molecule and the inter-nuclei distance is scaled by the distance at rest between the two nuclei. As a convention for the entire thesis, the harmonic oscillator model is denoted in blue color and the anharmonic oscillator model in red color. For reference, the vibrational quantum levels of the two approaches are included in horizontal lines.

The Morse and Hooke's potential energy functions substantially differ in the description of the intra-molecular interactions. Specifically, the Morse potential energy tends asymptotically to the dissociation energy of the chemical species, whereas Hooke's law tends to infinity. This difference has a substantial consequence on the vibrational quantum levels obtained for both models. While the Morse potential asymptotically tends to the dissociation energy with a finite number of vibrational quantum levels, the harmonic oscillator model remains unbounded with the results of an infinite number of vibrational quantum levels.

The present section focuses on gaining physical insights in the vibrational modelling rather than solving Eq. (4.2) with the intra-molecular interactions described with Eq. (4.1). No further justification on the validity and full derivation will be provided in this thesis. For further explanation, the reader is referred to Morse [34] or a quantum mechanics textbook [170].

Under the assumption of the Morse potential, the vibrational energies are formulated,

$$\varepsilon_v=h\nu\left(i+\frac{1}{2}\right)-\frac{(h\nu)^2}{4\varepsilon_d}\left(i+\frac{1}{2}\right)^2, \tag{4.3}$$

where the fundamental frequency is defined as

$$\nu=\frac{\alpha}{2\pi}\sqrt{\frac{\varepsilon_d}{m}}. \tag{4.4}$$

The vibrational energy modelled with the Morse potential is constituted of two terms. The first term is equivalent to the harmonic oscillator model. The second term is a negative second-order term that is responsible for an asymptotic curve towards the dissociation limit.

To compare the two vibrational models at an equivalent level, it is necessary to follow the same convention. For this purpose, the vibrational energy, Eqs. (2.33) and (4.3), can be re-written in the form of a function that accounts for spectroscopy constants only. To achieve this transformation, the first step consists in expressing both the fundamental frequency and dissociation energy

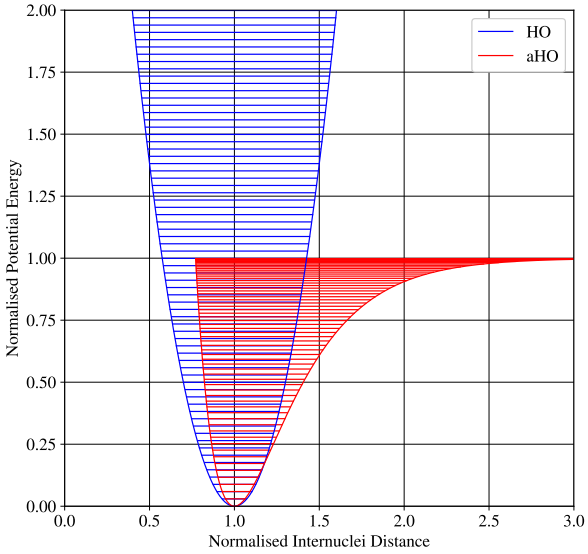

(a) Nitrogen molecule.

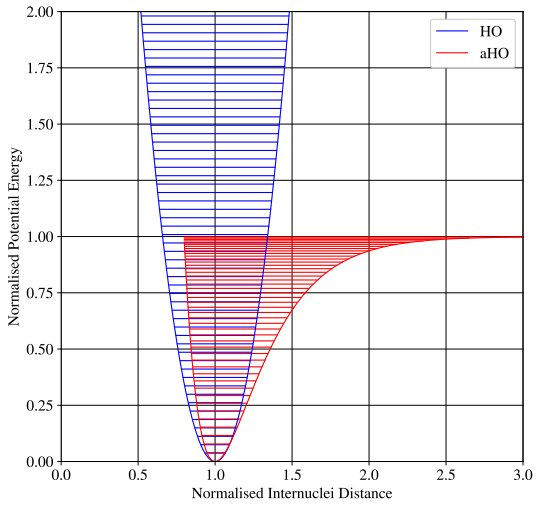

(b) Oxygen molecule.

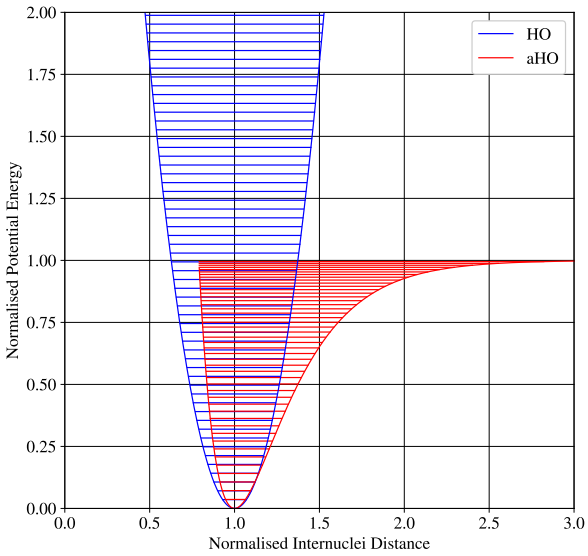

(c) Nitric oxide molecule.

Figure 4.1: Potential energy for three diatomic molecules in their ground electronic state.

in terms of spectroscopy constants

$$\nu = c\omega_e, \tag{4.5}$$

and,

$$\varepsilon_d = \frac{(hc)^2}{4\omega_e\chi_e}, \tag{4.6}$$

where ω_e and $\omega_e\chi_e$ are two spectroscopic constants.
Substituting Eqs. (4.5)-(4.6) in Eq. (2.33), the harmonic oscillator model becomes,

$$\varepsilon_v = hc\omega_e\left(i+\frac{1}{2}\right). \tag{4.7}$$

Applying a similar transformation to Eq. (4.3), the Morse vibrational energy reads,

$$\varepsilon_v = hc\omega_e\left(i+\frac{1}{2}\right) - \omega_e\chi_e\left(i+\frac{1}{2}\right)^2. \tag{4.8}$$

The most popular sources for obtaining these constants are the National Institute of Standards and Technology (NIST) database [25] or the Huber and Herzberg tables [26]. However, Da Silva *et al*. [51] have reported that the use of these database often over-estimates the number of vibrational quantum levels and the dissociation energy of a molecule. Therefore, the spectroscopic constants used in this thesis have been fitted to high-fidelity PES data from Armenise and Esposito [194] for all three molecular species. Table 4.1 presents the fitted spectroscopy constants along with the values extracted from the Huber and Herzberg tables [26] for three molecular systems lying at the ground state level.

Table 4.1: Spectroscopy constants for three diatomic molecules in their ground electronic state.

Species	Huber and Herzberg [26]		Fitted	
	$\omega_e\ (cm^{-1})$	$\omega_e\chi_e\ (cm^{-1})$	$\omega_e\ (cm^{-1})$	$\omega_e\chi_e\ (cm^{-1})$
$N_2(X^1\ \sum_g^+)$	2358.57	14.324	2419.32	17.867
$O_2(X^3\ \sum_g^-)$	1580.19	11.981	1688.17	16.425
NO $(X^2\ \Pi_r)$	1904.20	14.075	1967.28	17.305

The comparison of the vibrational energies for N_2, O_2 and NO are depicted in Fig. 4.2a. The vibrational energies are calculated with both sets of spectroscopic constants shown in Tab. 4.1 and are normalised by the dissociation energy. The calculation of the vibrational energy with the Huber and Herzberg table [26] values are represented by solid lines, while those based on the fitted spectroscopic constants are represented in dashed lines. The PES calculations [194] are included for reference. The two vibrational models are differentiated by the color convention previously defined.

In Chapter 2, the foundation of the harmonic oscillator model has been detailed. This vibrational model is based on an equally spaced distribution of the vibration quantum levels which, in turn, leads to a linear trend of the vibrational energy. In contrast, the anharmonic oscillator model differs from uniformity. Specifically, this model incorporates a second-order negative term that decreases the spacing between levels as the level increases. This behaviour is noticeable in Fig. 4.2, with a high concentration of energy in the high-lying vibrational quantum levels.

Consider the vibrational excitation of a nitrogen molecule. The vibrational energies computed with the Huber and Herzberg tables [26] reproduce the PES calculations for the first 8 vibrational quantum levels. Beyond this limitation, the vibrational energy diverges as the vibrational quantum level increases. This discrepancy indicates that these spectroscopic constants overestimate the vibrational energy leading to smaller number of vibrational quantum levels lying below the dissociation energy.

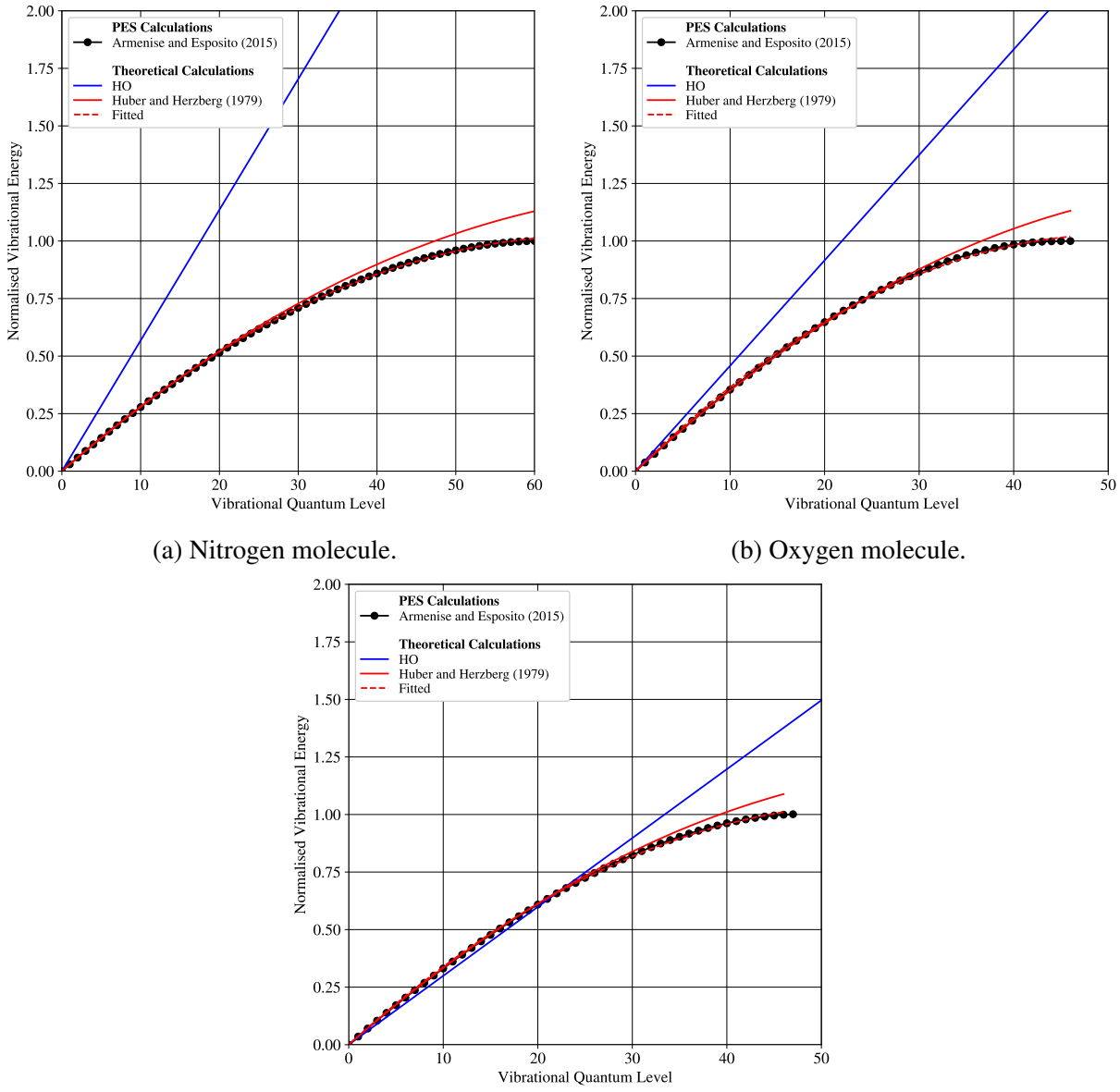

(a) Nitrogen molecule.

(b) Oxygen molecule.

(c) Nitric oxide molecule.

Figure 4.2: Vibrational energy for three diatomic molecules at the ground state level.

The maximum vibrational quantum levels preceding dissociation energy are summarized in Tab. 4.2 for the three molecular species. The selection of the vibrational model has a direct impact on the vibrational quantum level achieved at the dissociation energy. For a nitrogen molecule under the harmonic oscillator assumption, the dissociation limit is reached for a quantum level of 33, while under the anharmonic oscillator assumption, the dissociation occurs at quantum level 47 for the vibrational energies computed with the Huber and Herzberg tables [26] or 58 for vibrational energies fitted on PES calculations. A modification of the maximum vibrational quantum level allowed before dissociation of the molecule may result in noticeable changes in the chemical activity of the molecule.

For instance, Grover *et al.* [125] presents a comparative study of two independently developed

PESs for N_3 and N_4 systems at the University of Minnesota and NASA Ames Research Center. It is shown that PES developed at the University of Minnesota describes the rotational-less ground electronic states of N_2 with 55 vibrational quantum levels while the PES developed at NASA Ames Research Center describes it with 61 vibrational quantum levels. The different approach in constructing the two PES is also noticeable in the rovibrational quantum levels in which the NASA Ames Research Center's PES describes N_2 with an additional 192 rovibrational quantum levels. The study demonstrates that the two PES not only differ from their description of the internal quantum levels of N_2 but also on the dissociation reaction rates of $N_2 + N_2$ and $N_2 + N$ and the vibrational temperature and atomic fraction flow fields for a reactive nitrogen flow past a cylinder at freestream conditions: $Ma_\infty = 20$ and $Kn_\infty = 0.015$. In light of Grover *et al.* [125], it is reasonable to conclude that considering an anharmonic oscillatory model instead of the harmonic oscillator model will have significant implications on the macroscopic properties of the gas as well as its composition.

Although this fundamental aspect is of interest in the context of high-speed flow simulations, chemical reaction rates are not investigated in the present chapter but will be later addressed in Chapters 5 and 6.

Table 4.2: Maximum vibrational quantum levels before the dissociation barrier for three diatomic molecule in their ground electronic state.

Species	HO	Huber and Herzberg [26]	Fitted
$N_2(X^1\Sigma_g^+)$	33	47	58
$O_2(X^3\Sigma_g^-)$	26	36	42
$NO(X^2\Pi_r)$	27	39	44

Another outcome highlighted in Fig. 4.2 is the validity of the harmonic oscillator assumption. It is perceptible that, due to the linear behaviour, the harmonic oscillator model is an acceptable hypothesis in a configuration where only a small portion of vibrational levels are excited. In other words, harmonic oscillator remains valid for low enthalpy flows, but as the temperature increases, it should be replaced by an anharmonic oscillator model.

4.2 Vibrational Modelling in DSMC

This section presents the numerical techniques employed to integrate the anharmonic oscillator model into *dsmcFoam+*. The equilibrium sampling procedure remains largely unchanged and the implementation of the anharmonic oscillator model can be viewed as a generalisation of the technique presented in Chapter 3. Similarly, the redistribution of the vibrational energy in the event of a collision is a relatively simple adaptation since the procedure is similar to the treatment of the electronic energy. The primary challenge arises in the calculation of vibrational temperature which requires the resolution of a non-linear system.

4.2.1 Equilibrium Sampling

The harmonic oscillator model contributes two degrees of freedom and a similar treatment to that of the rotational mode was adopted to initialise the vibrational quantum level of particle. It is important to emphasise that this specific treatment is only applicable for a non-truncated harmonic oscillator. Otherwise, the mean degree of freedom falls below two, necessitating a distinct approach. In contrast, an anharmonic oscillator model contributes more than two degrees of freedom, rendering the approach outlined in Chapter 3 inadequate for the initialisation of the vibrational quantum levels. Instead, the vibrational quantum level of a particle is determined based on a given temperature T, e.g. wall, boundary or initialisation temperatures, using the distribution function,

$$f(\varepsilon_i) \propto \frac{e^{-\frac{\varepsilon_{v,i}}{kT}}}{\sum_j e^{-\frac{\varepsilon_{v,j}}{kT}}} \delta(\varepsilon_v - \varepsilon_{v,i}). \tag{4.9}$$

However, it is not possible to sample a vibrational quantum level directly from the distribution; hence, an acceptance-rejection scheme is employed. This procedure involves sampling a random vibrational quantum level from the following distribution,

$$f' = \frac{f(\varepsilon_i)}{f_{max}} = \frac{e^{-\frac{\varepsilon_{v,i}}{kT}}}{e^{-\frac{\varepsilon_{v,i_{max}}}{kT}}}. \tag{4.10}$$

where i_{max} is the vibrational quantum level for which Eq. (4.9) is a maximum.
The sampling of the vibrational quantum level follows the procedure described in Chapter 3: A random quantum level is sampled between 0 and i_{max}; this random quantum level is accepted if Eq. (4.10) satisfies $f' > \mathcal{R}$; otherwise, the random quantum level is rejected and the preceding steps are repeated until a suitable quantum level is returned.

4.2.2 Post-Collision Sampling

In a collision between two particles, the redistribution of the vibrational energy follows the procedures outlined in Chapter 3. First, the particle is tested for vibrational energy exchange; if the particle is not accepted, the function returns the initial vibrational quantum level. If an inelastic collision is accepted, the maximum available post-collision vibrational quantum level, $i^\star_{max}$, is computed and a post-collision quantum level is uniformly chosen between 0 and $i^\star_{max}$. Finally, a value of $i^\star$ is selected from the probability ratio using an acceptance-rejection technique.
As presented in Chapter 3, the first step consists in defining a quantized collision temperature which is herein slightly modified to accommodate the use of an anharmonic oscillator such that Eq. (3.27) becomes,

$$T_c = \frac{\varepsilon_{v,i^\star_{max}}}{k(\frac{7}{2} - \omega_{A,B})}, \tag{4.11}$$

where the maximum vibrational quantum level is obtained by looping through the list of vibrational energies and finding the vibrational quantum level that satisfies $\varepsilon_{v,i} > \varepsilon_c$.
If the vibrational collision number is based the collision temperature, Eqs. (3.29) and (3.30) are calculated with the modified temperature, Eq. (4.11); otherwise, the vibrational energy exchange is tested against a random number as described in Chapter 3. If the colliding partner is accepted for vibrational relaxation, the potential post-collision vibrational quantum level of the particle is uniformly chosen between $i = 0$ and the maximum possible level i_{max}. The acceptance-rejection method is applied to select a value of $i^\star$ from the distribution,

$$f(\varepsilon_c, \varepsilon_{i^\star}) = \left(1 - \frac{\varepsilon_{v,i^\star}}{\varepsilon_c}\right)^{\frac{3}{2}-\omega_{A,B}}, \tag{4.12}$$

where $\varepsilon_{v,i^\star}$ refers to the vibrational energy at quantum level $i^\star$ calculated with Eq. (2.33) for the harmonic oscillator model and with Eq. (4.3) for the anharmonic oscillator model.
These modifications of the original post collision sampling scheme can be seen as a generalisation of the procedure. The relations herein presented can be used by both harmonic and anharmonic oscillator models. The main differences lie in the calculation of the maximum allowed vibrational quantum level, i_{max} and the probability calculation where the vibrational energies are calculated with Eq. (4.3) for the anharmonic oscillator model instead of Eq. (2.33) for the harmonic oscillator model.

4.2.3 Vibrational Temperature

The measurement of the vibrational temperature under the hypothesis of an anharmonic oscillator represents a challenge. In contrast with its counterpart, an anharmonic oscillator model does not benefit from a simple derivation of the vibrational temperature. The explanation lies in the definition of the partition function which reads,

$$Q_v = \sum_i e^{\frac{-\varepsilon_{v,i}}{kT_v}}. \tag{4.13}$$

Due to the nature of the anharmonic oscillator model, the summation cannot be eliminated and Eq. (4.13) represents its simplest form. Similarly, when evaluating the total mean vibrational energy, an analytical expression analogous to the harmonic oscillator model is not feasible. Instead, it is expressed as,

$$e_v = \frac{\sum_i \varepsilon_{v,i} e^{\frac{-\varepsilon_{v,i}}{kT_v}}}{\sum_i e^{\frac{-\varepsilon_{v,i}}{kT_v}}}. \tag{4.14}$$

The only means to obtain this temperature is through an iterative methodology to approximate one of the thermodynamic properties. In this thesis, a new way of solving this issue is proposed;

using a Newton iterative methodology. This method is versatile, exhibits fast convergence and consumes minimal computational resources. It involves applying a Taylor expansion around a specific value and truncating terms beyond the first order. As the series is truncated to retain only first-order terms, the function must be smooth to be reasonably approximated by a tangent. For the measurement of the vibrational temperature, it is convenient to define an objective function, i.e. f, that comprises the total mean vibrational energy, as per Eq. (4.14) and the mean vibrational energy in the cell denoted as $e_{v,cell}$,

$$f = e_{v,cell} - e_v. \tag{4.15}$$

A Newton iterative approach consists in minimizing the objective function. By definition, the mean vibrational energy is monotonic; hence, it does not contain local minima. Consequently, utilizing a Newton iterative method to solve the vibrational temperature problem is well-suited. However, this method is sensitive to the initial value set at the beginning of the process and a coarse initial value can delay convergence. To avoid this, a pre-optimized procedure has been designed to closely approach the DSMC value with a scanning process. Once this initial guess is known, the value is transferred to the main Newton loop to refine the vibrational temperature value by comparing the gradient of the function, the function itself and the initial guess to a tolerance factor.

4.3 Adiabatic Reactor Simulations

The implementation of a new model in a numerical solver necessitates thorough verification to ensure its accuracy and reliability. To achieve complete verification, this section presents a series of four adiabatic reactor cases, involving both thermal equilibrium and non-equilibrium scenarios. It is important to reiterate that, in all the cases presented here, the chemical reactions are disregarded.

4.3.1 Vibrational Temperature

The measurement of the vibrational temperature represents an important property to verify. It does not only inform on the measurement technique but also verifies the initialisation of the correct vibrational energy to the particle. Therefore, adiabatic reactor simulations are conducted with molecular oxygen as the working gas. These simulations involve a cubic cell with a volume of about 6.65×10^{-12} m^3. The time step employed for all cases is 1.0×10^{-9} s. The adiabatic reactors are filled with one million of DSMC simulator particles where each DSMC DSMC represents 5×10^6 real particles. Internal energies are redistributed through a serial application of the quantum LB method [131]. The inter-molecular collisions are computed with the VHS model [17] at a reference temperature of $T_{ref} = 273$ K with the species properties summarized in Tab. 4.3. The rotational, vibrational and electronic collision numbers are set to unity since

these play no role in the measurement of the vibrational temperature. The adiabatic reactors are initialised in thermal equilibrium conditions, with temperatures ranging from 0 to 20,000 K. The vibrational temperature is monitored and sampled over 10^6 time steps. Both the harmonic and anharmonic oscillator models are employed for this verification case.

Table 4.3: Species properties at a reference temperature of 273 K.

Chemical Species	m $(\times 10^{-27}\ kg)$	d $(\times 10^{-10}\ m)$	ω $(-)$	ω_e (cm^{-1})	$\omega_e\chi_e$ (cm^{-1})	θ_r (K)	θ_v (K)	θ_d (K)
O_2	53.12	4.07	0.77	1688.165	16.425	2.064	2256	59,500
O	26.56	3.00	0.80	–	–	–	–	–
N_2	46.50	4.17	0.74	2419.322	17.867	2.869	3371	113,500
N	23.25	3.00	0.80	–	–	–	–	–
NO	49.81	4.20	0.79	1967.283	17.305	2.400	2719	75,500

Figure 4.3 shows the measurement of the vibrational temperature for the anharmonic oscillator model, compared against those of the harmonic oscillator model. Excellent agreement is found between the new measurement technique and the traditional technique presented in Chapter 3. This demonstrates the correct implementation of the initialisation and post-collision sampling and the new measurement technique.

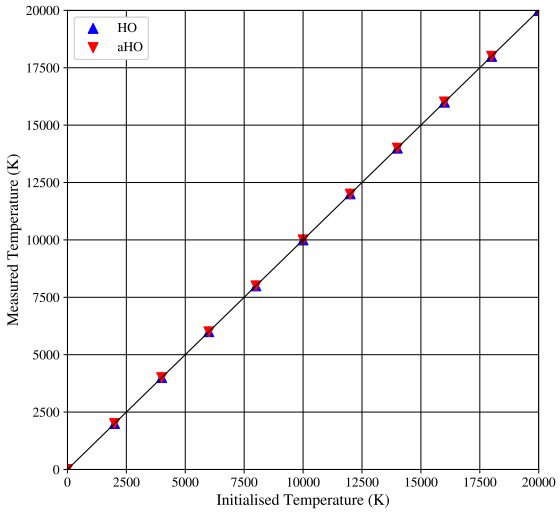

Figure 4.3: Comparison between the initialised vibrational temperature and the DSMC calculation.

4.3.2 Vibrational Density Function

The transition from a linear behaviour with a harmonic oscillator model to a non-linear behaviour signifies a distinct response to external excitation. As detailed in Sec. 4.1, it has been

observed that, due to the negative non-linear term, a larger portion of the vibrational energy concentrates in the high-lying vibrational quantum levels compared to the harmonic oscillator model. This observation has significant implications for the high-lying vibrational quantum level population. Since the population density is a function of the internal vibrational energy, a modification of the distribution profile is expected. As it represents a fundamental characteristic of the anharmonic oscillator model, this quantity is chosen as a verification test case for the implementation of the anharmonic oscillator model.

Adiabatic reactor simulations are conducted to measure the population of the vibrational quantum level of three molecules in thermal equilibrium conditions. These simulations consist of a single cubic cell with edge length 1.88×10^{-4} m and periodic boundaries filled with one million DSMC simulator particles. The inter-molecular collisions are computed with the VHS model with the species properties summarised in Tab. 4.3 for a reference temperature of $T_{ref} = 273$ K. The rotational and vibrational collision numbers are set to unity since these play no role in the measurement of the quantum-level populations. A fixed time step size of 1×10^{-9} s is adopted. The population of each quantum level is sampled for 10^6 time steps and recorded for three different temperatures: 5000 K, $10,000$ K and $15,000$ K.

Since the system remains in thermal equilibrium conditions for the duration of the simulations, the vibrational quantum levels are expected to follow the Boltzmann distribution,

$$f(\varepsilon_i) = \frac{e^{\frac{-\varepsilon_{v,i}}{kT}}}{\sum_j e^{\frac{-\varepsilon_{v,j}}{kT}}}. \tag{4.16}$$

Figure. 4.4 presents a comparison between the DSMC calculations for the harmonic oscillator and anharmonic oscillator models against the analytical expression, Eq. (4.16). The DSMC results are denoted by markers, the analytical solutions are depicted by solid lines and each temperature is associated with a respective colour. Figure. 4.4 shows that the numerical results are in excellent agreement with the analytical solutions for all three molecules, demonstrating the successful implementation of the anharmonic oscillator model in *dsmcFoam+*.

4.3.3 Adiabatic Relaxation

The second test involves verifying whether a correct equilibrium temperature can be reached from a given thermal non-equilibrium situation. To do this, the adiabatic reactor is initialised in thermal non-equilibrium conditions where $T_t = T_r = 20,000$ K and $T_v = 0$ K. The working gas are the three diatomic molecules aforementioned, i.e. N_2, O_2 and NO. The adiabatic reactor follows the previous setups with the exception that a constant fraction of $1/5$ and $1/50$ collisions are allowed to result in rotational and vibrational relaxation, respectively.

Starting from thermal non-equilibrium conditions, a relaxation process is initiated by binary collisions between particles and the corresponding exchange of internal energies. After a certain

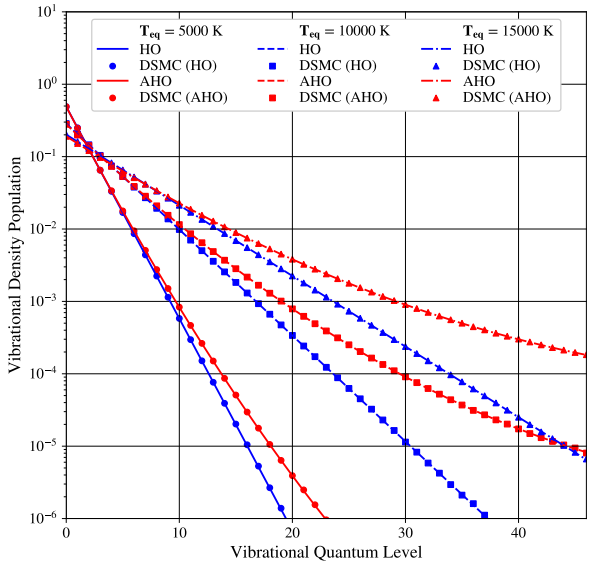

(a) Nitrogen molecule.

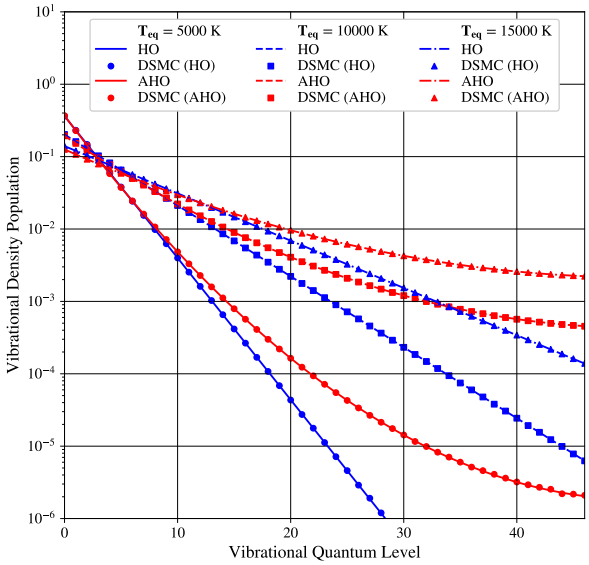

(b) Oxygen molecule.

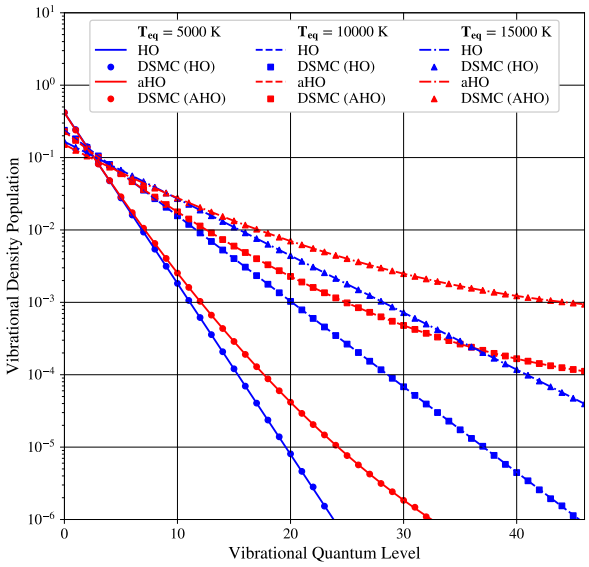

(c) Nitric oxide molecule.

Figure 4.4: Probability distribution of vibrational quantum levels for three diatomic molecules.

time has elapsed, a thermal equilibrium state is reached and the theoretical equilibrium temperature is formulated,

$$T_{eq} = \frac{\xi_{t,i}T_{t,i} + \xi_{r,i}T_{r,i} + \xi_{v,i}T_{v,i}}{\xi_{t,f} + \xi_{r,f} + \xi_{v,f}}, \tag{4.17}$$

where the subscripts $(.)_i$ and $(.)_f$ refer to the initial and final times.

The results of the adiabatic reactor simulations are depicted in Fig. 4.5. Figure 4.5 follows the colour convention established for all the figures presented in the thesis. The translational, rotational, vibrational and electronic temperatures are distinguished by solid, dashed, dashed-dotted and dotted lines. For completeness, the theoretical equilibrium temperatures for all working gas and vibrational models are depicted in solid and dashed black lines.

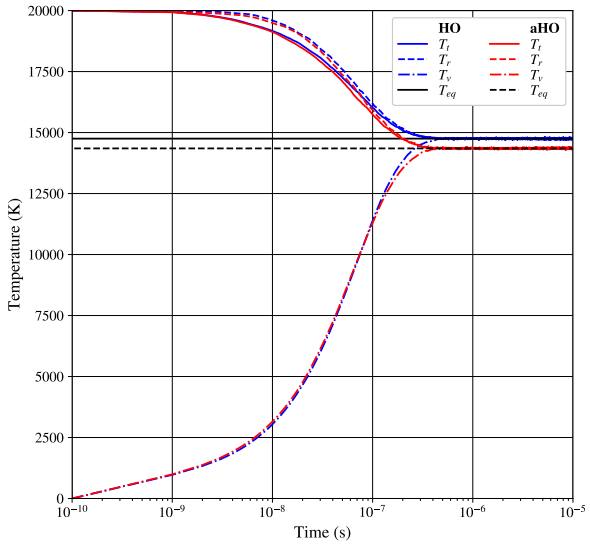

(a) Nitrogen molecule.

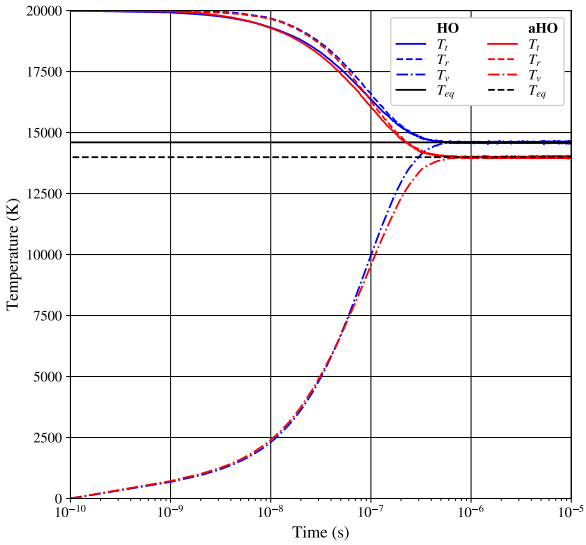

(b) Oxygen molecule.

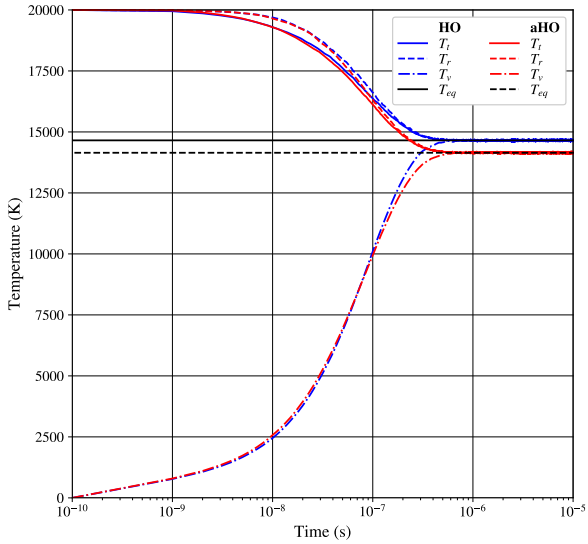

(c) Nitric oxide molecule.

Figure 4.5: Relaxation to equilibrium of an adiabatic reactor initialised with $T_t = T_r = 20,000$ K and $T_v = 0$ K for three molecules.

Figure 4.5 shows that for all three molecular systems, internal temperatures come into thermal equilibrium after enough collisions have occurred. It can also be observed that the theoretical predictions are correctly recovered by the two vibrational models. Figure 4.5 shows that a slight increment of temperature differentiates these two models at equilibrium. The change in thermal equilibrium state is readily derived from the internal mean energy of the molecules. Considering the vibrational energy of a molecule, it is evident from Eqs. (2.33) and (4.3) that,

$$\forall v \in \mathbb{N},\ \varepsilon_v^{aHO} \leq \varepsilon_v^{HO}. \tag{4.18}$$

It follows,

$$\forall T \in \mathbb{R},\ \sum_{v} e^{-\frac{\varepsilon_v^{aHO}}{kT}} \geq \sum_{v} e^{-\frac{\varepsilon_v^{HO}}{kT}}, \tag{4.19}$$

therefore,

$$\forall T \in \mathbb{R},\ e_v^{aHO} \geq e_v^{HO}. \tag{4.20}$$

As a results, for an adiabatic process the equilibrium temperature of a gas modelled with an anharmonic oscillator model must be lower than that of a gas modelled with a harmonic oscillator model,

$$T_{eq}^{aHO} \leq T_{eq}^{HO}. \tag{4.21}$$

It is important to emphasise that the temperature difference between the two vibrational models depends on the spectroscopic constants of the molecule. As discussed in the context of specific heat capacity, weakly bounded molecules, e.g. O_2, exhibit significant deviations at lower temperatures between the two vibrational models. In contrast, strongly bounded molecular systems, e.g. N_2 and NO, indicate a more pronounced contribution from their vibrational and electronic modes to the mean internal energy at higher temperatures.

4.3.4 Thermodynamic Properties

In the development of statistical mechanics, the total partition function of a system represents a fundamental role in bridging microscopic and macroscopic properties. Nevertheless, the partition function offers limited physical insights. In contrast, the specific heat capacities and the heat capacity ratio hold an important role in most engineering applications. Therefore, the measurement of the specific heat capacities of three molecules in thermal equilibrium conditions is considered as a verification case.

A series of adiabatic reactor simulations are conducted to measure the specific heat capacity of the aforementioned three molecules. These simulations follow the same setup as the vibrational density verification case. The specific heat capacity is measured for temperatures ranging between 2000 and 20,000 K and over 10^5 samples are taken to reduce the numerical scatter. The electronic excited states of N_2, O_2 and NO are those suggested by Liechty [188]. The spectroscopy constants are extracted from the NIST database [25] with an exception for the ground electronic state, where the spectroscopic constants are fitted on PES calculations as presented in Sec. 4.1. It is important to emphasise that this contribution is sometimes omitted [195–197] in the description of the molecular modes. The effects of this contribution on the thermodynamic properties of the molecules are also highlighted throughout this chapter. Since the system is in thermal equilibrium conditions, the DSMC results can be assessed against the analytical formulation, Eq. (2.44). For completeness, the DSMC results are also compared against a selection of theoretical studies that includes a coupling between the internal modes: McBride *et al*. [24], Jaffe [30], Capitelli *et al*. [28] and Qin *et al*. [29]. These studies provide the thermody-

namic properties for a variety of non-reactive gases for temperatures ranging from 2000 to over 20,000 K and more.

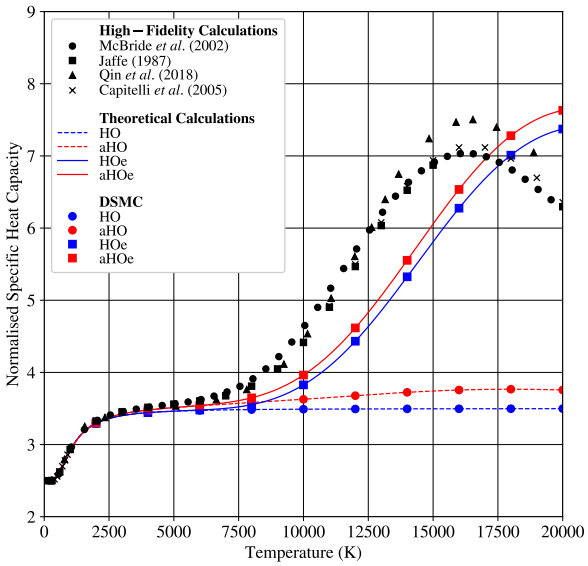

(a) Nitrogen molecule.

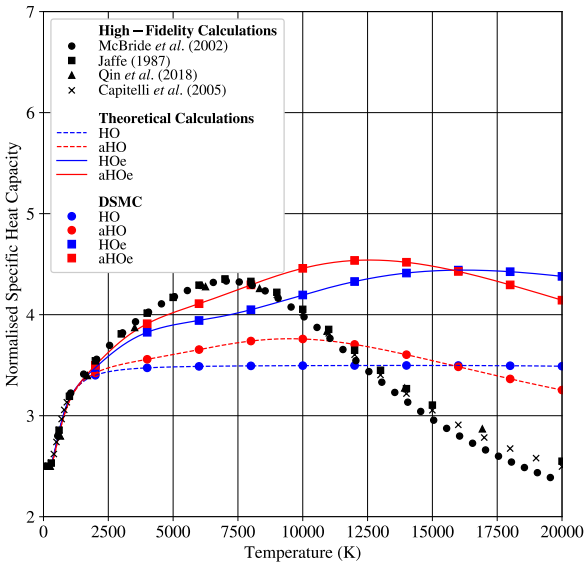

(b) Oxygen molecule.

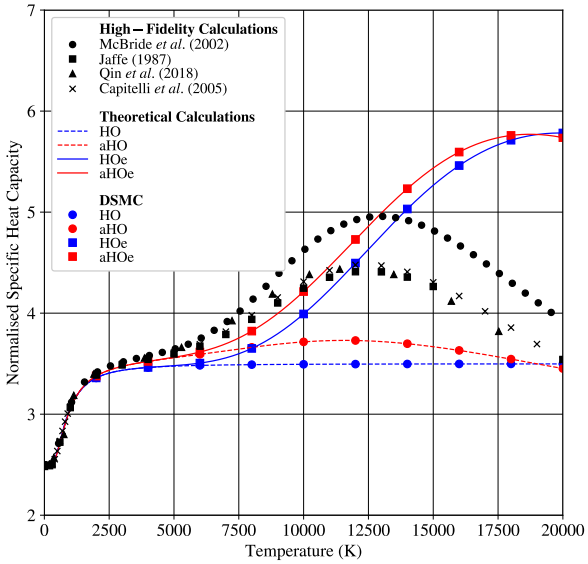

(c) Nitric oxide.

Figure 4.6: Comparison of two vibrational models on the specific heat capacity of three molecules.

Figure 4.6 compares the specific heat capacity of three molecules where vibrational excitation is described with the harmonic oscillator and the anharmonic oscillator models, with the electronic mode being either enabled or disabled. The two vibrational models are differentiated by the color convention. It is shown that the DSMC results are in excellent alignment with the analytical formulation of the specific heat capacity, Eq. (2.44), for all three molecular species under the range of temperatures considered; hence verifying the implementation in *dsmcFoam+*.
Furthermore, Fig. 4.6 shows that the two vibrational models yield comparable results for low

temperatures, however, for moderate-to-high temperatures, the two vibrational models exhibit significant deviations from one to another. This discrepancy is merely the result of the distribution of the vibrational energy across the vibrational quantum levels. In Fig. 4.4, it was observed that at low temperatures, the two vibrational models predict similar distributions of vibrational quantum levels. Since the specific heat capacity of a system is derived from these distributions, the two models are expected to predict similar specific heat capacities under these conditions. In contrast, as the temperature increases, the population of the two vibrational models deviate from one to another, leading to deviation in the thermodynamic properties.
Figure 4.6 also outlines the importance of considering the electronic mode within the calculation of the specific heat capacity. The inclusion of the electronic mode significantly improves the reproduction of the compilation of high-fidelity calculations [24, 28–30]. Nevertheless, it becomes apparent that even at moderate temperatures, the specific heat capacity of the gas deviates from the selection of theoretical studies. This discrepancy lies in the assumption made at the beginning of this chapter, where it was assumed that molecular species follow the Born-Oppenheimer approximation, allowing the internal modes of the molecular species to be treated independently. This assumption prohibits the modelling of any interaction between the internal modes such as the coupling between the vibronic and rovibronic couplings. These contributions will be thoroughly examined throughout this thesis, commencing with the vibronic coupling in Chapter 7 and investigating the rovibronic coupling in Appendix. A.

4.4 Hypersonic Flow

In the preceding sections, the anharmonic oscillator model has been verified for adiabatic reactor simulations. In the present section, a more complex scenario is considered involving a nonreactive air mixture past a cylindrical body with freestream conditions extracted from the US Standard Atmosphere [198] and summarised in Tab. 4.4. These conditions correspond to a typical Earth atmospheric reentry at an altitude of 75 km. To follow the conclusions drawn about Fig. 4.6, which has evidenced the importance of considering all the internal modes of the chemical species, the electronic excited states of N_2 and O_2 are herein considered.
The hypersonic flow simulations are set up as follows. The geometry represents a two-dimensional slice of a cylinder with a domain length equal to one diameter upstream of the stagnation point. The computational domain extends to a length of one diameter upstream of the stagnation point. The mesh is refined near the stagnation point to ensure the cell size, Δx, remains smaller than the local mean free path, λ, resulting in a total number of 65,516 cells. The numerical mesh is populated with a total number of 5.5×10^6 DSMC simulator particles at a steady state. The time step is carefully chosen to be an order of magnitude smaller than the mean collision time and the cell residence time which results in $\Delta t = 1 \times 10^{-8}$ s. Inter-molecular collisions are computed with the VHS model [17] for a reference temperature of $T_{ref} = 273$ K. The redistribution of internal

Table 4.4: Freestream conditions.

Parameter	Values
Altitude (km)	75
Temperature (K)	200.2
Number density (m^{-3})	9.33×10^{20}
Speed ($m.s^{-1}$)	7000
O_2 mole fraction (%)	0.21
N_2 mole fraction (%)	0.79
Ma_∞	24.6
Kn_∞	0.013

energies is modelled by a serial application of the quantum LB method [131, 150]. A finite probability of $P_r = 0.2$, $P_v = 0.02$ and $P_e = 0.002$ are, respectively, considered for rotational, vibrational and electronic relaxation, as suggested by Bird [17]. In this study, the electronic temperature is calculated with the approach developed by Liechty and Lewis [141] and derived from the ratio of the Boltzmann distribution of the ground state and the first electronic states. The gas-surface interactions are treated as fully diffuse with an isothermal wall at temperature $T_w = 1000$ K. A total of 10^5 samples are taken after steady-state to reduce the numerical scatter.

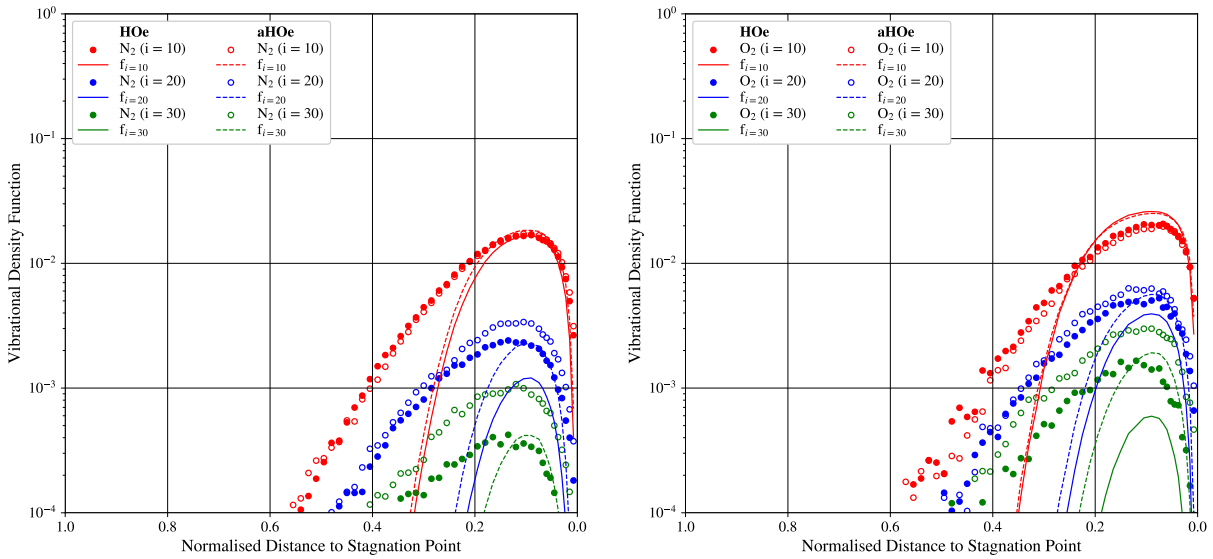

(a) Vibrational population of N_2.

(b) Vibrational population of O_2.

Figure 4.7: Vibrational populations of three vibrational quantum levels of N_2 and O_2 along the stagnation streamline for a nonreactive air mixture flow over a cylinder with freestream conditions $Ma_\infty = 24.67$ and $Kn_\infty = 0.013$.

The influence of the vibrational models on the vibrational population of N_2 and O_2 of three vibrational quantum levels along the stagnation streamline is depicted in Fig. 4.7. For reference, the Boltzmann distribution of these three quantum levels is included. Figure 4.7 shows that the two vibrational models exhibit distinct populations of the selection of vibrational quantum

levels for N_2 and O_2. Specifically, the aHOe model present a larger population of the high-lying vibrational quantum levels in comparison to its counterpart. Additionally, Fig. 4.7 shows that the population of the vibrational quantum levels largely deviates from the Boltzmann distribution. Note that this discrepancy is not surprising considering the assumptions made in the derivation of the Boltzmann distribution, see Chapter 2. Specifically, it is assumed that the temperature of the system is high enough to promote a spare distribution of the particle over the permissible energy levels of the system such that the Bose-Einstein statistics and Fermi-Dirac statistics are indistinguishable, and that the system is in thermal equilibrium. While the former assumption is achieved in most aerothermodynamic applications, the latter is rarely encountered. In the present scenario, Fig. 4.8 indicates that the air mixture flow exhibits strong thermal non-equilibrium between the internal modes throughout the shock wave. This demonstrates the impracticality of determining a vibrational temperature based on the assumption that the vibrational quantum levels follow Boltzmann statistics.

Additionally, Fig. 4.7 indicates a significant excitation of the electronic states upstream of the shock wave. This phenomenon is a consequence of the degree of rarefaction that is sufficient for a particle to collide with the surface of the body and travel backwards without enough inelastic collisions to de-excite the particle; thus, carrying post-shock information upstream the bow-shock. This phenomenon is a non-equilibrium effect occurring in high Knudsen numbers and characterised by a non-Maxwellian velocity distribution. This phenomenon has also been observed previously [53, 168, 169, 199–201] and will be further studied in Chapter 7.

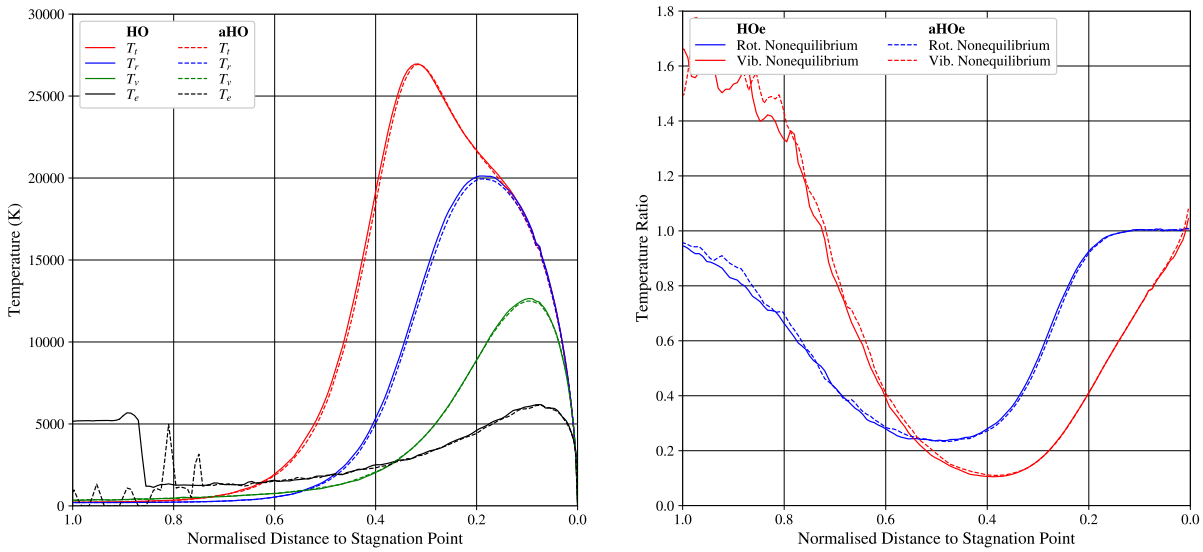

(a) Internal temperatures.

(b) Non-Equilibrium factor.

Figure 4.8: Internal temperatures and non-equilibrium factor of the air mixture along the stagnation streamline.

The surface heat flux and pressure are important parameters for various applications. The surface heat flux and pressure are depicted in Fig. 4.9. The normalization of the surface heat flux is

based on the freestream energy flux, while that of pressure is based on the freestream pressure. The surface properties are plotted against the azimuthal angle measured from its centre, with an angle of 0° denoting the stagnation point and an angle of 90° denoting the top of the cylinder. The surface properties calculated with an anharmonic oscillator model show similar predictions to the harmonic oscillator model. At the surface temperature of $T_w = 1000$ K, the translational and rotational modes dominate the physics and the vibrational and electronic modes are only partially activated. Therefore, the differences between the two vibrational models are insignificant since only the first few vibrational quantum levels are occupied.

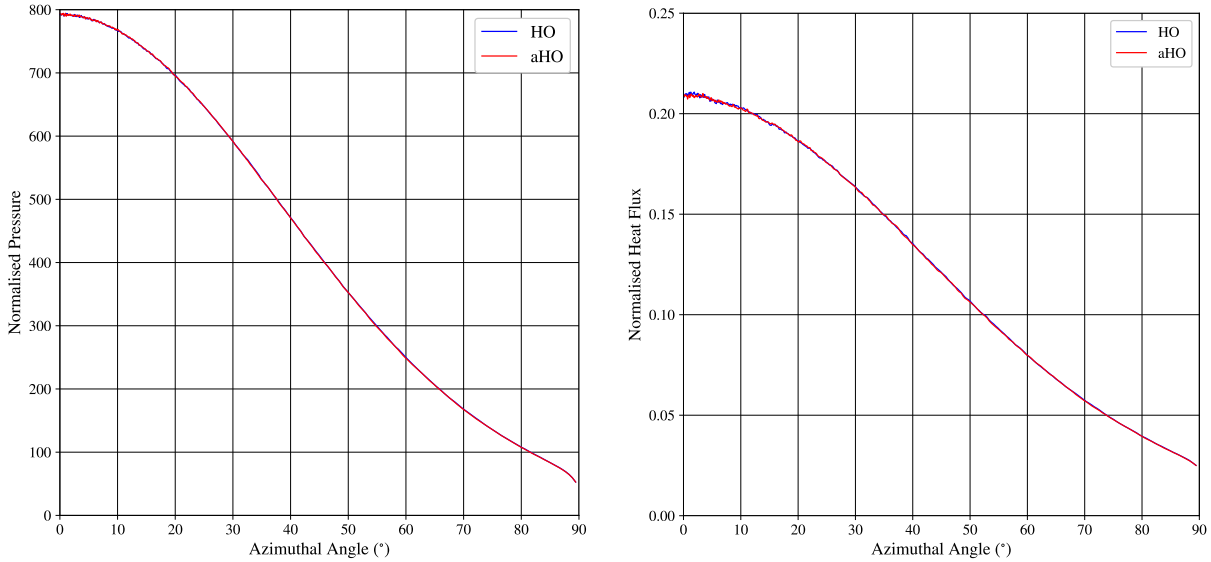

(a) Surface pressure.

(b) Surface heat flux.

Figure 4.9: Comparison of the surface properties for a nonreactive air mixture flow over a cylinder with freestream conditions $\mathrm{Ma}_\infty = 24.67$ and $\mathrm{Kn}_\infty = 0.013$.

4.5 Summary

The merits of different vibrational models for use in DSMC simulations have been discussed and analysed. An anharmonic oscillator model has been implemented within *dsmcFoam+* and verified for a series of four adiabatic reactor simulations to reproduce fundamental parameters, such as the vibrational population, the thermal equilibrium and thermodynamic properties of a gas. Additionally, the anharmonic oscillator model has been applied to a hypersonic flow past a cylindrical body at an Earth's altitude of about 75 km.

The series of adiabatic reactor simulations have demonstrated a successful implementation of the anharmonic oscillator model in *dsmcFoam+*. It has been shown that the harmonic and anharmonic oscillator models exhibit strong deviation in the population of the high-lying vibrational quantum levels. Specifically, the anharmonic oscillator model predicts a higher population of high-lying vibrational quantum levels which suggests a significant difference in the modelling of the chemical activity of chemical species in comparison to the harmonic oscillator model. Furthermore, the relaxation to thermal equilibrium has evidenced that the two vibrational models exhibit different thermal equilibrium states. Additionally, the study of thermodynamic properties has outlined the importance of including all internal modes and describing the interaction between the internal modes to recover the correct thermodynamic properties.

In the context of a canonical hypersonic Earth's reentry flow, it has been observed that the two vibrational models exhibit different population of the vibrational quantum levels downstream the shock wave. It is also shown that the population of these quantum levels largely deviate from the assumption of a Boltzmann distribution. Such a discrepancy is anticipated to lead to deviation in the chemical activity of the chemical species. Therefore, further investigations into the modelling of chemical reactions using the two vibrational models will be explored in subsequent chapters.

Chapter 5

Quantum Kinetic Chemistry Model with an Anharmonic Oscillator Model: Derivation and Limitations *

This chapter presents a custom version of the original quantum-kinetic chemistry models, in which vibrational excitation is modelled with an anharmonic oscillator model. The new QK model is investigated for four of the most representative dissociation reactions occurring during a reentry into Earth's atmosphere. Firstly, the new formulations are compared against an extensive compilation of well-established theoretical chemistry models, experimental measurements and high-fidelity calculations in both thermal equilibrium and non-equilibrium conditions. Then, the limitations of these formulations are assessed for thermal non-equilibrium conditions relevant to planetary reentry applications.

5.1 Quantum-Kinetic Chemical Model

5.1.1 Original QK model

Consider the collision between a molecular species AB and an inert species M. A potential post-collision vibrational quantum level for AB is selected through an acceptance-rejection routine from the distribution,

$$f = \left(1 - \frac{i^\star k\theta_v}{\varepsilon_c}\right)^{\frac{3}{2}-\omega}, \tag{5.1}$$

where the collision energy of a particle pair (AB - M) is expressed as the sum of the relative translational energy of the pair and the pre-collision vibrational energy of the molecule under consideration, i.e. $\varepsilon_c = \varepsilon_{AB,M,t} + \varepsilon_{AB,v}$ and $i^\star$ refers to the post-collision quantum level that is

*A large portion of the work presented in this Chapter is published in **C. H. B. Civrais**, C. White and R. Steijl. Quantum kinetics chemistry models with an anharmonic oscillator model. Model derivation and limitations, *Physics of Fluids*, 36(8):086120, 2024. doi: 10.1063/5.0215706.

uniformly chosen between 0 and a maximum vibrational quantum level, i_{max}, calculated as,

$$i_{max} = \left\lfloor \frac{\varepsilon_t + \varepsilon_{v,i}}{k\theta_v} \right\rfloor. \tag{5.2}$$

If the maximum vibrational quantum level lies beyond the dissociation quantum level, a dissociation reaction, e.g. AB + M $\longrightarrow$ A + B + M, occurs. The condition for AB to dissociate is therefore,

$$i_{max} > \left\lfloor \frac{\theta_d}{\theta_v} \right\rfloor. \tag{5.3}$$

Consider colliding partner AB at a given vibrational quantum level i, the probability P_d of the translational energy exceeding the difference between ε_v and ε_d is given by,

$$P_d = \frac{\Gamma\left[\frac{5}{2} - \omega, \frac{(i_d - i)\theta_v}{kT}\right]}{\Gamma\left[\frac{5}{2} - \omega\right]}, \tag{5.4}$$

where $\Gamma(s,x)$ is the upper incomplete gamma function.
The corresponding dissociation reaction rate of AB is given by summing these probabilities up to the dissociation energy, multiplying by the collision rate between chemical species AB and M and dividing by the number density of the species, i.e. partition functions which read,

$$k_d(T) = R_{AB-M}(T)\gamma_{AB-M}(T). \tag{5.5}$$

where R_{AB-M} is the collision rate between species AB and M and γ_{AB-M} defines the fraction of collisions between chemical species AB and M that possesses sufficient energy to meet the dissociation criterion.
For a thermal equilibrium VHS gas, the collision rate between species AB and M is given by,

$$R_{AB-M}(T) = \frac{2(r_{AB,ref} + r_{M,ref})^2}{\varsigma}\sqrt{\frac{2\pi k T_{ref}}{\mu_{AB-M}}}\left(\frac{T}{T_{ref}}\right)^{1-\omega_{AB-M}}, \tag{5.6}$$

where r_{ref} is the VHS reference radius defined at a reference temperature T_{ref} and ς is a symmetry factor that is equal to 2 for similar chemical species and 1 for dissimilar chemical species. For a thermal equilibrium VHS gas, with i as the pre-collision vibrational state of species AB, $\gamma_{AB,M}$ takes the form of,

$$\gamma_{AB,M}(T) = (1 - e^{\frac{-\theta_v}{T}})\sum_{i=0}^{i_{max}} e^{\frac{-i\theta_v}{T}}\Gamma\left[\frac{5}{2} - \omega_{AB,M}, \frac{(i_d - i)\theta_v}{T}\right]. \tag{5.7}$$

In the particular situation where the translational and vibrational energies being distributed according to their equilibrium distributions but at different temperatures, i.e. $T_t = T_r \neq T_v$, an analytical expression has been proposed by Bond *et al.* [202]. Recently, this formulation has

been further extended by Civrais *et al.* [136] to incorporate anharmonicity and it reads,

$$k_{neq}(T_t,T_v) = R_{AB,M}\sum_{i=0}^{i_{max}}\Gamma\left[\frac{5}{2}-\omega_{AB,M},\frac{k\theta_d-\varepsilon_{v,i}}{kT_t}\right]\frac{e^{-\frac{\varepsilon_{v,i}}{kT_v}}}{Q_v(T_v)}+B\sum_{i_{max}+1}^{\infty}\frac{e^{-\frac{\varepsilon_{v,i}}{kT_v}}}{Q_v(T_v)}. \tag{5.8}$$

The second term, preceded by the parameter B, is suggested by Bond *et al.* [202] to take into account whether the vibrational model is truncated to the dissociation limit or not. For truncated vibrational models, the parameter B is set to zero and to unity for non-truncated vibrational models.

5.1.2 QK-aHO model

The QK-aHO model is a new version of the original QK model [130] in which the vibrational energy is modelled with an anharmonic oscillator model [135–137]. In this extension, the vibrational energy is described with the Morse anharmonic oscillator model [34], defined as Eq. (4.8). The QK-aHO model logically follows the conceptualisation of the original QK model. Nevertheless, the consideration of an anharmonic oscillator model to describe the vibrational excitation of molecular species imposes three modifications to the original QK model: the post-collision sampling, the dissociation probability, and the dissociation reaction rates.

Considering an anharmonic oscillator model requires sampling a potential post-collision vibrational quantum level through an acceptance-rejection routine with probability

$$P' = \frac{P}{P_{max}} = \left(1-\frac{\varepsilon_{v,i^\star}}{\varepsilon_c}\right)^{\frac{3}{2}-\omega}, \tag{5.9}$$

where the maximum vibrational quantum level is obtained by looping through the list of vibrational energies calculated from Eq. (4.8) and finding the vibrational quantum level that satisfies $\varepsilon_c > \varepsilon_{v,i^\star}$.

As in the original QK model, a dissociation of AB occurs if the collision energy is greater than the dissociation energy; hence, the corresponding dissociation probability yields,

$$P_d = \frac{\Gamma\left[\frac{5}{2}-\omega,\frac{\varepsilon_d-\varepsilon_{v,i}}{kT}\right]}{\Gamma\left[\frac{5}{2}-\omega\right]}. \tag{5.10}$$

The modelling of the vibrational energy with an anharmonic oscillator model solely applies to the chemical procedures; consequently, the collision rate, Eq. (5.6), remains unchanged. Nevertheless, a modification of the dissociation probability readily imposes a change in the fraction of collisions with sufficient energy to experience a dissociation reaction. Specifically, the change from a linear to a non-linear distribution of the vibrational energy across the vibrational quantum

levels constrain $\gamma_{AB,M}$ to take the form of,

$$\gamma_{AB,M}(T) = \frac{\sum_{i=0}^{i_{max}} e^{-\frac{\varepsilon_{v,i}}{kT}} \Gamma\left[\frac{5}{2} - \omega_{AB,M}, \frac{\varepsilon_d - \varepsilon_{v,i}}{kT}\right]}{\sum_{j=0}^{j_{max}} e^{-\frac{\varepsilon_{v,j}}{kT}}}. \tag{5.11}$$

Similarly, in thermal non-equilibrium conditions, Eq. (5.8) is subject to similar modifications and reads,

$$k_{neq}(T_t, T_v) = R_{AB-M} \sum_{i=0}^{i_d} \mathcal{G}\left[\frac{5}{2} - \omega_{AB-M}, \frac{\varepsilon_d - \varepsilon_{v,i}}{kT_t}\right] \times \frac{e^{-\frac{\varepsilon_{v,i}}{kT_v}}}{Q_v(T_v)} \quad + B \sum_{i_d+1}^{\infty} \frac{e^{-\frac{\varepsilon_{v,i}}{kT_v}}}{Q_v(T_v)}. \tag{5.12}$$

5.2 Thermal Equilibrium

To verify the successful implementation of the new formulations and to compare the dissociation reaction rates of the two QK models, a series of simulations are conducted in both thermal equilibrium and non-equilibrium conditions. These simulations involve an adiabatic reactor represented by a single cubic cell with a side length of 1.88×10^{-4} m filled with one million DSMC simulator particles and periodic boundaries. The VHS model is used to compute the inter-molecular collisions with the species properties summarised in Table 4.3 for a reference temperature of $T_{ref} = 273$ K. A fixed time step of 1×10^{-9} s is adopted. For each simulation, a single dissociation reaction is considered, with the colliding partner assumed to be chemically active, internal energy transfer between collision partners disabled and the reaction process itself deactivated. This approach enables the sampling of reaction rates at a constant temperature. The electronic excitation of the chemical species is disregarded and it is assumed that chemical reactions occur from ground electronic excited states. The rotational and vibrational collision numbers are set to unity since these play no role in the measurement of collision and reaction rates. Simulations are run for over 10^4 iterations to reduce the numerical scatter.

In *dsmcFoam+*, the dissociation reactions are grouped into two categories [133]: Type I dissociation reactions for molecule-molecule and Type II dissociation reactions for molecule-atom. In the present study, the influence of modelling the vibrational excitation with an aHO model on thermal equilibrium reaction rates is quantified for temperatures ranging from 4000 K to 20,000 K for two Type I dissociation reactions, Reaction 1 and Reaction 2 and two Type II dissociation reactions, Reaction 3 and Reaction 4.

$$O_2 + O_2 \longrightarrow O_2 + O + O \tag{Reaction 1}$$

$$N_2 + N_2 \longrightarrow N_2 + N + N \tag{Reaction 2}$$

$$O_2 + O \longrightarrow O + O + O \qquad \text{(Reaction 3)}$$

$$N_2 + N \longrightarrow N + N + N \qquad \text{(Reaction 4)}$$

The DSMC reaction rates for Reaction 1-Reaction 4 are compared against the analytical solution, Eq. (5.5), and the compilation of experimental results, QCT calculations, and DMS results tabulated in Tab. 1.1. In its development, the QK model [130] was not intended to compete with these sophisticated approaches but rather to provide a phenomenological model that accurately predicts chemical reaction rates up to a certain degree of fidelity. Therefore, it is expected that there may be cases in which the QK models are in disagreement with the QCT calculations. In the present chapter, the experimental measurements are considered as a primary baseline. In the situation where experimental measurements are not available for the temperature range of interest, the high-fidelity calculations will be considered as an alternative baseline model.

Consider the dissociation of oxygen in a collision with another oxygen molecule, Reaction 1. Figure 5.1a compares the DSMC reaction rates for the HO and aHO models against the analytical solution, Eq. (5.5), and the aforementioned compilation of past studies. The abscissa shows the inverse of the temperature, i.e. 20,000/T, with the reaction rates plotted on the ordinate axis.

Figure 5.1a demonstrates that the analytical expression of the QK models, Eq. (5.5), provides an excellent alignment with the DSMC reaction rates for the range of temperature considered; hence providing a verification of the implementation of the new QK models in *dsmcFoam+*. Additionally, Fig. 5.1a indicates that the dissociation reaction is more likely to occur with the aHO model than the HO model for the whole range of temperatures. As discussed in the previous section about Fig. 4.2, this increase in the dissociation reaction rates results from the non-linear distribution of vibrational energy across the vibrational quantum levels which, in turn, modifies the dissociation quantum level and fraction of collision with enough energy to dissociate.

Figure 5.1a indicates that the QK models present a reasonable reproduction of the compilation of past studies, even though, slight deviations are shown from from the experimental measurements [77] and high-fidelity calculations [85, 87, 89].It is worth mentioning that this deviation is not unique to the QK models; it is also observed in most of the selection of past studies, except for Boyd's reaction rates. This discrepancy can be attributed to the omission of the rotational mode and the chemical activity of the electronic excited states. In the QCT calculations, the rotational mode is treated with a quantum approach whereas in the QK model, the contribution of the rotational mode to the reaction rates is disregarded. While for low temperatures, these quantum effects may be insignificant, at high temperatures such a contribution influences the chemical activity as shown in Grover *et al.* [89]. Furthermore, it is evident in Andrienko and Boyd [93], Chaudhry *et al.* [85], and Jo *et al.* [99] that adding the contribution of electronic excited states to the global dissociation rates significantly improves the reproduction of experimental measurements from Streicher *et al.* [75, 77]. The discrepancy between the QCT calculations and the QK

model outlines the importance of modelling electronic excited states and their chemical activity for accurately reproducing experimental measurements.

The study follows with the investigation of the Type I nitrogen dissociation, Reaction 2. The dissociation reaction rates are depicted in Fig. 5.1b. Figure 5.1b shows that the QK models predict higher reaction rates compared to the experimental results. This deviation from the experimental measurements is also observable in the selection of past studies and QCT calculations. Similar justification to those provided for Reaction 1 can here be drawn. The QK models provide close alignment with the QCT calculations for the whole range of temperatures. Similar to Type I oxygen dissociation, Fig. 5.1b indicates that a nitrogen molecule has a higher probability of dissociating with the aHO model.

Furthermore, Figs. 5.1a and 5.1b show that the QK-aHO model is in better agreement with the compilation of high-fidelity calculations for N_2 than it is for O_2. The primary difference between the QK models and the high-fidelity calculations lies in the mathematical considerations about the internal modes. Specifically, the QK models solely promote chemical reactions from the translational and vibrational modes whereas QCT or DMS incorporate the rotational mode and the interactions between modes. Molecular oxygen is known to exhibit significant rotational-vibrational coupling effects even at moderate temperatures whereas molecular nitrogen exhibits similar effects at much higher temperatures. Consequently, the difference shown in Figs. 5.1a and 5.1b originates from the rotational-vibrational coupling effects which occur at much lower temperatures for O_2 than for N_2 [85, 86, 107]. Note that this difference between the two molecular systems is not unique to the dissociation reaction rates but it is also observable in the corresponding specific heats, see Figs. 4.6.

Figures 5.1c and 5.1d repeat the comparison of Figs. 5.1a and 5.1b, with the corresponding atom as the collision partner. DSMC reaction rates are consistent with the selection of past studies, experimental measurements and the corresponding QCT calculations, see Tab. 1.1. The DSMC results for Type II dissociation reactions present a reasonable agreement with the compilation of past studies, leading to analogous conclusions as those drawn for Type I dissociation reactions.

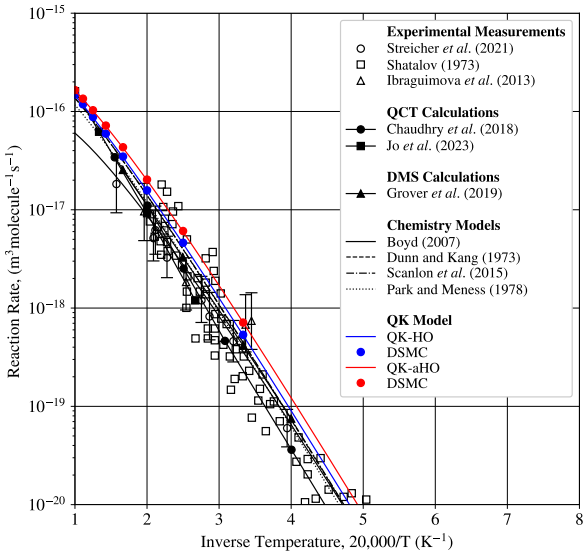

(a) $O_2 + O_2 \longrightarrow O + O + O_2$.

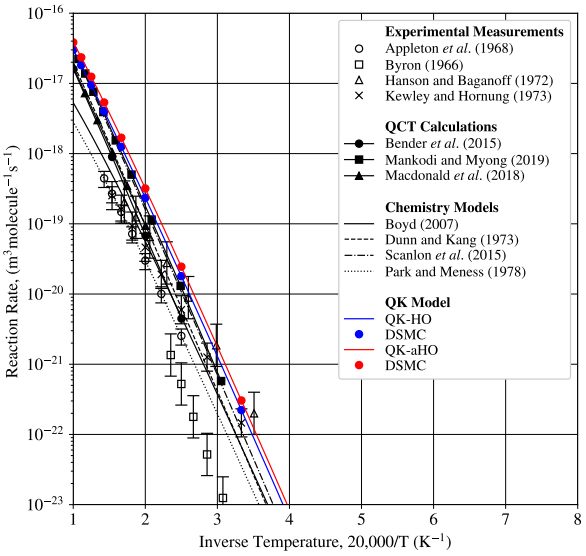

(b) $N_2 + N_2 \longrightarrow N + N + N_2$.

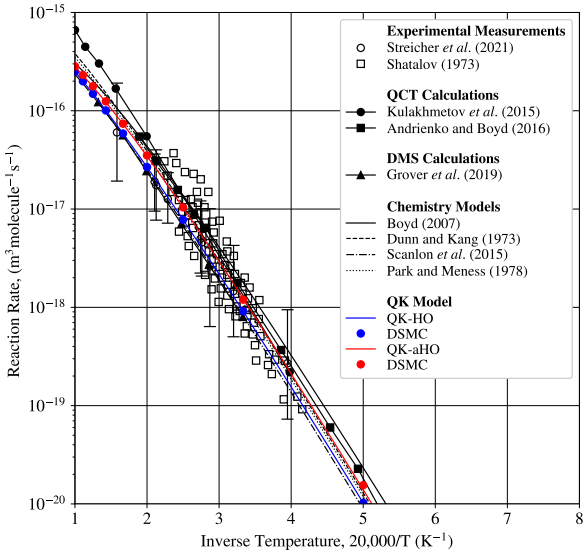

(c) $O_2 + O \longrightarrow O + O + O$.

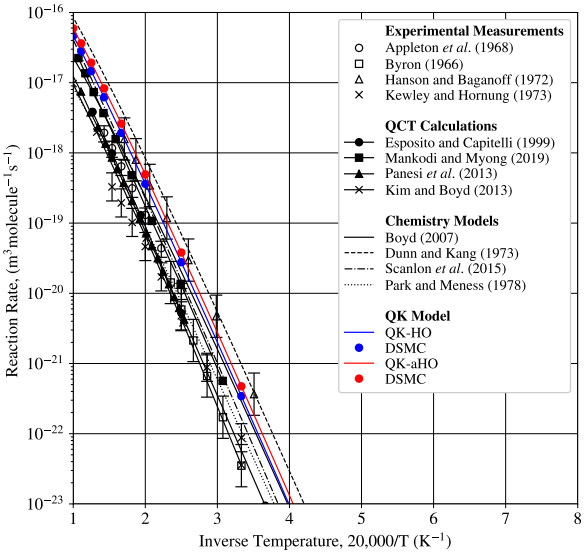

(d) $N_2 + N \longrightarrow N + N + N$.

Figure 5.1: Thermal equilibrium dissociation reaction rates of Reaction 1-Reaction 4.

5.3 Thermal Non-Equilibrium

5.3.1 Comparison to Non-Equilibrium Chemistry Models

In the previous section, the comparison of the two vibrational models was limited to chemical reactions in thermal equilibrium. The previous four dissociation reactions, i.e. Reaction 1-Reaction 4, are now regarded in thermal non-equilibrium conditions, i.e. $T_t = T_r \neq T_v$. These reactions are studied for the three trans-rotational temperatures prescribed in Tab. 5.1 and for vibrational temperatures ranging from 4000 K to 20,000 K. The validity of the QK model predictions is first verified against the thermal non-equilibrium quantum-kinetic model [202]. The predictions of the QK model are then evaluated against a selection of thermal non-equilibrium chemistry models: the Kuznetsov model [119], the Macheret-Fridman model [44] and the Treanor-Marrone model [117]. Additionally, the results of the QK model are also compared against the compilation of past studies shown in Tab. 1.2.

Table 5.1: Thermal non-equilibrium scenarios.

Reaction	$T_{t,1}$ (K)	$T_{t,2}$ (K)	$T_{t,3}$ (K)	Data type	Reference
$O_2 + O_2 \longrightarrow O + O + O_2$	8000	10 000	15 000	DMS	Grover and Schwartzentruber [88]
$O_2 + O \longrightarrow O + O + O$	5000	10 000	20 000	QCT	Kulakhmetov *et al.* [91]
$N_2 + N_2 \longrightarrow N + N + N_2$	8000	10 000	20 000	Experimental	Losev *et al.* [72]
$N_2 + N \longrightarrow N + N + N$	7500	10 000	15 000	QCT	Jaffe *et al.* [107]

Multi-temperature models have adopted another formalism to describe the influence of non-equilibrium conditions on the reaction rates through a dimensionless parameter $Z_{neq}(T_t, T_v)$, known as the thermal non-equilibrium factor, such that

$$Z_{neq}(T_t, T_v) = \frac{k_{neq}(T_t, T_v)}{k_{eq}(T_t)}. \tag{5.13}$$

This factor is particularly appreciated in the community as it eliminates the influence of the collision model and only retains the core contribution of non-equilibrium conditions on the reaction rates. Therefore, this formalism will be adopted to compare the QK results against the selection of chemistry models.

In this chapter, a selection of three chemistry models has been selected which are composed of the Kuznetsov model [119], the Macheret-Fridman model [44] and the Treanor-Marrone model [117]. An extensive description of these chemistry models can be consulted in Losev *et al.* [119] along with the suggestion on the selection of the tunable parameters of these chemistry models.

Figures 5.2-5.5 compare the DSMC thermal non-equilibrium dimensionless parameter against the three chemistry models, DMS results [88], QCT calculations [85, 92, 102, 107] and experimental fits [72] for Reaction 1-Reaction 4. The abscissa shows the inverse vibrational tem-

perature and $Z_{neq}(T_t, T_v)$ is plotted on the ordinate axis, blue lines and markers refer to the HO model, red lines and markers to the aHO model. High fidelity calculations are denoted by black solid lines with markers, the three chemistry models in black lines and experimental fits in open symbols. Similar to the equilibrium sections, the experimental fits and QCT calculations are assumed to be the most reliable thermal non-equilibrium parameters and are, thus, intended to be reproduced.

Consider the dissociation of oxygen colliding with another oxygen molecule, Reaction 1. Figure 5.2 demonstrates that the DSMC results are in excellent agreement with the theoretical predictions of the non-equilibrium QK theory for all three trans-rotational temperatures; hence, demonstrating successful implementation of the new formulation under thermal non-equilibrium conditions. The DSMC results exhibit a notable deviation from the DMS results reported by Grover and Schwartzentruber [88] for typical post-shock flow conditions ($T_t > T_v$). This deviation is not exclusive to the QK models; it is also observed for all three trans-rotational temperatures with the Kuznetsov and Macheret-Fridman models. While the definition of the adjustable parameter of the Treanor-Marrone model remains unclear [145, 203–206], it emerges as the model that most closely reproduces the DMS results. For typical nozzle flow conditions ($T_t < T_v$), the DSMC results demonstrate good abilities to reproduce the DMS results, unlike the observed deviation in post-shock flow conditions. In nozzle flow conditions, the chemical reactions are primarily influenced by the vibrational excitation of the molecular species. This suggests that, in these flow conditions, the utilisation of the vibrational energy has enabled sufficient dissociation reactions for the QK model to closely reproduce DMS results. For post-shock flow conditions, the discrepancy between the QK model and the DMS results can therefore be attributed to an excessive usage of the translational contribution. Additionally, Fig. 5.2 indicates that the two QK models predict similar non-equilibrium factors. The two QK models originate from the same chemistry model based on the assumption that chemical reactions occur from the translational and vibrational contributions of the colliding pair. Figure 5.2 shows that the QK models excessively rely on the translational contribution to promote chemical reactions, thereby eliminating any benefits of modelling the vibrational excitation with a more detailed approach. Note that this observation is not unique to Reaction 1, but it is also noticeable in all other chemical reactions, i.e. Reaction 2–Reaction 4.

Figure 5.3 repeats the previous comparison with Type I nitrogen dissociation, Reaction 2. Figure 5.3 shows good agreement with the analytical expression of the modified QK model which serves as a verification of the implementation of the new formulation in thermal non-equilibrium. The baseline database for this chemical reaction is the experimental fit reported by Losev *et al*. [72] for typical post-shock flow conditions ($T_t > T_v$) and the QCT calculations reported by Bender *et al*. [102] for typical nozzle flow conditions ($T_t < T_v$). For $T_t > T_v$, the DSMC results demonstrate poor reproduction of the baseline database, whereas, for near-equilibrium conditions and $T_t < T_v$, the DSMC results are found to be in closer agreement with the baseline

database. It must be emphasised that, in contrast with the QCT calculations and experimental measurements, the QK model only accounts for dissociation reactions occurring by means of the relative translational energy of the pair and the pre-collision vibrational energy of the molecule; hence, real-gas effects such as rotational-vibrational coupling and/or non-adiabatic electronic transitions are not included. Further improvements to the model are required to closely reproduce the baseline database.

Figures 5.4 and 5.5 repeat the comparison for Reaction 3 and Reaction 4, respectively. Similar conclusions to those drawn for Figs. 5.2 and 5.3 also stand. Overall, the QK models show similar predictive capabilities to the other chemistry models, all of which tend to over-predict the reaction rates from QCT calculations for typical post-shock flow conditions. For typical nozzle flow conditions, the DSMC reaction rates demonstrate reasonable alignment with the QCT calculations.

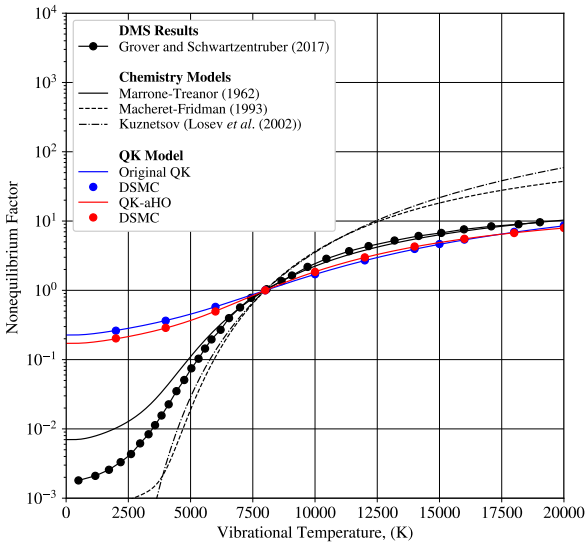

(a) $T_{t,r}$ = 8000 K.

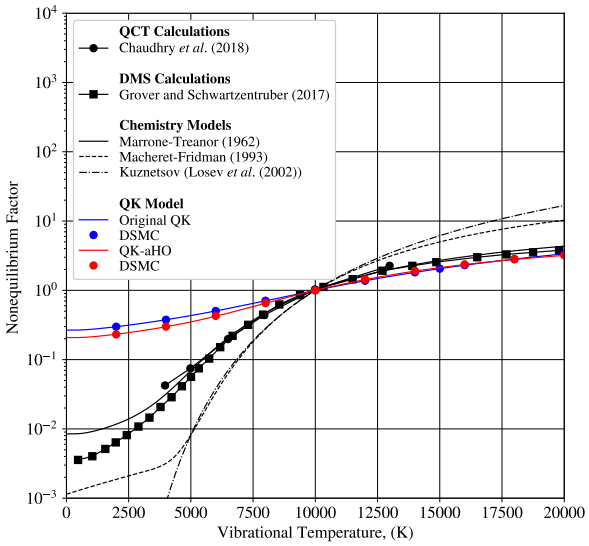

(b) $T_{t,r}$ = 10,000 K

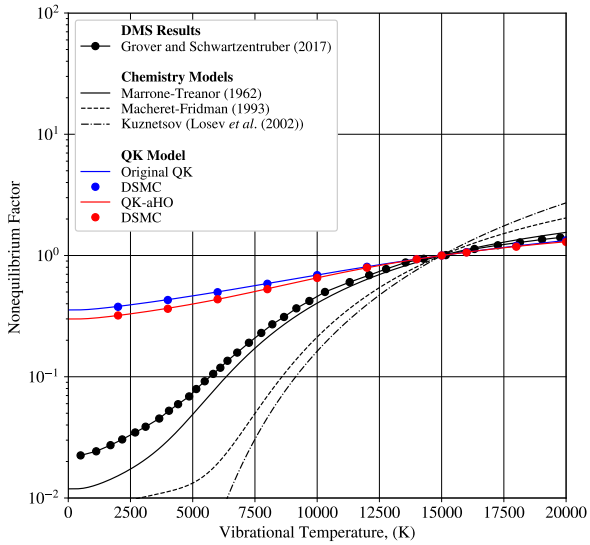

(c) $T_{t,r}$ = 15,000 K

Figure 5.2: Comparison of thermal non-equilibrium dimensionless parameters for $O_2 + O_2 \longrightarrow O + O + O_2$.

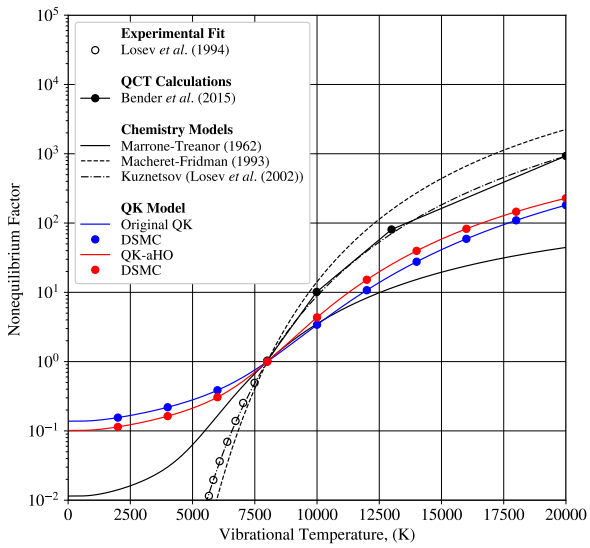

(a) $T_{t,r}$ = 8000 K

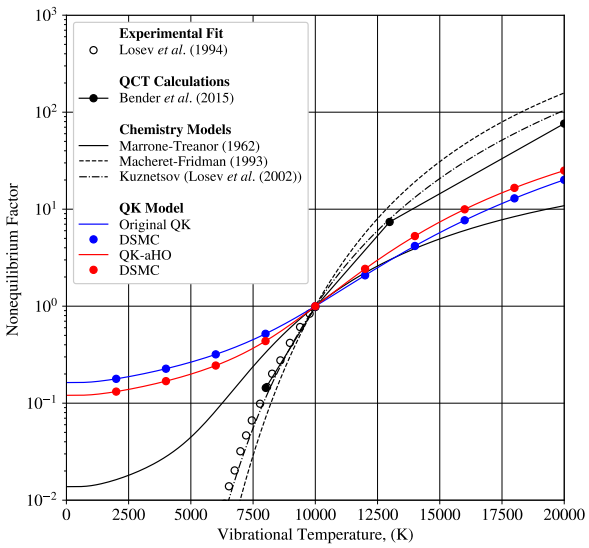

(b) $T_{t,r}$ = 10,000 K

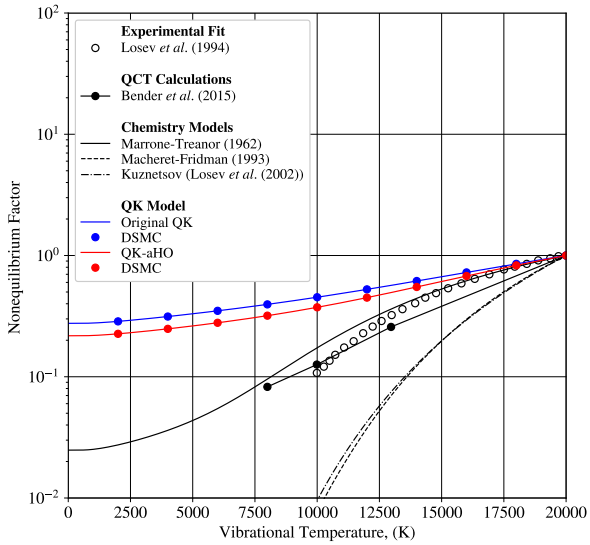

(c) $T_{t,r}$ = 20,000 K

Figure 5.3: Comparison of thermal non-equilibrium dimensionless parameters for $N_2 + N_2 \longrightarrow N + N + N_2$.

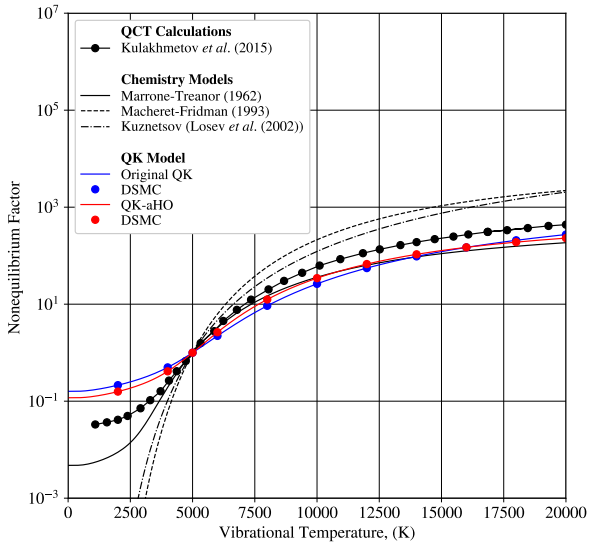

(a) $T_{t,r}$ = 5000 K

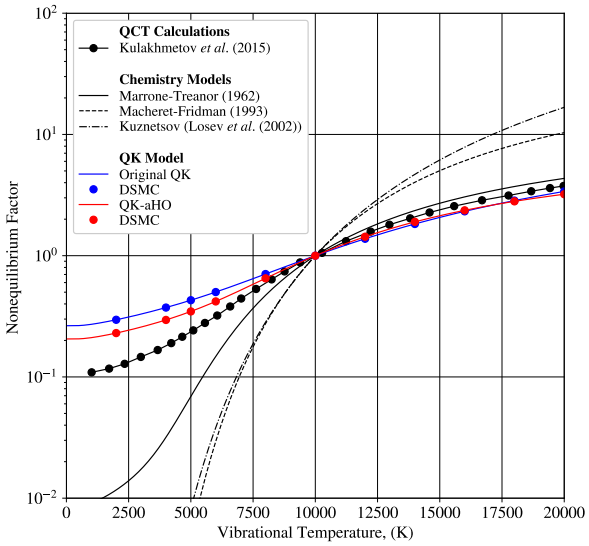

(b) $T_{t,r}$ = 10,000 K

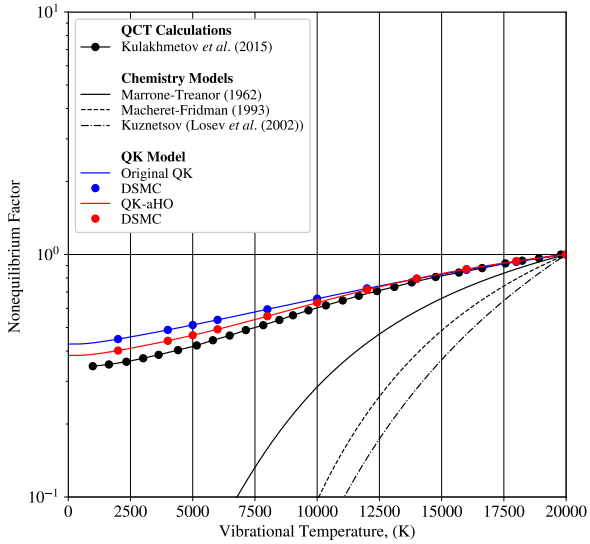

(c) $T_{t,r}$ = 20,000 K

Figure 5.4: Comparison of thermal non-equilibrium dimensionless parameters for $O_2 + O \longrightarrow O + O + O$.

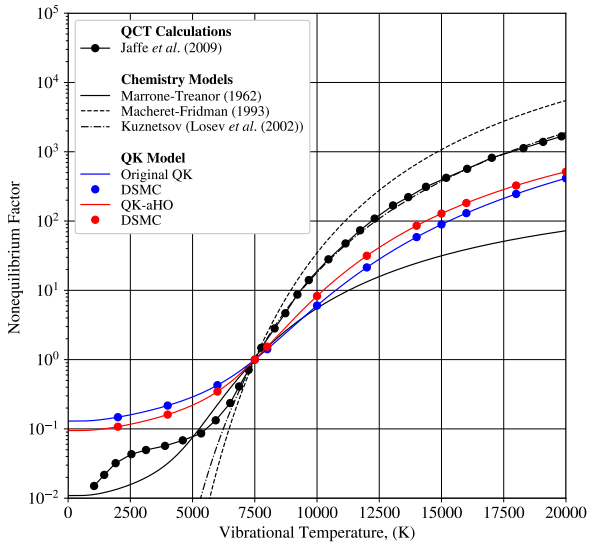

(a) $T_{t,r}$ = 7500 K

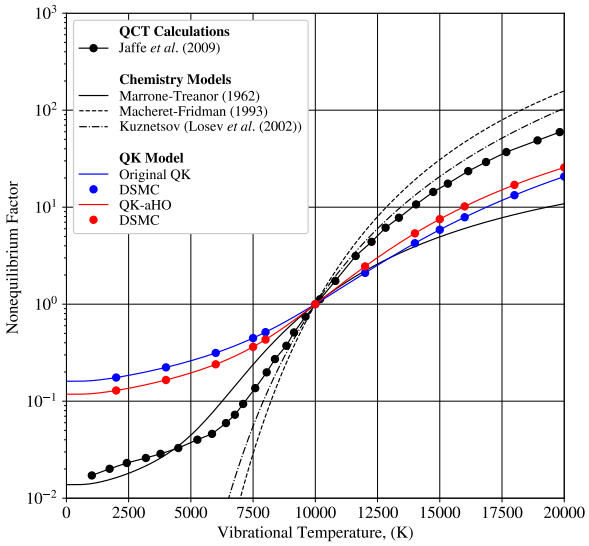

(b) $T_{t,r}$ = 10,000 K

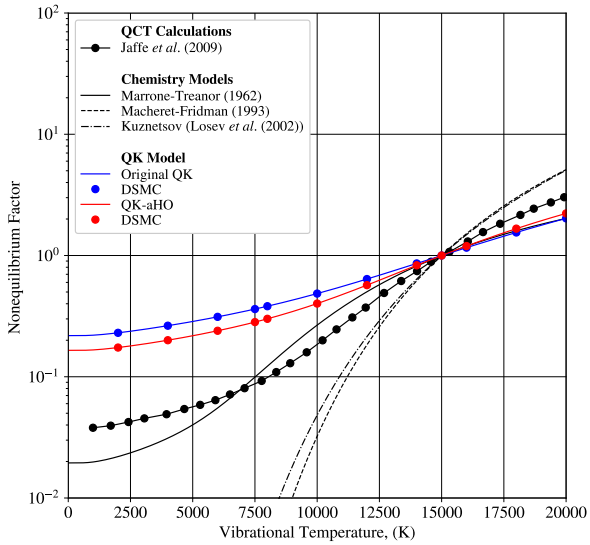

(c) $T_{t,r}$ = 15,000 K

Figure 5.5: Comparison of thermal non-equilibrium dimensionless parameters for $N_2 + N \longrightarrow N + N + N$.

5.3.2 Comparison to Experimental Non-Equilibrium Factor

A large number of chemical mechanisms relevant to typical hypersonic applications have received significant attention through extensive experimental investigations, see Tab. 1.1. Under thermal non-equilibrium, complexity arises for the measurement of reaction rates and only two chemical reactions have been studied experimentally, see Tab. 1.2. A rare example of such measurements exists in the work of Sergievskaya *et al*. [71], where reaction rates for the dissociation of molecular oxygen, Reaction 1, is reported.

The measurements were conducted using the shock tube facilities of the Moscow State University. These measurements were carried out by means of multichannel UV and visible absorption spectroscopy. They involved maintaining the vibrational excitation of molecular oxygen at a constant temperature, i.e. $T_v = 4200$ K, while ensuring that the translational and rotational temperatures are in thermal equilibrium. The reaction rates were measured for trans-rotational temperatures ranging from 4000 K up to $10,000$ K.

Figure 5.6 presents a comparison of the QK models to the experimental measurements reported by Sergievskaya *et al*. [71]. The triangle markers represent the upper and lower limits of the measurements. For consistency with the experimental results, the non-equilibrium reaction rates are represented in terms of the thermal non-equilibrium factor, $Z_{neq}(T_t, T_v)$, expressed in logarithmic scale. For completeness, the analytical predictions of the QK models, Eqs. (5.5)-(5.11) and results produced by Gallis *et al*. [203] using the original QK model have been added for reference.

For a trans-rotational temperature of 4200 K, the DSMC results, analytical predictions and results reported by Gallis *et al*. [203] intersect. At this temperature, the gas is in thermal equilibrium with the result that the thermal non-equilibrium factor equals unity. As the translational temperature increases, the thermal non-equilibrium factor also increases. The QK models qualitatively predict the experimental measurements except for the original QK model at translational temperatures in excess of 9000 K. Note that this behaviour is also reported by Gallis *et al*. [203]. The new QK model remains within the bounds of the experimental measurements for the range of translational temperatures considered. This observation highlights an advantage of modelling the vibrational excitation with an anharmonic oscillator model. Furthermore, it provides strong evidence regarding the ability of the new QK model to reproduce non-equilibrium reaction rates.

5.4 Model Limitations

Figures 5.2-5.5 have demonstrated that for the four dissociation reactions, Reaction 1-Reaction 4, in post-shock flow conditions the QK model under-predicts QCT calculations [88, 92, 102, 107] whereas for nozzle flow conditions, the QK model exhibits reasonable reproduction of QCT calculations. The justification for this discrepancy lies in an excessive utilisation of the translational mode to promote dissociation reactions. The present section aims to assess the

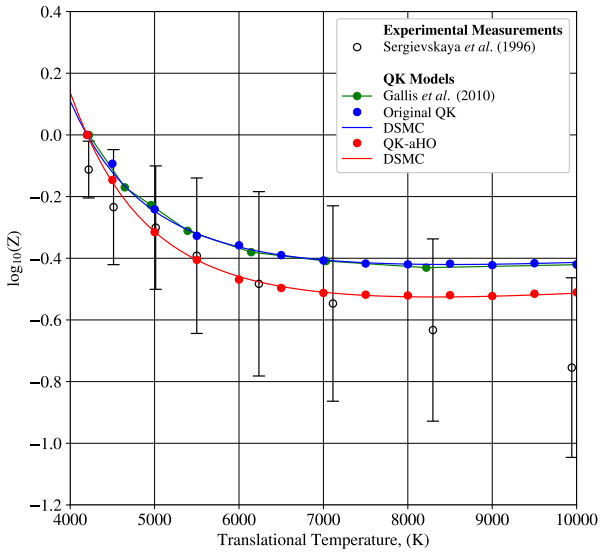

Figure 5.6: Comparison of the thermal non-equilibrium factor between DSMC and measured reaction rates for $O_2 + O_2 \longrightarrow O + O + O_2$, $T_t = T_r$ and $T_v = 4200$ K.

limitations of the QK-aHO model by demonstrating the contributions of the translational and vibrational modes to the reaction rates of all four dissociation reactions, i.e. Reaction 1-Reaction 4, in thermal non-equilibrium conditions.

The pure translational contribution to the dissociation reaction rates can be extracted after mathematical manipulations of Eq. (5.12) and reads,

$$k_{d,t} = R_{AB,M}\Gamma\left(\frac{5}{2} - \omega_{AB,M}, \frac{\varepsilon_d}{kT_t}\right). \tag{5.14}$$

Similarly, the pure vibrational contribution can be isolated from Eq. (5.12) and reads,

$$k_{d,v} = R_{AB,M}\sum_{i_{max}+1}^{\infty}\frac{e^{-\frac{\varepsilon_{v,i}}{kT_v}}}{Q_v(T_v)}. \tag{5.15}$$

Note that Eqs. (5.14) and (5.15) have been extracted without consideration of the vibrational model; hence, they can be used to predict the translational and vibrational contributions of both QK-HO and QK-aHO models.

The influence of these two contributions on the dissociation reaction rates of Reaction 1-Reaction 4 are herein evaluated for thermal non-equilibrium conditions, i.e. trans-rotational temperature of 10,000 K and for vibrational temperatures ranging from 4000 K to 20,000 K. The influence of Eqs. (5.14) and (5.15) are depicted in Fig. 5.7. The translational contribution is denoted with the dashed pink line and the vibrational contribution is denoted with the pink dash-dotted line. The reaction rates of the high-fidelity calculations [85, 102, 107] are included for reference.

For such thermal non-equilibrium conditions, it becomes evident that the translational mode contributes by a constant factor to the dissociation reaction rate, Eq. (5.14), whereas Eq. (5.15)

varies with the vibrational temperature. This behaviour is illustrated in Fig. 5.7, where the translational mode contributes by a constant fraction of the collision rates and the vibrational contribution increases with higher vibrational temperatures.

It is apparent that for all dissociation reactions the QK model excessively relies on the relative translational energy, leading to greater dissociation reaction rates than the QCT results. This excessive use not only over-predicts the high-fidelity calculations [85,102,107] but also conceals the advantages of modelling the anharmonic behaviour of chemical species. Note that the pure vibrational contribution presents a similar trend to the high-fidelity calculations [85, 102, 107]; albeit, an order of magnitude lower. It is reasonable to suppose that the QK model could benefit from a reduction in the translational contribution, compensated by an increase in the vibrational contribution.

It is important to emphasise that the QK model was not originally designed to compete with high-fidelity calculations derived from first principles. Furthermore, none of the models presented herein achieves a reasonable reproduction of the dissociation reaction rates reported by high-fidelity studies. However, in the view of Fig. 5.7, it can reasonably be concluded that excessive utilisation of the relative translational energy is responsible for over-predicting the experimental fits and high-fidelity calculations in both thermal equilibrium and non-equilibrium. Further efforts will be presented in Chapter 6 to improve the reproduction of experimental measurements and high-fidelity calculations in both thermal equilibrium and non-equilibrium.

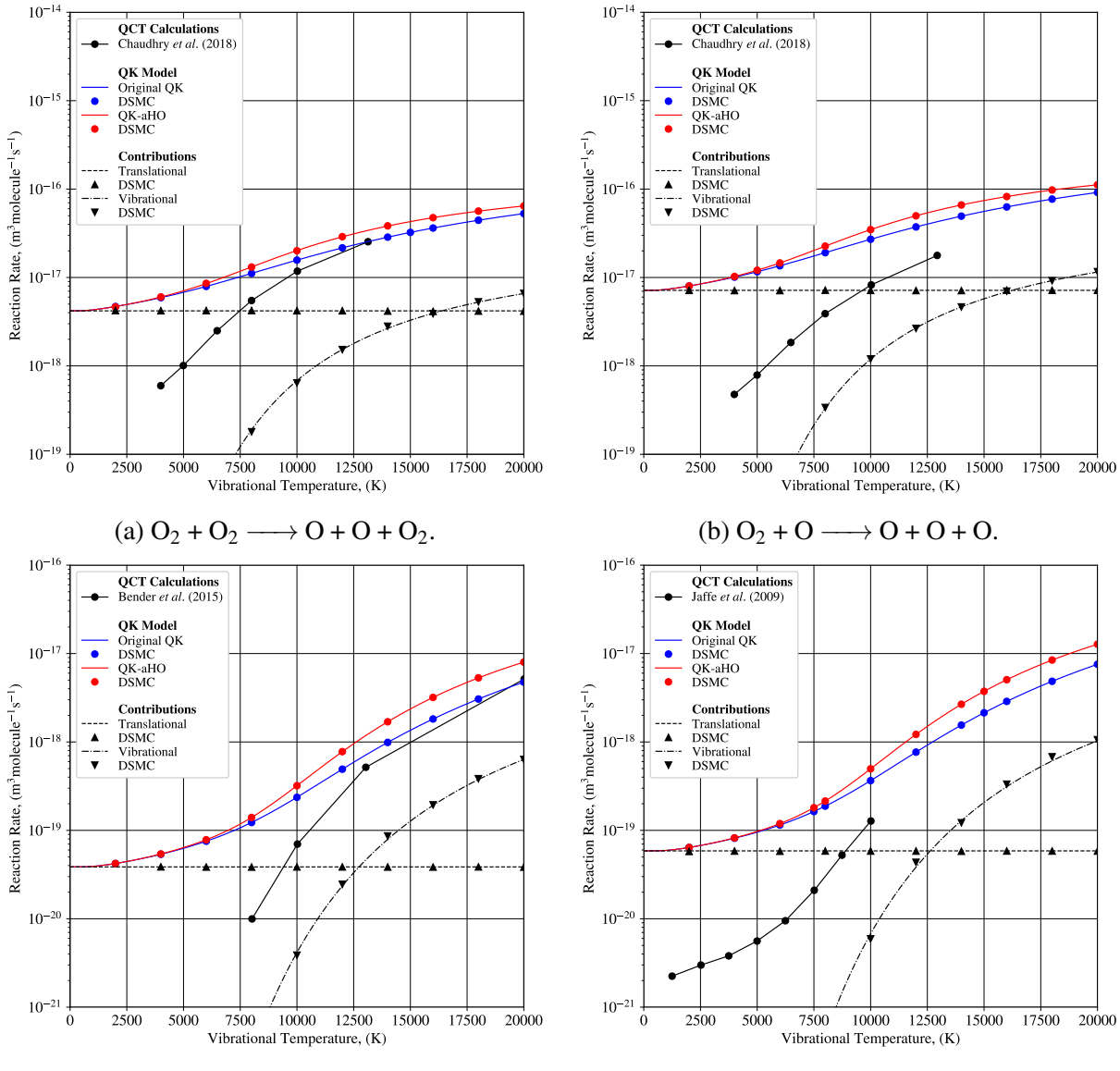

(a) $O_2 + O_2 \longrightarrow O + O + O_2$.

(b) $O_2 + O \longrightarrow O + O + O$.

(c) $N_2 + N_2 \longrightarrow N + N + N_2$.

(d) $N_2 + N \longrightarrow N + N + N$.

Figure 5.7: Limits of the QK model for dissociation reactions in thermal non-equilibrium.

5.5 Summary

The merits of a custom version of the original quantum-kinetic model are discussed and analysed. A new expression for the dissociation reaction rates in which the vibrational excitation is modelled with an anharmonic oscillator model has been derived and implemented in *dsmcFoam+*. The new formulations are tested for four dissociation reactions in the context of thermal equilibrium and thermal non-equilibrium.

For thermal equilibrium conditions, the DSMC results are compared against results from the literature in the form of the modified-Arrhenius rates, semi-empirical models, experimental results and QCT calculations. It is shown that the DSMC reaction rates are in excellent alignment with the new quantum-kinetic model, demonstrating the successful implementation of the new QK models in *dsmcFoam+*. The QK theory provides a good agreement with a compilation of numerous studies, i.e. experimental, theoretical, QCT and DMS calculations. It is also found that dissociation reactions are more likely to occur with an aHO model due to its non-linear nature.

The thermal non-equilibrium study shows that the DSMC results are in excellent agreement with the corresponding analytical solution, again demonstrating the successful implementation of the new formulations. The new QK formulations demonstrate equally good capabilities as the selection of theoretical and empirical chemistry models in the reproduction of the high-fidelity calculations, i.e. QCT calculations and DMS results. Furthermore, the comparison to the experimental measurements for the dissociation of oxygen in thermal non-equilibrium indicates that the prediction of QK-aHO remains within the bounds of the measurement uncertainties. In contrast, for any translational temperatures in excess of 9000 K and a vibrational temperature of about 4200 K, the original QK model overestimates the non-equilibrium factor. For both $T_t > T_v$ and $T_t < T_v$ flow conditions, the new QK models provide closer reproduction to the baseline model in comparison to the original QK models. However, the new QK models tend to overestimate the reaction rates at low vibrational temperatures.

The assessment of the limitations of the QK models has highlighted an excessive utilisation of the relative translational energy and under-utilisation of the pre-collision vibrational energy to promote dissociation reactions. Therefore, the following chapter will focus on deriving new expressions for the QK models to better reproduce experimental measurements and/or high-fidelity calculations.

Chapter 6

Quantum Kinetic Chemistry Model with an Anharmonic Oscillator Model: Extension and Validation *

This chapter presents an extension of the QK-aHO models following the suggestion drawn in the preceding chapter to accurately reproduce recent experimental measurements and high-fidelity calculations. Firstly, these new formulations are extensively investigated for 19 chemical reactions, dissociation and exchange reactions, for Earth's upper-atmospheric reentry under thermal equilibrium and non-equilibrium conditions. Then, the new models are validated against an extensive compilation of well-established theoretical chemistry models, experimental measurements and QCT calculations. Finally, the extended QK models are utilised to reproduce flight conditions of the space transport system second mission at an altitude of 92.35 km.

6.1 Quantum Kinetic Chemical Models

6.1.1 Dissociation Reactions

The QK-aHO model is now extended to accurately reproduce high-fidelity calculations and experimental measurements based on the findings reported in Chapter 5. This extension consists of introducing two constant tunable parameters, namely, υ_1 and υ_2, to compensate for the excessive use of the relative translational energy. These modifications apply solely to the chemistry procedures; consequently, inelastic collisions, Eq. (5.1), and collision rates, Eq. (5.6), remain unchanged.

Consider the generic dissociation reaction AB + M $\longrightarrow$ A + B + M. The condition for a dissociation reaction to occur and its corresponding dissociation probability are adjusted by means

*A large portion of the work presented in this Chapter is published in **C. H. B. Civrais**, C. White and R. Steijl. "Quantum kinetics chemistry models with an anharmonic oscillator model. Model extension and validation". (submitted)

of the two tunable parameters. Specifically, a dissociation reaction now occurs if the modified collision energy exceeds the modified dissociation energy,

$$\varepsilon_{AB-M,t} + \upsilon_2 \varepsilon_{AB,v} > \upsilon_1 \varepsilon_d. \tag{6.1}$$

Considering that the dissociation reaction operates in thermal equilibrium, the corresponding probability P_d of dissociation occurring is obtained from

$$P_d = \frac{\Gamma[\frac{5}{2} - \omega, \frac{\upsilon_1 \varepsilon_d - \upsilon_2 \varepsilon_v}{kT}]}{\Gamma[\frac{5}{2} - \omega]}. \tag{6.2}$$

Similarly, the fraction of collisions with sufficient energy for AB to dissociate, Eq. (5.11), is revisited and it reads,

$$\gamma_{AB-M}(T) = \frac{\sum_{i=0}^{i_d} e^{-\frac{\varepsilon_{v,i}}{kT}} \Gamma\left[\frac{5}{2} - \omega_{AB-M}, \frac{\upsilon_1 \varepsilon_d - \upsilon_2 \varepsilon_{v,i}}{kT}\right]}{\sum_{j=0}^{j_{max}} e^{-\frac{\varepsilon_{v,j}}{kT}}} + \frac{\sum_{i=i_{max}}^{\infty} e^{-\frac{\varepsilon_{v,i}}{kT}}}{\sum_{j=0}^{j_{max}} e^{-\frac{\varepsilon_{v,j}}{kT}}}. \tag{6.3}$$

The primary objective of υ_1 to act upon the dissociation energy with the intention to diminish the contribution of the translational mode on the reaction rate, while υ_2 acts upon the vibrational energy to artificially boost its contribution to the dissociation reaction. The introduction of these two parameters not only affects the translational and vibrational contributions but also imposes a redefinition of the dissociation quantum level. Specifically, for Eq. (6.3) to be fully defined, the dissociation quantum level, i_{max}, must satisfy,

$$\upsilon_2 \varepsilon_v > \upsilon_1 \varepsilon_d. \tag{6.4}$$

Note that Eq. (6.4) has significant implications on the dissociation quantum level, i_d. Specifically, in the QK-aHO model, the dissociation quantum level is obtained as the last vibrational quantum level immediately below the dissociation energy, such that i_d represents the last vibrational quantum satisfying $\varepsilon_v > \varepsilon_d$. Since υ_2 acts upon the vibrational energy and υ_1 on the dissociation energy, the last vibrational quantum level satisfying Eq. (6.4) may differ from that obtained from the condition $\varepsilon_v > \varepsilon_d$. For instance, in the case of molecular oxygen colliding with molecular oxygen, $i_d = 34$ satisfies Eq. (6.4), while $i_d = 43$ satisfies the condition $\varepsilon_v > \varepsilon_d$. Moreover, the vibrational energies have been fitted on PES calculations [194], restricting these to values below the dissociation energy, with the last vibrational quantum level corresponding to the dissociation quantum level. By adjusting the dissociation energy, Eq. (6.4), there exist cases where some vibrational quantum levels lie beyond the modified dissociation quantum level. Consider the previous example, there are 9 vibrational quantum levels lying beyond the modified dissociation limits, i.e. $\upsilon_1 \varepsilon_d$. In another word, dissociation reactions can now occur from lower

vibrational quantum levels compared to the original QK models, leading to vibrational energy extending beyond the modified dissociation quantum level. Therefore, a second term in Eq. (6.3) must be included to account for the contribution of these vibrational quantum levels. Note that a similar treatment has been suggested by Bond *et al.* [202] for deriving an analytical expression for the QK models in thermal non-equilibrium conditions, Eqs. (5.8) and (5.12).
Similarly, in thermal non-equilibrium conditions, Eq. (5.12) is subject to similar modifications to that applied for Eq. (6.3) and reads,

$$\gamma_{AB-M}(T_t,T_v) = \sum_{i=0}^{i_d} \Gamma\left[\frac{5}{2}-\omega_{AB-M}, \frac{\upsilon_1\varepsilon_d-\upsilon_2\varepsilon_{v,i}}{kT_t}\right]\frac{e^{-\frac{\varepsilon_{v,i}}{kT_v}}}{Q_v(T_v)} + \sum_{i_d+1}^{\infty}\frac{e^{-\frac{\varepsilon_{v,i}}{kT_v}}}{Q_v(T_v)}. \tag{6.5}$$

6.1.2 Exchange Reactions

An exchange reaction involves one stable molecule and one radical before and after the reaction occurs. These reactions are formulated as

$$\mathrm{AB}+\mathrm{C} \underset{k_b}{\overset{k_f}{\rightleftharpoons}} \mathrm{AC}+\mathrm{B}, \tag{Reaction 5}$$

where B and C are atoms and AB and AC are molecules.
Each of these reactions has a forward and a backward direction with an associated forward, $k_f(T)$ and backward, $k_b(T)$, reaction rate. The phenomenological DSMC procedure for these reactions is similar to the aforementioned dissociation procedure. An exchange reaction, e.g. Reaction 5, with activation energy E_a, takes place if, the collision energy between two colliding partners, i.e. AB – C, is greater than the activation energy, with a probability,

$$P_{ex} = \frac{\left(1-\frac{E_a}{\varepsilon_c}\right)^{\frac{3}{2}-\omega}}{\sum_{i=0}^{i_{max}}\left(1-\frac{\varepsilon_v}{\varepsilon_c}\right)^{\frac{3}{2}-\omega}}. \tag{6.6}$$

The forward macroscopic reaction rate for this process is given by Bird *et al.* [130] as,

$$k_f(T) = R_{AB-C}\frac{e^{\frac{-E_{a,f}}{kT}}}{Q_{AB,v}}\left(\frac{T}{T_{ref}}\right)^{1-\omega_{AB-C}}, \tag{6.7}$$

and the backward reaction rate as,

$$k_b(T) = R_{AC-B}\frac{e^{\frac{-E_{a,r}}{kT}}}{Q_{AC,v}}\left(\frac{T}{T_{ref}}\right)^{1-\omega_{AC-B}}, \tag{6.8}$$

where $E_{a,f}$ and $E_{a,b}$ are the activation energies of the forwards and backward exchange reaction. Bird [130] suggests to adjust the QK exchange reaction rate by redefining the activation en-

ergy as a function of the temperature to ensure the equilibrium constant is consistent with that predicted by the most representative reaction rates and statistical mechanics. For the forward reactions, the adjusted activation energy, $E_a^{'}$, takes the form of,

$$E_{a,f}^{'} = |h_{f,f}| \left(1 + a\left(\frac{T}{T_{ref}}\right)^{b}\right) \tag{6.9}$$

and for the backward reactions, it is,

$$E_{a,b}^{'} = a|h_{f,b}| \left(\frac{T}{T_{ref}}\right)^{b}, \tag{6.10}$$

where $h_{f,f}$ and $h_{f,b}$ are the forward and backward heat of formation, respectively.
In DSMC, it is good practice to avoid the utilisation of macroscopic temperature [130]; therefore, Eqs. (6.9) and (6.10) are evaluated at the collision temperature, that is,

$$T_c = \frac{\mu_{AB-M} c_r^2}{2k(\frac{5}{2} - \omega_{AB-M})}, \tag{6.11}$$

where c_r is the relative speed.
Under such circumstances, Bird [130] recommends the exchange factor a in Eqs. (6.9) and (6.10) to be substituted with

$$a^{'} = a\frac{(\frac{5}{2} - \omega_{AB-C})^{b}\Gamma(\frac{5}{2} - \omega_{AB-C})}{\Gamma(\frac{5}{2} - \omega_{AB-C} + b)}. \tag{6.12}$$

These new formulations, Eqs. (6.9) and (6.10) in tandem with Eqs. (6.11) and (6.12), supersede the default activation energy, E_a, in Eq. (6.7) and introduce two tunable quantities, a and b. It is important to notice that the exchange reaction rates are highly sensitive to the choice of the exponent parameter b. Averaging Eq. (6.11) over all collisions, the result is that $\overline{T_c} = \overline{T_{macro}}$. However, $\overline{T_{col}^b} = \overline{T_{macro}^b}$ only stands for b equal to either zero or unity. As shown in Scanlon *et al.* [133], the exchange reaction rates tuned with an exponent parameter different to zero or unity substantially deviate from the QK analytical expressions.

6.2 Thermal Equilibrium

To verify the implementation of the extended QK-aHO model and validate its predictions, a series of adiabatic reactor simulations are performed. These simulations are setup as follows. A single cubic cell with edge length 1.88×10^{-4} m, filled with one million DSMC simulator particles and using periodic boundaries in all directions is used for this purpose. A fixed time step size of 1×10^{-9} s is adopted. The inter-molecular collisions are computed with the VHS model with the species properties summarised in Table 4.3 for a reference temperature of $T_{ref} = 273$ K. The rotational and vibrational collision numbers are set to unity since these play no role in the

measurement of collision and reaction rates. Only one reaction is considered per simulation, collisions are enabled, the internal energy transfer between collision partners is disabled and the splitting of colliding partners is deactivated. This technique allows reaction rates to be sampled at a constant temperature.

6.2.1 Dissociation Reactions

In the present section, the implementation of the extended QK-aHO model is verified against its analytical expression, Eq. (6.3), and its predictions are validated against a compilation of experimental measurements and high-fidelity calculations for 12 dissociation reactions for temperatures ranging from 2500 K to 20,000 K.

The tunable parameters υ_1 and υ_2 are inferred using a non-linear least square fit approach on the most representative database to best reproduce both thermal equilibrium and non-equilibrium dissociation reaction rates. Experimental measurements are regarded as a primary baseline, however, in the absence of such databases, QCT calculations are considered as an alternative baseline model. The temperature range on which the tunable parameters υ_1 and υ_2 have been inferred, the database and the values of the two tunable parameters are reported for 12 dissociation reactions in Tab. 6.1. No experimental measurements or QCT calculations have yet been reported in the literature for the remaining 3 dissociation reactions, i.e. O_2 + NO, N_2 + NO and NO + O_2. Consequently, both tunable parameters υ_1 and υ_2 are set to unity for these reactions.

It is important to mention that in the development of the QK model [130] and its extended versions [135, 136, 141], only translational and vibrational modes are considered for a dissociation reaction to occur. Real gas effects, such as rovibrational coupling, i.e. centrifugal force and change in moment of inertia, and non-adiabatic, i.e. vibronic and rovibronic, transitions are not taken into account. While the primary aim of this chapter is to reproduce experimental measurements and high-fidelity calculations of dissociation reaction rates, it is crucial to acknowledge that the QK models may require further investigation to incorporate these real-gas effects.

Figures 6.1-6.3 compare DSMC reactions rates against the analytical solution, Eq. (6.3), and the compilation of experimental results, QCT calculations, and DMS results tabulated in Tab. 1.1 for the 12 dissociation reactions for which the values of υ_1 and υ_2 have been reported in Tab. 6.1. Note that the DMS method presents a comparable standard of accuracy to the QCT method as both methods are based on *ab initio* potential energy surfaces. Therefore, in the absence of experimental measurements and/or QCT calculations, DMS results are regarded as the most representative dataset available. The abscissa shows the inverse of the temperature, i.e. 20,000/T, with the reaction rates plotted on the ordinate axis. To ease the readability of the plots, a colour convention is adopted for the entire article. The extended QK model is denoted by solid red lines and the corresponding DSMC results in red markers. The predictions of the original QK model are included for reference and denoted by solid blue lines. Experimental measurements

Table 6.1: Fitting coefficients of the extended QK-aHO model and reference database for a selection of dissociation reactions.

Reaction	υ_1	υ_2	Temperature Range	Data type	Reference
$O_2 + O_2 \longrightarrow O + O + O_2$	1.850	2.050	6000-14 000	Experimental	Streicher *et al.* [77]
$O_2 + O \longrightarrow O + O + O$	1.098	1.090	6000-14 000	Experimental	Streicher *et al.* [77]
$O_2 + N_2 \longrightarrow O + O + N_2$	1.950	1.850	8000-20 000	QCT	Chaudhry *et al.* [85]
$O_2 + N \longrightarrow O + O + N$	1.748	1.878	4000-20 000	QCT	Torres *et al.* [90]
$O_2 + NO \longrightarrow O + O + NO$	1.000	1.000	-	-	-
$N_2 + O_2 \longrightarrow N + N + O_2$	1.481	1.430	8000-20 000	QCT	Chaudhry and Candler [86]
$N_2 + O \longrightarrow N + N + O$	1.727	1.718	4000-20 000	QCT	Jo *et al.* [99]
$N_2 + N_2 \longrightarrow N + N + N_2$	1.646	1.751	8000-15 000	Experimental	Appleton *et al.* [67]
$N_2 + N \longrightarrow N + N + N$	1.344	1.354	8000-15 000	Experimental	Appleton *et al.* [67]
$N_2 + NO \longrightarrow N + N + NO$	1.000	1.000	-	-	-
$NO + O_2 \longrightarrow N + O + O_2$	1.000	1.000	-	-	-
$NO + O \longrightarrow N + O + O$	6.323	6.412	4000-20 000	QCT	Torres *et al.* [90]
$NO + N_2 \longrightarrow N + O + N_2$	11.285	11.667	4600-7300	Experimental	Streicher *et al.* [79]
$NO + N \longrightarrow N + O + N$	4.138	4.252	4000-20 000	QCT	Jo *et al.* [99]
$NO + NO \longrightarrow N + O + NO$	0.920	0.998	4600-7300	Experimental	Streicher *et al.* [78]

are denoted by open symbols and the most representative high-fidelity calculations, i.e. QCT or DMS, are denoted by black solid-marker lines.

Figures 6.1-6.3 show an excellent agreement between the DSMC reaction rates and the analytical expression, Eq. (6.3), for the 12 dissociation reactions. This verifies the implementation of the extended QK-aHO model. Additionally, the extended QK-aHO models present an excellent reproduction of the baseline database for all dissociation reactions whether it be experimental measurements or high-fidelity calculations. This suggests that the numerical procedure employed to determine the two tunable parameters has been successful.

For all 12 dissociation reactions, the extended QK model presents a significant improvement to the original QK model in the reproduction of the compilation of past studies. Specifically, while the original QK model tends to overestimate the dissociation reaction rates, e.g. $O_2 + N_2$ or NO + N_2, the extended QK model lies within the experimental bounds of all dissociation reactions for the entire temperature range. This satisfactory reproduction of the compilation of experimental measurements and high-fidelity calculations demonstrates the benefits of the extended QK models over the original QK model. Nonetheless, for some chemical reactions, e.g. N_2 + N_2 and N_2 + N, experimental measurements [58, 59, 66, 67] present a large scatter lying within orders of magnitude. Therefore, new experimental measurements of these chemical reactions with reduced uncertainties are required to differentiate between models.

Additionally, Figs. 6.1-6.3 indicate that the extended QK-aHO model generally suggests slower reaction rates compared to the original QK model, except for NO+NO. This observation implies a slower chemical activity in typical hypersonic flow conditions compared to the original QK model, leading to a slower depletion of molecular species, i.e. O_2 and N_2. In the context of hypersonic flows, this implies an increased shock stand-off distance which would result in a

thicker thermal non-equilibrium region, thus resulting in a substantial increase in the surface heat flux.

The QCT calculations reported by Jo *et al*. [87] for O_2+O_2 are based on *ab-initio* PESs presented by Pakku *et al*. [207]. This description of $O_2 + O_2$ involves the modelling of the adiabatic rovibrational transition with anharmonic vibrational energy. For weakly bounded molecules such as O_2, the assumption of adiabatic transitions, i.e. no electronic-vibrational-rotational effects, is particularly restrictive considering that the first six electronic excited states of O_2 lie below the dissociation limit. Consequently, to account for dissociation from electronically excited states, these QCT calculations incorporate a correction factor of $16/3$ corresponding to the degeneracy of the electronic excited states. This factor follows the method developed by Nikitin [208] which assumes that the time scale for electronic and vibrational excitation is comparable in high thermal conditions. This approach has also been adopted in other studies involving the dissociation of O_2 such as Torres *et al*. [90], Chaudhry *et al*. [85], and Andrienko and Boyd [93]. Note that the addition of a correction factor is not unique to O_2+O_2 but it is utilised for many more chemical reactions [90]. These studies demonstrate the importance of this correction factor to achieve satisfactory reproduction of the experimental measurements provided by Streicher *et al*. [76,77]. Considering these studies, it is reasonable to suppose that dissociation reactions may not only arise from the ground excited state but also from electronic excited states.

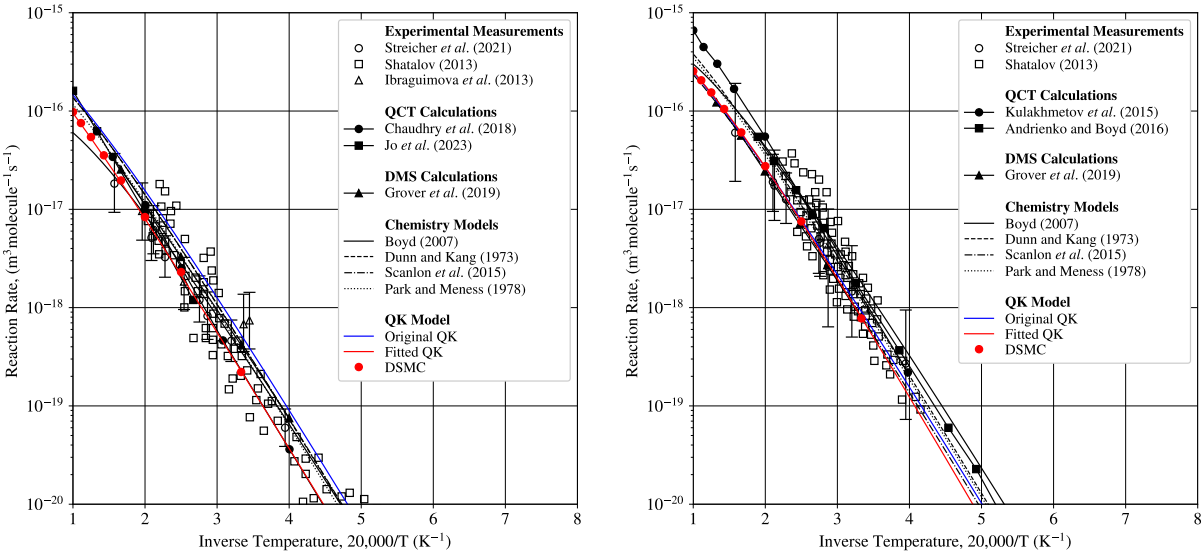

(a) $O_2 + O_2 \longrightarrow O + O + O_2$.

(b) $O_2 + O \longrightarrow O + O + O$.

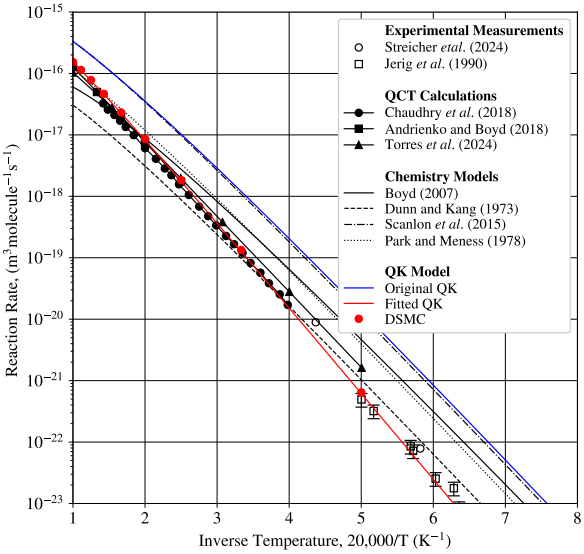

(c) $O_2 + N_2 \longrightarrow O + O + N_2$.

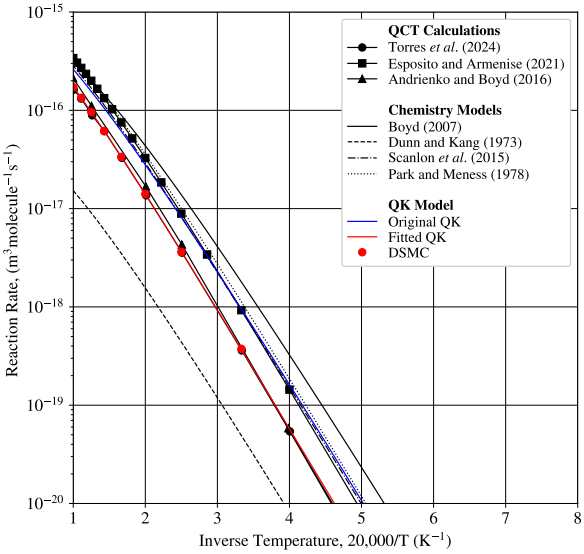

(d) $O_2 + N \longrightarrow O + O + N$.

Figure 6.1: Thermal equilibrium dissociation reaction rates of oxygen.

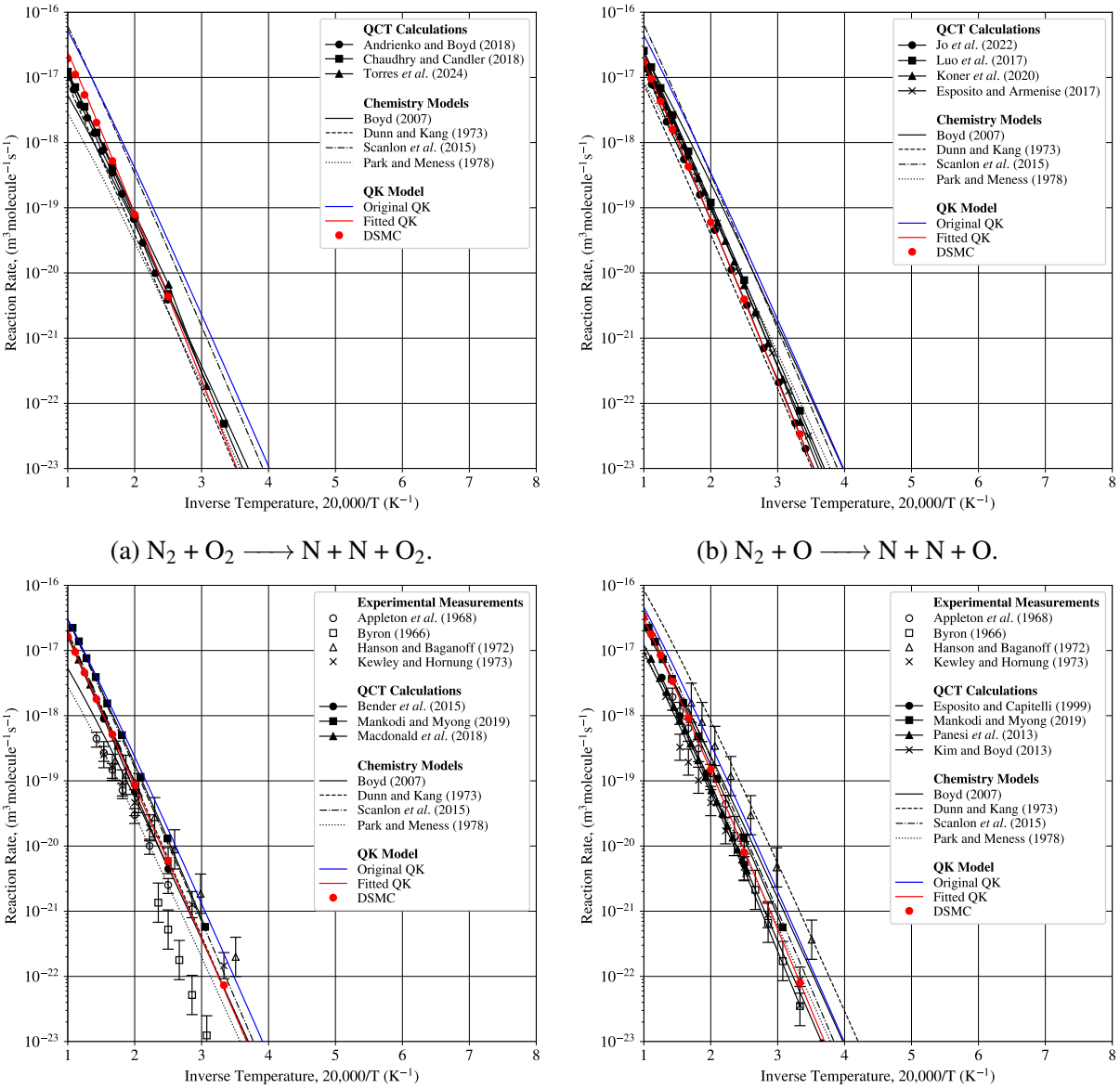

(a) $N_2 + O_2 \longrightarrow N + N + O_2$.

(b) $N_2 + O \longrightarrow N + N + O$.

(c) $N_2 + N_2 \longrightarrow N + N + N_2$.

(d) $N_2 + N \longrightarrow N + N + N$.

Figure 6.2: Thermal equilibrium dissociation reaction rates of nitrogen.

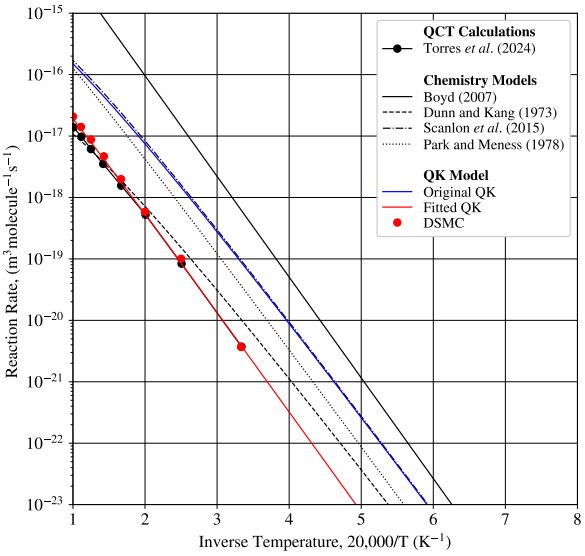

(a) NO + O $\longrightarrow$ N + O + O.

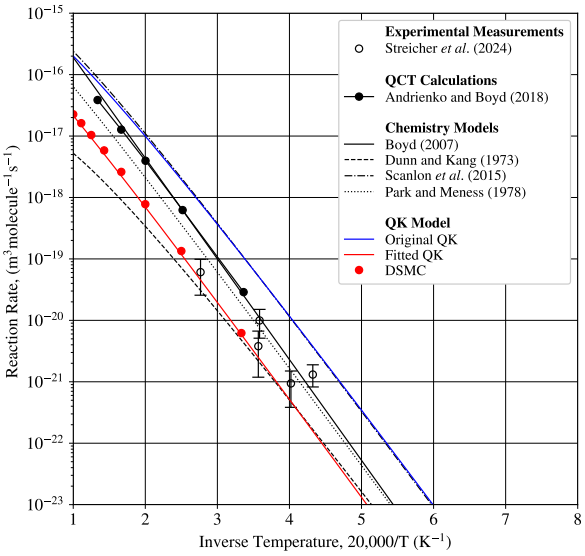

(b) NO + N_2 $\longrightarrow$ N + O + N_2.

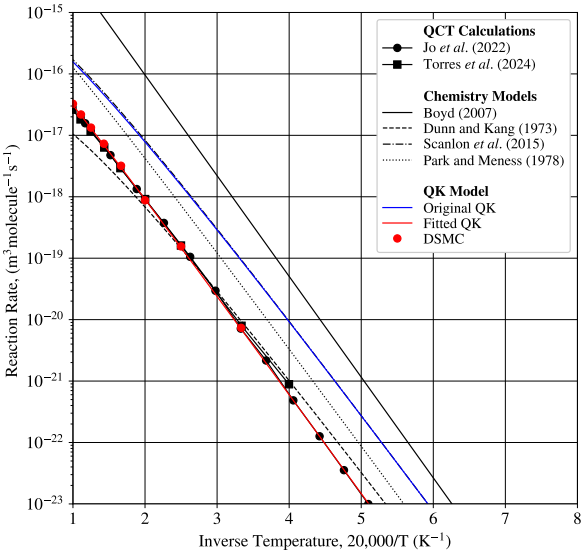

(c) NO + N $\longrightarrow$ N + O + N.

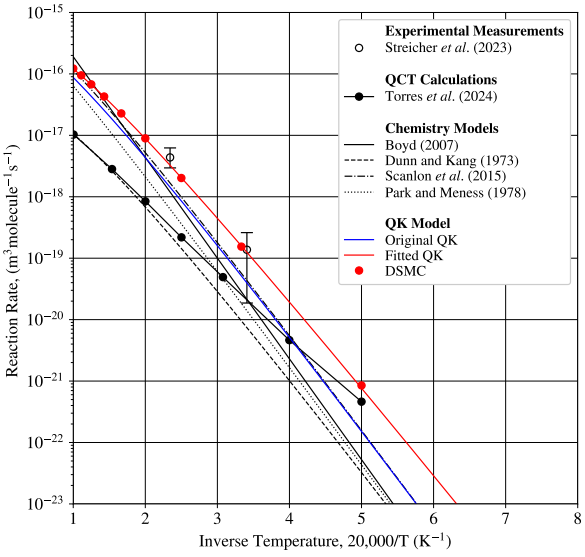

(d) NO + NO $\longrightarrow$ N + O + NO.

Figure 6.3: Thermal equilibrium dissociation reaction rates of nitric oxide.

6.2.2 Exchange Reactions

The investigation of the QK models in thermal equilibrium follows with a study of the formation of nitric oxide, NO. In high-enthalpy air flow, such as hypersonic Earth re-entry, nitric oxide is known to be one of the primary radiators [209]; hence, an accurate prediction of its formation is crucial. It has been established that NO is generated through the Zeldovich chemical mechanism [8] with the global chemical reaction described by Reaction 6,

$$N_2 + O_2 \rightleftharpoons 2NO \qquad \text{(Reaction 6)}$$

It is constituted of two elementary chemical reactions, Reaction 7 and Reaction 8.

$$N_2 + O \rightleftharpoons NO + N \qquad \text{(Reaction 7)}$$

$$O_2 + N \rightleftharpoons NO + O \qquad \text{(Reaction 8)}$$

Considering a generic exchange reaction Reaction 5, the forward rate of change of reactant AB is,

$$\frac{dn_{AB}}{dt} = -k_f(T) n_{AB} n_c, \tag{6.13}$$

and similarly, the backward rate of change is formulated,

$$\frac{dn_{AB}}{dt} = -k_b(T) n_{AC} n_b, \tag{6.14}$$

where n_{AB}, n_C, n_{AC} and n_B denote the number density of the reactants or products in the generic exchange reaction and $k_f(T)$ and $k_b(T)$ refer to the forward and backward reaction rates, respectively.

Statistical mechanics theory shows that the equilibrium constant of a chemical reaction, e.g. Reaction 5, is given by the ratio of the forward and the backward reaction rates,

$$K_{eq} = \frac{k_f}{k_b}. \tag{6.15}$$

In thermal equilibrium conditions, statistical mechanics theory also demonstrates that the equilibrium constant satisfies,

$$K_{eq} = \left(\frac{m_{AC} m_B}{m_{AB} m_C}\right)^{3/2} \frac{Q_{AC,r}}{Q_{AB,r}} \frac{Q_{AC,v}}{Q_{AB,v}} \frac{Q_{AC,e}}{Q_{AB,e}} \frac{Q_{B,e}}{Q_{C,e}} e^{-\frac{E_f}{kT}}, \tag{6.16}$$

where E_f is the reaction energy of the forward chemical mechanism, $Q_{AB,r}$ and $Q_{AC,r}$ are the

rotational partition function of species AB and AC, respectively.

In the classical limit, i.e. $T > \theta_{AB,r}$, the rotational partition function of a diatomic species AB is Eq. (2.50), see Tab. 4.3. Finally, the electronic partition function is formulated as Eq. (2.60). In the present chapter, the 7, 11, 15, 32, and 35 lowest electronic excited states of O_2, N_2, NO, O and N, respectively, are considered. The spectroscopic constants of these electronic excited states are extracted from the NIST database [25].

Past studies [130, 133, 180, 185] have reported the tunable parameters for the two Zeldovich exchange reactions, Reaction 7 and Reaction 8. Table 6.2 summarises a compilation of the tunable parameters for adjusting the activation energies of the Zeldovich reactions. In Scanlon *et al*. [133], these values have been selected as the optimum values to match the forward and backward rate of changes of nitric oxide, Eqs. (6.13) and (6.14), and the analytical expressions of the QK model for the forward and backward reactions, Eqs. (6.7) and (6.8). In Bird [130,180], these values are tuned such that the QK model reproduces the most representative reaction rates. Recently, Streicher *et al*. [80] have reported experimental measurements of the endothermic Zeldovich reactions, Reaction 7 (forward) and Reaction 8 (backward), with a high level of fidelity for temperatures ranging between 2500 K to 6600 K. These measurements are therefore considered as a reference to improve the accuracy of the QK model for the Zeldovich exchange reactions. The parameters for the endothermic reactions, Reaction 7 (forward) and Reaction 8 (backward), are inferred from the experimental measurements [80] by means of a least-square fit technique. No direct measurement of the exothermic exchange reactions exists; hence, the exothermic reaction rates must be estimated from the equilibrium constant and the endothermic reaction rates [87, 99, 116, 210]. Therefore, the tunable parameters for the exothermic reactions are obtained by searching for the optimum couple (a, b) for the equilibrium constant calculated as the ratio of the forward and the backward reaction rates, Eq. (6.15), to match the prediction of statistical mechanics theory, Eq. (6.16). The new set of tunable parameters is tabulated in Tab 6.2. It is important to reiterate that these parameters are highly dependent on the number of electronic excited states and their respective spectroscopic constants for the calculation of the vibrational energy and the number of vibrational quantum levels considered for each molecular species. Additionally, for consistency with the QK model, a fully uncoupled approach of the partition function has been considered; hence, any interactions between modes such as rovibronic coupling effects are disregarded, see Eqs. (2.50) and (2.60).

Table 6.2: Parameters for adjusting the activation energies of the Zeldovich reactions.

Reaction	Bird [180]		Scanlon *et al*. [133]		White [185]		*This thesis*	
	a	b	a	b	a	b	a	b
$N_2 + O \longrightarrow NO + N$	0.150	0.000	0.150	0.150	0.150	0.000	0.030	0.000
$NO + N \longrightarrow N_2 + O$	0.033	0.800	0.033	0.800	0.070	0.620	0.003	1.183
$O_2 + N \longrightarrow NO + O$	0.100	0.480	0.100	0.100	0.250	0.000	0.177	0.362
$NO + O \longrightarrow O_2 + N$	0.100	0.680	0.085	0.650	0.085	0.650	0.100	0.680

Figure 6.4 compares the DSMC reaction rates using the suggested parameters in Tab. 6.2 to the selection of past studies shown in Tab. 1.1, and the analytical QK expressions, Eqs. (6.7) and (6.9), with the parameters presented in Tab. 6.2 for the endothermic Zeldovich reactions, Reaction 7 (forward) and Reaction 8 (backwards). As in the previous section, the abscissa shows the inverse of the normalised temperature, $20,000/T$, and the reaction rates are plotted on the ordinate axis.

Figure 6.4 shows a good agreement for the entire range of temperature between the analytical expression of the QK model and the DSMC reaction rates, verifying the newly implemented chemistry models. It can also be observed that the extended QK model presents a significant improvement to the original QK model in the reproduction of the compilation of past studies. Specifically, for the two endothermic Zeldovich reactions, the extended QK model shows excellent agreement with experimental measurements and lies within the experimental bounds for the entire temperature range. This suggests that the fitting procedure of the tunable parameters for the endothermic exchange reactions has been successful.

Figures 6.5a and 6.5b present the equilibrium equilibrium constant of the Zeldovich reactions. This quantity is important in the determination of the tunable parameters for the exothermic reactions. It can be noticed that the DSMC results perfectly align with the analytical expression with the suggested parameters, demonstrating that the new expressions for the forward and the backward exchange reactions are correctly implemented in *dsmcFoam+*. These results also indicate a relatively good agreement with the prediction of statistical mechanics theory, Eq. (6.16), with the vibrational excitation model being either HO or aHO.

For completeness, the exothermic exchange reaction rates are depicted in Fig. 6.6 for Reaction 7 (backwards) and Reaction 8 (forward), respectively. The DSMC reaction rates are calculated with the parameters reported in Tab. 6.2 and compared against the compilation presented in Tab. 1.1, and the analytical QK expressions, Eqs. (6.7) and (6.10). Despite variations observed in the compilation of past studies, some of which deviate from the DSMC predictions, the reaction rates lie on a quasi-plateau for most of the temperature range. It is noteworthy that the reaction rates generally fall within a certain range, the latter reaction rates can be considered in reasonable agreement with the QK predictions. In some cases, the variations are within one order of magnitude, while for others, they are within a factor of 3 to 4, for most of the temperature range. Figures 6.6a and 6.6b also show that the QK model for the exothermic reactions is non-monotonic. It is worth mentioning that a similar trend has also been reported by Bird [130], Mallikarjun *et al*. [19], Scanlon *et al*. [133], and White [185]. Additionally, this behaviour is only encountered for the exothermic reaction rates and appears to be a feature of the QK model for these reactions. This can be attributed to the low activation energy of the exothermic exchange reactions.

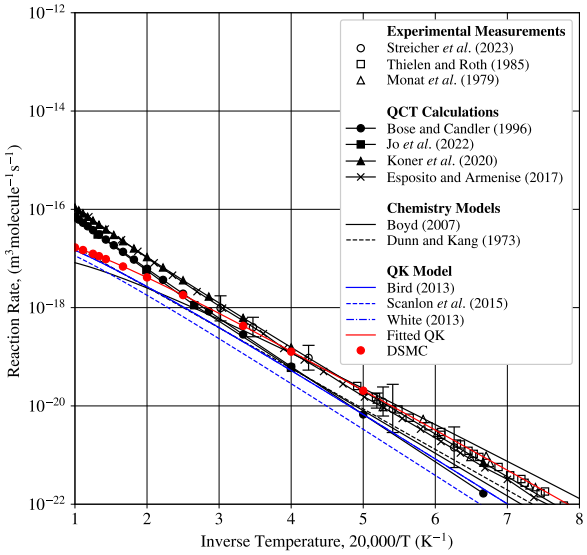

(a) $N_2 + O \longrightarrow NO + N$.

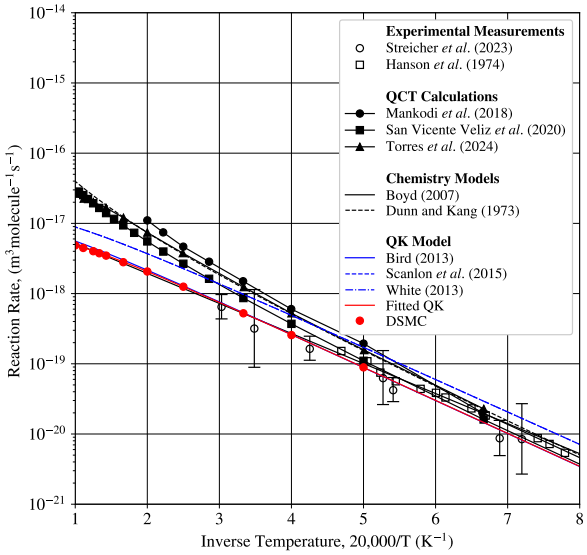

(b) $NO + O \longrightarrow O_2 + N$.

Figure 6.4: Thermal equilibrium endothermic exchange reaction rates of the Zeldovich reactions.

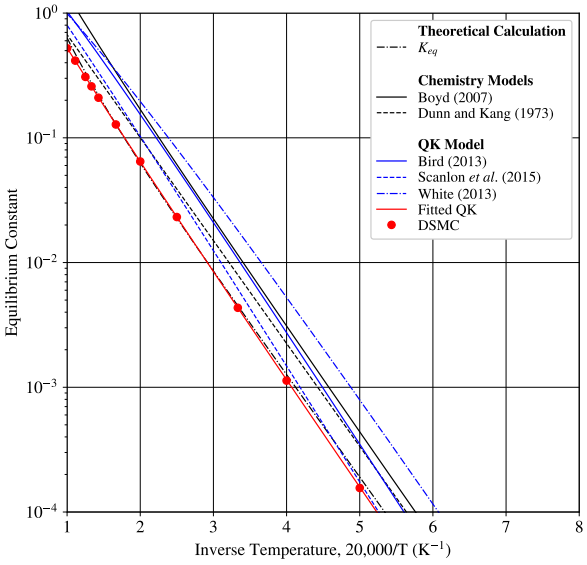

(a) $N_2 + O \rightleftharpoons NO + N$.

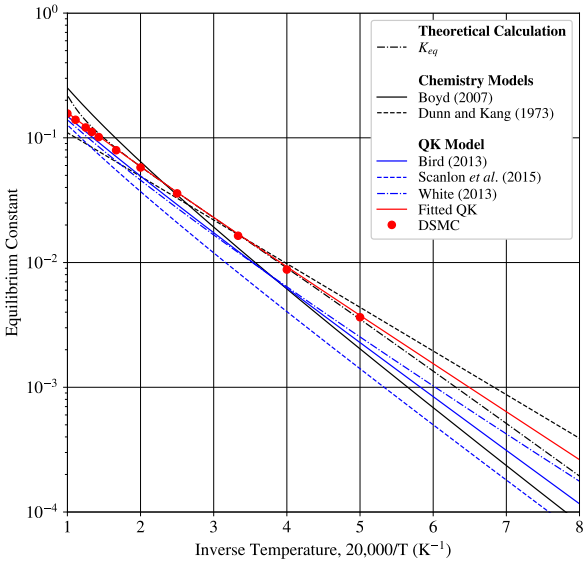

(b) $O_2 + N \rightleftharpoons NO + O$.

Figure 6.5: Equilibrium constant of the Zeldovich reactions.

6.3 Thermal Non-Equilibrium

6.3.1 Dissociation Reactions

In the previous sections, the reproduction of the dissociation reactions with the extended QK models was limited to chemical reactions in thermal equilibrium. A selection of six dissociation reactions is now regarded in thermal non-equilibrium. These dissociation reactions are studied for the conditions summarised in Tab. 6.3 involving three trans-rotational temperatures

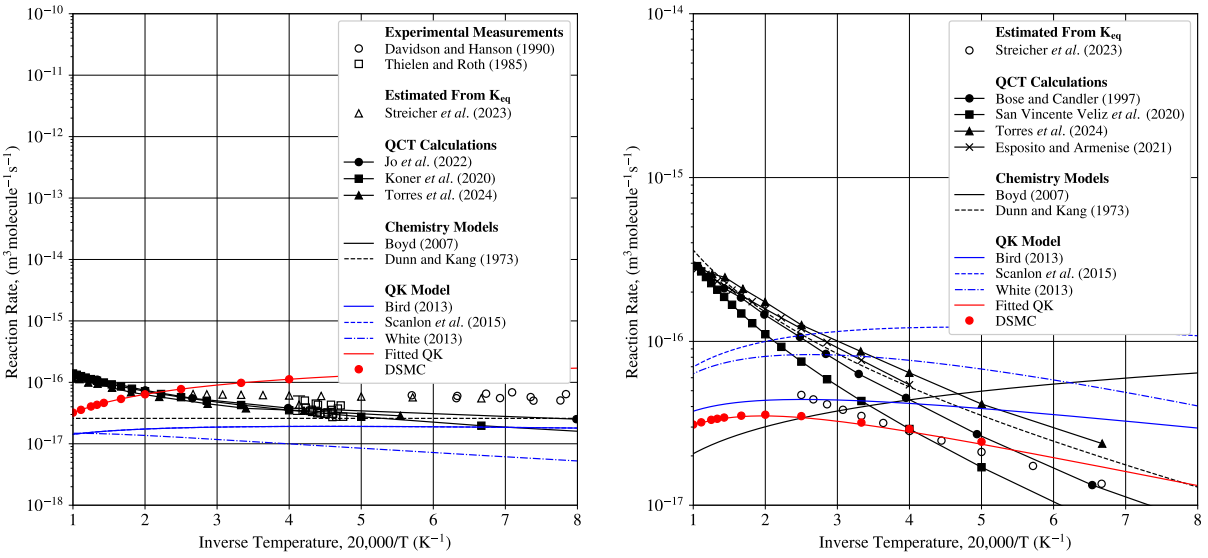

(a) $NO + N \longrightarrow N_2 + O$. (b) $O_2 + N \longrightarrow NO + O$.

Figure 6.6: Thermal equilibrium exothermic exchange reaction rates of the Zeldovich reactions.

and vibrational temperatures ranging from 4000 K to 20,000 K. The validity of the extended QK models predictions is first verified against the thermal non-equilibrium quantum-kinetics model, Eq. (6.5). The predictions of the QK model are then validated against the selection of experimental measurements, QCT calculations and DMS results summarised in Tab. 1.2.

Table 6.3: Thermal non-equilibrium scenarios and baseline database.

Reaction	$T_{t,1}$ (K)	$T_{t,2}$ (K)	$T_{t,3}$ (K)	Data type	Reference
$O_2 + O_2 \longrightarrow O + O + O_2$	8000	10 000	15 000	DMS	Grover and Schwartzentruber [88]
$O_2 + O \longrightarrow O + O + O$	5000	10 000	20 000	QCT	Kulakhmetov *et al.* [91]
$O_2 + N_2 \longrightarrow O + O + N_2$	8000	10 000	20 000	QCT	Andrienko and Boyd [95]
$N_2 + O_2 \longrightarrow N + N + O_2$	8000	15 000	20 000	QCT	Andrienko and Boyd [95]
$N_2 + N_2 \longrightarrow N + N + N_2$	8000	10 000	20 000	Experimental Fit	Losev *et al.* [72]
$N_2 + N \longrightarrow N + N + N$	7500	10 000	15 000	QCT	Jaffe *et al.* [107]

Figures 6.7-6.12 compare the DSMC thermal non-equilibrium dimensionless parameter against the compilation of past studies shown in Tab. 1.2 for the reactions and conditions presented in Tab. 6.3. The extended QK model is tuned with the parameters summarised in Tab. 6.1. The abscissa shows the vibrational temperature and the thermal non-equilibrium factor, $Z(T_t, T_v)$, is plotted on the ordinate axis. The extended QK model is denoted by solid red lines and DSMC results by red markers. The predictions of the original QK model are included for reference and denoted by solid blue lines.

Figures 6.7-6.12 demonstrate that the DSMC results are in excellent agreement with the theoretical predictions of the extended non-equilibrium QK theory, Eq. (6.8); hence, demonstrating successful implementation of the new formulation under thermal non-equilibrium conditions. Furthermore, the DSMC results present a satisfactory reproduction of the QCT calcu-

lations [85, 91, 95, 102, 107], DMS results [88] and experimental measurements [72] for both post-shock flow conditions, i.e. $T_t > T_v$, and nozzle flow conditions, i.e. $T_t < T_v$, for all three trans-rotational temperatures and all six chemical reactions. It is worth mentioning that, for low vibrational temperatures, QCT calculations inherently carry uncertainties of about a factor of 3 at best [145, 146], supporting the qualitative reproduction of these calculations by the extended QK model.

The values tabulated in Tab. 6.1 have been determined as the best compromise for qualitative reproduction of both thermal equilibrium and non-equilibrium reaction rates. Figures 6.7-6.12 demonstrate that the fitting procedure has been successful. However, it is important to reiterate that these tunable parameters have been obtained for temperatures up to 7300 K in some chemical reactions, e.g. NO + NO and NO + N_2, and extrapolations toward higher temperatures are performed due to the lack of a validation database. Additional experimental measurements and high-fidelity calculations are therefore required to further differentiate between chemistry models.

Additionally, it is important to stress that the extended QK models provide a significant improvement to the QK models, i.e. QK-HO [130] and QK-aHO [136], for both low and high vibrational thermal non-equilibrium conditions. This improvement has been achieved without the inclusion of typical real-gas effects such as rotational-vibrational coupling and non-adiabatic transition correction factors, which are incorporated in experimental measurements, QCT calculations, and DMS results. While a good reproduction of the baseline database is herein presented, further investigations are warranted to include these real-gas effects in the extended QK models.

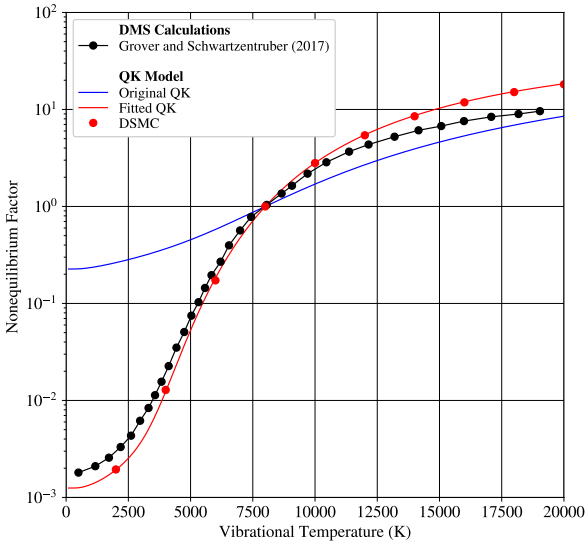

(a) $T_{t,r}$ = 8000 K.

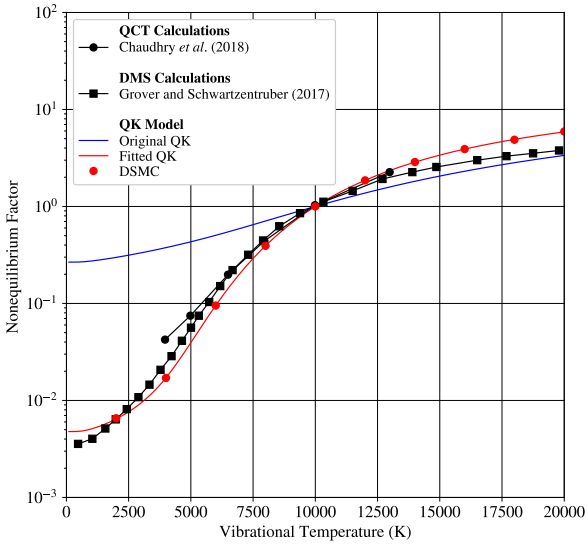

(b) $T_{t,r}$ = 10,000 K.

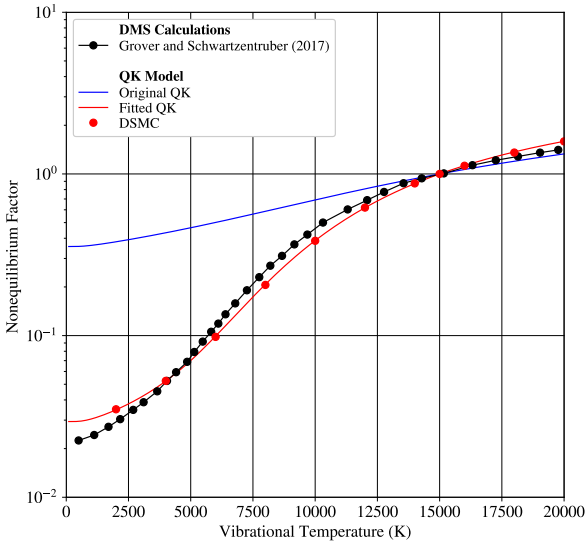

(c) $T_{t,r}$ = 15,000 K.

Figure 6.7: Thermal non-equilibrium factor for $O_2 + O_2 \longrightarrow O + O + O_2$.

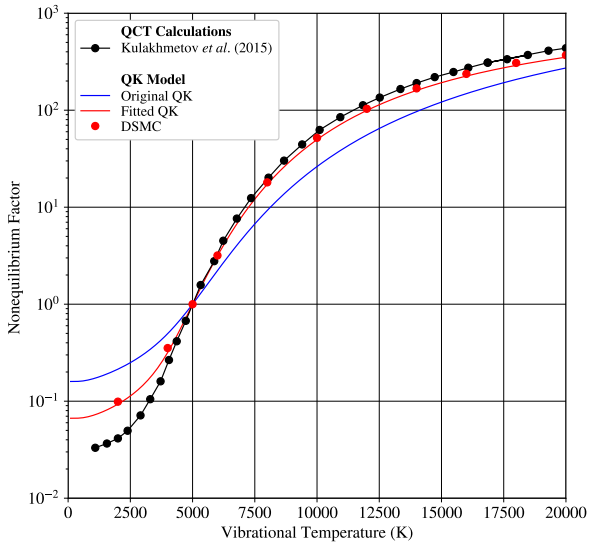

(a) $T_{t,r}$ = 5000 K.

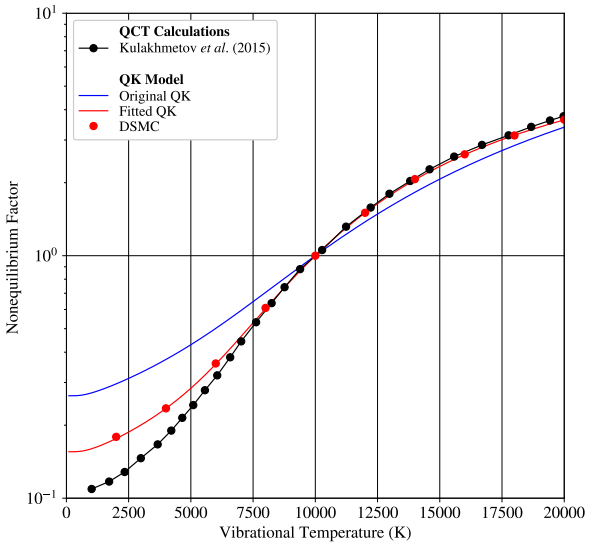

(b) $T_{t,r}$ = 10,000 K.

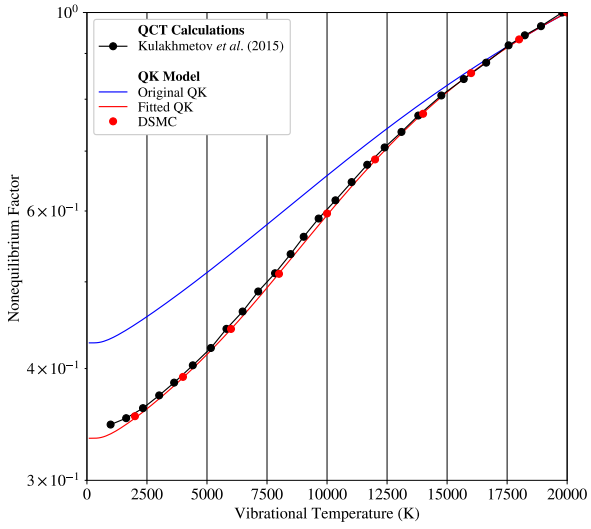

(c) $T_{t,r}$ = 20,000 K.

Figure 6.8: Thermal non-equilibrium factor for $O_2 + O \longrightarrow O + O + O$.

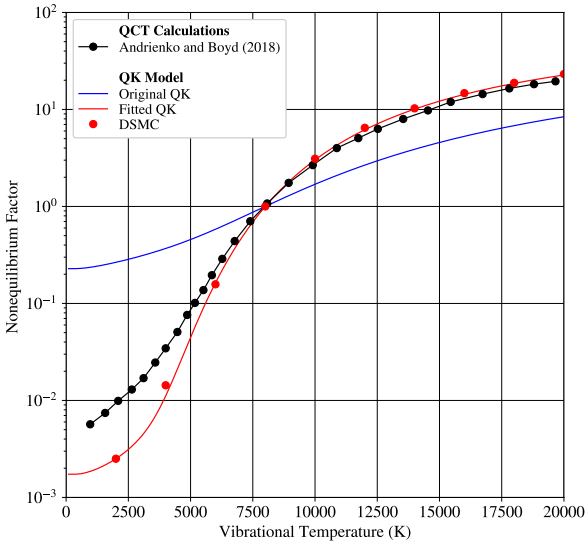

(a) $T_{t,r}$ = 8000 K.

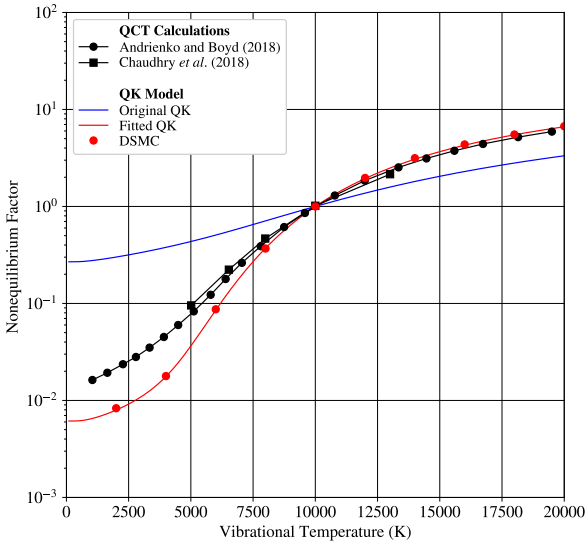

(b) $T_{t,r}$ = 10,000 K.

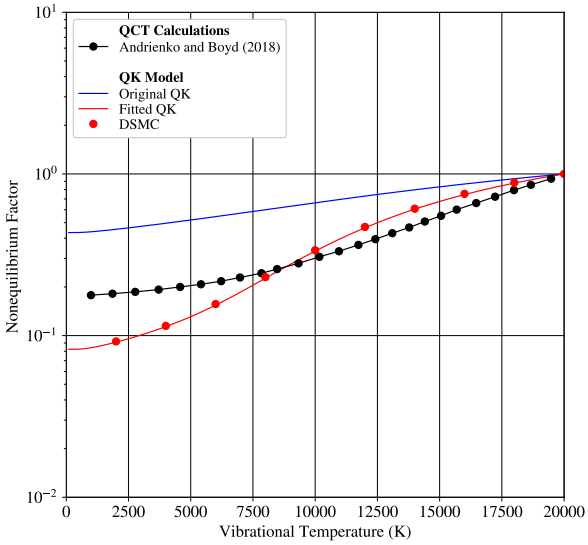

(c) $T_{t,r}$ = 20,000 K.

Figure 6.9: Thermal non-equilibrium factor for $O_2 + N_2 \longrightarrow O + O + N_2$.

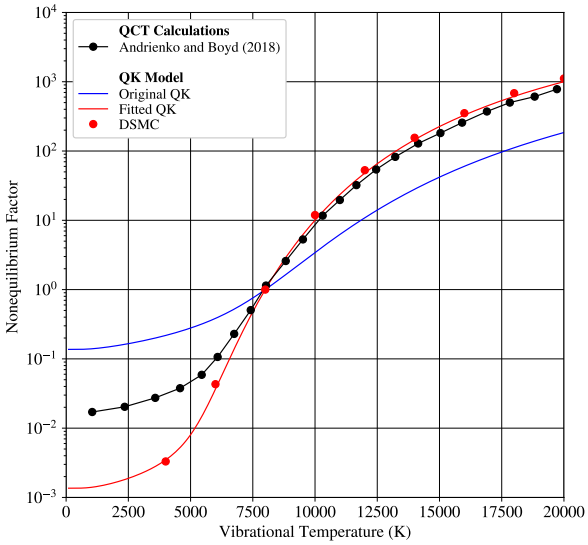

(a) $T_{t,r}$ = 8000 K.

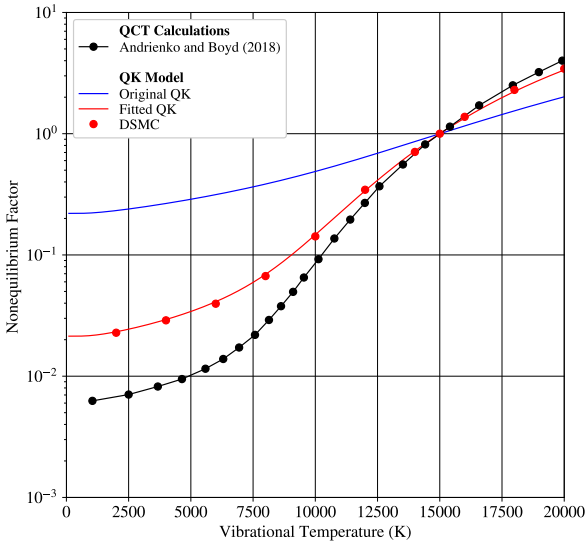

(b) $T_{t,r}$ = 15,000 K.

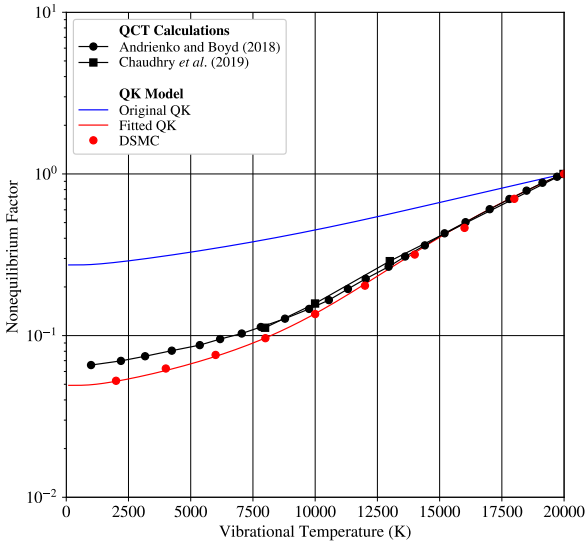

(c) $T_{t,r}$ = 20,000 K.

Figure 6.10: Thermal non-equilibrium factor for $N_2 + O_2 \longrightarrow N + N + O_2$.

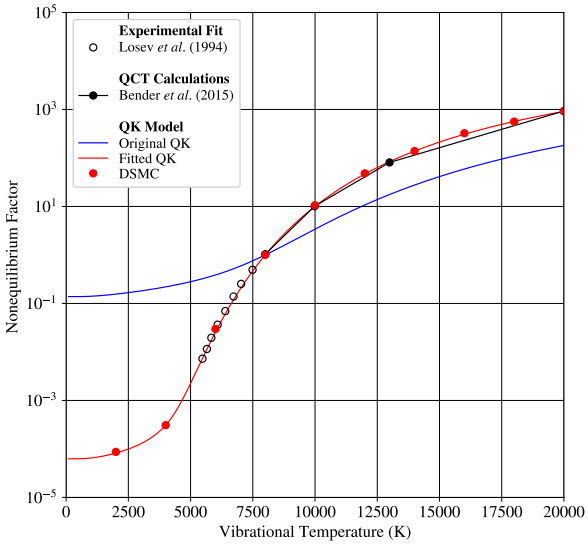

(a) $T_{t,r}$ = 8000 K.

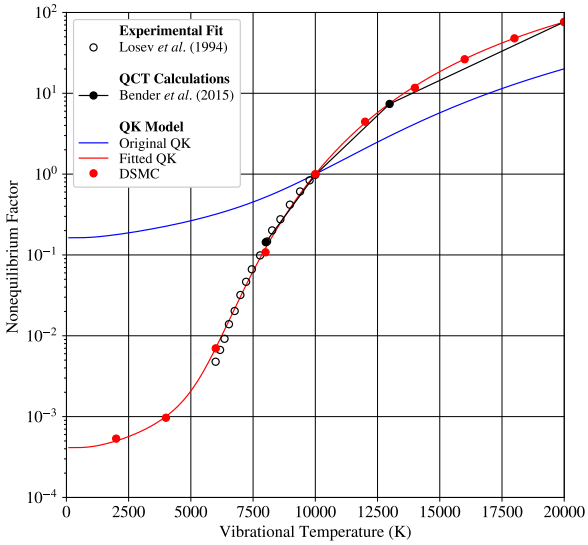

(b) $T_{t,r}$ = 10,000 K.

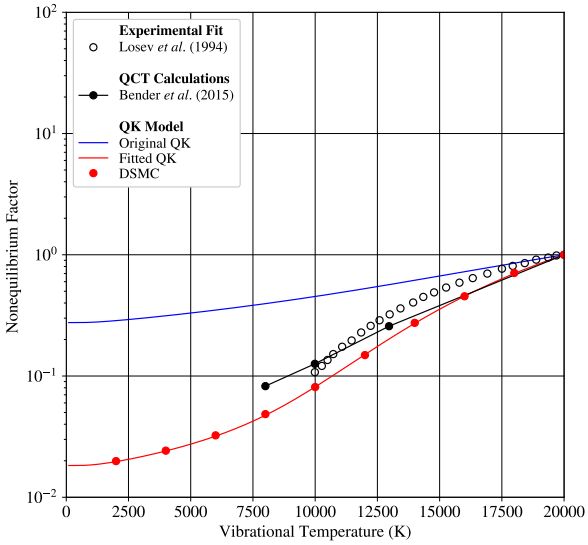

(c) $T_{t,r}$ = 20,000 K.

Figure 6.11: Thermal non-equilibrium factor for $N_2 + N_2 \longrightarrow N + N + N_2$.

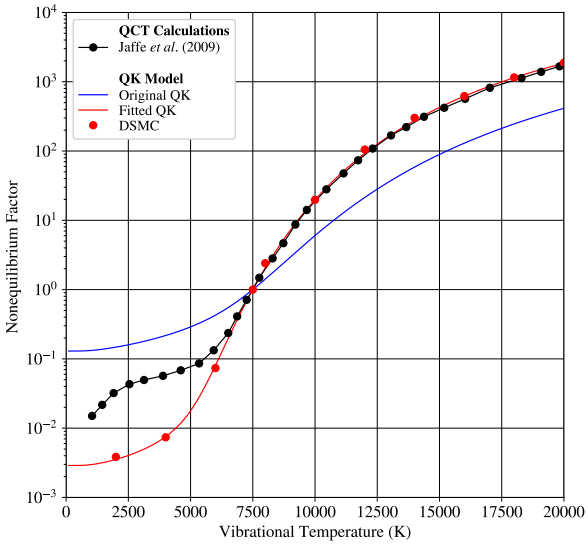

(a) $T_{t,r}$ = 7500 K.

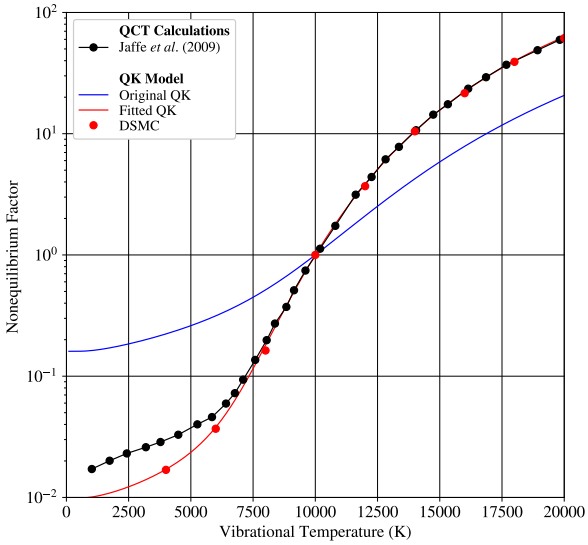

(b) $T_{t,r}$ = 10,000 K.

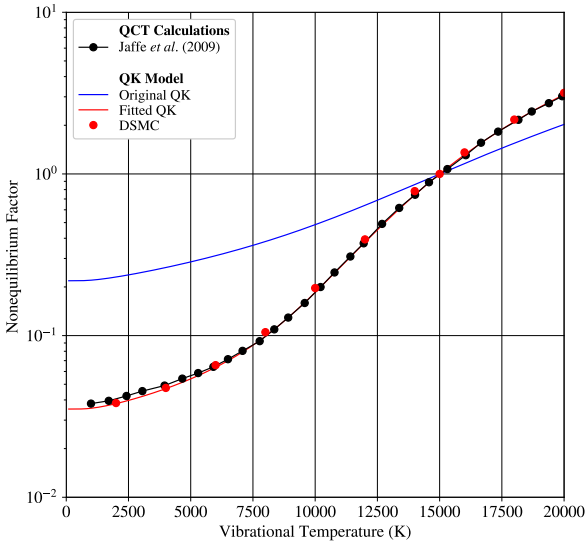

(c) $T_{t,r}$ = 15,000 K.

Figure 6.12: Thermal non-equilibrium factor for $N_2 + N \longrightarrow N + N + N$.

6.3.2 Exchange Reactions

The thermal non-equilibrium study follows with an investigation of the endothermic Zeldovich reaction, Reaction 7 (forward). This reaction is evaluated for the condition prescribed by Luo *et al*. [98], i.e. three trans-rotational temperatures, 5000 K, 10,000 K, and 15,000 K, and for vibrational temperatures ranging from 4000 K to 20,000 K. Considering that there exists no analytical expression of the QK models for the exchange reactions in thermal non-equilibrium, the present comparison is solely based on the DSMC reaction rates. The original QK model is tuned with the set of parameters suggested by Scanlon *et al*. [133] and the extended QK model with a set of parameters a and b previously introduced, see Tab. 6.2. The DSMC results are compared against a compilation of QCT calculations (Bose and Candler [113] and Luo *et al*. [98]) and chemistry models (α model [119] and Macheret [119]). Both chemistry models have tunable parameters whose values are those suggested in Losev et al. [119]. Specifically, for the α model, the tunable parameter is equated to 0.51 and for Macheret's model, the tunable parameter is equated to 0.25. An extensive presentation of the two chemistry models can be found in Losev et al. [119].

Figure 6.13 present a comparison between the DSMC reaction rates and the selection of past studies. The ordinate refers to the thermal non-equilibrium factor, the vibrational temperature, the blue markers refer to the HO model, and the red marker refers to the aHO model. As in the previous sections, chemistry models are denoted by black lines and QCT calculations are denoted by black solid-marker lines. The uncertainty of the QCT calculations reported by Luo *et al*. [98] is included for reference.

Figure 6.13 shows that the extended QK models present a good reproduction of the QCT calculations and chemistry models for typical post-shock flow conditions ($T_t > T_v$) whereas for typical nozzle flow conditions ($T_t < T_v$), the extended QK models exhibit a less favourable agreement with the QCT calculations. Interestingly, the original QK model presents a marginally better reproduction of Luo *et al*. [98] calculations compared to the extended QK models for all regimes. These results contrast with the studies of the Zeldovich exchange reactions in thermal equilibrium conditions where the tunable parameters for the endothermic reactions have been set to closely reproduce the most recent experimental measurements [80] for temperatures up to 7000 K. Once again, it is important to emphasise that QCT calculations incorporate real gas effects which, for consistency with the formulation of the QK models, have been disregarded for the determination of the parameters a and b, see Eq. (6.16). While this chapter presents a major improvement to the original QK models, it is evident that further efforts should be devoted to incorporating such effects into its core formulations. Additionally, it is important to emphasise that there exist very few studies involving QCT calculations of exchange reactions in thermal non-equilibrium to differentiate between the two models.

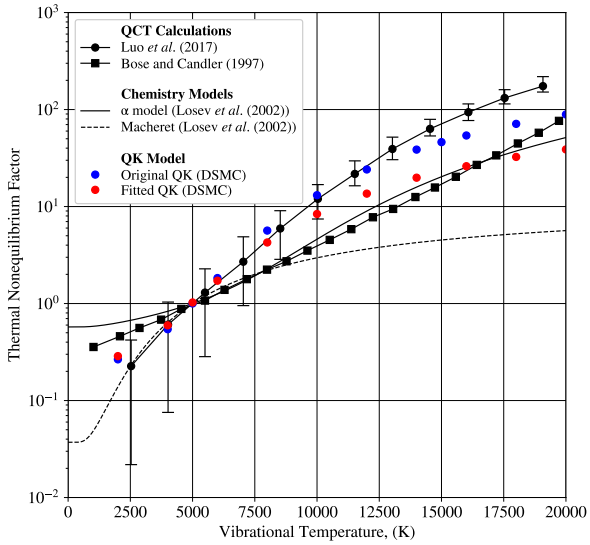

(a) $T_{t,r}$ = 5000 K.

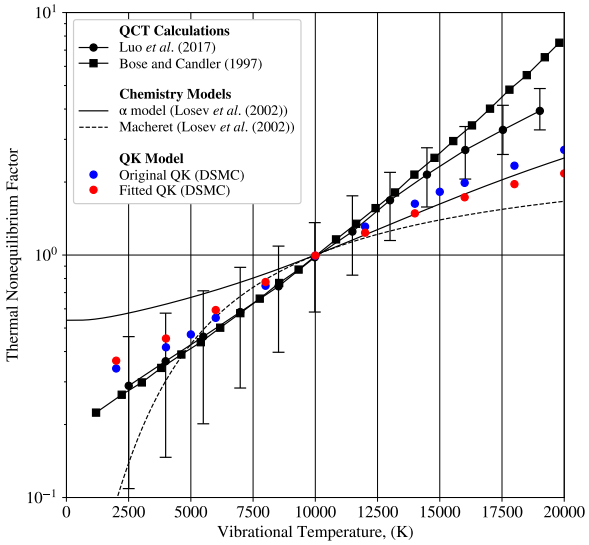

(b) $T_{t,r}$ = 10,000 K.

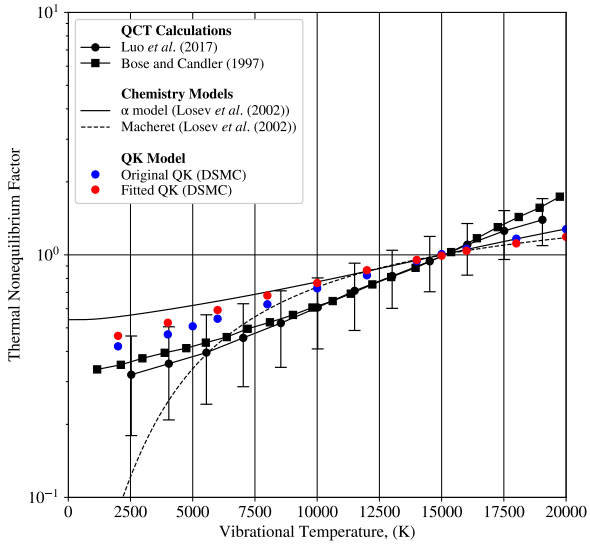

(c) $T_{t,r}$ = 15,000 K.

Figure 6.13: Thermal non-equilibrium factor for $N_2 + O \longrightarrow NO + N$.

6.4 Space Shuttle Forebody at 92.35 km

The validation of chemistry models for typical hypersonic flow conditions remains a challenging task due to the limited availability of experimental data and theoretical calculations. Gimelshein and Wysong [211] have shown an inconclusive comparison between the bias model fitted on QCT calculations and experimental measurements of the surface properties of a double-cone geometry and low sensitivity to the choice of the chemistry models for the comparison to experimental measurements of internal temperatures of the flow downstream of a reactive normal shock flow. Considering the difficulties in reproducing typical hypersonic flow conditions at ground level, the choice has been made to validate the extended QK-aHO model on in-flight measurements. Specifically, this section attempts to reproduce in-flight measure-

ments of the surface heat flux experienced by the Space Shuttle Columbia during its second mission [52, 212, 213] at an altitude of about 92.35 km.

The freestream conditions are extracted from Moss and Bird [212] and summarised in Tab. 6.4. Note that for reentry speeds in excess of 7.5 km/s, the effect of ionisation reactions and radiative heat transfer on the flow, e.g. Stardust reentry [214], cannot be neglected. For this flight altitude, ionisation reactions, charged species and electronic excited states can reasonably be omitted. Therefore, the air mixture is modelled with the five most dominant species in the air, i.e. N_2, O_2, NO, N and O and the chemical activity is constituted of a total of 19 chemical reactions, i.e. 15 dissociation reactions and 4 exchange reactions. The extended QK-aHO models are tuned with the parameters summarised in Tabs. 6.1 and 6.2. In contrast, original QK model is tuned with parameters a and b reported by Scanlon *et al*. [133], see Tab. 6.2, for the exchange reactions.

Table 6.4: Freestream conditions of the space transport system's second mission at an altitude of 92.35 km.

Parameter	Values
Altitude (km)	92.35
Temperature (K)	188
Number density (kg.m^{-3})	2.184×10^{-6}
Speed (km.s^{-1})	7.50
O_2 mole fraction (%)	0.217
N_2 mole fraction (%)	0.783
Ma_∞	27.89
Kn_∞	0.028

The geometry follows the equivalent axisymmetric body concept presented by Moss and Bird [212] to model the windward centerline of the Space Shuttle at a given angle of attack with an appropriate axisymmetric geometry at zero angle of attack. The geometry is a 5°-wedge slice of the equivalent axisymmetric body constructed with a hyperboloid with radius, $R_N = 1.296$ m and asymptotic body half angle $\theta = 41.15°$. The equation of the hyperboloid body is reported by Adams *et al*. [215] to accurately reproduce the original geometry of the Shuttle.

The computational domain extends to a length of 75 cm upstream of the stagnation point. The mesh is refined near the stagnation point to ensure the cell size, Δx, remains smaller than the local mean free path, λ, resulting in a total number of 117,945 cells. The time step is carefully chosen to be an order of magnitude smaller than the mean collision time and the cell residence time which results in $\Delta t = 1 \times 10^{-7}$ s. Inter-molecular collisions are computed with the VHS model [17] for a reference temperature of $T_{ref} = 273$ K. A finite probability of $P_r = 0.2$ and $P_v = 0.02$ are, respectively, considered for rotational and vibrational relaxation, as suggested by Bird [17]. The gas-surface interactions are partially diffusive with a wall temperature $T_w = 1043$ K and an accommodation coefficient of 0.8. The numerical mesh is populated with a total number of 1.59×10^7 DSMC simulator particles at steady state.

The comparison of the extended QK-aHO models and the original QK models are depicted in Fig. 6.14 for the mean internal temperatures and the concentration of the chemical species along the stagnation streamline. Note that the species densities are normalised by the local total number density at steady state. The extended QK-aHO models are denoted by dashed lines and the original QK models by solid lines. The flow properties along the stagnation streamline reported by Carlson and Bird [52] with a modified TCE model are included for reference and denoted with colour symbols.

Figure 6.14 shows that the extended QK models suggest a slower chemical activity compared to the original QK models. Specifically, it suggests a slower depletion of molecular species and a slower production of atomic species. Note that these results concur with the conclusion stated in the preceding sections. Furthermore, the extended QK models suggest higher mean internal temperatures compared to the original QK models which highlights the difference in the modelling of the chemical reactions.

Additionally, the two QK models suggest a larger shock stand-off distance in comparison to the TCE results reported by Carlson and Bird [52]. Carlson and Bird [52][Tab. I] have reported the use of species-specific vibrational relaxation numbers, which relies on the colliding partner, macroscopic temperature and two fitting parameters. In DSMC, it is good practice to avoid the use of macroscopic temperatures and instead rely solely on microscopic information. Consequently, a decision was made to adopt a constant vibrational relaxation number for all chemical species. This discrepancy in the modelling of vibrational relaxation significantly impacts both the shock stand-off distance and the variation in chemical activity.

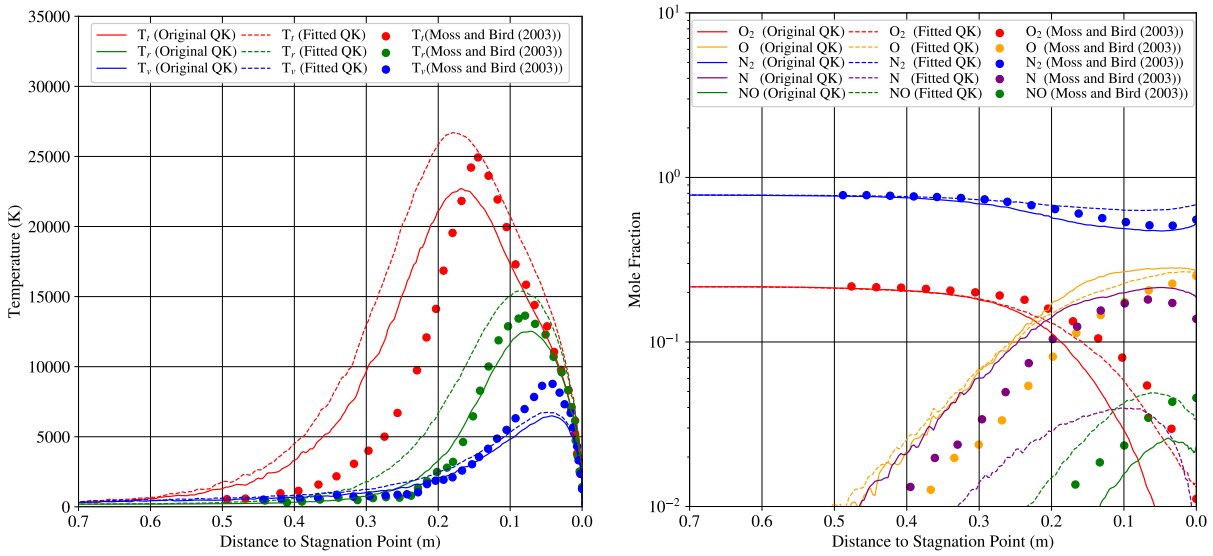

(a) Internal temperatures.

(b) Species concentrations.

Figure 6.14: Comparison of the QK models for the flow properties along the stagnation streamline.

Figure 6.15 repeats the comparison of the two QK models on the flow field for the mean trans-

lational and vibrational temperatures and the fraction of O_2, N_2, O and N. The two QK models readily differ for all six flow fields showing strong deviations in the shock thickness, stand-off distance and species concentration throughout the shock. Additionally, the extended QK models demonstrate a significantly non-equilibrium region downstream of the shock compared to its counterpart. This region is characterised by warm translational and vibrationally cold molecules which correspond to the left-hand side of Figs. 6.7-6.13. While the two models have shown minimal differences in the exchange reactions in such conditions, see Fig. 6.13, for the dissociation reactions in similar conditions, the two QK models have shown large differences, see Figs. 6.7-6.12. Consequently, the differences observed in the species fraction in Fig. 6.15 are merely the result of the dissociation reactions occurring downstream of the shock. Specifically, the extended QK models exhibit a slower depletion of molecular species and a slower production of atomic species compared to its counterpart.

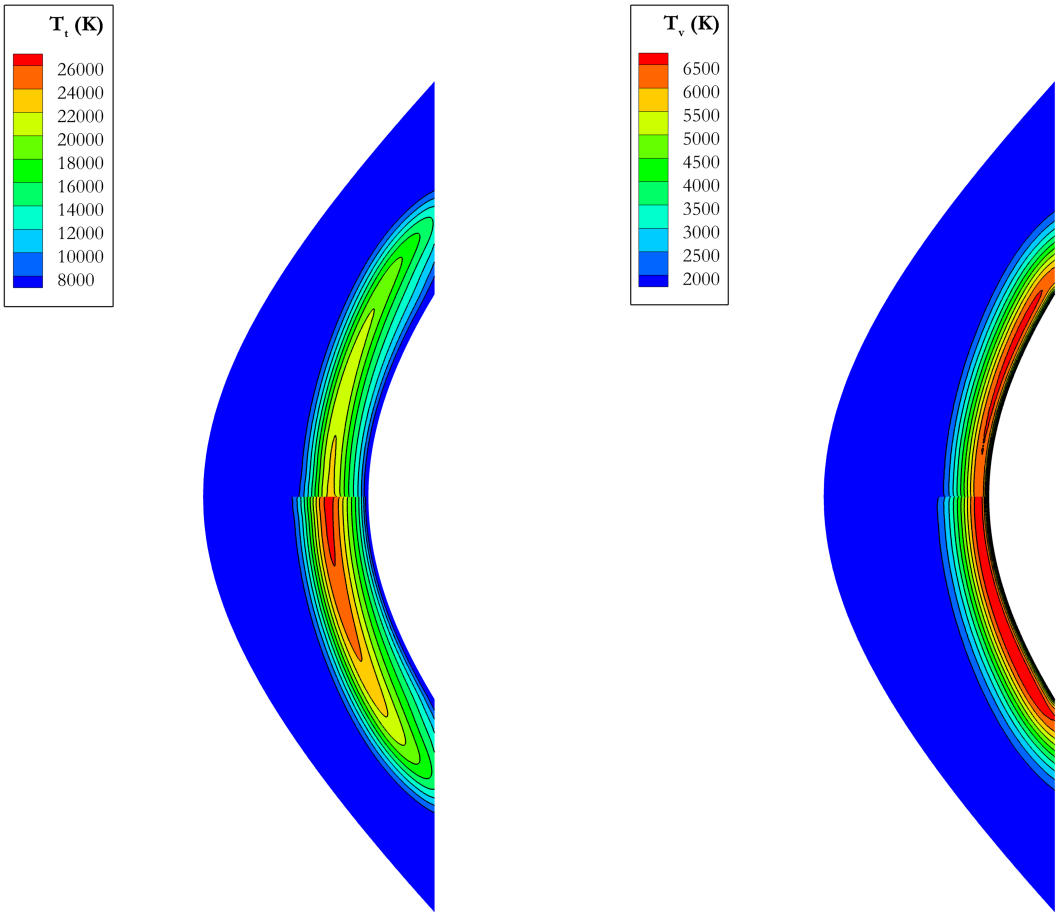

(a) Mean translational temperature.

(b) Mean vibrational temperature.

Figure 6.15: Flow field over the STS-II geometry at an altitude of about 92.35 km with the original QK (top) and extended QK (bottom) models.

Figure 6.16 compares the predictions of the original QK models and extended QK-aHO models against the surface heat flux in-flight measurements during the STS-II mission. The surface properties are plotted on the ordinate axis and the abscissa shows the azimuthal angle. The

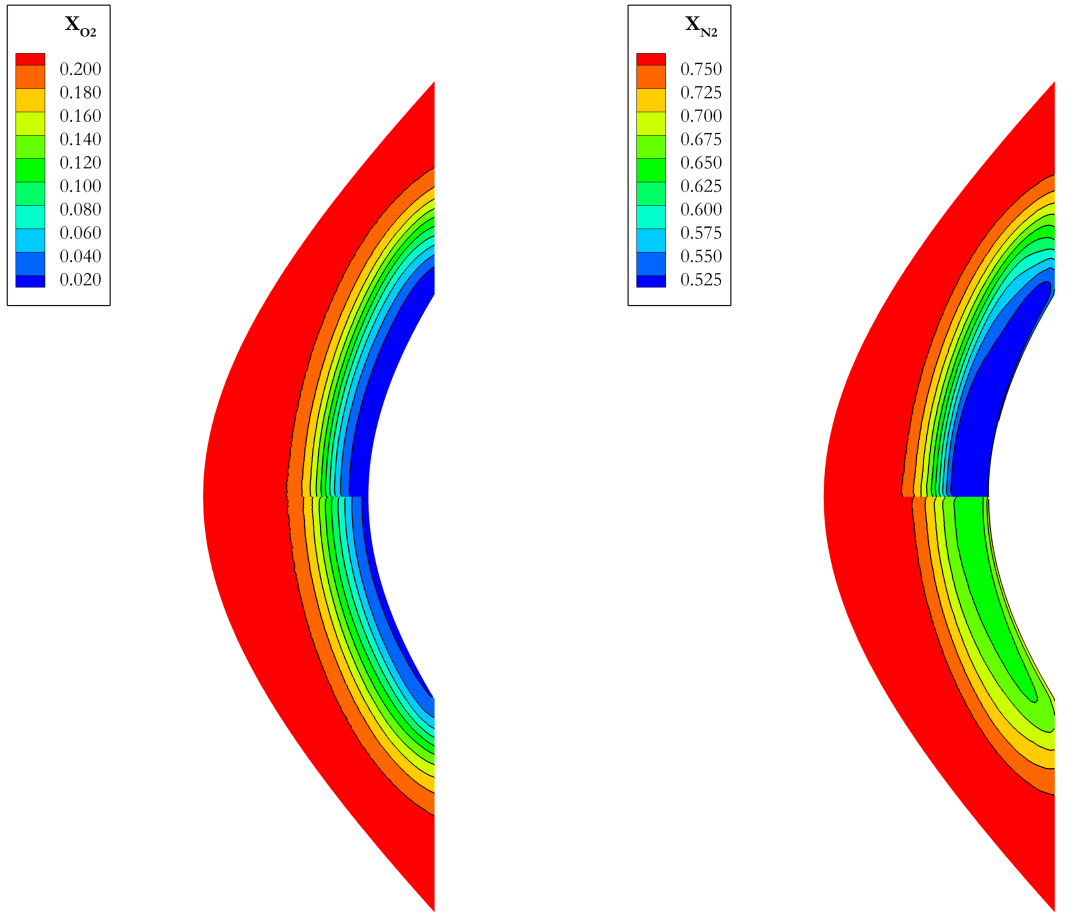

(c) Molecular oxygen fraction.

(d) Molecular nitrogen fraction.

Figure 6.15: Flow field over the STS-II geometry at an altitude of about 92.35 km with the original QK (top) and extended QK (bottom) models. (Cont.)

surface heat flux reported by Moss and Bird [212] with the TCE model is included for reference. The surface heat flux was measured to be approximately 6.3×10^4 J.m^{-2} at an axial distance of about 22 cm downstream of the stagnation point. For the STS-I mission, the uncertainties in-flight measurements of the surface heat flux have been assessed to be about 10% for surface temperatures in excess of 811 K [216]. For the STS-II mission, no uncertainties have been reported for the surface heat flux. However, Zoby [217] has reported the use of similar error bands to the STS-I mission for the surface heat flux measurements of the STS-II mission for altitudes comprised between 86.0 and 43.0 km. Despite the absence of uncertainty information in the reports by Moss and Bird [212] and Carlson and Bird [52], an error of 10% is herein considered for the in-flight measurements, even though altitude differs from that reported by Zoby [217].

Figure 6.16 shows that the extended QK-aHO models predict higher surface heat flux compared to the original QK models. At the location of the in-flight measurement, the extended QK-aHO models predict a surface heat flux of about 7.97×10^4 J.m^{-2} which represents an over-estimation of about 26.5 % of the in-flight measurements. The primary explanation for this increase has

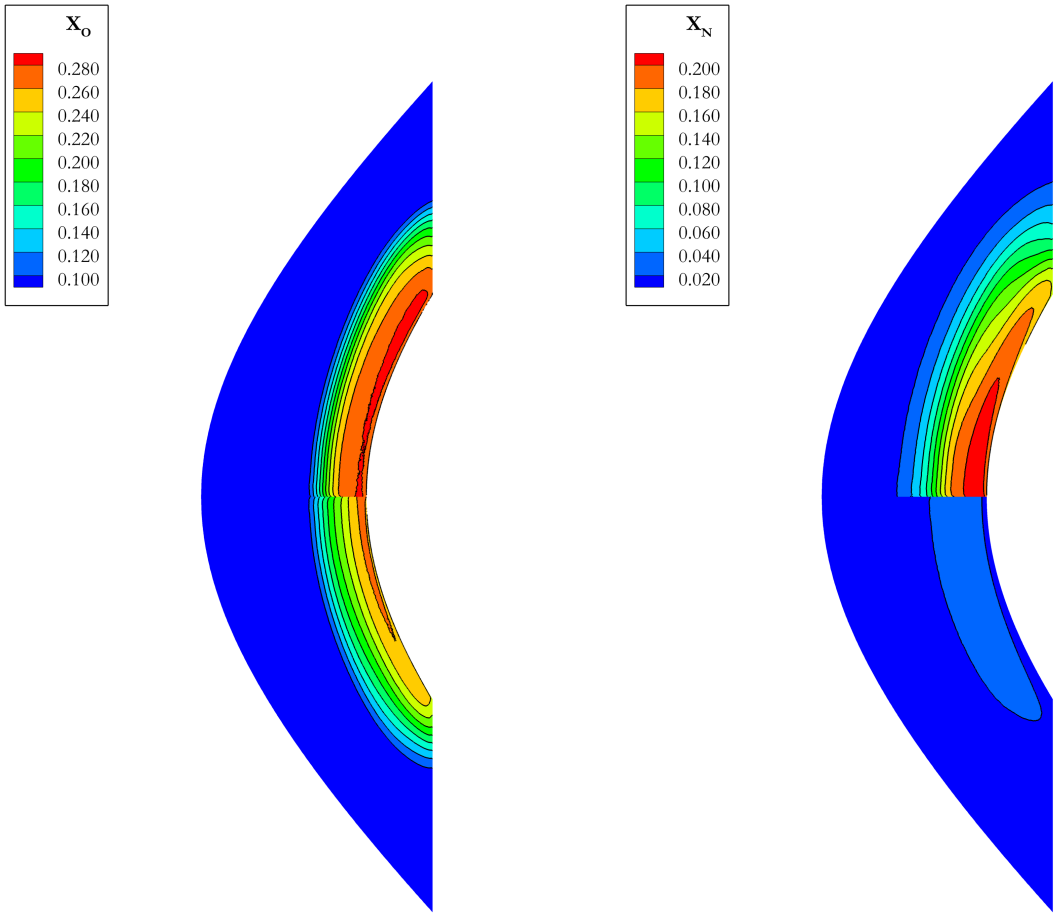

(e) Atomic oxygen fraction.

(f) Atomic nitrogen fraction.

Figure 6.15: Flow field over the STS-II geometry at an altitude of about 92.35 km with the original QK (top) and extended QK (bottom) models. (Cont.)

been stressed throughout this chapter. The extended QK-aHO models suggest slower dissociation reaction rates in comparison to the original QK models, see Figs. 6.1-6.3 and Figs. 6.7-6.8. This results in a displacement of the stand-off distance and a substantial increase in the mean translational temperature of the gas mixture, see Fig. 6.14, which imposes an increase in the surface heat flux. Note that this behaviour is not unique to the extended QK models as similar behaviour has also been reported by Carlson and Bird [52] for the validation of a new version of the TCE model, where their updated chemical reaction framework also significantly increased the heat flux. They noted that reducing the surface accommodation coefficient will reduce the heat flux.

For the extended QK models to lie in the bounds of the in-flight measurements, it would require an unrealistic accommodation coefficient and/or vibrational relaxation constant. Note that similar conclusions can be drawn from reconstruction of post-flight measurements of the heat flux of the the Intermediate eXperimental Vehicle during the rarefied portion of its reentry [197].

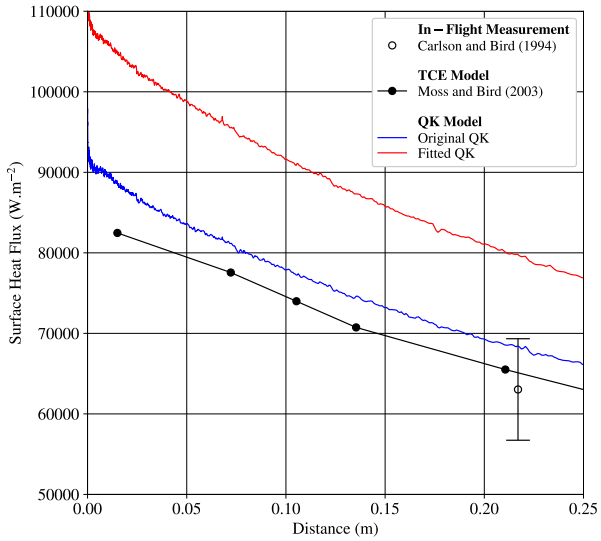

Figure 6.16: Comparison of the QK models for the surface heat flux.

6.5 Summary

Significant progress in high-temperature non-equilibrium flow research has been achieved over the last two decades through experimental, theoretical and computational studies to provide high-fidelity data allowing for model development, parameter adjustment and model validation. In the present chapter, an extension of the quantum-kinetic chemistry models under the assumption of an anharmonic oscillator model was developed. The merits of the extended QK models are investigated for the most representation of chemical reactions in an Earth atmospheric reentry involving a total of 19 chemical reactions, i.e. 15 dissociation reactions and 4 Zeldovich exchange reactions. The new formulations of the extended QK models involve a set of tunable parameters to closely reproduce experimental measurements and/or high-fidelity calculations. The extended QK models are extensively validated against a selection of experimental measurements, QCT calculations and DMS simulations for both thermal equilibrium and non-equilibrium conditions. Additionally, the extended QK models are validated against in-flight measurements of the STS-II mission.

In thermal equilibrium conditions, the tunable parameters for the dissociation reaction rates are determined by means of a non-linear least square fit on the baseline database. For the Zeldovich reactions, a similar technique is adopted to propose a new set of tunable parameters to reproduce the most representative experimental measurements. The DSMC reaction rates are in excellent agreement with the new formulation of the extended QK models, demonstrating the successful implementation of the new QK models in *dsmcFoam+*. Furthermore, the DSMC results are compared against an extensive selection of chemistry models in the form of the modified-Arrhenius rates, high-fidelity calculations and experimental measurements. For most of the dissociation reactions, the extended QK models present a significant improvement of the reproduction of the compilation of past studies. However, for some chemical reactions, e.g. $N_2 + N_2$

and N_2 + N, experimental measurements experimental measurements exhibit substantial scatter, spanning several orders of magnitude, making it difficult to distinguish between different chemistry models. Therefore, new experimental measurements of these chemical reactions with reduced uncertainties is required to differentiate between models. For the dissociation reactions, the extended QK models suggest a slower depletion of molecular species in comparison with the original QK models for all dissociation reactions with the exception of NO + NO. For the exchange reactions, the extended QK models suggest faster exchange reaction rates for Reaction 7 and slower exchange reaction rates for Reaction 8 in comparison to the original QK models.

In thermal equilibrium conditions, the DSMC results are in excellent agreement with the corresponding analytical solution, again demonstrating the successful implementation of the new formulations. For the dissociation reactions, the extended QK models indicate an excellent reproduction of experimental measurements, QCT calculations and DMS calculations for both typical post-shock flow conditions, i.e. $T_t > T_v$ and for typical nozzle flow conditions, i.e. $T_t < T_v$. Note that this constitutes a significant improvement to the original QK models which show reproductions of QCT calculations only for $T_t < T_v$ conditions. Additionally, the extended QK models show very good agreement with the α model for the two Zeldovich endothermic reactions, especially at low vibrational temperatures.

The extended QK models are validated for the reproduction of the in-flight measurements of surface heat flux during the STS-II mission. The study shows that the extended QK models suggest a slower depletion of molecular species which, in turn, imposes higher mean internal temperatures. Consequently, this leads to the extended QK models predicting higher surface heat flux in comparison to the original QK model. The extended QK models lie above the bounds of the in-flight measurements. In-flight measurements may be reproduced with the extended QK models with the use of unrealistic accommodation coefficients and vibrational relaxation numbers.

Chapter 7

Electronic Excited States Modelling *

Previous chapters of this thesis have considered the vibrational and electronic modes to be uncoupled, as is common in DSMC codes, however, Chapters 1, 5, 6 and Appendix A have evidenced that they are in reality coupled. This chapter presents a new mathematical model for coupling the electronic and vibrational modes of molecular species in DSMC. The model involves the development of new numerical techniques for the initialisation of particles in the domain, the redistribution of the internal energy after a collision and the measurement of the corresponding internal temperature. Firstly, the new model is verified against an extensive compilation of theoretical studies and compared against the uncoupled approach utilised in previous chapters for the reproduction of thermodynamic properties of molecular oxygen. Then, the model is applied to a typical hypersonic flow condition in Earth's atmosphere past an infinite cylindrical body at an altitude of 85 km.

7.1 Theoretical Background

The new model assumes a coupling between the vibrational and electronic modes which carries significant implications. Specifically, each electronic excited state has a unique set of vibrational levels described by

$$\varepsilon_{ve} = hc\kappa_{e,i} + hc\omega_{e,i}\left(j+\frac{1}{2}\right) - hc\omega_{e,i}\chi_{e,n}\left(j+\frac{1}{2}\right)^2, \tag{7.1}$$

where $\kappa_{e,i}$, $\omega_{e,i}$ and $\omega_{e,i}\chi_{e,i}$ are the spectroscopic constant of electronic states i and j is the vibrational quantum level. Note that throughout this chapter, indexes i and j will refer to the electronic and vibrational modes, respectively.

Considering an electronic state i, the maximum vibrational quantum level permissible is de-

*A large portion of the work presented in this Chapter is published in **C. H. B. Civrais**, M. Pfeiffer, C. White and R. Steijl. Modelling of the electronic excited states in direct simulation Monte Carlo, *Physics of Fluids*, 36(8):086112, 2024. doi: 10.1063/5.0215853.

termined as the vibrational quantum immediately before the dissociation energy of electronic state i, i.e. $\varepsilon_{ve}(i) < \varepsilon_d(i)$. For some electronic configurations, all the vibrational quantum levels lie below the corresponding dissociation energy. In this specific scenario, the maximum vibrational quantum level is determined as the last vibrational quantum level before the gradient $\frac{\partial \varepsilon_{ve(i)}}{\partial j}$ changes sign.

Since the electronic excited states allow for vibrational excitation, the corresponding distribution function consists of a coupled Boltzmann distribution such that,

$$f(\varepsilon_{i,j}) = \frac{N_{i,j}}{N} = \frac{g_i e^{-\varepsilon_{i,j}\beta}}{\sum_{i}^{i_{max}} \sum_{j}^{j_{max}(i)} g_i e^{-\varepsilon_{i,j}\beta}} = \frac{g_i e^{-\varepsilon_{i,j}\beta}}{Q}. \tag{7.2}$$

Additionally, adjusting the distribution function of the internal quantum numbers has implications for the thermodynamic properties. As shown in Eq. (7.2), the partition function becomes,

$$Q_{ve} = \sum_{i}^{i_{max}} \sum_{j}^{j_{max}} g_i e^{-\frac{\varepsilon_{i,j}}{kT}}. \tag{7.3}$$

with the mean internal energy formulated as,

$$e_{ve} = -\frac{\partial(lnQ)}{\partial\beta} = \frac{\sum_{i}^{i_{max}} \sum_{j}^{j_{max}} g_i \varepsilon_{i,j} e^{-\frac{\varepsilon_{i,j}}{kT}}}{\sum_{i}^{i_{max}} \sum_{j}^{j_{max}} g_i e^{-\frac{\varepsilon_{i,j}}{kT}}}. \tag{7.4}$$

and the isochoric specific heat capacity,

$$c_V = c_{V,t} + c_{V,r} + \frac{R}{k}\frac{\partial e_{ve}}{\partial T}. \tag{7.5}$$

As illustrated by Eqs. (4.16) and (7.2), the new model yields distinct distribution functions to the uncoupled approach presented in Chapters 3 and 4 for the vibrational and electronic modes. The uncoupled approach uses a single one-dimensional distribution function for each mode whereas the coupled approach introduces a two-dimensional distribution function that accounts for the coupling between the vibrational and electronic modes. This fundamental difference between the two approaches leads to significant consequences. Specifically, in the new coupled approach, a unique partition function, mean internal energy and specific heat capacity can be defined. From a numerical perspective, it imposes the definition of a unique mean internal temperature, i.e. T_{ve}. This contrasts with the traditional uncoupled approach which requires separate internal temperatures for each mode, i.e. T_v and T_e.

7.2 Electronic Excited States Modelling in DSMC

As highlighted in the previous section, the coupled approach has a two-dimensional distribution function which requires sampling of both the electronic and the vibrational quantum numbers simultaneously. The coupled approach is implemented in *dsmcFoam+* based on the procedure reported by Liechty and Lewis [141]. Three procedures are revisited to accommodate the vibrational excitation of the electronic excited states. These functions are the equilibrium sampling, the post-collision sampling, and the measurement of the corresponding mean temperature.

7.2.1 Equilibrium Sampling

To initially populate the numerical mesh, each particle is assigned a set of properties, including its quantum numbers. The distribution of these quantum numbers follows the Boltzmann distribution, Eq. (7.2). However, a set of quantum numbers, i.e. (i, j), cannot be directly sampled from Eq. (7.2), hence, an acceptance-rejection scheme is employed. This scheme involves selecting a pair of quantum numbers from the normalised distribution,

$$f' = \frac{f(\varepsilon_{i^\star,j^\star})}{f_{max}} = \frac{g_{i^\star} e^{-\frac{\varepsilon_{i^\star,j^\star}}{kT}}}{g_{i_s} e^{-\frac{\varepsilon_{i_s,j_s}}{kT}}}, \tag{7.6}$$

where (i_s, j_s) are the electronic and vibrational quantum numbers, respectively, for which Eq. (7.2) has a maximum. Note that the degeneracy differs from one electronic excited state to another, see Tab. 7.1. As a result, the maximum of Eq. (7.2) cannot be determined beforehand but must be searched for in each iteration.

Figure 7.1 illustrates the general procedure to assign the initial electronic and vibrational quantum numbers. The first step consists of searching for the electronic and vibrational quantum numbers, i.e. (i_s, j_s), for which Eq. (7.2) has a maximum. Then, a pair of electronic and vibrational quantum numbers, i.e. $(i^\star, j^\star)$, uniformly distributed between 0 and $i_{max} - 1$ and 0 and $j_{max} - 1$, respectively, are independently chosen randomly. Finally, an acceptance-rejection scheme is used to select a pair of electronic and vibrational quantum numbers, i.e. $(i^\star, j^\star)$, from the distribution, Eq. (7.6), that satisfies $f' > \mathcal{R}(0,1)$.

7.2.2 Post-Collision Sampling

In the DSMC method [17], the internal energies are commonly redistributed through a serial application of the quantum LB method [150]. The LB method samples the post-collision quantum numbers, i.e. i and j, from a combined distribution of the translational and the electronic-vibrational mode of the colliding particle. The translational distribution function inherently depends on the inter-molecular model employed as it defines the collision probability. The base

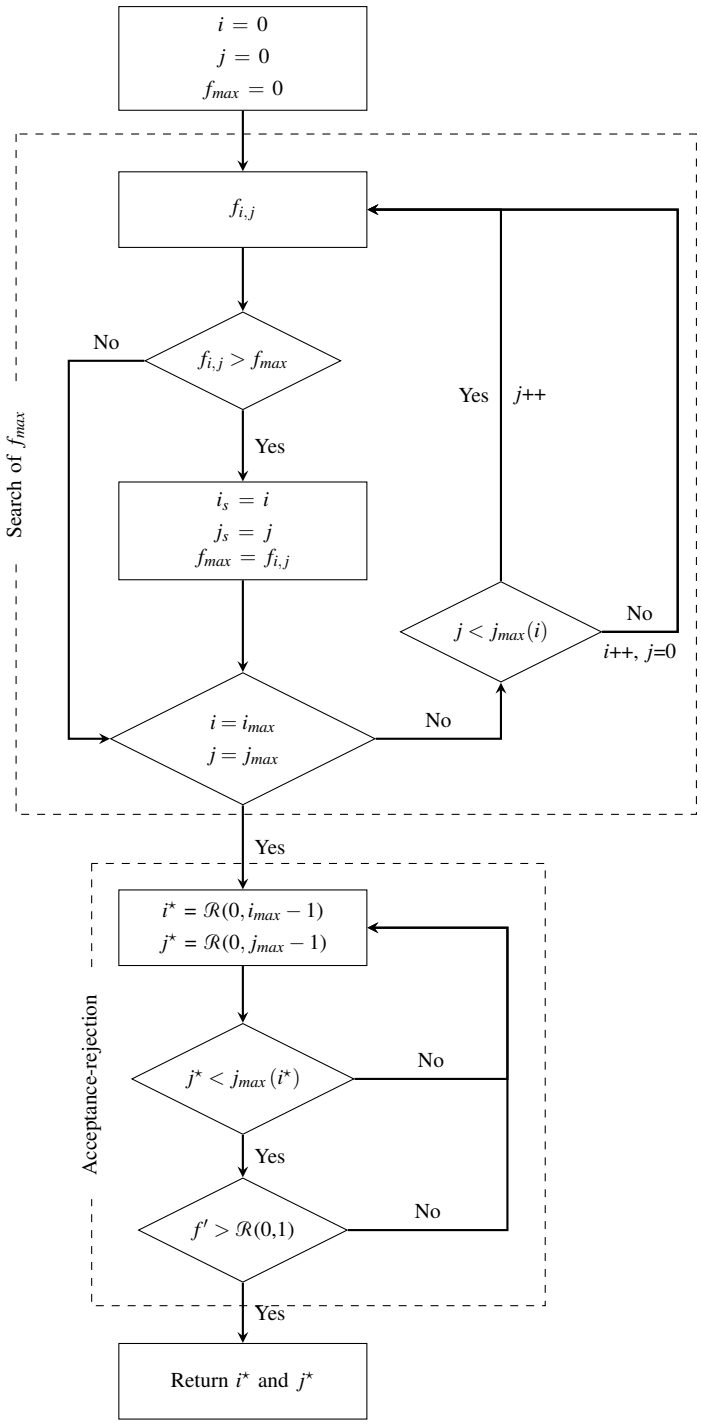

Figure 7.1: Flowchart of the equilibrium sampling function implemented in *dsmcFoam+*.

collision scheme is the VHS collision model developed by Bird [17]. For the VHS model, the probability distribution of translational energy during a collision is given by Eq. (3.17). Following the approach of Bergemann and Boyd [150], a Dirac delta function is applied to the

Boltzmann distribution, Eq. (7.2), to define the following continuous distribution function,

$$f(\varepsilon_{i,j}) = \frac{g_i e^{-\frac{\varepsilon_{i,j}}{kT}}}{\sum_i \sum_j g_i e^{-\frac{\varepsilon_{i,j}}{kT}}} \delta\left(\varepsilon_{ve} - \varepsilon_{i,j}\right). \tag{7.7}$$

Using Eqs. (7.7) and (3.17), the combined distribution for sampling post-collision quantum vibrational and electronic levels from the collision energy, $\varepsilon_c = \varepsilon_t + \varepsilon_{i,j} = \varepsilon_{t^\star} + \varepsilon_{i^\star,j^\star}$, is,

$$f(\varepsilon_c, \varepsilon_{i,j}) = \frac{g_i}{\Gamma(\frac{5}{2} - \omega) \sum_i \sum_j g_i e^{-\frac{\varepsilon_{i,j}}{kT}}} \left(\frac{\varepsilon_c - \varepsilon_{i,j}}{kT}\right)^{\frac{3}{2}-\omega} e^{-\frac{\varepsilon_c}{kT}}. \tag{7.8}$$

The LB scheme assumes that local thermodynamic equilibrium prevails and the collision energy remains constant across the redistribution process. Under these assumptions, the sampling of the post-collision quantum numbers can therefore be performed on a simplified distribution, i.e.

$$f(\varepsilon_c, \varepsilon_{i,j}) \propto g_i \left(\varepsilon_c - \varepsilon_{i,j}\right)^{\frac{3}{2}-\omega} \tag{7.9}$$

For similar reasons to that of the equilibrium sampling, an acceptance-rejection scheme is applied. The normalisation of the distribution is similarly obtained by searching for the pair of quantum numbers for which Eq. (7.9) has a maximum. The acceptance-rejection scheme is, therefore conducted on,

$$f' = \frac{f(\varepsilon_c, \varepsilon_{i^\star,j^\star})}{f_{max}} = \frac{g_{i^\star}\left(\varepsilon_c - \varepsilon_{i^\star,j^\star}\right)^{\frac{3}{2}-\omega}}{g_{i_s}\left(\varepsilon_c - \varepsilon_{i_s,j_s}\right)^{\frac{3}{2}-\omega}}. \tag{7.10}$$

Figure 7.2 presents the general procedure for assigning post-collision quantum numbers within the *dsmcFoam+* framework. Two inelastic mechanisms are distinguished depending on whether the particle experiences a vibrational excitation/de-excitation, Reaction 9,

$$\mathrm{AB(i,j) + M \longrightarrow AB(i,j') + M,} \tag{Reaction 9}$$

or electronic and vibrational excitation/de-excitation, Reaction 10,

$$\mathrm{AB(i,j) + M \longrightarrow AB(i',j') + M.} \tag{Reaction 10}$$

In Reaction 9, the energy exchange occurs from a change in the vibrational quantum number. In Reaction 10, the energy exchange involves an electronic transition, see Tab. 7.1, which, in turn, also necessitates a modification of the vibrational quantum number.

Typically, in DSMC simulations, a relaxation probability of $P_v = 0.02$ is allowed to result in vibrational excitation/de-excitation while a relaxation probability of $P_e = 0.002$ is allowed for

electronic energy exchange [151]. For the coupled approach to reproduce the two separate redistributions of internal energy in the uncoupled approach, two relaxation mechanisms, Reaction 9 and Reaction 10, are implemented in *dsmcFoam+*. Each mechanism operates with a relaxation probability, namely P_1 for Reaction 9 and P_2 for Reaction 10. Note that the relaxation probability P_2 is a conditional probability on P_1 to be true, see Fig. 7.2. Therefore, to reproduce the two separate redistributions of internal energy, P_1 must be set to 0.02 and P_2 to 0.1. Note that these relaxation probabilities are user-defined; hence, they can be modified to reproduce any baseline relaxation model.

The energy exchange involving vibrational energy, i.e. Reaction 9, follows the quantum LB approach. A detailed explanation for the vibrational excitation/de-excitation during an inelastic collision under the assumption of an anharmonic oscillator model can be found in Civrais *et al*. [31]. For brevity, the present section focuses on the redistribution of internal energy involving electronic and vibrational excitation/de-excitation.

If an inelastic collision is accepted for Reaction 10 energy exchange, the first step is to search the maximum allowed vibrational quantum number for each electronic excited state, i.e. (i_s, j_s), that satisfies $\varepsilon_c < \varepsilon_{i_s,j_s}$ and to determine a pair of quantum numbers for which the distribution function, Eq. (7.10), is maximum. Then, an acceptance-rejection procedure is performed to sample $(i^\star, j^\star)$ from the distribution, Eq. (7.10). Finally, a pair $(i^\star, j^\star)$ is accepted if Eq. (7.10) satisfies $f' > \mathcal{R}$; otherwise, the procedure is repeated until values for $(i^\star, j^\star)$ are obtained.

7.2.3 Vibronic Temperature

Finally, a point should be made about the calculation of the vibronic temperature. In the uncoupled approach, the vibrational and electronic modes, i.e. T_v and T_e, are treated separately leading to the one mean temperature for each mode. To maintain mathematical consistency with the two-dimensional distribution function, Eq. (7.2), a unique temperature, T_{ve}, must be defined for the vibronic mode. The difference between the two approaches will be assessed in the following sections.

The vibronic temperature ultimately represents a mean excitation of the vibronic mode. Since the electronic mode admits a set of vibrational levels the vibronic temperature is unable to reflect the vibrational excitation of each electronic excited state but, rather, a mean excitation of the electronic excited states and their corresponding vibrational quantum levels. Despite its minimal physical insights, the vibronic temperature serves the purpose of retaining the mean energy of a molecular system, making it valuable for verification exercise.

Furthermore, in the derivation, Eqs. (7.2)-(7.5), no assumption has been made regarding thermal equilibrium between the vibrational and electronic modes. Thus, these modes can exhibit thermal non-equilibrium with each other. These considerations contrast with the definition of T_{ve} employed in the vast majority of multi-temperature extended Navier-Stokes equations solvers based on Gnoffo *et al.* [218]; albeit, there exist high-speed and high-temperature CFD methods

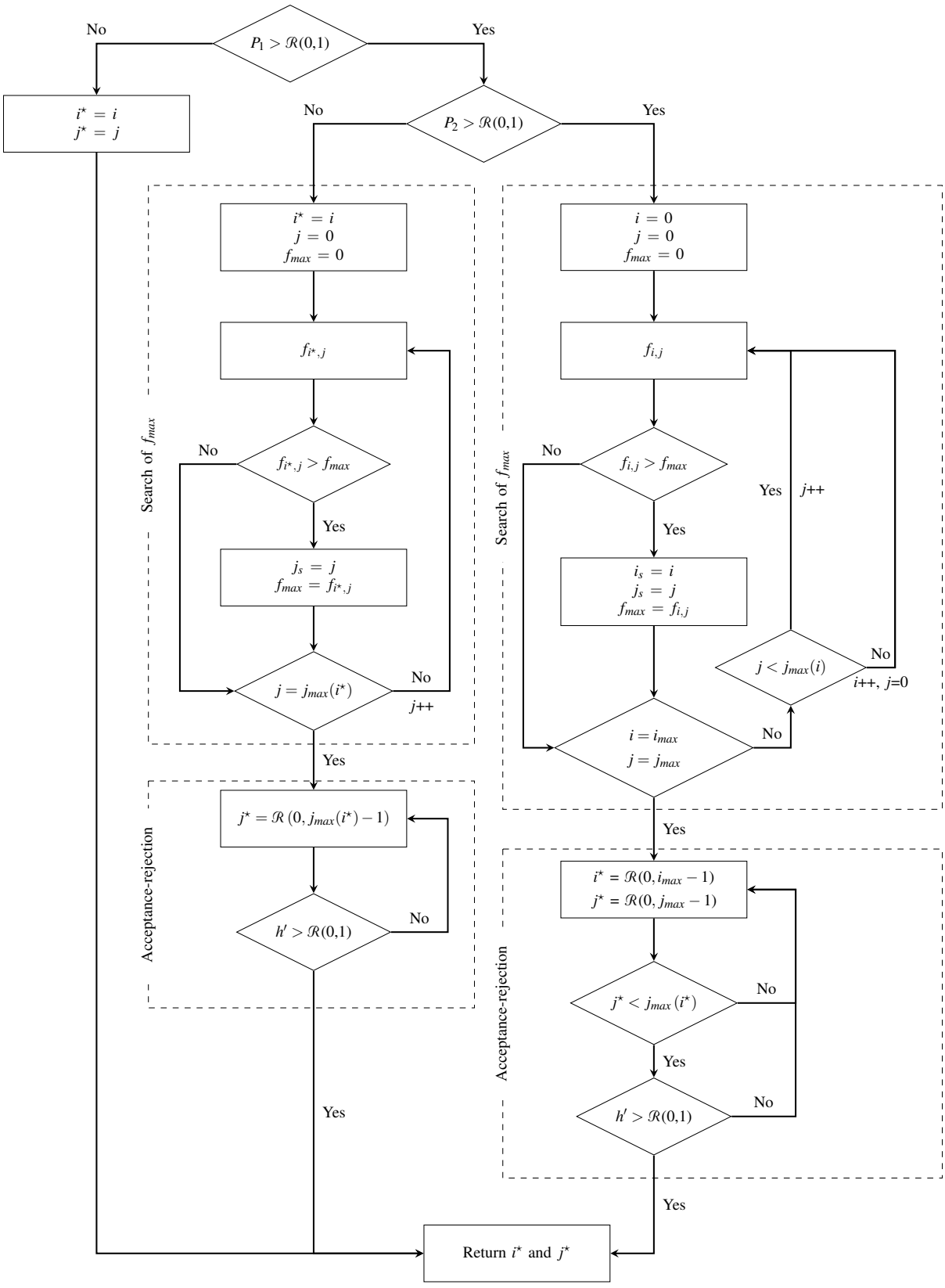

Figure 7.2: Flowchart of the post-collision sampling function implemented in *dsmcFoam+*.

which do not impose thermal equilibrium between modes [219–221].

In the uncoupled approach, where vibrational excitation is modelled with an infinite harmonic

oscillator, the mean vibrational degrees of freedom can be computed using the equipartition theorem, and the vibrational temperature is derived analytically from the mean vibrational quantum number. However, with an anharmonic oscillator model, the vibrational temperature cannot be derived analytically [31]. Specifically, it must be determined by solving an implicit equation. Similarly, to account for the vibrational excitation of the electronic excited states, the vibronic temperature cannot be directly calculated using the equipartition theorem. A similar approach to that described in Chapter 4 is herein adopted.

Consider a volume filled with chemical species s and a corresponding mean vibronic energy denoted e_s. Calculating the corresponding vibronic temperature involves resolving,

$$e_s - \frac{\sum_{i}^{i_{max}} \sum_{j}^{j_{max}(i)} g_i \varepsilon_{i,j} e^{-\frac{\varepsilon_{i,j}}{kT}}}{\sum_{i}^{i_{max}} \sum_{j}^{j_{max}(i)} g_i e^{-\frac{\varepsilon_{i,j}}{kT}}} = 0. \tag{7.11}$$

This implicit equation, Eq. (7.11), is numerically resolved with a Newton iterative approach. It involves initially evaluating Eq. (7.4) at a guessed temperature and comparing it to the mean vibronic energy in a cell. The procedure is repeated until a user-defined tolerance factor is reached.

7.3 Adiabatic Reactor Simulations

A series of adiabatic reactor simulations are conducted to verify the derivation and implementation of the coupled approach. A single cubic cell with edge length 1.88×10^{-4} m filled with one million DSMC simulator particles and periodic boundaries are used for this purpose. A fixed time step size of 1×10^{-9} s is adopted. The working gas is molecular oxygen with the electronic excited states summarized in Tab. 7.1. The inter-molecular collisions are processed with the VHS model [17] with the properties at a reference temperature T_{ref} of 273 K, see Tab. 4.3. The probabilities for a particle to experience Reaction 9 or Reaction 10 are those presented in the previous section unless stated otherwise.

The electronic excited states of molecular oxygen are those suggested by Liechty and Lewis [222]. The spectroscopy constants are extracted from the NIST database [25] with the exception of the ground state, i.e. $O_2(X^3\Sigma_g^-)$, which is extracted from Civrais *et al.* [136]. The spectroscopic constants of the electronic excited states of O_2 are summarized in Tab. 7.1. In addition, it is assumed that the electronic excited states conserve the collision properties of the ground state; hence, the mass, diameter and viscosity exponent of the electronic excited states are those of the ground state.

Table 7.1: Spectroscopy constants of the electronic excited states for molecular oxygen.

States	κ_e (eV)	g	ω_e (cm^{-1})	$\omega_e\chi_e$ (cm^{-1})	θ_v (K)	θ_r (K)	ε_d (eV)	j_{max}
$X^3\Sigma_g^-$	0.0	3	1688.17	16.43	2423.91	2.06	5.2	46
$a^1\Delta_g$	0.98	2	1483.5	12.9	2130.05	2.05	5.2	33
$b^1\Sigma_g^+$	1.63	1	1432.8	14.0	2057.25	2.01	5.2	29
$c^1\Sigma_u^-$	4.09	1	794.2	12.73	1140.33	1.31	5.2	16
$A'^3\Delta_u$	4.29	6	850.0	20.0	1220.45	1.38	5.2	13
$A^3\Sigma_u^+$	4.38	3	799.07	12.16	1147.32	1.31	5.2	10
$B^3\Sigma_u^-$	6.16	3	709.3	10.65	1018.43	1.18	7.16	15

7.3.1 Vibronic Temperature

The first verification involves the measurement of the vibronic temperature. The adiabatic reactor is initialised in thermal equilibrium conditions for temperatures ranging between 2000 and 20,000 K. The vibronic temperature is monitored and sampled for 10^5 iterations.

Table 7.2 shows that the measurement technique implemented for the calculation of the vibronic temperature is accurate across the temperature range considered. The numerical scatter of the measured temperature is inversely proportional to the square root of the sampling size [223]; hence, for a sampling size of about 10^5, the numerical scatter is about 0.3%. Table 7.2 shows that the difference between the initialised and measured temperatures reduces as expected. This demonstrates the correct implementation of both the initialisation algorithm and the new measurement technique.

Table 7.2: Comparison of the measured vibronic temperature against the initialised temperature.

Initialised Temperature (K)	Measured Temperature (K)	Error (%)
2000	1999.02	0.05
4000	4000.89	-0.02
6000	6002.21	-0.04
8000	7998.08	0.02
10 000	10 005.26	-0.05
12 000	12 003.56	-0.03
14 000	14 002.66	-0.02
16 000	16 001.78	-0.01
18 000	18 008.9	-0.05
20 000	20 003.35	-0.02

7.3.2 Adiabatic Relaxation

The next verification case assesses the capabilities of the model to reproduce the theoretical thermal equilibrium of a system initially in a state of thermal non-equilibrium. Two scenarios

are herein considered. The adiabatic reactor is initialised with a vibronic temperature greater or lower than the translational and rotational temperatures such that excitation or de-excitation of the electronic excited states and their vibrational quantum levels occurs as a result of the relaxation process. The two scenarios are of major interest in hypersonic flow conditions as the former is encountered in post-shock flow conditions ($T_t > T_{ve}$) and the latter is typically encountered in nozzle flow conditions ($T_t < T_{ve}$). For the excitation scenario, the adiabatic reactor is initialised in the following thermal non-equilibrium conditions: $T_t = T_r = 20,000$ K and $T_{ve} = 5000$ K, and for the de-excitation scenario with $T_t = T_r = 5000$ K and $T_{ve} = 20,000$ K. Under such conditions, a relaxation process towards a thermal equilibrium state is driven by inelastic collisions between particles and the corresponding exchange of internal energies. After a number of collisions have occurred, kinetic theory demonstrates that a system relaxes towards an equilibrium temperature that is defined as

$$T_{eq} = \frac{\xi_{t,i}T_{t,i} + \xi_{r,i}T_{r,i} + \xi_{ve,i}T_{ve,i}}{\xi_{t,f} + \xi_{r,f} + \xi_{ve,f}}, \tag{7.12}$$

where ξ_{ve} is the mean degree of freedom of the vibronic mode.

Figure 7.3 demonstrates that the DSMC results achieve excellent reproduction of the theoretical predictions for both the excitation and de-excitation scenarios. Quantitatively, for the excitation scenario, the theoretical equilibrium temperature is $T^{theo}_{eq,ex} = 13,740$ K and the equilibrium temperature measured in DSMC is $T^{DSMC}_{eq,ex} = 13,741$ K. For the de-excitation scenario, the theoretical equilibrium temperature is $T^{theo}_{eq,de-ex} = 10,521$ K and the equilibrium temperature measured in DSMC is $T^{DSMC}_{eq,de-ex} = 10,518$ K. Both scenarios show good reproduction of the theoretical prediction which demonstrates the successful implementation of the post-collision sampling technique.

7.3.3 Population of the Electronic Excited States

Figure 7.4 shows further verification of the model for the population of the electronic excited states and their corresponding vibrational quantum numbers. The adiabatic reactor is initialised in thermal equilibrium conditions, i.e. $T_t = T_r = T_{ve} = 10,000$ K and the population of each quantum number is sampled for 10^5 time-steps to reduce the scatter. The theoretical and DSMC two-dimensional distribution of energy across all electronic excited states and their corresponding vibrational quantum levels are depicted in Figs. 7.4a and 7.4b, respectively. Additionally, the total population of each electronic excited state, i.e. $f_i = \sum_j \frac{n_{i,j}}{n_{tot}}$, and the population of the vibrational quantum numbers of all seven electronic excited states are respectively depicted in Figs. 7.4c and 7.4d.

Figures 7.4a and 7.4b show that the DSMC achieves a good reproduction of the two-dimensional theoretical distribution for all quantum levels. Figure 7.4c demonstrates an excellent agreement

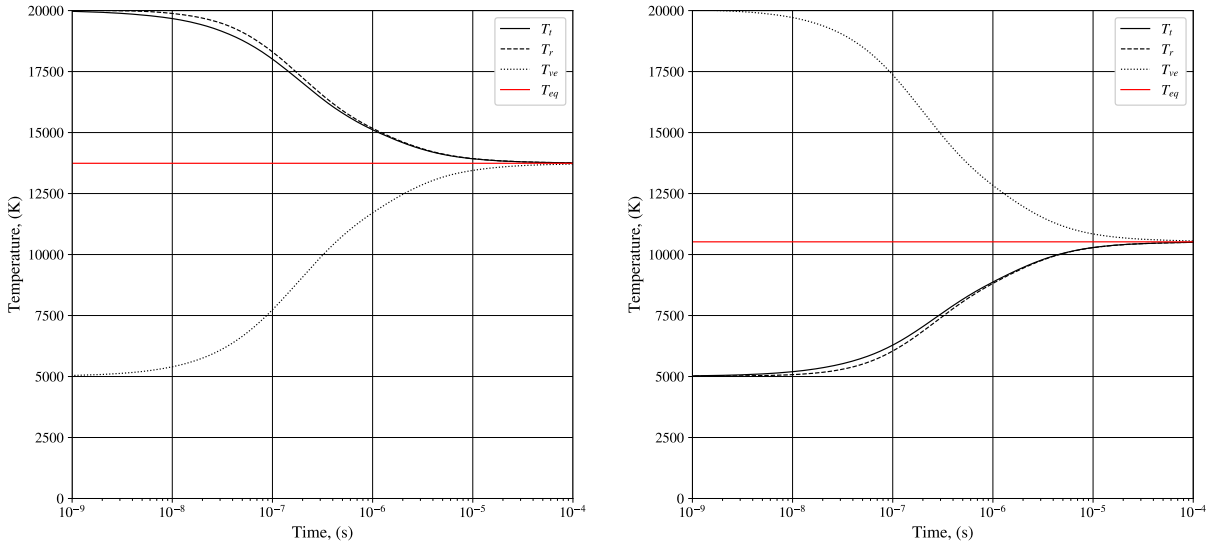

(a) Excitation scenario.

(b) De-excitation scenario.

Figure 7.3: Thermal relaxation of an adiabatic reactor into equilibrium for (a) electronic and vibrational excitation ($T_t = T_r = 20,000$ K and $T_{ve} = 5000$ K) and (b) electronic and vibrational de-excitation ($T_t = T_r = 5000$ K and $T_{ve} = 20,000$ K).

between the population of the electronic excited states and statistical mechanics theory. The consistency between DSMC results and the theoretical calculations, Eq. (7.2), serves as a further verification of the implementation of the model in the DSMC code. Similarly, Fig. 7.4d also confirms the accuracy of the model for the population of the vibrational quantum numbers in all seven electronic excited states. Some scatter is evident at the tails of the distributions. This is expected in a DSMC simulation, because the probability of finding a molecule in these higher vibrational levels is relatively small, resulting in a low signal-to-noise ratio.

7.3.4 Thermodynamic Properties

The uncoupled and coupled approaches are examined for the calculation of the isochoric-specific heat capacity. The adiabatic reactor is initialised in thermal equilibrium for temperatures ranging from 2000 K to 20,000 K and the thermodynamic properties are sampled for 10^5 time-steps to reduce the scatter. These results are compared against four numerical studies, i.e. Capitelli *et al*. [28], Jaffe [30], Qin *et al*. [29], and McBride *et al*. [24]. This represents a selection of many works available in the literature. Additionally, the specific heat capacity results presented in Civrais *et al*. [32] are included for reference.

Figure 7.5 compares the uncoupled and coupled approaches for the calculation of the isochoric specific heat capacity of molecular oxygen. The DSMC results are in excellent agreement with the theoretical calculations, Eq. (7.5), for the entire range of temperatures considered which serves as a verification of the implementation of the model in the DSMC code. Figure 7.5 illustrates the benefits of the coupled approach. This approach provides a more accurate description

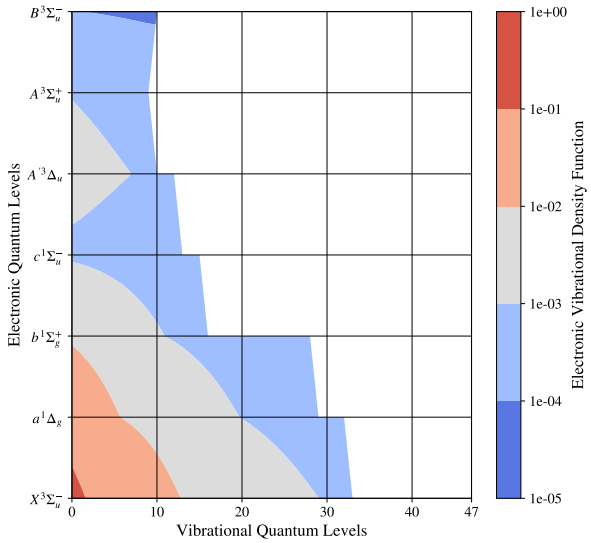

(a) Theoretical distribution.

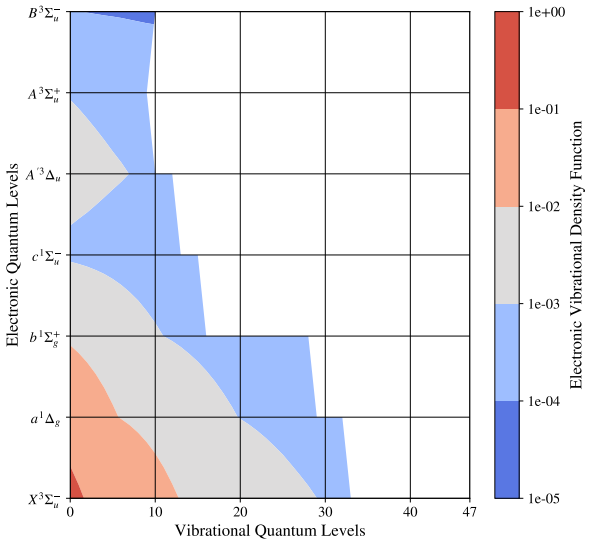

(b) DSMC.

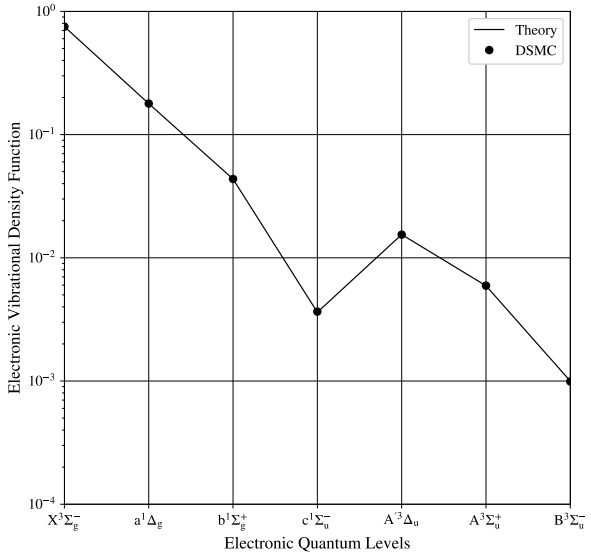

(c) Population of the electronic excited states, $f_i = \sum_j f_{i,j}$.

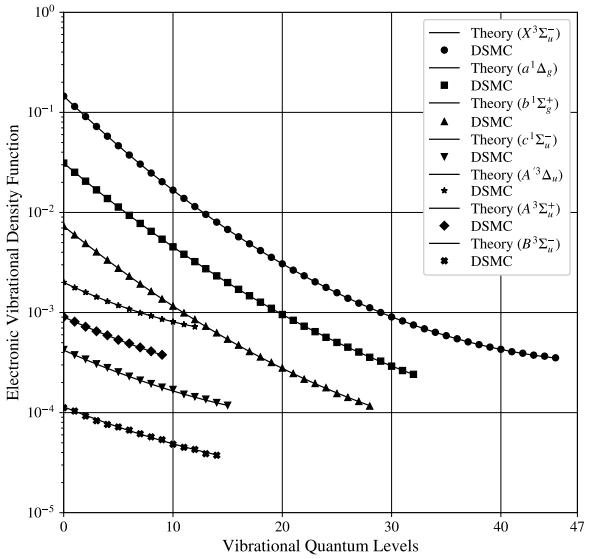

(d) Vibrational population of the electronic excited states, $f_{i,j}$.

Figure 7.4: Comparison of the population of the electronic excited states for molecular oxygen in thermal equilibrium ($T_t = T_r = T_{ve} = 10,000$ K).

of the specific heat capacity compared to its counterparts. Figure 7.5 emphasises the importance of including the electronic mode of molecular systems and modelling their corresponding vibrational excitation to yield accurate predictions in low to moderate temperatures.

For temperatures in excess of 7000 K, the coupled approach deviates from the prediction of past studies [24, 28–30]. In the derivation of the coupled approach, the rotational-vibrational coupling effects of the electronic excited modes have been disregarded. While this assumption holds for low-to-moderate temperatures, it becomes evident that as the temperature increases the coupled approach deviates from the compilation of past studies due to the omission of rotational-

vibrational coupling effects. To improve the accuracy of the coupled approach, further investigation should be directed towards incorporating the contribution of rotational-vibrational coupling effects [107, 224, 225]. Note that rotational-vibrational coupling involves the addition of numerous quantum levels to the molecular systems which would result in a noticeable increase in computational expense. Further discussions on the limitations of the coupled approach are developed in Appendix. A and exemplified with a canonical air mixture modelled with the five most representative species.

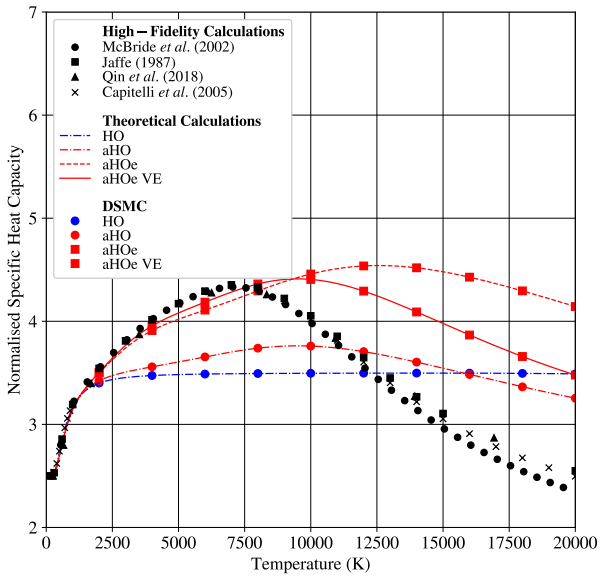

Figure 7.5: Comparison of the normalised isochoric specific heat capacity of molecular oxygen.

7.4 Hypersonic Flow

The present section aims to compare the uncoupled and coupled approaches for the simulation of a canonical nonreactive oxygen hypersonic flow past a cylindrical body entering Earth's atmosphere at an altitude of about 85 km. The freestream conditions are extracted from the US Standard Atmosphere [198] and summarised in Tab. 7.3.

The geometry represents a two-dimensional slice of a cylindrical body with diameter $d = 0.1$ m, with a domain length equal to two and a half radii upstream of the stagnation point. The mesh is refined near the stagnation point to ensure that the cell size, Δx, remains around one-quarter of the local mean free path, λ, throughout, resulting in a total of 32,400 cells. The time step is carefully chosen to be an order of magnitude smaller than both the mean collision time and the cell residence time, the latter of which corresponds to the time for a DSMC simulator particle to cross a cell length under the freestream conditions. To maintain a minimal number of 100 particles per cell throughout, the numerical mesh is populated with a total number of 8.59×10^6 DSMC simulator particles at steady state. Similar to the adiabatic reactor simulations, the inter-

Table 7.3: Free stream parameters.

Parameter	Values
Altitude (km)	85
Temperature (K)	186.95
Number density (m^{-3})	1.45×10^{20}
Pressure (Pa)	0.374
Speed (km s^{-1})	7.50
Ma_∞	28.76
Kn_∞	0.085

molecular collisions are computed with the VHS model [17] for a reference temperature of $T_{ref} = 273$ K. To reproduce the typical relaxation behaviour of the uncoupled approach, a constant probability of $P_1 = 0.02$ and $P_2 = 0.1$ for a particle to undergo Reaction 9 and Reaction 10, respectively, is applied. The gas-surface interactions are fully diffusive with an isothermal wall at temperature $T_w = 1000$ K. A total of 10^5 samples are taken after steady-state to reduce the numerical scatter. To illustrate the structure of the flow, the internal temperatures and velocity magnitude along the stagnation streamline are presented in Fig. 7.6. The distance to the stagnation point is normalised by the diameter of the cylinder. A value of 0 refers to the inlet boundary conditions and 2.5 refers to the stagnation point.

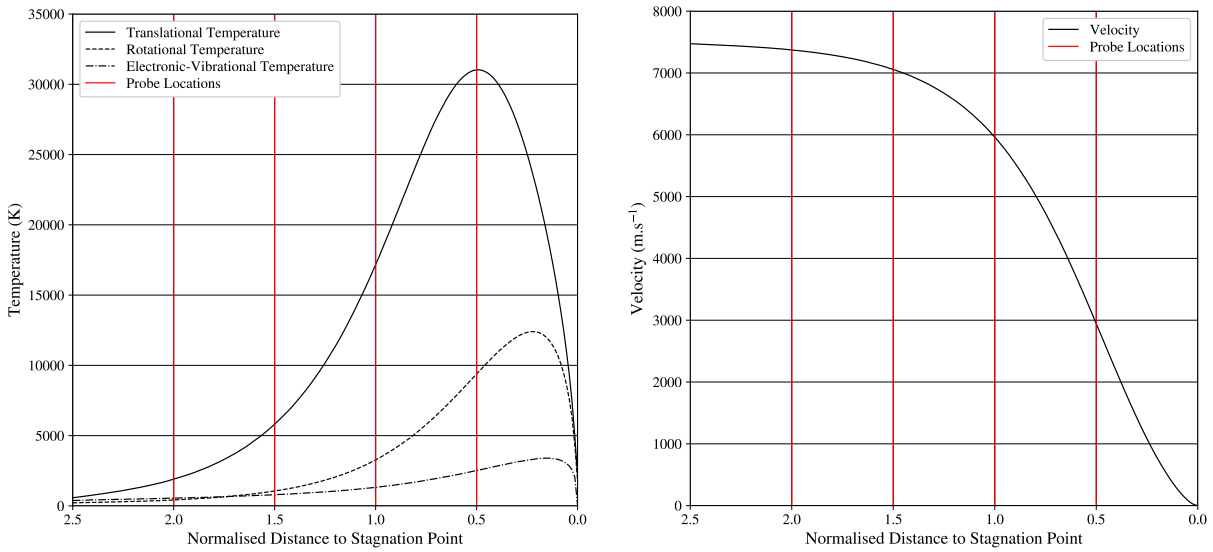

(a) Internal temperatures.

(b) Velocity.

Figure 7.6: Flow properties along the stagnation streamline.

As mentioned in Chapter 1, the standard approach to couple DSMC and radiation transport solvers consists of transferring the uncoupled internal temperatures, i.e. rotational, vibrational, and electronic, calculated by the DSMC solver into a radiation solver. Note that these internal temperatures are calculated by assuming a Boltzmann distribution and resolving an implicit

equation for both vibrational and electronic temperatures [31]. However, radiation solvers, e.g. NEQAIR [160], PARADE/PICLas [49, 159], Specair [161], integrate a fully coupled approach. Specifically, these solvers compute the radiative properties in a cell from the distribution function of the internal quantum levels. To compute these radiative properties, an assumption on the distribution function is made where it is assumed to follow Boltzmann statistics [49, 53] or the non-equilibrium quasi-steady-state method [156, 165].

The main objective of this section is twofold: to compare the two approaches for the distribution of the internal quantum levels measured by the DSMC method and to assess the assumption that the internal quantum levels are distributed according to the Boltzmann distribution. For both approaches, the vibrational and electronic density functions are calculated with the local internal temperatures, namely $f = f_i(T_v)f_j(T_e)$ for the uncoupled approach and $f = f_{i,j}(T_{ve})$ for the coupled approach.

Figure 7.7 compares the DSMC results for the population of the internal quantum levels and the corresponding Boltzmann distribution along the stagnation streamline. The DSMC results are denoted by colour markers, where solid symbols refer to the uncoupled approach and open symbols to the coupled approach, and the Boltzmann distributions are denoted by colour lines where solid lines refer to the uncoupled approach and dashed lines refer to the coupled approach. Similar to Fig. 7.6, the distance to the stagnation point is normalised by the diameter of the cylinder. A value of 0 refers to the inlet boundary conditions and 2.5 refers to the stagnation point.

Downstream of the shock wave, Fig. 7.7 shows that the highest vibrational and electronic quantum levels exhibit large deviations from the assumption of a Boltzmann distribution. These high-lying quantum levels are of primary importance for the modelling of the radiative properties of molecular species. Furthermore, a noticeable discrepancy arises between assuming a Boltzmann distribution corresponding to the cell temperature and density, and the actual distribution observed in DSMC simulations, which could represent a source of error in typical flow-radiation coupling.

Figure 7.7 also indicates a significant population of the high-lying quantum levels in the upstream region. This non-equilibrium effect manifests itself in Knudsen number regimes in which the degree of rarefaction is sufficient for a particle to collide with the surface of the body and travel backwards without undergoing sufficient collisions with any other particles to de-excite the quantum levels to return to an equilibrium distribution; hence, carrying post-shock information upstream of the bow-shock. This non-equilibrium effect is characterised by a strong deviation from a Maxwell velocity distribution to the extent of quasi-Maxwellian or bi-modal distributions [156]. Note that this phenomenon has also been observed previously [53, 199–201].

The deviation from the Boltzmann distribution is further investigated at four locations throughout the shock wave denoted by vertical red lines in Fig. 7.6 with thermal conditions summarised in Tab. 7.4. A series of adiabatic reactor simulations initialised with the thermal conditions

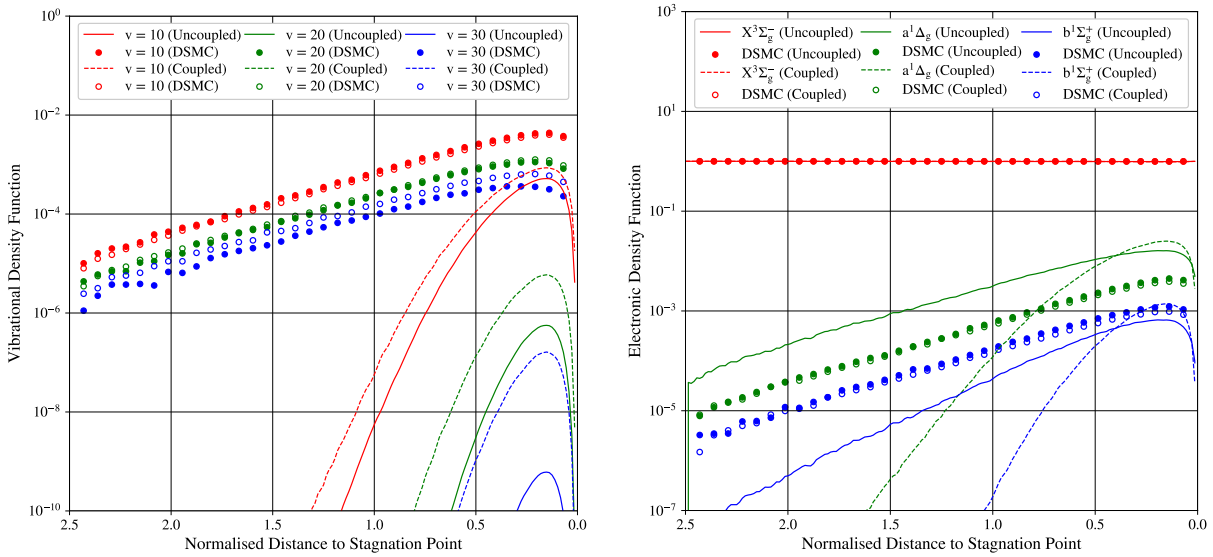

(a) Vibrational density function of three vibrational quantum levels of O_2 ground state.

(b) Electronic density function of the first three electronic state of O_2.

Figure 7.7: Comparison of the DSMC results against Boltzmann distribution along the stagnation streamline.

Table 7.4: Thermal flow conditions in four cells along the stagnation streamline.

$\frac{x}{D}$	T_t (K)	T_r (K)	T_{ve} (K)
2.000	1902.70	423.40	550.06
1.500	5813.31	1059.91	795.58
1.000	17 168.40	3273.69	1311.87
0.500	31 031.00	9390.44	2518.74

summarised in Tab. 7.4 is performed. Figure 7.8 shows the Boltzmann distribution and DSMC measurements of the coupled approach for the first three electronic states of O_2 obtained along the stagnation line. Contrastingly, Fig. 7.9 shows the Boltzmann distribution and DSMC measurements obtained from the series of adiabatic reactor simulations. The DSMC results are denoted by colour markers and the Boltzmann distributions by colour lines.

Figure 7.8 shows that the Boltzmann distributions at all four locations are significantly different to the DSMC measurements along the stagnation streamline whereas, Fig. 7.9 indicates that the DSMC simulations precisely reproduce the theoretical vibrational density function for the same thermal conditions in an adiabatic reactor. This demonstrates that the different distributions in the hypersonic case are due to non-equilibrium effects that a radiation solver would not be capturing using solely the temperatures.

So far, the comparison of the two approaches was limited to the population of the quantum levels along the stagnation streamline. In Fig. 7.10, the total number density of the first six electronic states of O_2, i.e. $n_i = \sum_j n_{i,j}$, measured in the DSMC simulations are regarded for the flow field.

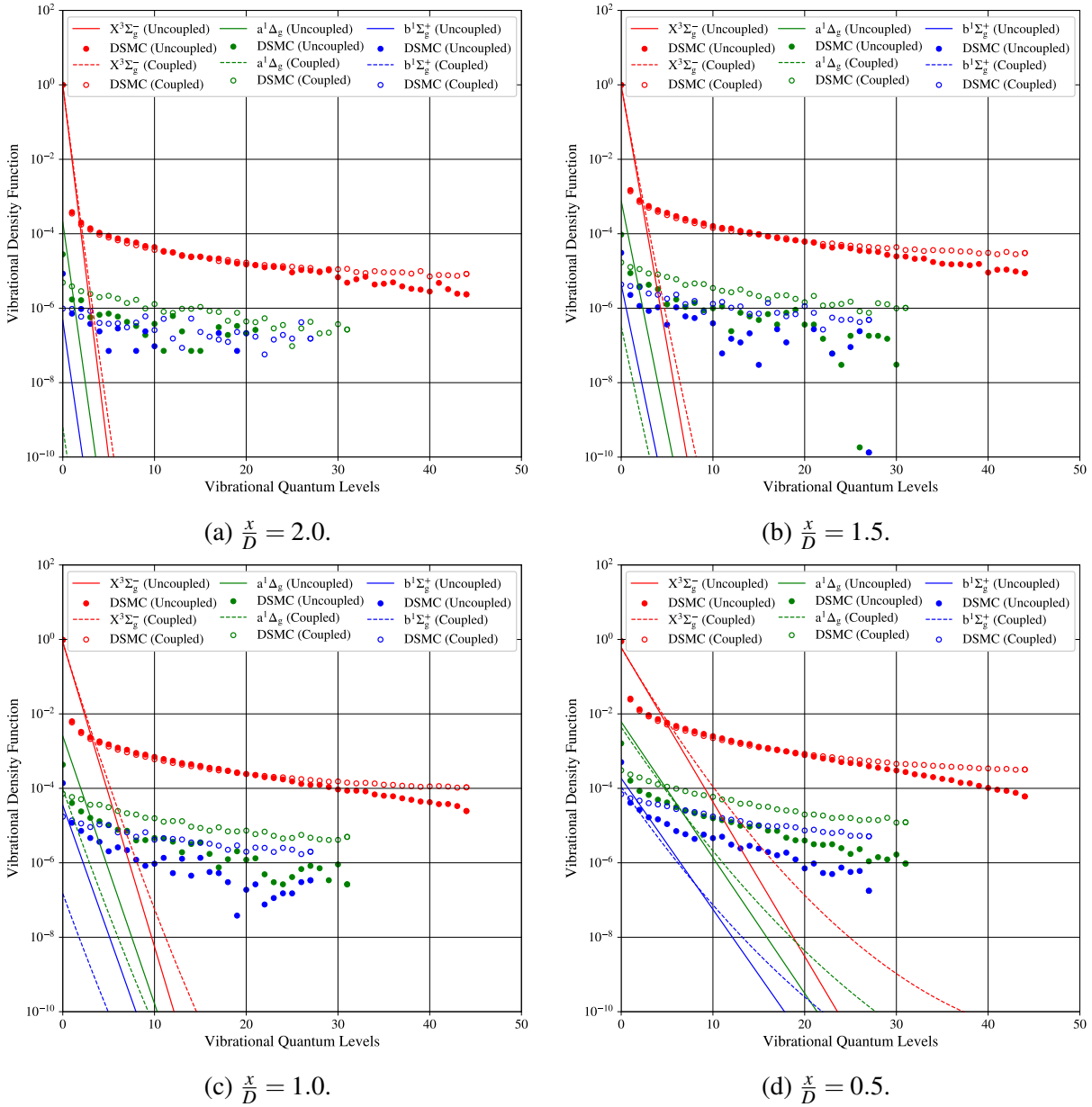

(a) $\frac{x}{D} = 2.0$. (b) $\frac{x}{D} = 1.5$.

(c) $\frac{x}{D} = 1.0$. (d) $\frac{x}{D} = 0.5$.

Figure 7.8: Vibrational density function of the first three electronic excited states at four locations along the stagnation streamline.

As anticipated, Fig. 7.10 indicates that the ground electronic state is the most populated. Both approaches offer a similar description of the distribution of the ground state throughout the domain. However, the two approaches differ in the distribution for all the electronic excited states herein considered. Specifically, the coupled approach predicts lower populations of the electronic excited states in comparison to the uncoupled approach. This discrepancy arises from the difference in the modelling of the vibrational energies of the electronic excited states in each approach. The coupled approach implies that each electronic state can excite a unique set of vibrational levels, see Fig. 7.4. In contrast, the uncoupled approach assumes that each electronic state can only excite the same set of vibrational energies as the ground electronic state. In the

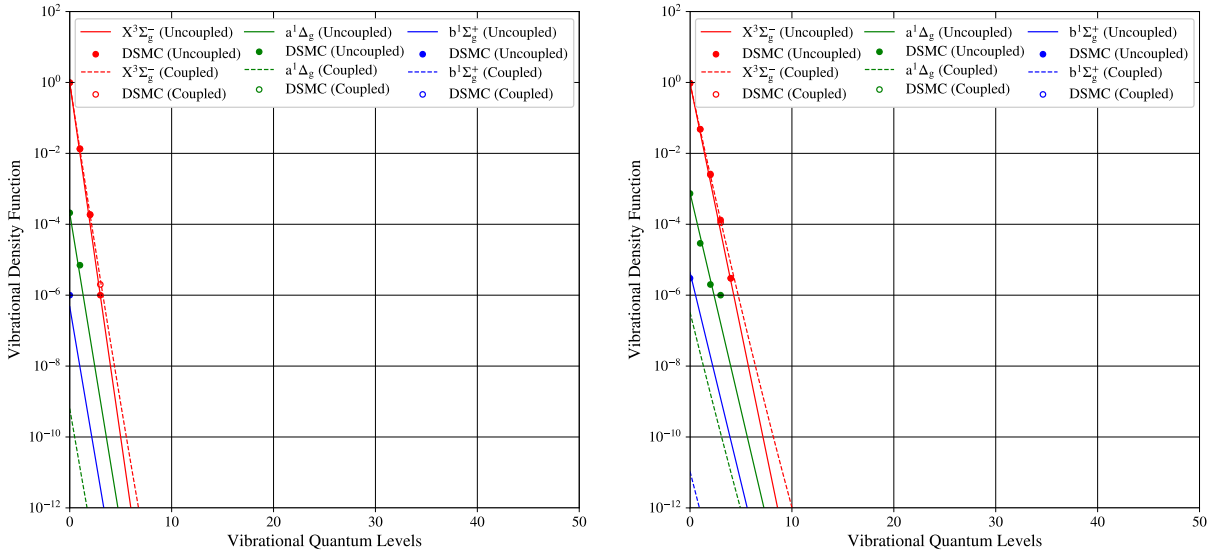

(a) $\frac{x}{D} = 2.0$.

(b) $\frac{x}{D} = 1.5$.

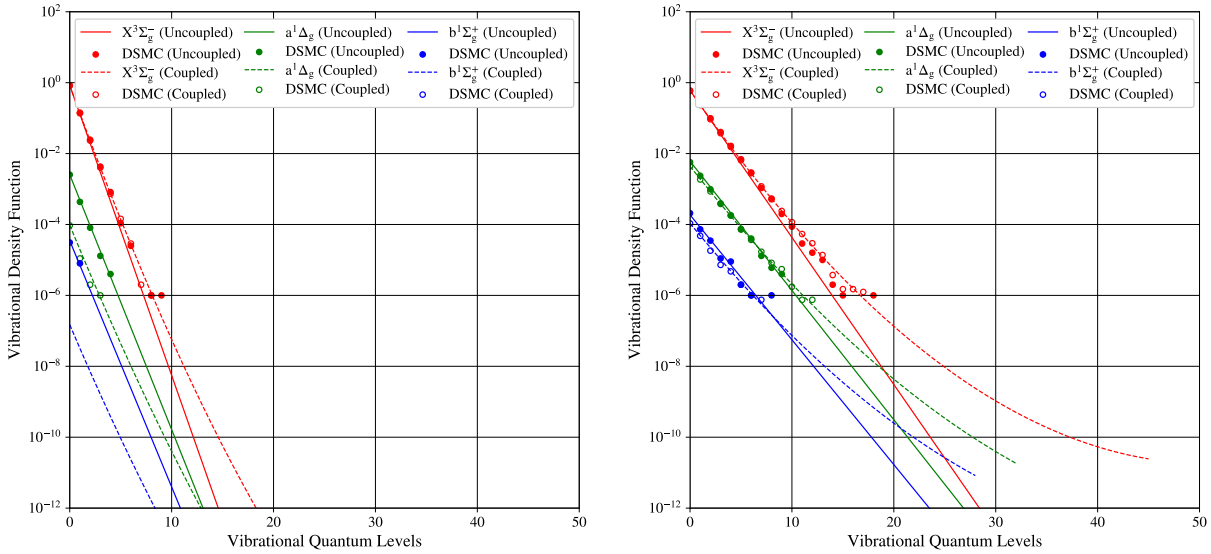

(c) $\frac{x}{D} = 1.0$.

(d) $\frac{x}{D} = 0.5$.

Figure 7.9: Vibrational density function of the first three electronic excited states measured in a series of adiabatic reactor simulations with thermal conditions corresponding to four locations along the stagnation streamline.

context of a flow-radiation coupling, such a difference between the two approaches in terms of the distribution of the electronic excited states throughout the domain could lead to a significant difference in the radiation properties.

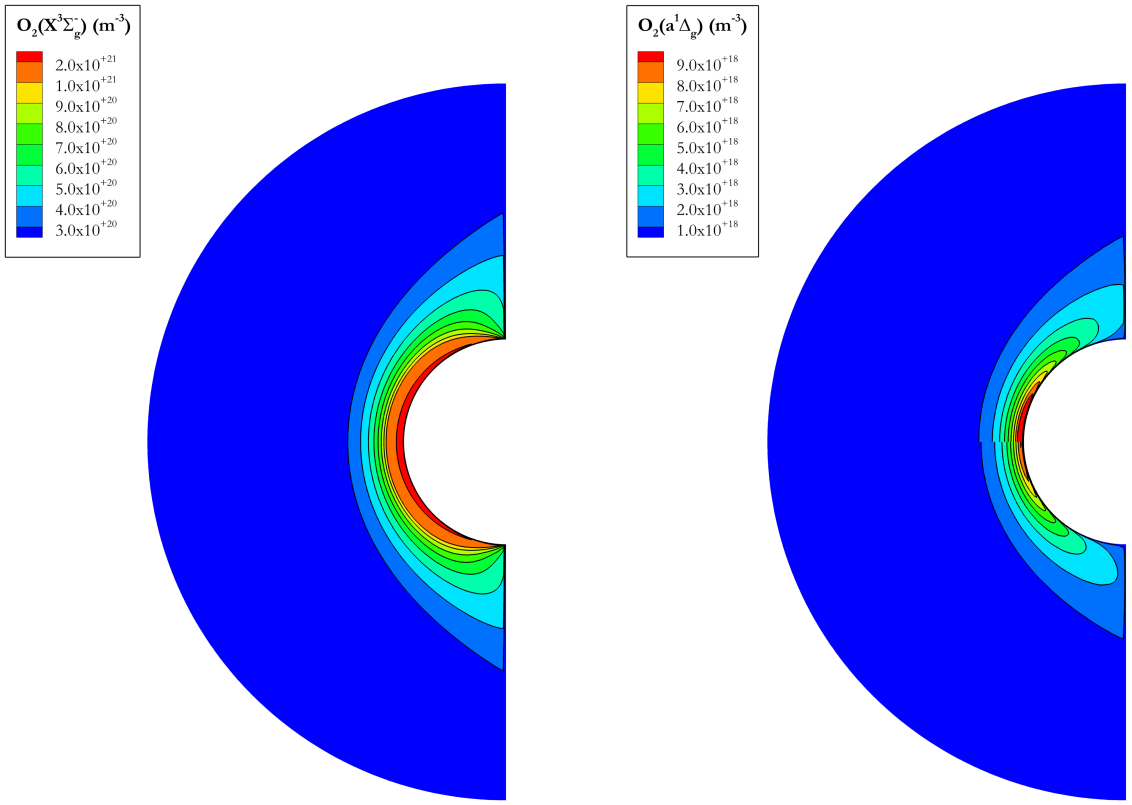

(a) Ground electronic state.

(b) First electronic excited state.

Figure 7.10: Population of the electronic states of O_2. Uncoupled approach (top) and coupled approach (bottom).

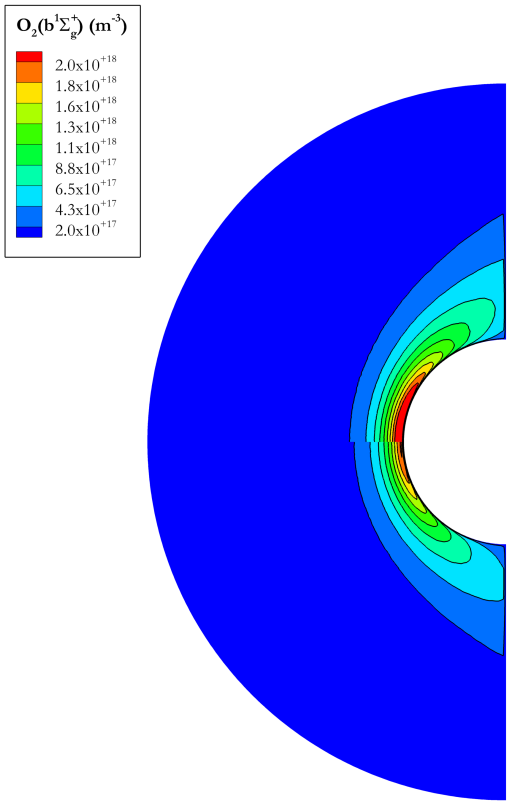

(c) Second electronic excited state.

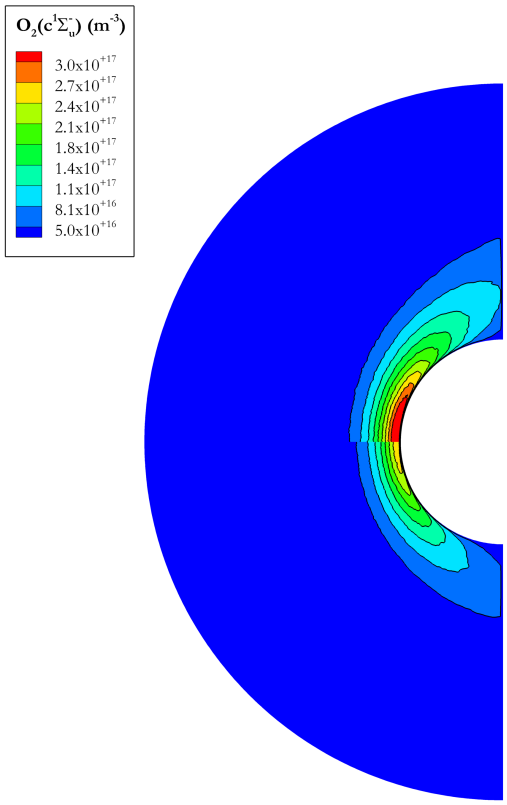

(d) Third electronic excited state.

Figure 7.10: Population of the electronic states of O_2. Uncoupled approach (top) and coupled approach (bottom). (Cont.)

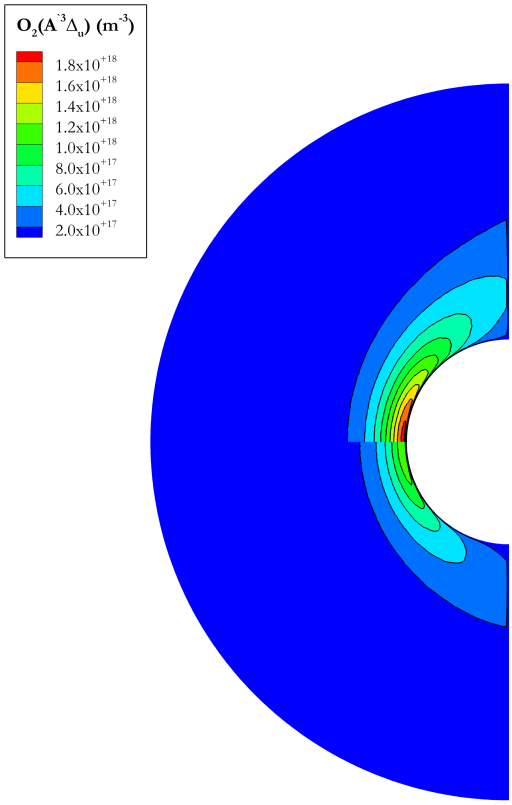

(e) Fourth electronic excited state.

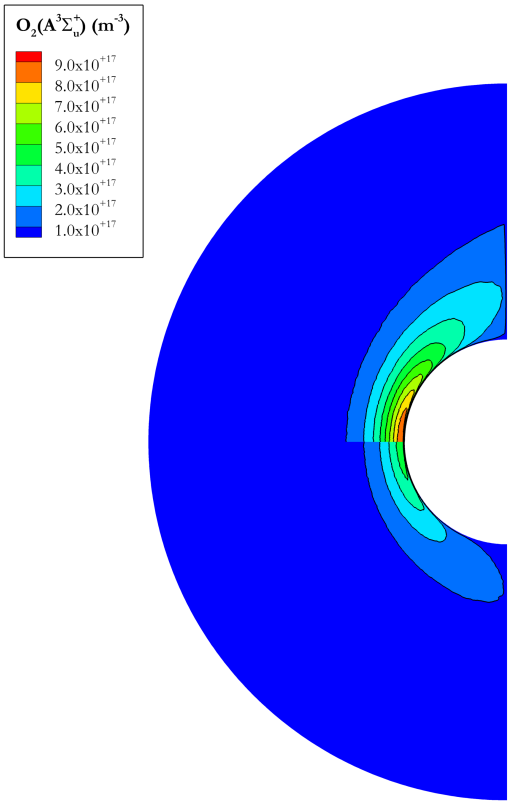

(f) Fifth electronic excited state.

Figure 7.10: Population of the electronic states of O_2. Uncoupled approach (top) and coupled approach (bottom). (Cont.)

7.5 Summary

A new model for modelling the vibrational excitation of the electronic excited states is developed and implemented in a DSMC solver. The new model is verified against an extensive compilation of theoretical studies for both thermal equilibrium and non-equilibrium conditions. Additionally, the new model is evaluated against the traditional uncoupled approach utilised in DSMC for a canonical hypersonic non-reactive oxygen gas flow past a cylindrical body at an altitude of about 85 km.

The series of adiabatic reactor simulations has shown excellent agreement between theoretical predictions and DSMC results, thereby demonstrating the successful implementation of a DSMC solver. Furthermore, the coupled approach has been shown to improve the reproduction of a compilation of past studies for the specific heat capacity of molecular oxygen compared to the uncoupled approach.

The hypersonic flow scenario has revealed that the assumption of the quantum levels being distributed according to the Boltzmann distribution is not adequate. In high Knudsen number regimes, non-equilibrium effects lead to significant deviations between the local distribution of quantum levels and that predicted by the Boltzmann distribution calculated from internal temperatures. Consequently, one should benefit from the capability of DSMC solvers to keep track of the local distribution of energy across the internal quantum levels and solely rely on these distributions for the determination of the radiative properties. Furthermore, the coupled approach has demonstrated a lower population of electronic excited states compared to the uncoupled approach. This discrepancy is attributed to the possibility for each electronic excited state to allow vibrational excitation; hence, providing additional channels for redistributing internal energy during collisions. Such a difference in the distribution of electronic excited states between the two approaches is expected to result in significant modifications in the radiation properties.

Chapter 8

Conclusions & Perspectives

8.1 Conclusions

This thesis focuses on the development and implementation of new aerothermodynamics models for moderately to highly rarefied flow regimes using the DSMC method. Three key models were developed and integrated into a DSMC solver, focusing on vibrational modelling of molecular species, chemical reaction modelling, and modelling of electronic excited states. The implementation of all models was verified for a compilation of systematic adiabatic reactor simulations. Subsequently, each model was validated against the most representative experimental measurements, high-fidelity calculations, and analytical models. Finally, all three models were applied to numerically investigate realistic applications. A detailed summary of findings was provided at the end of each chapter. All objectives of this thesis were satisfied. An overview of the main conclusions is as follows.

Vibrational Modelling

In Chapter 4, an anharmonic oscillator model has been implemented into a DSMC solver. The vibrational energies have been fitted on high-fidelity potential energy surfaces. The model has been verified against the probability distribution of vibrational quantum levels, specific heat capacity and thermal relaxation of a gas to equilibrium. The study shows that the anharmonic oscillator model predicts a larger population of high-lying vibrational quantum levels which carry significant implications in the modelling of the chemical activity of chemical species. Furthermore, the anharmonic oscillator model is applied to a canonical Earth atmospheric reentry at an altitude of 75 km in which the anharmonic oscillator model exhibits different topologies of internal mode excitation in the flow field in comparison to the traditional harmonic oscillator model.

Chemistry Modelling

In Chapters 5 and 6, a custom version of the QK models has been proposed in which the vibrational excitation is modelled with an anharmonic oscillator model. While the new formulations have demonstrated a reasonable reproduction of most representative reaction rates in thermal equilibrium conditions, they have shown some limitations in reproducing the baseline model in thermal non-equilibrium conditions. It has been demonstrated that the QK models excessively rely on the relative translational energy of the colliding pair to promote chemical reactions. These findings have motivated the development of an extension to the QK models with the addition of tunable parameters. The numerical evaluation of the models has shown excellent reproduction of the baseline database for both thermal equilibrium and non-equilibrium conditions. These new formulations are major improvements over the original QK models for modelling chemical reactions with the DSMC method. Furthermore, the new formulations have been applied to reproduce in-flight measurements of the surface heat flux of the second mission of the Space Shuttle Columbia. The extended QK models is shown to predict a surface heat flux beyond the bounds of the in-flight measurements.

Internal Mode Coupling

In Chapter 7, a new model for modelling the interactions between the vibrational and electronic modes of molecular species has been proposed. Specifically, it assumes that each electronic excited state allows for vibrational excitation described by an anharmonic oscillator model. The model has been verified against the probability distribution of vibrational and electronic quantum levels, specific heat capacity and thermal relaxation of a gas to equilibrium. Furthermore, the new model has been applied to simulate a canonical hypersonic flow past a cylindrical body, entering Earth's atmosphere at an altitude of about 85 km. The study shows that the traditional assumption of the quantum levels being distributed according to the Boltzmann distribution is inaccurate. Additionally, the coupled approach suggests a lower population of electronic excited states compared to the uncoupled approach, which may carry significant implications to the radiative heat flux when coupling DSMC and radiation transport solver.

8.2 Perspectives

The main area of future work from the present thesis arises from the modelling of the interactions between the internal modes which spans across three major research topics: internal mode coupling, chemistry modelling and DSMC-radiation coupling.

Internal Mode Coupling

Chapter 1 and Appendix A have outlined the importance of describing the interaction between the internal modes to correctly reproduce the thermodynamic and transport properties of chemical species. In Chapter 7, the first step towards such a sophisticated approach has been derived and successfully implemented in a DSMC solver. However, further improvement is required to fully describe the interaction between the internal modes. Specifically, the rotational mode is traditionally modelled with a continuous approach in the DSMC method; hence, requiring to be addressed in the first place before considering any more sophisticated modelling. Boyd [226, 227] has proposed a quantised approach of the rotational mode, however, this model remains limited to a quantised rigid-rotor model which corresponds to the first term in Eq. (A.12). It is evident in Appendix A that a non-rigid rotor is required to correctly describe the interactions between the rotational and vibrational modes. Therefore, further improvement should be made to develop and implement in a DSMC solver a non-rigid rotor based on Boyd [226, 227]. Subsequently, a fully coupled approach of the internal modes following the mathematical derivations in Appendix A could be implemented in a DSMC solver.

Chemistry Modelling

While the modelling of the internal modes with a fully coupled approach readily improves the description of the flow physics, one point should be made regarding the chemistry modelling under such a sophisticated approach. As discussed in Chapters 5 and 6, the QK models assume that chemical reaction only occurs from the contribution of the translational and vibrational modes of the colliding partners and that each internal modes are individually treated. These assumptions limit the QK models to describing only a fraction of the real-gas effects occurring in aerothermodynamic applications. For a more realistic approach to be considered that accounts for such real-gas effects, chemical reactions would occur not only from translational and vibrational contributions but also from rotational, and electronic contributions giving rise to a larger set of chemical processes. Therefore, for the coupled approach developed in Appendix A to be fully implemented in a DSMC solver, an extension of the QK models that incorporates these additional contributions to the chemical reactions is required.

Radiation

In recent years, there has been a growing interest in coupling DSMC methods with radiation transport solvers, e.g. PARADE [159], NEQAIR [160], or Specair [161], for various investigations [49, 53, 162–165]. The standard approach to couple DSMC and radiation solvers consists of transferring the uncoupled internal temperatures, i.e. rotational, vibrational and electronic, calculated by the DSMC solver into the radiation solver. Unlike DSMC solvers, these radiation solvers adopt a fully coupled approach, incorporating all types of interactions between internal

modes. Specifically, these solvers compute the radiative properties in a cell from the distribution function of the internal quantum levels. To compute these radiative properties, an assumption on the distribution function is made whether it is assumed to follow Boltzmann statistics [49,53] or the QSS method [156, 165]. With the development of a fully coupled approach derived from similar considerations to that applied in radiation solvers, a new coupling between DSMC and radiation transport solvers solely relying on the distribution of the quantum levels in the cell without additional assumptions on the form of the distribution function would then be feasible. Such a sophisticated approach would ultimately be validated against experimental measurements for the reproduction of radiation flux, e.g. NASA electric arc shock tube (EAST) [228–231].

Appendix A

Rovibronic Modelling

Throughout this thesis, two approaches have been extensively discussed: one where the internal modes were fully uncoupled, i.e. Chapter 4, and another one where the internal modes were partially coupled, i.e. Chapter 7. It has been evidenced that adopting a coupled approach for the description of the internal modes leads to a more accurate reproduction of the thermodynamic and transport properties. This appendix introduces an approach based on a past study reported by Jaffe [30] where the internal modes are fully coupled, i.e. rotational-vibrational-electronic coupling. A graphical illustration of the traditional approach (Chapters 4-6), vibronic modelling (Chapter 7), and rovibronic modelling is depicted in Fig. A.1.

Mathematical Description

Consider a chemical species with a given triplet of quantum levels (n, v, J). Statistical mechanics theory demonstrates that the distribution function of its internal energy is governed by,

$$f_{n,v,J} = \frac{g_n g_J e^{-\frac{\varepsilon_{n,v,J}}{kT}}}{\sum_{n}^{n_{max}} \sum_{v}^{v_{max}(n)} \sum_{J}^{J_{max}(n,v)} g_n g_J e^{-\frac{\varepsilon_{n,v,J}}{kT}}} = \frac{g_n g_J e^{-\frac{\varepsilon_{n,v,J}}{kT}}}{Q}, \tag{A.1}$$

where $\varepsilon_{n,v,J}$ is the internal energy of such configuration expressed as a summation of all its contributions,

$$\varepsilon(n,v,J) = \varepsilon_e(n) + \varepsilon_v(n,v) + \varepsilon_r(n,v,J). \tag{A.2}$$

The electronic contribution $\varepsilon_e(n)$ is the minimal amount of energy required to promote an electron from the ground electronic configuration to a higher electronic state. This energy is calculated from Eq. (2.37).

The vibrational contribution $\varepsilon_v(n,v)$ describes the vibrational excitation of an electronic state. The traditional approach to describe the vibrational excitation of a given electronic state with a polynomial expression such as the Dunham model [35]. For the ground electronic configuration

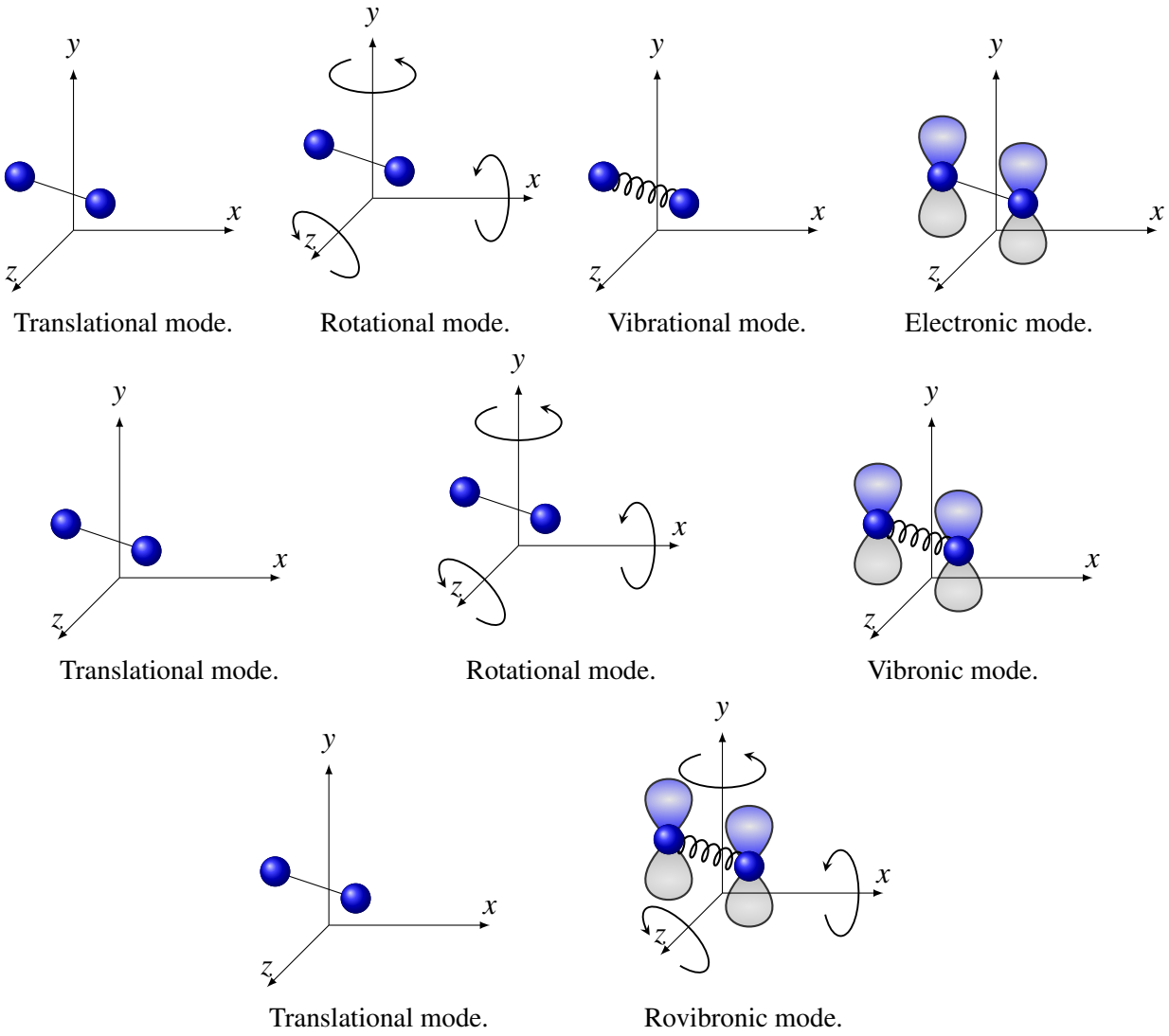

Figure A.1: Illustration of the modelling of the internal modes of a diatomic molecule.

of a diatomic molecule, the Dunham model describes the vibrational excitation of such molecule as a rotating vibrator which takes the form,

$$\varepsilon_{vr}(v,J) = \sum_i \sum_j K(i,j) \left(v+\frac{1}{2}\right)^i J^j (J+1)^j, \tag{A.3}$$

where $K(i,j)$ gives the spectroscopic constant of indexes (i,j), i.e. $K(0,0) = \omega_e$, $K(1,0) = \omega_e\chi_e$, $K(2,0) = \omega_e\gamma_e$ and so on.

The most popular sources for obtaining the spectroscopic constants, i.e. ω_e, $\omega_e\chi_e$ and $\omega_e\gamma_e$, are the NIST [25] or the Huber and Herzberg tables [26]. However, Chapter 4 has evidenced that these spectroscopic constants over-estimate the number of vibrational quantum levels and under-estimate the dissociation quantum level. Considering the large uncertainties and the lack of spectroscopic constants beyond $\omega_e\chi_e$, the infinite summations have been truncated for both rotational and vibrational contributions to the second order which allows to recover the non-rigid

rotor and Morse anharmonic oscillator model. Following these considerations, $\varepsilon_v(n,v)$ follows the description adopted in Chapter 7, see Eq. (7.1), in which the vibrational energy is calculated as,

$$\varepsilon_v(n,v) = hc\left[\omega_e(n)\left(v+\frac{1}{2}\right) - \omega_e(n)\chi_e(n)\left(v+\frac{1}{2}\right)^2\right]. \tag{A.4}$$

The rotational contribution $\varepsilon_r(n,v,J)$ describes the rotational-vibrational interaction of the n^{th} electronic states which is calculated as,

$$\varepsilon_r(n,v,J) = B_v(n,v)J(J+1) - D_v(n,v)J^2(J+1)^2, \tag{A.5}$$

with,

$$B_v(n,v) = B_e(n) + \alpha_e(n)\left(v+\frac{1}{2}\right), \tag{A.6}$$

and,

$$D_v(n,v) = D_e(n) + \beta_e(n)\left(v+\frac{1}{2}\right). \tag{A.7}$$

If one of the spectroscopic constants is not reported by any of the spectroscopic databases [25, 26], the constant is taken to zero except for D_e and β_e which are calculated as,

$$D_e = \frac{4B_e^3}{\omega_e^2}, \tag{A.8}$$

$$\beta_e = D_e\left(\frac{8\omega_e\chi_e}{\omega_e} - \frac{5\alpha_e}{B_e} - \frac{\alpha_e^2}{24B_e^3}\right). \tag{A.9}$$

The main challenge associated with the derivation of the thermodynamic properties from Eq. (A.1) is to determine the maximum electronic, vibrational and rotational quantum levels, namely n_{max}, $v_{max}(n)$ and $J_{max}(n,v)$ respectively.

The total number of electronic quantum levels, namely n_{max}, is limited to the availability of the electronic configurations reported in the aforementioned tables.

For a given electronic excited state, the maximum vibrational quantum level is determined as the last vibrational quantum level immediately below the dissociation quantum level such that it satisfies,

$$\varepsilon_v(n,v) < \varepsilon_d(n,J=0), \tag{A.10}$$

where $\varepsilon_d(n,J=0)$ is the rotationless dissociation energy of the n^{th} electronic excited state. For some electronic configurations, all the vibrational quantum levels lie below the corresponding dissociation energy. In this specific scenario, v_{max} is determined as the last vibrational quantum level before the gradient $\frac{\partial\varepsilon(n,v)}{\partial v}$ changes sign.

For a given electronic excited state, the allowed rotational and vibrational quantum levels are

defined by the inequality,

$$\varepsilon_e(n) + \varepsilon_v(n,v) + \varepsilon_r(n,v,J) < U\left(r_{max}(n,J),n,J\right), \tag{A.11}$$

where $U(r,n,J)$ is the potential energy function and $r_{max}(n,J)$ is the position at which the potential energy function admits a maxima for $r > r_{eq}$.
For any triplet of quantum levels (n,v,J) that satisfies $\varepsilon(n,v,J) < D_e(n)$, the molecular remains bounded and these states are termed bounded states. Furthermore, there exist combinations of triplets (n,v,J) for which $\varepsilon(n,v,J) > D_e(n)$ that does not necessarily result in a dissociation of the diatomic molecule. These triplets are referred to as quasi-bounded states. Beyond a certain rotational quantum level namely J_{lim}, the potential energy function becomes completely repulsive. This region of the potential energy function is referred to as free-bounded states. In this representation, all rotational quantum levels lying below J_{lim} can be populated. An illustration of the bound, quasi-bound and free bound state regions of N_2, O_2 and NO are shown in Fig. A.2.
For consistency with the truncation of the internal energy to the second order, the potential energy function is assumed to be a summation of the Morse potential function [34] and the centrifugal potential [174],

$$U(r,n,J) = \varepsilon_d(n)\left(1 - e^{-2\alpha(n)\frac{r-req(n)}{req(n)}}\right)^2 + B_e(n)\left(\frac{r_{eq}(n)}{r}\right)^2 J(J+1), \tag{A.12}$$

where B_e is a spectroscopic constant, α is a spectroscopic constant that controls the width of the potential function and it is derived from,

$$\alpha(n) = \frac{\omega_e(n)}{4\sqrt{B_e(n)\varepsilon_d(n)}}. \tag{A.13}$$

The rotational quantum level separating the possible quasi-bound state to the free-states regions, J_{lim}, is defined, for $r > r_{eq}$, as the last quantum level before the gradient, $\frac{\partial U(r,n,J)}{\partial r}$, changes sign that is,

$$\begin{cases} \frac{\partial U(r)}{\partial r} \leq 0 & \forall\, r \\ \frac{\partial U(r)}{\partial r} > 0 & \exists\, r \geq r_{eq}. \end{cases} \tag{A.14}$$

The outer position of the quasi-bound state region $r_{max}(n,J)$ is determined by searching the maximum of the potential energy function for $r > r_{eq}$ such that,

$$U\left(r_{max}(n,J),n,J\right) = max\left(U(r,n,J)\right). \tag{A.15}$$

Finally, Eq. (A.11) allows to determine the maximum rotational quantum level J_{max} for each vibrational quantum level that satisfies $v < v_{max}$.

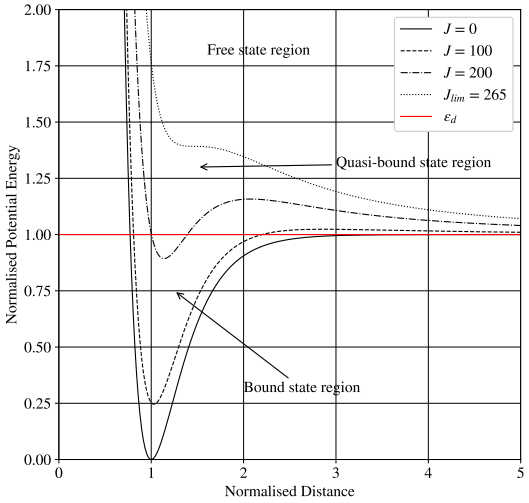

(a) Nitrogen molecule.

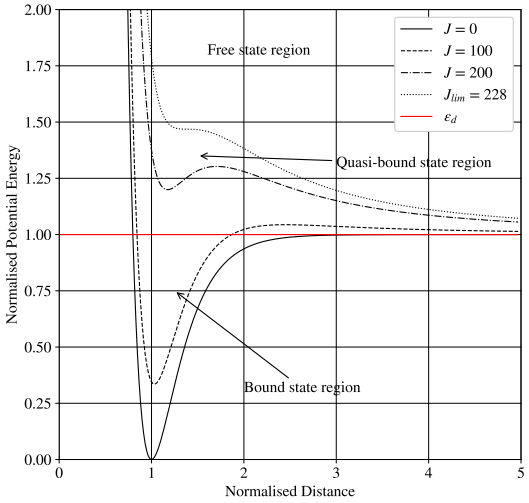

(b) Oxygen molecule.

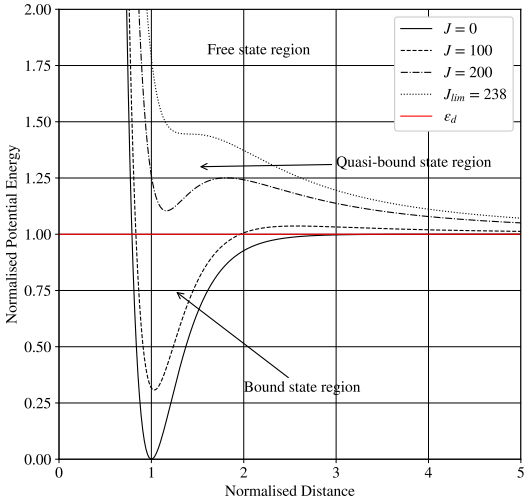

(c) Nitric oxide molecule.

Figure A.2: Potential energy curves at different rotational quantum levels for the ground electronic state of N_2, O_2 and NO.

Results and Discussion

Figure. A.3 compares the normalised isochoric specific heat capacity, i.e. $\frac{c_V}{R}$, of N_2, O_2 and NO against a compilation of theoretical studies [24, 28–30] for temperatures ranging from 0 to 20,000 K. The theoretical predictions of the previous approaches presented throughout this thesis are included for reference.

Figure. A.3 shows that a complete description of the interaction between the internal modes provides a better reproduction of the compilation of past studies for the entire range of temper-

atures. The discrepancy between the theoretical calculations and the past studies is the results of the assumption applied about the truncation of the vibrational energy and the selection of the electronic excited states. These calculations are herein reported to serve as a verification exercise for future implementation of the third approach presented in Fig. A.1 in a DSMC solver.

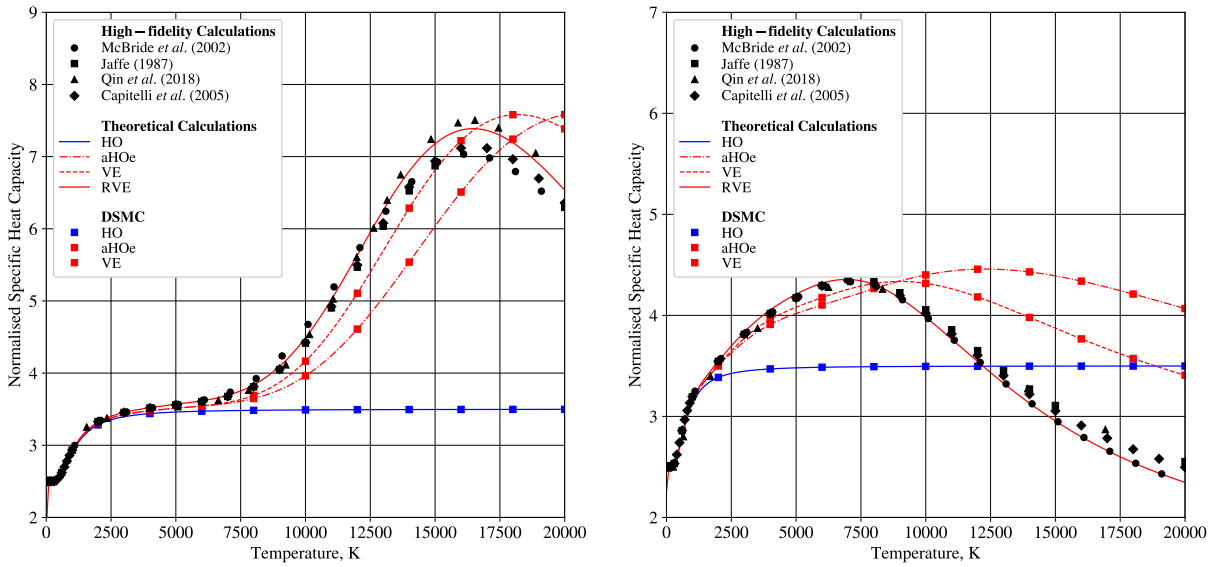

(a) Nitrogen molecule.

(b) Oxygen molecule.

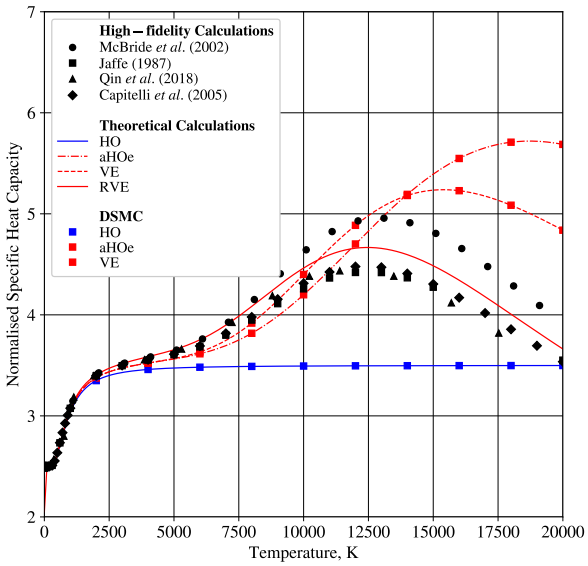

(c) Nitric oxide molecule.

Figure A.3: Normalised isochoric specific heat capacity of N_2, O_2 and NO.

Table. A.1 summarises the total number of quantum levels considered for each approach for N_2, O_2 and NO. The description of the interactions between the internal modes adds complexity to the mathematical modelling, to the extent of the addition of significant quantum levels. From a numerical perspective, the coupling of N internal modes results in a N-dimensional distribution function, see Eq. (A.1), on which sampling procedures, e.g. equilibrium and post-collisions, are performed. From Fig. A.3, it is clear that a fully coupled approach provides the best reproduction

of the past studies; however, it involves a total number of quantum levels that is two to three orders of magnitude higher than the uncoupled approach. This significant increase in the total number of quantum levels motivates the development of efficient sampling routines for such an approach to be considered in a DSMC solver.

Table A.1: Comparison of the total number of quantum levels considered for the three approaches for the most dominant diatomic species in Earth's atmosphere for each approach.

Chemical Species	Uncoupled*	Partially coupled†	Fully coupled‡
N_2	67	374	54,284
O_2	48	146	17,512
NO	59	245	28,477

*Continuum treatment of the rotational mode, anharmonic oscillator model and inclusion of the electronic modes.

†Continuum treatment of the rotational mode and coupling between the vibrational and electronic modes.

‡Quantised treatment of the rotational mode and full coupling between the internal modes.

Bibliography

[1] G. V. Candler. Rate effects in hypersonic flows. *Annual Review of Fluid Mechanics*, 51:379–402, 2019.

[2] J. Urzay. Supersonic combustion in air-breathing propulsion systems for hypersonic flight. *Annual Review of Fluid Mechanics*, 50:593–627, 2018.

[3] B. Chanetz, J. Délery, P. Gilliéron, P. Gnemmi, E. R. Gowree, and P. Perrier. Hypersonic wind tunnels. In *Experimental Aerodynamics: An Introductory Guide*, pages 135–164. Springer International Publishing, 2020.

[4] P. A. Gnoffo. Planetary–entry gas dynamics. *Annual Review of Fluid Mechanics*, 31(1):459–494, 1999.

[5] C. Park. *Nonequilibrium Hypersonic Aerothermodynamics*. John Wiley & Sons, 1st edition, 1990.

[6] J. D. Anderson. *Hypersonic and High-Temperature Gas Dynamics*. American Institute of Aeronautics and Astronautics, 3rd edition, 2019.

[7] Y. B. Zeldovich. The oxidation of nitrogen in combustion and explosions. *J. Acta Physicochimica*, 21:577, 1946.

[8] Y. B. Zeldovich, G. I. Barenblatt, V. B. Librovich, and G. M. Makhviladze. *Mathematical Theory of Combustion and Explosions*. Consultants Bureau, 1985.

[9] D. F. Potter. *Modelling of Radiating Shock Layers for Atmospheric Entry at Earth and Mars*. PhD thesis, University of Queensland, 2011.

[10] I. D. Boyd and T. E. Schwartzentruber. *Nonequilibrium Gas Dynamics and Molecular Simulation*, volume 42 of *Cambridge Aerospace Series*. Cambridge University Press Inc, 1st edition, 2017.

[11] G. A. Bird. Monte Carlo simulation of gas flows. *Annual Review of Fluid Mechanics*, 10(1):11–31, 1978.

[12] S. Chapman and T. G. Cowling. *The Mathematical Theory of Non-uniform Gases: An Account of the Kinetic Theory of Viscosity, Thermal Conduction and Diffusion in Gases*. Cambridge University Press, 3rd edition, 1970.

[13] D. Burnett. The distribution of velocities in a slightly non-uniform gas. *Proceedings of the London Mathematical Society*, s2-39(1):385–430, 1935.

[14] C. Cercignani. *Rarefied Gas Dynamics: From Basic Concepts to Actual Calculations*. Cambridge University Press, 2000.

[15] H. Grad. On the kinetic theory of rarefied gases. *Communications on Pure and Applied Mathematics*, 2(4):331–407, 1949.

[16] P. L. Bhatnagar, E. P. Gross, and M. Krook. A model for collision processes in gases. I. Small amplitude processes in charged and neutral one-component systems. *Physical Review*, 94:511–525, 1954.

[17] G. A. Bird. *Molecular Gas Dynamics and the Direct Simulation of Gas Flows*. Oxford University Press Inc, 1994.

[18] D. Espinosa. *An Open-Source Hybrid CFD-DSMC Solver for High-Speed Flows*. PhD thesis, University of Strathclyde, 2018.

[19] S. Mallikarjun, V. Casseau, W. G. Habashi, S. Gao, and A. Karchani. Hybrid Navier-Stokes-direct simulation Monte Carlo automatic mesh optimization for hypersonics. *Journal of Thermophysics and Heat Transfer*, pages 1–28, 2023.

[20] N. Vasileiadis and C. White. hybridDCFoam: A coupled DSMC/Navier–Stokes–Fourier solver for steady-state multiscale rarefied gas flows. *Advances in Engineering Software*, 193:103669, 2024.

[21] D. G. Goodwin, H. K. Moffat, and R. L. Speth. Cantera: An object-oriented software toolkit for chemical kinetics, thermodynamics, and transport processes, 2018.

[22] S. Gordon and B. J. McBride. Computer Program for Calculation of Complex Chemical Equilibrium Compositions and Applications I. Analysis. Technical Report RP-1311, National Aeronautics and Space Administration, October 1994.

[23] B. J. McBride and S. Gordon. Computer Program for Calculation of Complex Chemical Equilibrium Compositions and Applications II. Users Manual and Program Description. Technical Report RP-1311, National Aeronautics and Space Administration, June 1996.

[24] B. J. McBride, M. J. Zehe, and S. Gordon. NASA Glenn Coefficients for Calculating Thermodynamic Properties of Individual Species. Technical Report TP-2002-211556, National Aeronautics and Space Administration, September 2002.

[25] P. J. Linstrom and W. G. Mallard. *NIST Chemistry WebBook, NIST Standard Reference Database Number 69*. National Institute of Standards and Technology, (retrieved January 30, 2024).

[26] K. P. Huber and G. Herzberg. *Molecular Spectra and Molecular Structure*, volume 1. Springer, 1st edition, 1979.

[27] I. A. Leyva. The relentless pursuit of hypersonic flight. *Physics Today*, 70(11):30–36, 2017.

[28] M. Capitelli, G. Colonna, D. Giordano, L. Maraffa, A. Casavola, P. Minelli, D. Pagano, L.D. Pietanza, and F. Taccogna. Tables of Internal Partition Functions and Thermodynamic Properties of High-Temperature Mars-Atmosphere Species from 50 K to 50,000 K. Technical Report STR-246, European Space Agency Publications Division, October 2005.

[29] Z. Qin, J. M. Zhao, and L. H. Liu. High-temperature partition functions, specific heats and spectral radiative properties of diatomic molecules with an improved calculation of energy levels. *Journal of Quantitative Spectroscopy and Radiative Transfer*, 210:1–18, 2018.

[30] R. Jaffe. The calculation of high-temperature equilibrium and nonequilibrium specific heat data for N_2, O_2 and NO. In *22nd Thermophysics Conference*, Honolulu, HI, AIAA Paper 1987-1633, 1987.

[31] C. H. B. Civrais, C. White, and R. Steijl. Vibrational modeling with an anharmonic oscillator model in direct simulation Monte Carlo. *Journal of Thermophysics and Heat Transfer*, 37(3):534–548, 2022.

[32] C. H. B. Civrais, C. White, and R. Steijl. Extension of the normal shock wave relations for calorically imperfect gas. *Shock Waves*, 33:533–551, 2023.

[33] C. H. B. Civrais, C. White, and R. Steijl. Influence of anharmonic oscillator model for flows over a cylindrical body. *AIP Conference Proceedings*, 2996(1):080008, 2024.

[34] P. M. Morse. Diatomic molecules according to the wave mechanics. II. Vibrational levels. *Physical Review*, 34(1):57, 1929.

[35] J. L. Dunham. The energy levels of a rotating vibrator. *Physical Review*, 41(6):721, 1932.

[36] I. V. Adamovich and J. W. Rich. Three-dimensional nonperturbative analytic model of vibrational energy transfer in atom–molecule collisions. *The Journal of Chemical Physics*, 109(18):7711–7724, 1998.

[37] I. V. Adamovich, S. O. Macheret, J. W. Rich, and C. E. Treanor. Vibrational relaxation and dissociation behind shock waves. Part I - Kinetic rate models. *AIAA Journal*, 33(6):1064–1069, 1995.

[38] I. V. Adamovich. Three-dimensional analytic model of vibrational energy transfer in molecule-molecule collisions. *AIAA Journal*, 39(10):1916–1925, 2001.

[39] I. V. Adamovich. Three-dimensional analytic probabilities of coupled vibrational-rotational-translational energy transfer for DSMC modeling of nonequilibrium flows. *Physics of Fluids*, 26(4):046102, 04 2014.

[40] I. D. Boyd and E. Josyula. State resolved vibrational relaxation modeling for strongly nonequilibrium flows. *Physics of Fluids*, 23(5):057101, 2011.

[41] G. D. Billing and E. R. Fisher. VV and VT rate coefficients in N_2 by a quantum-classical model. *Chemical Physics*, 43(3):395–401, 1979.

[42] A. B. Weaver, V. Ayyaswamy, and A. Alexeenko. Implementation challenges and performance of forced harmonic oscillator model in direct simulation Monte Carlo. In *44th AIAA Thermophysics Conference*, San Diego, CA, AIAA Paper 2013-2783, 2013.

[43] H. Luo, A. A. Alexeenko, and S. O. Macheret. Development of an impulsive model of dissociation in direct simulation Monte Carlo. *Physics of Fluids*, 31(8):087105, 2019.

[44] S. O. Macheret and J. W. Rich. Nonequilibrium dissociation rates behind strong shock waves: Classical model. *Chemical Physics*, 174(1):25–43, 1993.

[45] Y. Babou, Ph. Rivière, M-Y. Perrin, and A. Soufiani. High-temperature and nonequilibrium partition function and thermodynamic data of diatomic molecules. *International Journal of Thermophysics*, 30(2):416–438, 2009.

[46] K. M. Hanquist, R. S. Chaudhry, I. D. Boyd, J. Streicher, A. Krish, and R. Hanson. Detailed thermochemical modeling of O_2-Ar mixtures in reflected shock tube flows. In *Virtual, AIAA AVIATION 2020 FORUM*, AIAA Paper 2020-3275, 2020.

[47] S. M. Jo, M. Panesi, and J. G. Kim. Prediction of shock standoff distance with modified rotational relaxation time of air mixture. *Physics of Fluids*, 33(4):047102, 04 2021.

[48] E. Pannier and C. O. Laux. RADIS: A nonequilibrium line-by-line radiative code for CO_2 and HITRAN-like database species. *Journal of Quantitative Spectroscopy and Radiative Transfer*, 222-223:12–25, 2019.

[49] J. Beyer, M. Pfeiffer, and S. Fasoulas. Non-equilibrium radiation modeling in a gas kinetic simulation code. *Journal of Quantitative Spectroscopy and Radiative Transfer*, 280:108083, 2022.

[50] M. L. da Silva, V. Guerra, and J. Loureiro. A review of non-equilibrium dissociation rates and models for atmospheric entry studies. *Plasma Sources Science and Technology*, 18(3):034023, 2009.

[51] M. L. da Silva, V. Guerra, J. Loureiro, and P. A. Sá. Vibrational distributions in N_2 with an improved calculation of energy levels using the RKR method. *Chemical Physics*, 348(1–3):187–194, 2008.

[52] A. B. Carlson and G. A. Bird. Implementation of a Vibrationally Linked Chemical Reaction Model for DSMC. Technical Report TM-109109, National Aeronautics and Space Administration, April 1994.

[53] J. Beyer, P. Nizenkov, S. Fasoulas, and M. Pfeiffer. Simulation of radiating non-equilibrium flows around a capsule entering Titan's atmosphere. *AIP Conference Proceedings*, 2996(1):200002, 2024.

[54] C. Park. Review of chemical-kinetic problems of future NASA missions, I: Earth entries. *Journal of Thermophysics and Heat Transfer*, 7(3):385–398, 1993.

[55] C. Park, J. T. Howe, R. L. Jaffe, and G. V. Candler. Review of chemical-kinetic problems of future NASA missions, II: Mars entries. *Journal of Thermophysics and Heat Transfer*, 8(1):9–23, 1994.

[56] D. L. Baulch, D. D. Drysdale, and D. Horne. *Evaluated Kinetic Data for High Temperature Reactions. Vol. 2: Homogeneous Gas Phase Reactions of the H_2 - N_2 - O_2 System*, volume 2. University of Leeds, 1973.

[57] S. R. Byron. Measurement of the rate of dissociation of oxygen. *The Journal of Chemical Physics*, 30(6):1380–1392, 1959.

[58] R. K. Hanson and D. Baganoff. Shock-tube study of nitrogen dissociation rates using pressure measurements. *AIAA Journal*, 10(2):211–215, 1972.

[59] D. J. Kewley and H. G. Hornung. Free-piston shock-tube study of nitrogen dissociation. *Chemical Physics Letters*, 25(4):531–536, 1974.

[60] D. F. Davidson and R. K. Hanson. High temperature reaction rate coefficients derived from N-atom ARAS measurements and excimer photolysis of NO. *International Journal of Chemical Kinetics*, 22(8):843–861, 1990.

[61] W. L. Flower R. K. Hanson and C. H. Kruger. Determination of the rate constant for the reaction $O + NO \rightarrow N + O_2$. *Combustion Science and Technology*, 9(3-4):79–86, 1974.

[62] E. Freedman and J. W. Daiber. Decomposition rate of nitric oxide between 3000 and 4300 K. *The Journal of Chemical Physics*, 34(4):1271–1278, 04 1961.

[63] K. L. Wray and J. D. Teare. Shock-tube study of the kinetics of nitric oxide at high temperatures. *The Journal of Chemical Physics*, 36(10):2582–2596, 05 1962.

[64] J. P. Monat, R. K. Hanson, and C. H. Kruger. Shock tube determination of the rate coefficient for the reaction $N_2 + O \rightarrow NO + N$. *Symposium (International) on Combustion*, 17(1):543–552, 1979. Seventeenth Symposium (International) on Combustion.

[65] K. Thielen and P. Roth. Resonance absorption measurements of N and O atoms in high temperature NO dissociation and formation kinetics. *Symposium (International) on Combustion*, 20(1):685–693, 1985. Twentieth Symposium (International) on Combustion.

[66] S. Byron. Shock-tube measurement of the rate of dissociation of nitrogen. *The Journal of Chemical Physics*, 44(4):1378–1388, 1966.

[67] J. P. Appleton, M. Steinberg, and D. J. Liquornik. Shock-tube study of nitrogen dissociation using vacuum-ultraviolet light absorption. *The Journal of Chemical Physics*, 48(2):599–608, 1968.

[68] M. Camac and A. Vaughan. O_2 dissociation rates in O_2-Ar mixtures. *The Journal of Chemical Physics*, 34(2):460–470, 1961.

[69] L. Jerig, K. Thielen, and P. Roth. High-temperature dissociation of oxygen diluted in argon or nitrogen. *AIAA Journal*, 29(7):1136–1139, 1991.

[70] O. P. Shatalov. Molecular dissociation of oxygen in the absence of vibrational equilibrium. *Combustion, Explosion and Shock Waves*, 9(5):610–613, 1973.

[71] A. Sergievskaya, E. Kovach, S. Losev, and N. Kuznetsov. Thermal nonequilibrium models for dissociation and chemical exchange reactions at high temperatures. In *31st Thermophysics Conference*, New Orleans, LA, AIAA Paper 96-1895, 1996.

[72] S. Losev, V. Makarov, and V. Nikolsky. Thermochemical nonequilibrium kinetic models in strong shock waves on air. In *6th Joint Thermophysics and Heat Transfer Conference*, Coloroda Springs, CO, AIAA Paper 94-1990, 1994.

[73] L. B. Ibraguimova, A. L. Sergievskaya, V. Y. Levashov, O. P. Shatalov, Y. V. Tunik, and I. E. Zabelinskii. Investigation of oxygen dissociation and vibrational relaxation at temperatures 4000–10,800 K. *The Journal of Chemical Physics*, 139(3):034317, 2013.

[74] B. A. Cruden and A. M. Brandis. Measurement of radiative non-equilibrium for air shocks between 7-9 km/s. In *47th AIAA Thermophysics Conference*, Denver, CO, AIAA Paper 2017-4535, 2017.

[75] J. W. Streicher, A. Krish, S. Wang, D. F. Davidson, and R. K. Hanson. Measurements of oxygen vibrational relaxation and dissociation using ultraviolet laser absorption in shock tube experiments. In *AIAA Scitech 2019 Forum*, San Diego, CA, AIAA Paper 2019-0795, 2019.

[76] J. W. Streicher, A. Krish, R. K. Hanson, K. M. Hanquist, R. S. Chaudhry, and I. D. Boyd. Shock-tube measurements of coupled vibration-dissociation time-histories and rate parameters in oxygen and argon mixtures from 5000 K to 10,000 K. *Physics of Fluids*, 32(7):076103, 2020.

[77] J. W. Streicher, A. Krish, and R. K. Hanson. Coupled vibration-dissociation time-histories and rate measurements in shock-heated, nondilute O_2 and O_2-Ar mixtures from 6000 to 14,000 K. *Physics of Fluids*, 33(5):056107, 2021.

[78] J. W. Streicher, A. Krish, and R. K. Hanson. High-temperature vibrational relaxation and decomposition of shock-heated nitric oxide: I. Argon dilution from 2200 to 8700 K. *Physics of Fluids*, 34(11), 2022.

[79] J. W. Streicher, A. Krish, and R. K. Hanson. High-temperature vibrational relaxation and decomposition of shock-heated nitric oxide: II. Nitrogen dilution from 1900 to 8200 K. *Physics of Fluids*, 34(11), 2022.

[80] J. W. Streicher, A. Krish, and R. K. Hanson. Laser absorption study of the $N_2 + O \rightarrow NO + N$ and $NO + O \rightarrow O_2 + N$ Zeldovich reactions in shock-heated N_2O mixtures. *Physics of Fluids*, 35(4), 2023.

[81] J. W. Streicher, S. C. Barnes, A. Krish, and R. K. Hanson. Vibrational-state-resolved oxygen and nitric oxide time-history measurements in shock-heated, high-temperature air. In *AIAA SCITECH 2024 Forum*, Orlando, FL, AIAA Paper 2024-0227, 2024.

[82] M. G. Dunn and S. Kang. Theoretical and Experimental Studies of Reentry Plasmas. Technical Report CR-2232, National Aeronautics and Space Administration, April 1973.

[83] C. Park and G. P. Menees. Odd nitrogen production by meteoroids. *Journal of Geophysical Research: Oceans*, 83(C8):4029–4035, 1978.

[84] K. L. Wray. *Chemical Kinetics of High Temperature Air*, chapter Chemical Kinetics of High Temperature Air, pages 181–204. Elsevier, 1962.

[85] R. S. Chaudhry, M. S. Grover, J. D. Bender, T. E. Schwartzentruber, and G. V. Candler. Quasiclassical trajectory analysis of oxygen dissociation via O_2, O, and N_2. In *2018 AIAA Aerospace Sciences Meeting*, Kissimmee, FL, AIAA Paper 2018-0237, 2018.

[86] R. S. Chaudhry and G. V. Candler. Statistical analyses of quasiclassical trajectory data for air dissociation. In *AIAA Scitech 2019 Forum*, San Diego, CA, AIAA Paper 2019-0789, 2019.

[87] S. M. Jo, S. Venturi, J. G. Kim, and M. Panesi. Rovibrational internal energy transfer and dissociation of high-temperature oxygen mixture. *The Journal of Chemical Physics*, 158(6), 2023.

[88] M. S. Grover and T. E. Schwartzentruber. Internal energy relaxation and dissociation in molecular oxygen using direct molecular simulation. In *47th AIAA Thermophysics Conference*, Denver, CO, AIAA Paper 2017-3488, 2017.

[89] M. S. Grover, E. Torres, and T. E. Schwartzentruber. Direct molecular simulation of internal energy relaxation and dissociation in oxygen. *Physics of Fluids*, 31(7):076107, 2019.

[90] E. Torres, E. C. Geistfeld, and T. E. Schwartzentruber. High-temperature nonequilibrium air chemistry from first principles. *Journal of Thermophysics and Heat Transfer*, 38(2):260–291, 2024.

[91] M. Kulakhmetov, M. Gallis, and A. Alexeenko. Effect of O_2 + O *ab initio* and Morse additive pairwise potentials on dissociation and relaxation rates for nonequilibrium flow calculations. *Physics of Fluids*, 27(8):087104, 2015.

[92] M. Kulakhmetov, M. Gallis, and A. Alexeenko. *Ab initio*-informed maximum entropy modeling of rovibrational relaxation and state-specific dissociation with application to the O_2 + O system. *The Journal of Chemical Physics*, 144(17):174302, 2016.

[93] D. A. Andrienko and I. D. Boyd. Rovibrational energy transfer and dissociation in O_2-O collisions. *The Journal of Chemical Physics*, 144(10):104301, 2016.

[94] F. Esposito and M. Capitelli. Quasiclassical trajectory calculations of vibrationally specific dissociation cross-sections and rate constants for the reaction O + $O_2(v) \rightarrow$ 3O. *Chemical Physics Letters*, 364(1):180–187, 2002.

[95] D. A. Andrienko and I. D. Boyd. Vibrational energy transfer and dissociation in O_2-N_2 collisions at hyperthermal temperatures. *The Journal of Chemical Physics*, 148(8):084309, 2018.

[96] F. Esposito and I. Armenise. Reactive, inelastic, and dissociation processes in collisions of atomic nitrogen with molecular oxygen. *The Journal of Physical Chemistry A*, 125(18):3953–3964, 2021.

[97] D. Andrienko and I. D. Boyd. Thermal relaxation of molecular oxygen in collisions with nitrogen atoms. *The Journal of Chemical Physics*, 145(1):014309, 2016.

[98] H. Luo, M. Kulakhmetov, and A. Alexeenko. *Ab initio* state-specific N_2 + O dissociation and exchange modeling for molecular simulations. *The Journal of Chemical Physics*, 146(7):074303, 02 2017.

[99] S. M. Jo, S. Venturi, M. P. Sharma, A. Munafò, and M. Panesi. Rovibrational-specific QCT and master equation study on $N_2(X^1\Sigma_g^+)$ + O(3P) and $NO(X^2\Pi)$ + N(4S) systems in high-energy collisions. *The Journal of Physical Chemistry A*, 126(21):3273–3290, 2022.

[100] D. Koner, J. C. S. V. Veliz, R. J. Bemish, and M. Meuwly. Accurate reproducing kernel-based potential energy surfaces for the triplet ground states of N_2O and dynamics for the N + NO $\leftrightarrow$ O + N_2 and N_2 + O $\rightarrow$ 2N + O reactions. *Physical Chemistry Chemical Physics*, 22(33):18488–18498, 2020.

[101] F. Esposito and I. Armenise. Reactive, inelastic, and dissociation processes in collisions of atomic oxygen with molecular nitrogen. *The Journal of Physical Chemistry A*, 121(33):6211–6219, 2017.

[102] J. D. Bender, P. Valentini, I. Nompelis, Y. Paukku, Z. Varga, D. G. Truhlar, T. E. Schwartzentruber, and G. V. Candler. An improved potential energy surface and multi-temperature quasiclassical trajectory calculations of N_2 + N_2 dissociation reactions. *The Journal of Chemical Physics*, 143(5):054304, 2015.

[103] R. L. Macdonald, R. L. Jaffe, D. W. Schwenke, and M. Panesi. Construction of a coarse-grain quasi-classical trajectory method. I. Theory and application to N_2–N_2 system. *The Journal of Chemical Physics*, 148(5):054309, 02 2018.

[104] T. K. Mankodi and R. S. Myong. Quasi-classical trajectory-based non-equilibrium chemical reaction models for hypersonic air flows. *Physics of Fluids*, 31(10):106102, 2019.

[105] P. Valentini, T. E. Schwartzentruber, J. D. Bender, I. Nompelis, and G. V. Candler. Direct molecular simulation of nitrogen dissociation based on an *ab initio* potential energy surface. *Physics of Fluids*, 27(8):086102, 08 2015.

[106] F. Esposito and M. Capitelli. Quasiclassical molecular dynamic calculations of vibrationally and rotationally state selected dissociation cross-sections: N + $N_2(v, j) \rightarrow$ 3N. *Chemical Physics Letters*, 302(1–2):49–54, 1999.

[107] R. Jaffe, D. Schwenke, and G. Chaban. Theoretical analysis of N_2 collisional dissociation and rotation-vibration energy transfer. In *47th AIAA Aerospace Sciences Meeting including The New Horizons Forum and Aerospace Exposition*, Orlando, FL, AIAA Paper 2009-1569, 2009.

[108] M. Panesi, R. L. Jaffe, D. W. Schwenke, and T. E. Magin. Rovibrational internal energy transfer and dissociation of $N_2(^1\Sigma_g^+)$-$N(^4S_u)$ system in hypersonic flows. *The Journal of Chemical Physics*, 138(4), 2013.

[109] J. G. Kim and I. D. Boyd. State-resolved master equation analysis of thermochemical nonequilibrium of nitrogen. *Chemical Physics*, 415:237–246, 2013.

[110] P. Valentini, T. E. Schwartzentruber, J. D. Bender, and G. V. Candler. Dynamics of nitrogen dissociation from direct molecular simulation. *Phys. Rev. Fluids*, 1:043402, Aug 2016.

[111] D. Andrienko and I. D. Boyd. State-resolved characterization of nitric oxide formation in shock flows. In *2018 AIAA Aerospace Sciences Meeting*, Kissimmee, FL, AIAA Paper 2018-1233, 2018.

[112] D. Bose and G. V. Candler. Thermal rate constants of the $N_2 + O \rightarrow NO + N$ reaction using *ab-initio* $^3a''$ and $^3a'$ potential energy surfaces. *The Journal of Chemical Physics*, 104(8):2825–2833, 1996.

[113] D. Bose and G. V. Candler. Simulation of hypersonic flows using a detailed nitric oxide formation model. *Physics of Fluids*, 9(4):1171–1181, 04 1997.

[114] D. Bose and G. V. Candler. Thermal rate constants of the $O_2 + N \rightarrow NO + O$ reaction based on the $a^{2\prime}$ and $a^{4\prime}$ potential-energy surfaces. *The Journal of Chemical Physics*, 107(16):6136–6145, 1997.

[115] T. K. Mankodi, U. V. Bhandarkar, and B. P. Puranik. Cross-sections for $O_2 + N$ system using the QCT method. *Chemical Physics Letters*, 704:21–26, 2018.

[116] J. C. San Vicente Veliz, D. Koner, M. Schwilk, R. J. Bemish, and M. Meuwly. The N(4S) + $O_2(X^3\Sigma_g^-) \longleftrightarrow$ O(3P) + $NO(X^2\Pi)$ reaction: thermal and vibrational relaxation rates for the $2A'$, $4A'$ and $2A''$ states. *Physical Chemistry Chemical Physics*, 22:3927–3939, 2020.

[117] C. E. Treanor and P. V. Marrone. Effect of dissociation on the rate of vibrational relaxation. *The Physics of Fluids*, 5(9):1022–1026, 1962.

[118] P. V. Marrone and C. E. Treanor. Chemical relaxation with preferential dissociation from excited vibrational levels. *The Physics of Fluids*, 6(9):1215–1221, 1963.

[119] S. A. Losev, B. V. Potapkin, S. O. Macheret, and G. G. Chernyi. *Physical and Chemical Processes in Gas Dynamics: Physical and Chemical Kinetics and Thermodynamics of Gases and Plasmas, Volume II*. American Institute of Aeronautics and Astronautics, 2002.

[120] R. B. Bernstein. *Atom-Molecule Collision Theory: A Guide for the Experimentalist*. Plenum Press, June 1979.

[121] T. E. Schwartzentruber, M. S. Grover, and P. Valentini. Direct molecular simulation of nonequilibrium dilute gases. *Journal of Thermophysics and Heat Transfer*, 32(4):892–903, 2018.

[122] P. Norman, P. Valentini, and T. Schwartzentruber. GPU-accelerated classical trajectory calculation direct simulation Monte Carlo applied to shock waves. *Journal of Computational Physics*, 247:153–167, 2013.

[123] D. Bruno, A. Frezzotti, and G. P. Ghiroldi. Oxygen transport properties estimation by classical trajectory–direct simulation Monte Carlo. *Physics of Fluids*, 27(5):057101, 05 2015.

[124] M. S. Grover and P. Valentini. *Ab initio* simulation of hypersonic flows past a cylinder based on accurate potential energy surfaces. *Physics of Fluids*, 33(5):051704, 2021.

[125] M. S. Grover, P. Valentini, T. E. Schwartzentruber, R. L. Jaffe, N. J. Bisek, and A. M. Verhoff. Comparative analysis of internal energy excitation and dissociation of nitrogen predicted by independently developed *ab initio* potential energy surfaces. *Physical Review Fluids*, 7:123401, 2022.

[126] Z. Gu and W. Ubachs. A systematic study of Rayleigh-Brillouin scattering in air, N_2, and O_2 gases. *The Journal of Chemical Physics*, 141(10):104320, 09 2014.

[127] D. Bruno, A. Frezzotti, and G. P. Ghiroldi. Rayleigh–Brillouin scattering in molecular oxygen by CT-DSMC simulations. *European Journal of Mechanics - B/Fluids*, 64:8–16, 2017. Special Issue on Non-equilibrium Gas Flows.

[128] M. S. Grover, A. M. Verhoff, P. Valentini, and N. J. Bisek. First principles simulation of reacting hypersonic flow over a blunt wedge. *Physics of Fluids*, 35(8):086106, 08 2023.

[129] P. Valentini, M. S. Grover, A. M. Verhoff, and N. J. Bisek. Near-continuum, hypersonic oxygen flow over a double cone simulated by direct simulation Monte Carlo informed from quantum chemistry. *Journal of Fluid Mechanics*, 966:A32, 2023.

[130] G. A. Bird. The QK model for gas-phase chemical reaction rates. *Physics of Fluids*, 23(10):106101, 2011.

[131] C. Borgnakke and P. S. Larsen. Statistical collision model for Monte Carlo simulation of polyatomic gas mixture. *Journal of Computational Physics*, 18(4):405–420, 1975.

[132] M. A. Gallis, R. B. Bond, and J. R. Torczynski. A kinetic-theory approach for computing chemical-reaction rates in upper-atmosphere hypersonic flows. *The Journal of Chemical Physics*, 131(12):124311, 2009.

[133] T. J. Scanlon, C. White, M. K. Borg, R. C. Palharini, E. Farbar, I. D. Boyd, J. M. Reese, and R. E. Brown. Open–source direct simulation Monte Carlo chemistry modeling for hypersonic flows. *AIAA Journal*, 53(6):1670–1680, 2015.

[134] R. M. Wagnild and M. A. Gallis. Continuum Simulations of Hypersonic Flows in Chemical and Thermal Nonequilibrium. *Journal of Thermophysics and Heat Transfer*, 32(4):846–860, 2018.

[135] C. H. B. Civrais, C. White, and R. Steijl. Evaluation of a kinetic-theory approach for chemical reaction rates in upper-atmosphere hypersonic flows. In *AIAA AVIATION 2023 Forum*, San Diego, CA & Virtual, AIAA Paper 2023-3809, 2023.

[136] C. H. B. Civrais, C. White, and R. Steijl. Quantum kinetics chemistry models with an anharmonic oscillator model. Model derivation and limitations. *Physics of Fluids*, 36(8):086120, 08 2024.

[137] C. H. B. Civrais, C. White, and R. Steijl. Quantum kinetics chemistry models with an anharmonic oscillator model. Model extension and validation. *Physics of Fluids*, (submitted).

[138] S. N. Dhurandhar and A. Bansal. Chemical kinetics study in rarefied martian atmosphere using quantum kinetics model. *Physics of Fluids*, 30(11):117104, 2018.

[139] D. Gao, B. He, C. Wu, G. Cai, and L. Liu. Post-reaction internal energy distributions of quantum-kinetics model for simulating chemical reactions of polyatomic molecules. *Physics of Fluids*, 35(1):017120, 2023.

[140] M. Maigler, V. Pessina, and J. Schein. Predicting lift and drag coefficients during hypersonic Mars reentry using hyStrath. *Physics of Fluids*, 36(4):046105, 2024.

[141] D. S. Liechty and M. J. Lewis. Extension of the quantum-kinetic model to lunar and Mars return physics. *Physics of Fluids*, 26(2):027106, 2014.

[142] S. Trivedi, R. S. Cant, and J. K. Harvey. Molecular level simulations of combustion processes using the DSMC method. *Combustion Theory and Modelling*, 25(2):351–363, 2021.

[143] B. L. Haas and I. D. Boyd. Models for direct Monte Carlo simulation of coupled vibration–dissociation. *Physics of Fluids A: Fluid Dynamics*, 5(2):478–489, 1993.

[144] D. C. Wadsworth and I. J. Wysong. Vibrational favoring effect in DSMC dissociation models. *Physics of Fluids*, 9(12):3873–3884, 1997.

[145] H. Luo, I. B. Sebastião, A. A. Alexeenko, and S. O. Macheret. Classical impulsive model for dissociation of diatomic molecules in direct simulation Monte Carlo. *Physical Review Fluids*, 3(11):113401, 2018.

[146] H. Luo, A. A. Alexeenko, and S. O. Macheret. Assessment of classical impulsive models of dissociation in thermochemical nonequilibrium. *Journal of Thermophysics and Heat Transfer*, 32(4):861–868, 2018.

[147] I. J. Wysong and S. F. Gimelshein. Comparison of DSMC reaction models with QCT reaction rates for nitrogen. In *AIP Conference Proceedings*, volume 1786. AIP Publishing, 2016.

[148] I. D. Boyd, D. Bose, and G. V. Candler. Monte Carlo modeling of nitric oxide formation based on quasi-classical trajectory calculations. *Physics of Fluids*, 9(4):1162–1170, 1997.

[149] D. Liechty and M. Lewis. Treatment of electronic energy level transition and ionization following the particle-based chemistry model. In *48th AIAA Aerospace Sciences Meeting Including the New Horizons Forum and Aerospace Exposition*, Orlando, FL, AIAA Paper 2010-449, 2010.

[150] F. Bergemann and I. D. Boyd. New discrete vibrational energy model for the direct simulation Monte Carlo method. In *Rarefied Gas Dynamics: Experimental Techniques and Physical Systems*, pages 174–183. American Institute of Aeronautics and Astronautics, 1994.

[151] G. A. Bird. Nonequilibrium radiation during re-entry at 10 km/s. In *22nd Thermophysics Conference*, Honolulu, HI, AIAA Paper 1987-1543, 1987.

[152] A. B. Carlson and H. A. Hassan. Radiation modeling with direct simulation Monte Carlo. *Journal of Thermophysics and Heat Transfer*, 6(4):631–636, 1992.

[153] J. C. Taylor, A. B. Carlson, and H. A. Hassan. Monte Carlo simulation of radiating reentry flows. *Journal of Thermophysics and Heat Transfer*, 8(3):478–485, 1994.

[154] J. M. Burt and E. Josyula. DSMC modeling of nonequilibrium electronic excitation and emission for hypersonic sensor applications. In *45th AIAA Thermophysics Conference*, Dallas, TX, AIAA Paper 2015-2511, 2015.

[155] J. M. Burt and E. Josyula. Direct simulation Monte Carlo modeling of gas electronic excitation for hypersonic sensing. *Journal of Thermophysics and Heat Transfer*, 31(4):858–870, 2017.

[156] Z. Li, T. Ozawa, I. Sohn, and D. A. Levin. Modeling of electronic excitation and radiation in non-continuum hypersonic reentry flows. *Physics of Fluids*, 23(6):066102, 2011.

[157] M. A. Gallis and J. K. Harvey. Nonequilibrium thermal radiation from air shock layers modeled with direct simulation Monte Carlo. *Journal of Thermophysics and Heat Transfer*, 8(4):765–772, 1994.

[158] M. A. Gallis and J. K. Harvey. Atomic species radiation from air shock layers modelled with DSMC. In *6th Joint Thermophysics and Heat Transfer Conference*, Colorado Springs, CO, AIAA Paper 1994-2018, 1994.

[159] A. J. Smith. ESA plasma RAdiation DatabasE (PARADE). development history, status, current developments and future prospects. In *Radiation of High Temperature Gases in Atmospheric Entry*, volume 533 of *ESA Special Publication*, pages 75–83, Noordwijk, The Netherlands, 2003.

[160] A. M. Brandis and B. A. Cruden. NEQAIR V15.0 Release Notes: Nonequilibrium and Equilibrium Radiative Transport and Spectra Program. Technical Report ARC-E-DAA-TN72963, National Aeronautics and Space Administration, November 2019.

[161] C. O. Laux. *Optical Diagnostics and Radiative Emission of Air Plasmas*. PhD thesis, Stanford University, 1993.

[162] C. J. Capon, M. Brown, C. White, T. Scanlon, and R. R. Boyce. pdFOAM: A PIC-DSMC code for near-Earth plasma-body interactions. *Computers & Fluids*, 149:160–171, 2017.

[163] T. Binder, M. Pfeiffer, and S. Fasoulas. Validation of grid current simulations using the particle-in-cell method for a miniaturized ion thruster. *AIP Conference Proceedings*, 2132(1):040003, 2019.

[164] R. Jambunathan and D. A. Levin. Kinetic, 3-D, PIC-DSMC simulations of ion thruster plumes and the backflow region. *IEEE Transactions on Plasma Science*, 48(6):2017–2034, 2020.

[165] I. T. Karpuzcu, M. P. Jouffray, and D. A. Levin. Collisional radiative modeling of electronically excited states in a hypersonic flow. *Journal of Thermophysics and Heat Transfer*, 36(4):982–1002, 2022.

[166] T. Ozawa, D. A. Levin, A. Wang, and M. Modest. Development of coupled particle hypersonic flowfield–photon Monte Carlo radiation methods. *Journal of Thermophysics and Heat Transfer*, 24(3):612–622, 2010.

[167] I. Sohn, Z. Li, D. A. Levin., and M. F. Modest. Coupled DSMC-PMC radiation simulations of a hypersonic reentry. *Journal of Thermophysics and Heat Transfer*, 26(1):22–35, 2012.

[168] C. H. B. Civrais, M. Pfeiffer, C. White, and R. Steijl. Modelling of the electronic excited states in high-temperature flows. *Physics of Fluids*, 36(8):086112, 2024.

[169] C. H. B. Civrais, C. White, R. Steijl, and M. Pfeiffer. Development of a coupled vibrational-electronic model in DSMC. *AIP Conference Proceedings (in preparation)*, 2024.

[170] P. W. Atkins and R. S. Friedman. *Molecular Quantum Mechanics*. Oxford University Press Inc, 5th edition, 2011.

[171] J. P. Lowe and K. Peterson. *Quantum Chemistry*. Elsevier, 3rd edition, 2011.

[172] S. Schrödinger. An undulatory theory of the mechanics of atoms and molecules. *Physical Review*, 28(6):1049, 1926.

[173] F. Jensen. *Introduction to Computational Chemistry*. John Wiley & Sons, 1st edition, 2017.

[174] W. G. Vincenti and C. H. Kruger. *Introduction to Physical Gas Dynamics*. John Wiley & Sons, 1965.

[175] D. C. Catling and J. F. Kasting. *Atmospheric Evolution on Inhabited and Lifeless Worlds*. Cambridge University Press Inc, 2017.

[176] G. A. Bird. Approach to translational equilibrium in a rigid sphere gas. *The Physics of Fluids*, 6(10):1518–1519, 1963.

[177] G. A. Bird. Definition of mean free path for real gases. *The Physics of Fluids*, 26(11):3222–3223, 1983.

[178] G. A. Bird. Perception of numerical methods in rarefied gasdynamics. In *Rarefied Gas Dynamics: Theoretical and Computational Techniques*, volume 118, pages 211–226. American Institute of Aeronautics and Astronautics, 1989.

[179] W. Wagner. A convergence proof for Bird's direct simulation Monte Carlo method for the Boltzmann equation. *Journal of Statistical Physics*, 66(3):1011–1044, 1992.

[180] G. A. Bird. *The DSMC Method*. CreateSpace Independent Publishing Platform, 2013.

[181] M. S. Ivanov and S. V. Rogasinsky. Theoretical analysis of traditional and modern schemes of the DSMC method. In *Proceeding International Symposium Rarefied Gas Dynamics 17th*, pages 629–642, 1991.

[182] K. Koura. Null-collision technique in the direct-simulation Monte Carlo method. *The Physics of Fluids*, 29(11):3509–3511, 11 1986.

[183] O. M. Belotserkovskii and V. E. Yanitskii. The statistical particles-in-cells method for solving rarefied gas dynamics problems. *USSR Computational Mathematics and Mathematical Physics*, 15(5):101–114, 1975.

[184] E. Roohi and S. Stefanov. Collision partner selection schemes in DSMC: From micro/-nano flows to hypersonic flows. *Physics Reports*, 656:1–38, 2016.

[185] C. White. *Benchmarking, Development and Applications of an Open Source DSMC Solver*. PhD thesis, University of Strathclyde, 2013.

[186] C. N. Hinshelwood. *The Kinetics of Chemical Change*. Clarendon Press, 1940.

[187] G. A. Bird. A comparison of collision energy-based and temperature-based procedures in DSMC. *AIP Conference Proceedings*, 1084:245–250, 2008.

[188] D. S. Liechty. *Extension of a Kinetic Approach to Chemical Reactions to Electronic Energy Levels and Reactions Involving Charged Species with Application to DSMC Simulations*. PhD thesis, University of Maryland, 2013.

[189] T. J. Scanlon, E. Roohi, C. White, M. Darbandi, and J. M. Reese. An open source, parallel DSMC code for rarefied gas flows in arbitrary geometries. *Computers & Fluids*, 39(10):2078–2089, 2010.

[190] G. B. Macpherson. *Molecular Dynamics Simulation in Arbitrary Geometries for Nanoscale Fluid Mechanics*. PhD thesis, University of Strathclyde, 2008.

[191] M. K. Borg. *Hybrid Molecular-Continuum Modelling of Nano-Scale Flows*. PhD thesis, University of Strathclyde, 2010.

[192] H. C. Weller, G. Tabor, H. Jasak, and C. Fureby. A tensorial approach to computational continuum mechanics using object-oriented techniques. *Computers in Physics*, 12(6):620–631, 1998.

[193] C. White, M. K. Borg, T. J. Scanlon, S. Longshaw, B. John, D. R. Emerson, and J. M. Reese. dsmcFoam+: An OpenFOAM based direct simulation Monte Carlo solver. *Computer Physics Communications*, 224:22–43, 2018.

[194] I. Armenise and F. Esposito. N_2, O_2, NO state-to-state vibrational kinetics in hypersonic boundary layers: The problem of rescaling rate coefficients to uniform vibrational ladders. *Chemical Physics*, 446:30–46, 2015.

[195] A. J. Eggers. One-Dimensional Flows of an Imperfect Diatomic Gas. Technical Report TR-959, National Advisory Committee for Aeronautics, January 1949.

[196] NASA Ames Research Staff. Charts for Compressible Flow. Technical Report TR-1135, National Aeronautics and Space Administration, January 1953.

[197] M. Schouler, Y. Prévereaud, and L. Mieussens. IXV post-flight reconstruction and analysis of the aerothermodynamic measurements along the rarefied portion of the reentry trajectory. *International Journal of Heat and Mass Transfer*, 178:121582, 2021.

[198] National Oceanic and Atmospheric Administration. U.S. Standard Atmosphere. Technical Report TM-X-74335, National Aeronautics and Space Administration, October 1976.

[199] D. Liechty, C. Johnston, and M. Lewis. Comparison of DSMC and CFD solutions of Fire II including radiative heating. In *42nd AIAA Thermophysics Conference*, Honolulu, HI, AIAA Paper 2011–3494, 2011.

[200] T. Ozawa, Z. Li, I. Sohn, and D. Levin. Modeling of electronic excitation and radiation for hypersonic re-entry flows in DSMC. In *48th AIAA Aerospace Sciences Meeting Including the New Horizons Forum and Aerospace Exposition*, Orlando, FL, AIAA Paper 2010-987, 2010.

[201] M. Pfeiffer, J. Beyer, J. Vaubaillon, P. Matlovič, J. Tóth, S. Fasoulas, and S. Löhle. Numerical simulation of an iron meteoroid entering into Earth's atmosphere using DSMC and a radiation solver with comparison to ground testing data. *Icarus*, 407:115768, 2024.

[202] R. B. Bond, M. A. Gallis, and J. R. Torczynski. DSMC predictions of non-equilibrium reaction rates. *AIP Conference Proceedings*, 1333:1203–1208, 2011.

[203] M. A. Gallis, R. B. Bond, and J. R. Torczynski. Assessment of collisional-energy-based models for atmospheric species reactions in hypersonic flows. *Journal of Thermophysics and Heat Transfer*, 24(2):241–253, 2010.

[204] O. Kunova, E. Kustova, and A. Savelev. Generalized Treanor-Marrone model for state-specific dissociation rate coefficients. *Chemical Physics Letters*, 659:80–87, 2016.

[205] E. Kustova, E. Nagnibeda, G. Oblapenko, A. Savelev, and I. Sharafutdinov. Advanced models for vibrational-chemical coupling in multi-temperature flows. *Chemical Physics*, 464:1–13, 2016.

[206] M. Capitelli, F. Esposito, E. V. Kustova, and E. A.Nagnibeda. Rate coefficients for the reaction $N_2(i) + N \rightarrow 3N$: a comparison of trajectory calculations and the Treanor-Marrone model. *Chemical Physics Letters*, 330(1–2):207–211, 2000.

[207] Y. Paukku, Z. Varga, and D. G. Truhlar. Potential energy surface of triplet O_4. *The Journal of Chemical Physics*, 148(12):124314, 2018.

[208] E. Nikitin. *Theory of Elementary Atomic and Molecular Processes in Gases*. Clarendon Press, 1974.

[209] I. D. Boyd. Modelling of associative ionization reactions in hypersonic rarefied flows. *Physics of Fluids*, 19(9):096102, 2007.

[210] I. D. Boyd. Modeling backward chemical rate processes in the direct simulation Monte Carlo method. *Physics of Fluids*, 19(12), 2007.

[211] S. F. Gimelshein and I. J. Wysong. Nonequilibrium air flow predictions with a high-fidelity direct simulation Monte Carlo approach. *Physical Review Fluids*, 4(3):033405, 2019.

[212] J. N. Moss and G. A. Bird. Direct simulation of transitional flow for hypersonic reentry conditions. *Journal of Spacecraft and Rockets*, 40(5):830–843, 2003.

[213] J. Shinn, J. Moss, and A. Simmonds. Viscous-shock-layer heating analysis for the shuttle windward-symmetry plane with surface finite catalytic recombination rates. In *3rd Joint Thermophysics, Fluids, Plasma and Heat Transfer Conference*, St. Louis, MO, AIAA Paper 1982-0842, 1982.

[214] T. K. Mankodi, U. V. Bhandarkar, and B. P. Puranik. Hypersonic flow over Stardust re-entry capsule using *ab-initio* based chemical reaction model. *Acta Astronautica*, 162:243–255, 2019.

[215] J. C. Adams, Jr., W. R. Martindale, A. W. Mayne, Jr., and E. O. Marchand. Real Gas Scale Effects on Hypersonic Laminar Boundary-Layer Parameters Including Effects of Entropy-Layer Swallowing. Technical Report AEDC-TR-75-2, Arnold Engineering Development Center (XO), Arnold Air Force Station, TN, October 1974.

[216] D. A. Throckmorton. Benchmark determination of shuttle orbiter entry aerodynamic heat-transfer data. *Journal of Spacecraft and Rockets*, 20(3):219–224, 1983.

[217] V. E. Zoby. Analysis of STS-2 experimental heating rates and transition data. *Journal of Spacecraft and Rockets*, 20(3):232–237, 1983.

[218] P. A. Gnoffo. Conservation Equations and Physical Models for Hypersonic Air Flows in Thermal and Chemical Nonequilibrium. Technical Report TP-2867, National Aeronautics and Space Administration, 1989.

[219] G. Colonna, I Armenise, D. Bruno, and M. Capitelli. Reduction of state-to-state kinetics to macroscopic models in hypersonic flows. *Journal of Thermophysics and Heat Transfer*, 20(3):477–486, 2006.

[220] M. Panesi, T. E. Magin, A. Bourdon, A. Bultel, and O. Chazot. Electronic excitation of atoms and molecules for the FIRE II flight experiment. *Journal of Thermophysics and Heat Transfer*, 25(3):361–374, 2011.

[221] A. Munafò, N. N. Mansour, and M. Panesi. A reduced-order NLTE kinetic model for radiating plasmas of outer envelopes of stellar atmospheres. *The Astrophysical Journal*, 838(2):126, 2017.

[222] D. S. Liechty and M. Lewis. Electronic energy level transition and ionization following the quantum-kinetic chemistry model. *Journal of Spacecraft and Rockets*, 48(2):283–290, 2011.

[223] G. A. Bird. Sophisticated DSMC. In *Notes prepared for a short course at the DSMC07 meeting*. Sandia National Laboratories, September 2007.

[224] T. E. Magin, M. Panesi, A. Bourdon, R. L. Jaffe, and D. W. Schwenke. Coarse-grain model for internal energy excitation and dissociation of molecular nitrogen. *Chemical Physics*, 398:90–95, 2012.

[225] J. G. Kim and I. D. Boyd. Monte Carlo simulation of nitrogen dissociation based on state-resolved cross sections. *Physics of Fluids*, 26(1):012006, 2014.

[226] I. D. Boyd. Rotational–translational energy transfer in rarefied nonequilibrium flows. *Physics of Fluids A: Fluid Dynamics*, 2(3):447–452, 1990.

[227] I. D. Boyd. Relaxation of discrete rotational energy distributions using a Monte Carlo method. *Physics of Fluids A: Fluid Dynamics*, 5(9):2278–2286, 1993.

[228] B. A. Cruden. Absolute Radiation Measurements in Earth and Mars Entry Conditions. Technical Report ARC-E-DAA-TN13965, National Aeronautics and Space Administration, April 2014.

[229] B. A. Cruden and D. W. Bogdanoff. Shock radiation tests for Saturn and Uranus entry probes. *Journal of Spacecraft and Rockets*, 54(6):1246–1257, 2017.

[230] B. A. Cruden and A. M. Brandis. Measurement of radiative nonequilibrium for air shocks between 7 and 9 km/s. *Journal of Thermophysics and Heat Transfer*, 34(1):154–180, 2020.

[231] K. J. Higdon, B. A. Cruden, A. M. Brandis, D. S. Liechty, D. B. Goldstein, and P. L. Varghese. Direct simulation Monte Carlo shock simulation of Saturn entry probe conditions. *Journal of Thermophysics and Heat Transfer*, 32(3):680–690, 2018.